LEABHARLANN CHOLÁISTE NA TRÍONÓIDE, BAILE ÁTHA CLIATH | TRINITY COLLEGE LIBRARY DUBLIN
Ollscoil Átha Cliath | The University of Dublin

Terms and Conditions of Use of Digitised Theses from Trinity College Library Dublin

Copyright statement

All material supplied by Trinity College Library is protected by copyright (under the Copyright and Related Rights Act, 2000 as amended) and other relevant Intellectual Property Rights. By accessing and using a Digitised Thesis from Trinity College Library you acknowledge that all Intellectual Property Rights in any Works supplied are the sole and exclusive property of the copyright and/or other IPR holder. Specific copyright holders may not be explicitly identified. Use of materials from other sources within a thesis should not be construed as a claim over them.

A non-exclusive, non-transferable licence is hereby granted to those using or reproducing, in whole or in part, the material for valid purposes, providing the copyright owners are acknowledged using the normal conventions. Where specific permission to use material is required, this is identified and such permission must be sought from the copyright holder or agency cited.

Liability statement

By using a Digitised Thesis, I accept that Trinity College Dublin bears no legal responsibility for the accuracy, legality or comprehensiveness of materials contained within the thesis, and that Trinity College Dublin accepts no liability for indirect, consequential, or incidental, damages or losses arising from use of the thesis for whatever reason. Information located in a thesis may be subject to specific use constraints, details of which may not be explicitly described. It is the responsibility of potential and actual users to be aware of such constraints and to abide by them. By making use of material from a digitised thesis, you accept these copyright and disclaimer provisions. Where it is brought to the attention of Trinity College Library that there may be a breach of copyright or other restraint, it is the policy to withdraw or take down access to a thesis while the issue is being resolved.

Access Agreement

By using a Digitised Thesis from Trinity College Library you are bound by the following Terms & Conditions. Please read them carefully.

I have read and I understand the following statement: All material supplied via a Digitised Thesis from Trinity College Library is protected by copyright and other intellectual property rights, and duplication or sale of all or part of any of a thesis is not permitted, except that material may be duplicated by you for your research use or for educational purposes in electronic or print form providing the copyright owners are acknowledged using the normal conventions. You must obtain permission for any other use. Electronic or print copies may not be offered, whether for sale or otherwise to anyone. This copy has been supplied on the understanding that it is copyright material and that no quotation from the thesis may be published without proper acknowledgement.

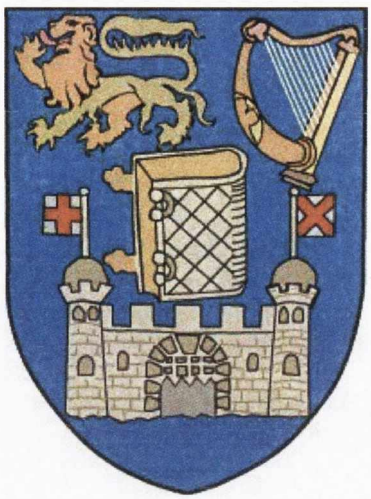

Atomistic models and time-dependent simulations of spin dynamics in isolated and current-carrying systems

by

Anna Pertsova

A thesis submitted for the degree of
Doctor of Philosophy

School of Physics
Trinity College Dublin

August 2012

TRINITY COLLEGE
2 4 MAY 2013
LIBRARY DUBLIN

Thesis 10028

Declaration

I, Anna Pertsova, hereby declare that this thesis has not been submitted as an exercise for a degree at this or any other University.

It comprises work performed entirely by myself during the course of my Ph.D. studies at Trinity College Dublin. I was involved in a number of collaborations, and where it is appropriate my collaborators are acknowledged for their contributions.

I agree that the Library may lend or copy this thesis upon request.

The dimmed outlines of phenomenal things all merge into one another unless we put on the focusing-glass of theory, and screw it up sometimes to one pitch of definition and sometimes to another, so as to see down into different depths through the great millstone of the world.

James Clerk Maxwell

Abstract

Understanding and ultimately controlling the dynamics of electrons and their spins is an important aspect of spin-based electronics. Recent experimental advances open up new possibilities for probing spin dynamics with very high spatial and temporal resolution, i.e. in atomic-sized systems and at sub-picosecond time scales. At these lengths and times quantum effects and atomistic details can not be neglected and the applicability of classical models is limited. Therefore, there is a need to develop new methodologies and computational tools for atomistic modeling of spin dynamics, in particular in the presence of electric currents. In this Thesis we construct a computational scheme, capable of describing the time evolution of spin systems both in isolation and under current-carrying conditions. The method has been developed in the spirit of the tight-binding model but it is transferable to more accurate first-principles methods such as density functional theory. This computational tool is then used to investigate time-dependent phenomena in the systems of interest.

Firstly, we study the dynamical response to external excitations of itinerant electrons in atomic chains. The calculated excitation spectra reveal a number of interesting features, characteristic of one-dimensional fermionic systems. Secondly, we explore the possibility of electrostatic gate control of the dynamical exchange interaction between two well-separated localized spin-impurities, linked by a mono-atomic chain. The spin dynamics is treated at the Ehrenfest level, with the interaction between the impurity spins and the itinerant electrons spins described by the s-d model. We demonstrate that by applying an electrostatic gate in the middle of the chain particular resonance conditions can be triggered, for which the dynamics becomes highly non-linear.

Finally, we present a time-dependent study of electron transport in a strongly correlated quantum dot. This is described within the framework of adiabatic lattice density functional theory, equipped with a novel exchange-correlation functional, specifically tailored to deal with electron correlations in one-dimensional systems. In agreement with earlier findings, we show that Coulomb blockade manifests itself in the time-dependent transport as a dynamical state with rapidly oscillating currents and charge

densities. In addition, we calculate, from dynamical simulations in the long-time limit, the I-V characteristics of the dot and the linear-response conductance as a function of the gate voltage. In particular, we find a negative differential conductance (NDC) at some critical bias voltages, which becomes more pronounced with increasing the strength of the electron-electron interaction on the dot. Although calculations at the mean-field (Hartree) level do not reproduce this result, we show that the NDC is primarily caused by the finite bandwidth of the electrodes. This is a strong indication that in the calculations performed with methods, that do not explicitly use the wideband approximation in the electrodes, one needs to carefully subtract the finite-bandwidth effects, in order to attribute NDC solely to electron-electron interactions.

Acknowledgements

I am indebted to many people for their help and guidance during the time, which I spent working on this dissertation.

First of all I would like to thank my supervisor Prof. Stefano Sanvito for his continuous help, guidance and support during my Ph.D. studies. His enthusiasm, insight into science and dedication to research have been an inspiration for me and working under his supervision has been an incredible privilege.

I would also like to express my gratitude to Dr. Maria Stamenova, from whom I have learned about spin dynamics and who helped me with different matters during my Ph.D. studies. Her input to this work, through her ideas, insights and expertise, is very much appreciated.

Next, I would like to thank Prof. Tchavdar Todorov, who has greatly influenced the direction of this Thesis through his own work and has provided advice and assistance in the final stages of the dissertation.

I am truly thankful to my examiners Prof. Stefan Kurth and Prof. Mauro Ferreira for their time, exceptionally helpful comments and inspiring discussions during the Viva. Prof. Ferreira, who is also the Director of Postgraduate studies in the School of Physics, has offered his full support and assistance during the submission process, for which I am very grateful.

Special thanks goes to Prof. Anatoly Vladimirovich Vedyayev, who was my supervisor during the undergraduate studies in Moscow State University. Without his help I would not have come this far.

I also owe a great deal of gratitude to all my colleagues in the Computational Spintronics Group. In particular, I would like to thank Ivan Rungger and Aaron Hurley for reading my papers and for providing insightful comments. I also thank Ivan for useful discussions about my work. I am grateful to Mauro Mantega, who has actually finished his Ph.D. at the same time as me, for providing some data on DFT calculations

for silicon. I thank Awadhesh Narayan for helping me with the tight-binding model for silicon, which I eventually included in the Thesis. I am also thankful to Akinlolu Akande for sharing his expertise in BALDA functional.

Next come my officemates - Andrea Droghetti, Kapildeb Dolui and Thomas Cathcart. Thanks for keeping me company and for creating such a great working atmosphere. Other members of our group include Clotilde Cucinotta, Sandip Bhattacharya, Thomas Archer, Amaury de Melo Souza, Nadjib Baadji and Igor Popov. I should also mention the former members of the group - Das Pemmaraju, Nuala Caffrey, Sankar Kesanakurthi, Xihua Chen and Ruairi Hanafin. Thank you *all* for your kindness and support.

I would also like to thank Stefania Negro, who is taking care of all administrate and financial issues and has been extremely helpful and supportive.

The computer resources and the help with our local machines have been provided by the TCHPC stuff members, who all have been very helpful.

I also gratefully acknowledge the financial support of Science Foundation of Ireland that made this work possible.

Finally I am forever grateful to my family - my mother Olga, my grandmother Margarita, Nadjib and Radmilo. Their support and encouragement throughout these years have helped me cross the finish line.

The template for this Thesis has been provided by www.sunilpatel.co.uk.

Contents

Declaration iii

Abstract v

Acknowledgements vii

List of Figures xiii

1 General Introduction 1
- 1.1 Spintronics: overview of the field . . . 2
- 1.2 Spin dynamics and spin control . . . 4
- 1.3 Theoretical description of spin dynamics . . . 5
- 1.4 Thesis Outline . . . 6

2 Atomistic simulations of spin dynamics: theoretical framework 11
- 2.1 Introduction . . . 11
- 2.2 Probing spin dynamics at the atomic scale . . . 12
- 2.3 Theoretical approaches to spin dynamics – different levels of description 17
  - 2.3.1 Landau-Lifshitz-Gilbert equation . . . 17
  - 2.3.2 Micromagnetics . . . 24
  - 2.3.3 Atomistic approaches . . . 25
- 2.4 Spin dynamics in finite atomic-scale systems . . . 28
  - 2.4.1 General scheme for spin dynamics . . . 29
  - 2.4.2 Tight-binding model . . . 36
  - 2.4.3 Ehrenfest spin dynamics . . . 42
  - 2.4.4 Computational scheme – time integrator . . . 45
- 2.5 Summary . . . 49

3 Itinerant electron dynamics in atomic chains 51
- 3.1 Introduction . . . 51

3.2 Dynamics upon weak perturbation: linear response 54
3.3 Excitations in atomic chains: time-domain analysis 57
3.4 Analysis of dynamics in the frequency domain 59
3.5 Calculated excitation spectra 66
3.6 Similarities to quantum spin chains 70
3.7 Introducing a single spin-impurity 75
3.8 Summary 79

4 Electrical control of spin dynamics in a one-dimensional device 81
4.1 Introduction 81
4.2 Model system 84
4.3 Dynamics of the itinerant spins with frozen impurities 87
4.3.1 No external gate 87
4.3.2 Electrostatic gate applied 89
4.4 Combined quantum-classical spin dynamics in the presence of a gate . . 93
4.5 Analysis of dynamical amplitudes 98
4.6 Summary 101

5 Time-dependent electron transport at the atomic scale: theoretical framework 103
5.1 Introduction 103
5.2 Formulation of the electronic transport problem 105
5.3 Landauer approach to steady-state transport 108
5.4 Nonequilibrium Green's function formalism 111
5.4.1 Definitions 112
5.4.2 Equilibrium Green's functions 114
5.4.2.1 Perturbation expansion at zero and non-zero temperature 114
5.4.2.2 Green's functions in the energy domain 116
5.4.2.3 Spectral function 118
5.4.3 Nonequilibrium Green's functions – Keldysh formalism 120
5.4.4 Application to the steady-state transport 124
5.5 Multiple-probe battery approach to electronic open boundaries 127
5.5.1 Transport setup 128
5.5.2 Steady-state formalism 130
5.5.3 Time-dependent formalism 134
5.5.3.1 General case 134
5.5.3.2 Approximations 137
5.6 Test simulations 144
5.6.1 Resonant dimer 144
5.6.2 Spin-excitation in open atomic chain 148
5.7 Summary 151

6 Time-dependent electron transport through a strongly correlated quantum dot 153

6.1 Introduction 153
6.1.1 Derivative discontinuity in static DFT 154
6.1.2 Steady state versus time-dependent approach 161
6.1.3 Combining a new approach to electron transport with a novel exchange-correlation functional 164
6.2 Phenomenology of quantum dots 165
6.2.1 Coulomb blockade 167
6.2.2 Kondo effect in quantum dots 172
6.3 Lattice density functional theory for a strongly correlated quantum dot 176
6.3.1 Model system and transport setup in the multiple-probe assembly 176
6.3.2 Anderson impurity Hamiltonian for an interacting nanojunction 176
6.3.3 Bethe-Ansatz Local Density Approximation 180
6.3.4 Transport equations 184
6.4 Results 186
6.4.1 Non-interacting case 186
6.4.2 Interacting case 188
6.4.2.1 Time-dependent transport 188
6.4.2.2 Steady-state transport from time-dependent simulations 192
6.5 Summary 198

7 Conclusions and Future work **201**

A Adiabatic perturbation in a two-level system **207**

B Multiple probe approach: derivations **211**
B.1 Perturbative expansion of the time-evolution operator 211
B.2 Calculation of the open-boundary terms 212
B.3 Dephasing factor in the injection terms 214

C Anderson impurity model for a strongly correlated quantum dot: approximate solution **217**

D Publications stemming from this work **221**

Bibliography **223**

List of Figures

2.1 Schematic of an optical pump-probe scheme. 13
2.2 A cartoon illustrating a basic STM experiment. 15
2.3 Vector representation of the angular momentum (a) and of the magnetic dipole moment of a current loop (b). 19
2.4 Larmor precession of the magnetization vector $\boldsymbol{M}$ around the magnetic field $\boldsymbol{H}$ as described by the equation of motion with and without the damping term. 22
2.5 Comparison between the electronic band structure of the Si(100) surface in (p2×2)-reconstruction, obtained with DFT (from Ref. [169]), and with the tight-binding model. 38
2.6 Scheme of the time-dependent algorithm. 48

3.1 Cartoon of the model system considered in this section: a local excitation in a monoatomic chain. 58
3.2 Time-evolution of the nonequilibrium charge density distribution, $\delta\rho_i(t) = \sum_\sigma \rho_{ii}^{\sigma\sigma}(t_0) - \rho_{ii}^{\sigma\sigma}(t)$, along the chain. 59
3.3 The group velocity v_g of the wave packet as a function of the hopping integral γ, obtained from the time-dependent simulation for each γ (full circles) and from the analytical expression (solid line). 60
3.4 Comparison between the linear response result and the calculated Fourier spectra of $\delta\rho_1(t)$ and $\delta\rho_N(t)$. 62
3.5 Two-dimensional Fourier transform of $\delta\rho_i(t)$. 67
3.6 Two-dimensional Fourier transform of $\delta\rho_i(t)$ for (a) $\rho_0 = 0.5$, (b) $\rho_0 = 0.6$ and (c) $\rho_0 = 0.8$. 69
3.7 The transverse dynamic structure factor, representing the two-fermion excitation spectrum of the spin-1/2 XY model in transverse magnetic field (h). 72
3.8 (a) Cartoon of spinon excitations. (b) Inelastic neutron scattering data for $KCuF_3$ from Ref. [147]. The inset shows the structure of $KCuF_3$ from Ref. [75] 73
3.9 Model system considered in this section: two classical vectors, representing the itinerant spin $\boldsymbol{s}$ and the spin of the impurity $\boldsymbol{S}$ coupled via the exchange interaction. 76
3.10 Two leading frequencies in the Fourier spectra of $S_x(t)$ and $s_x(t)$ as functions of the exchange interaction J. 78

4.1 Model system: two localized spin-impurities are electronically connected by a monoatomic wire, where electrons can flow. An electrostatic gate is applied to some of the interconnecting sites. 85
4.2 Spin-excitation in a one-dimensional wire. (a) Time-dependence of the spin-polarization on the first site (Δs_1^z). (b) Initial spin-polarization $s^z(t_0)$ as a function of the site index. (c) Time and space evolution of Δs_i^z. 88
4.3 Schematic of the gate-dependence of the ground-state energy spectrum of $\hat{H}_{\rm el}$. 90
4.4 Top panels: $\mathrm{dFT}[\Delta s_i^z(t)](k,\omega)$ for $\rho_0 = 0.5$ and (a) $V_{\rm g} = 0.2|\gamma|$, (b) $V_{\rm g} = 2.2|\gamma|$ and (c) $V_{\rm g} = 4.6|\gamma|$. Bottom panels: $\mathrm{dFT}[\Delta s_i^z(t)](k,\omega)$ for $V_{\rm g} = 0$ and (d) $\rho_0 = 0.5$, (e) $\rho_0 = 0.6$ and (f) $\rho_0 = 0.8$ 92
4.5 Time evolution of the x-components of the localized spins $S_1^x(t)$ and $S_2^x(t)$ and the corresponding Fourier spectra for (a, d) $V_{\rm g} = 0.1|\gamma|$, (b, e) $V_{\rm g} = 2.2|\gamma|$ and (c, f) $V_{\rm g} = 4.6|\gamma|$. 94
4.6 (a) Time evolution of the energy transfer, $\Delta E(t)$, between electronic and localized spins for $V_{\rm g} = 2.2|\gamma|$. The inset shows the maximum value of the energy transfer, ΔE_{max}, as a function of $V_{\rm g}$. (b) Evolution of the electron populations of different parts of the chain for $V_{\rm g} = 2.2|\gamma|$. . . . 96
4.7 (a) $\mathrm{dFT}[\Delta s_i^x(t)](k,\omega)$ for $V_{\rm g} = 0$. (b) The difference between $\mathrm{dFT}[\Delta s_i^x(t)]$ (k,ω) for $V_{\rm g} = 2.2|\gamma|$ and for $V_{\rm g} = 0$. 97
4.8 Adiabatic variation with the gate voltage of a few eigenvalues around the Fermi level. 99
4.9 (a) $A^N_{\rm max}$ and $A^N_{\rm sum}$ (see text for details) as functions of the applied gate voltage. (b) The frequency of the mode related to the pair of eigenstates ($m = 15$) around the Fermi level and (c) its corresponding amplitude as functions of the gate voltage. 100

5.1 Schematic of a typical electronic transport setup: a central region, representing a nanoscale object, is sandwiched between two macroscopic electrodes attached to a battery. 104
5.2 Typical interpretation of the electronic transport problem: an *open* system consisting of a scattering region bridging two electrodes, which are connected to external reservoirs. 106
5.3 Schwinger-Keldysh contour. 122
5.4 Electronic transport setup investigated within the NEGF framework: a scattering region bridging two semi-infinite electrodes, attached (at their infinite borders) to external reservoirs. 125
5.5 Transport setup in the MPB approach: the central region C is sandwiched between two finite electrodes L and R. A probe P_i ($i \in \mathrm{L}, \mathrm{R}$) is attached to each atom i in L and R electrode. 129
5.6 Test system A. The central region consists of two atoms at positions i_1 and i_2, with the on-site energies ε_1 and ε_2 and the hopping δ between them, embedded in a $2N_{\rm d}$-sites long mono-atomic chain. 144

5.7 Differential conductance $G = dI/dV$ of the dimer as a function of the applied bias voltage V, calculated with SS MPB method and with exact NEGF. 145
5.8 Current I through the dimer as a function of the applied bias voltage V, calculated with TD MPB, SS MPB and exact NEGF. 147
5.9 Differential conductance $G = dI/dV$ of the dimer as a function of the applied bias voltage V, calculated using TD MPB and SS MPB for the same parameters as in Fig. 5.8. 148
5.10 Test system B. The central region consists of an impurity site at position i_0 with a frozen local spin $\boldsymbol{S}$, embedded in a $2N_{\mathrm{d}}$-atoms long chain, which is attached to two 1D leads with N_α atoms for $\alpha = \mathrm{L}, \mathrm{R}$. 149
5.11 (a) Spatially-resolved time evolution of the spin-polarization in the electrodes and in the central region, 20 fs before and 100 fs after the spin-excitation. (b) Initial spin-polarization of S as a function of the site index. 150

6.1 Schematic of the dependence of the total energy, E, (a) and the derivative of the total energy, $\partial E/\partial N$, (b) on the fractional particle number N. 156
6.2 (a) Schematic of a quantum dot in lateral geometry. (b) Scanning electron microscope image of a GaAs-(Ga,Al)As double quantum dot device (from Ref. [65]). 166
6.3 A schematic illustration of the effective energy level structure of the quantum dot in the constant interaction model. (a) Linear-response regime: Coulomb blockade. (b) Linear-response regime: lifting of Coulomb blockade by varying the gate voltage. (c) Lifting of Coulomb blockade by applying the source-drain voltage. 169
6.4 (a) A schematic illustration of the Coulomb blockade oscillations. (b) Experimentally observed Coulomb blockade oscillations (from Ref. [208]). 170
6.5 (a) A schematic illustration of the "Coulomb staircase". (b) Experimentally measured I-V characteristics of a Coulomb island for two different values of the gate voltage (from Ref. [208]). 171
6.6 (a) A schematic illustration of the "Coulomb diamond". (b) Experimentally measured differential conductance of the GaAs-(Ga,Al)As quantum dot as a function of the source-drain and the gate voltages (from Ref. [86]). 172
6.7 A magnetic impurity embedded in a metallic host: Kondo effect. 173
6.8 The Kondo resonance in the single-level quantum dot attached to the source and the drain electrodes: schematic illustration. 174
6.9 A cartoon illustrating the characteristic features of the linear-response conductance (G) of the quantum dot, which exhibits the Kondo effect, as a function of the gate voltage (V_{g}). 175
6.10 Model system: a quantum dot attached to two 1D leads, each comprising $N_{\mathrm{L/R}}$ sites. 176

6.11 (a) The BALDA potential (v_{XC}) and (b) the total effective KS potential (v_{KS}) as functions of the occupation of the dot (n_0) for $U = 1$, $U = 2$ and $U = 3$. 183
6.12 Current through the quantum dot, I_0, as a function of the source-drain voltage, V_{sd}, for zero gate voltage (V_{g}=0), calculated using the both exact NEGF and the TD MPB method, and for two configurations of the leads: $\varepsilon_{\mathrm{L/R}}$=0 and $\varepsilon_{\mathrm{L/R}}$=$\pm V_{\mathrm{sd}}/2$. The inset shows the I-V characteristics obtained with the TD MPB approach for $\varepsilon_{\mathrm{L/R}}$=0 and three different gate voltages, V_{g}=1.0, 1.5 and 2.0 eV. 187
6.13 Real-time evolution of the quantum dot: (a) Charge density of the dot (n_0) for four different values of the source-drain voltage, V_{sd}=1.3, 1.6, 1.7, and 1.9 eV. The inset shows the fluctuation of the density around unity. (b) Current through the dot, I_0, for V_{sd}=1.6 eV and V_{sd}=1.3 eV, and the corresponding Kohn-Sham potential (v_{KS}) for V_{sd}=1.6 eV. . . . 189
6.14 Real-time evolution of the quantum dot in the closed-boundary setup: (a) Charge density of the dot (n_0) for V_{sd}=1.2, 1.3, and 1.4 eV. Current through the dot, I_0, and the corresponding Kohn-Sham potential, v_{KS}, for (b) V_{sd}=1.2 eV, (c) V_{sd}=1.3 eV, and (d) V_{sd}=1.4 eV. 191
6.15 Differential conductance of the dot as a function of the gate voltage (V_{g}) for the Kohn-Sham potential, v_{KS}, and for the Hartree potential, v_{H}, with U=1, 2, and 3 eV, and for the non-interacting case. The inset shows a comparison between the density-dependence of v_{KS} and v_{H} for the same values of U. 193
6.16 (a) Differential conductance, (b) charge density and (c) the Kohn-Sham potential of the dot as functions of the gate voltage (V_{g}) for the full discontinuous potential, v_{KS}, and for the Hartree potential, v_{H}, with U=2 eV, and for the non-interacting case. 195
6.17 Current through the dot, I_0, as a function of the source-drain voltage, V_{sd}, for v_{KS} and different values of U. 196
6.18 Current (a), density (b) and on-site potential (c) of the dot as a function of the source-drain voltage, V_{sd}, for v_{KS} with $U = 5$ eV and for v_{H} with $U = 9$ eV. The inset shows v_{KS} and v_{H} as functions of the dot density for the same values of U. 197

A.1 Adiabatic variation of eigenvalues of $\hat{H}(t)$ with the gate potential V: $e_1(t)$ [red] and $e_2(t)$ [blue]. The dashed lines show the diabatic eigenvalues ε_0 and $\varepsilon_0 + V$. 208

B.1 The distribution $\tilde{f}(\omega)$ as a function of ω for $k = 10$, $k = 100$ and a very large positive k ($k \to \infty$). 216

C.1 (a) The normalized linear-response conductance G/G_0 ($G_0 = 2e^2/h$) as a function of ε_d/Γ for $U/\Gamma = 0$, $U/\Gamma = 2$, $U/\Gamma = 5$, and $U/\Gamma = 10$. (b) The total occupation of the quantum dot, $n = \sum_\sigma n^\sigma$ ($n^\uparrow = n^\downarrow$), as a function of ε_d/Γ for the same values of U/Γ. 220

To my family.

Chapter 1

General Introduction

The theory of quantum mechanics successfully resolved the conflicts that emerged at the turn of the twentieth century from the attempts to use the laws of classical mechanics and electrodynamics to explain atomic phenomena. The understanding of the experimental facts, which previously did not fit into the classical picture, such as the stability of atoms and the photoelectric effect, followed naturally from the quantum theory. However, when the new theory was applied to the description of the atomic structure using the concept of point-charge electrons, it produced the results that contradicted experiments. At that time the discrepancies were attributed to the "duplexity" phenomena, since the experimentally observed number of stationary states for an electron in an atom appeared to be twice the number given by theory [60].

In the attempt to explain these phenomena, a number of physicists, including Sommerfeld, Landé and Pauli, recognized the need to introduce a new degree of freedom, in addition to the charge and the angular momentum of an electron [251]. A physical interpretation of this new degree of freedom, or *spin*, as a consequence of an electron spinning around its own axis clockwise or anticlockwise, was proposed by Uhlenbeck and Goudsmit in 1925. However, it required Dirac's fully quantum-mechanical relativistic equation (1928), governing the motion of electrons, to show that the spin of the electron emerges naturally from mathematics [60]. It was later discovered that, in fact, the spin is the fundamental property of all elementary particles.

Despite its elusive quantum-mechanical nature, the existence of the spin has a profound effect on the physical world. Magnetism, a fundamental phenomenon whose applications are ubiquitous in many areas of technology, can only be understood in

the framework of quantum theory and it is a direct consequence of the existence of the electron spin and its statistics [10, p. 672]. The fact that nucleons composing the atomic nuclei have spins allows the observation of the nuclear magnetic resonance (NMR) in absorption spectra [228], caused by transitions between nuclear spin levels in an applied magnetic field. This phenomenon is routinely used in magnetic resonance imaging (MRI) [92]. The same concept, applied to electronic spin levels, is the basis of the electron spin resonance (ESR) spectroscopy [205].

The more familiar quantum property of the electron - its charge - has already been at the heart of the microelectronics revolution, that followed the development of the integrated circuit in 1958 [129]. The continuous downscaling of the electronic devices, in which the information is expressed in the form of logical bits, "ones" and "zeros, corresponding to the existence or absence of electric charge, has led to unprecedented growth of the microelectronics industry. This is often summarized in Moores Law [1], which states that the number of transistors in an integrated circuit, and therefore the computer processing power, doubles every 18 months. It is expected, however, that, as the size of individual logical elements approaches the ultimate atomic limit, this trend will not be able to continue [52], due to heat generation problems and quantum-mechanical effects. These major limitations stimulate the interest in alternative electronic devices, that would exploit *both* the charge and the spin of the electron. In fact, the classical magnetic data-storage technology is already using the electron spin indirectly through its macroscopic manifestation, e.g. the magnetization of a magnetic bit [173]. However, the possibility of directly using the spin as an intrinsic quantum-mechanical property of the electron has come into focus only recently, with the advent of a new research field, the so-called *spin electronics*, or *spintronics* [59].

1.1 Spintronics: overview of the field

The origin of spintronics can be traced back to a number of fundamental discoveries that resulted from the investigations of spin-polarized electron transport in magnetic nanostructures in the late 1980s [68]. This includes the observation of the injection of spin-polarized current from a ferromagnet into a normal metal [115] and the discovery of the interlayer exchange coupling [81].[1] The culmination of these research efforts has

[1]Interlayer exchange coupling is the interaction between the magnetizations of two ferromagnetic layers separated by a non-ferromagnetic spacer [236].

been the discovery and explanation of the giant magnetoresistance (GMR) effect [16, 24].

GMR is observed in multilayered structures, for example in spin-valves, formed by alternating ferromagnetic (FM) and non-magnetic metal layers. Depending on the relative orientation of the magnetizations of the FM layers, the electrical resistance of such structures varies from small (for parallel orientation) to large (for antiparallel orientation), leading to a "giant" (large in magnitude) magnetoresistance. The physical origin of this phenomenon is the difference in the conduction properties of the two spin-channels in a ferromagnet: an electron passing through the spin-valve will be scattered more if its spin is opposite to the direction of the magnetization of the FM layer.

Due to the interlayer exchange coupling, for a certain width of the non-magnetic spacer and in the absence of an external magnetic field, the magnetizations of the FM layers are antiparallel to each other [24], which results in a large resistance. By applying a strong enough magnetic field, the magnetizations can be aligned parallel to each other, leading to a reduction of the electrical resistance. Therefore a GMR spin-valve can be used as a sensitive detector of changing magnetic fields, such as those arising from magnetic bits in a hard-disk drive. Indeed, soon after the discovery of GMR the first computer hard-disk drives, that employed the GMR elements in their read heads, have appeared on the market, accelerating even more the growth of magnetic data-storage density.

The operation of modern hard-disc read heads relies on the tunneling magnetoresistance (TMR) effect [118]. This effect is similar to GMR and it is observed in magnetic tunnel junctions (MTJ), which consist of alternating ferromagnetic and thin insulating layers [182]. Magnetoresistance of such structures can be at least one order of magnitude larger than that of GMR spin-valves [108]. Furthermore, the arrays of MTJ elements have been combined with traditional semiconductor technology to form a new type of non-volatile memory, namely Magnetoresistive Random Access Memory (MRAM) [4].

Since the discovery and successful commercialization of GMR several lines of research have emerged [68], with the aim of finding new ways to control the spin, which will either add new functionalities to conventional electronics or help the development of devices that operate in a completely different way. The goal of *semiconductor spintronics* [14], for example, is to generate, manipulate and detect spin-polarized currents in semiconductors, taking advantage of the long spin lifetime [128] and coherence [127] in these materials.

Another important subdivision of spintronics relies on the *spin-transfer torque* (STT) mechanism [207], which allows to control the magnetization with spin-polarized currents. STT arises from the transfer of angular momentum from the spin-polarized current to the magnetization of a magnetic system, an effect predicted by Berger [21] and Slonczewski [227] in the late 1990s. STT is at the heart of a new non-volatile technology, the so-called Spin-Transfer-Torque-based Random Access Memory (STT-RAM) [62], which has the advantage of lower power consumption and better scalability over conventional MRAM.

Molecular spintronics [221] is another rapidly growing area of research, whose aim is to combine the concepts and ideas of spintronics with the unique properties, versatility and functionality, associated with organic materials. A particularly attractive yet extremely challenging perspective is that of constructing spintronic devices based on single-molecule junctions, where a magnetic molecule is placed between metallic electrodes [26].

Finally, one of the most ambitious goals of spintronics is the development of spin-based quantum computing and information processing, where electron spins and, in fact, nuclear spins are considered as robust candidates for qubits [87]. Although any practical realization is beyond reach of today's technology, some spectacular examples of single-spin control and basic logic operations has been already demonstrated in quantum dots [204] and nitrogen-vacancy (NV) color centers in diamond [88].

1.2 Spin dynamics and spin control

A unifying goal of all the diverse research activities in the field of spintronics is to exploit the spin degree of freedom as a new state variable for information processing and computation [73]. Understanding and controlling the dynamics of electrons and their spins in various solid-state and molecular systems at increasingly smaller time and length scales is an important step in this direction.

Recent experimental advances, among them scanning tunneling spectroscopy of magnetic atoms on surfaces [91] and coherent control of single-spin centers in bulk media [88], have demonstrated the possibility to probe the spin state with atomic resolution and even at the single-spin level. Moreover, the development of time-resolved optical pump-probe schemes has led to the first observation of magnetization dynamics

at the picosecond scale [19] and later to the demonstration of ultrafast (femtosecond) laser-induced magnetization switching [130]. This clearly indicates that the ultimate time scale for spin dynamics is in the femtosecond range.

At these times and lengths, the conventional approaches to manipulating a magnetic state, using magnetic fields alone, are limited by scalability issues. This has triggered the search for alternative methods of spin control, that involve electric fields of some form [44]. In addition to laser-induced magnetization switching, other ways of inducing and manipulating spin dynamics by purely electrical means have been demonstrated. These include current-induced switching [141, 184], microwave oscillations of magnetization [132] based on the STT mechanism [207], and electrostatic control of the spin-density in spin-transistor type devices [113, 284].

1.3 Theoretical description of spin dynamics

The need for understanding and developing a quantitative description of spin dynamics at atomic time and length scales poses new challenges for theory. At these dimensions quantum effects and atomistic details can not be neglected and the applicability of classical phenomenological models, based on macroscopic description of magneto-dynamics, is limited. It is therefore necessary to develop new methodologies and computational methods for atomistic modeling of spin dynamics. Explicitly time-dependent schemes, based on the integration of the equations of motion for the electronic and spin degrees of freedom, are expected to play an increasingly important role [235]. In particular, such real-time dynamical simulations may provide insight into the electronic and magnetic response of a system to external perturbations beyond the linear-response regime.

The extension of the density functional theory to time-dependent phenomena involving spins provides a natural platform for *ab initio* spin-dynamics simulations [37, 39, 160]. However, the existing practical implementations of *ab initio* spin dynamics [8, 9] are still limited to relatively small system sizes. Additional complications arise when the spin dynamics is investigated in the presence of electric currents. As this is essentially a spin-dependent electron transport problem, the methods that have been well-established for isolated systems need to be extended, in one way or another, to include the transport open-boundary conditions [265]. At this point, we enter the realm of atomistic simulations of spin transport in the time domain [235] - a new field, which is still in its infancy, with many conceptual and technical challenges lying ahead.

While large-scale spin-dynamics simulations of realistic systems, especially under current carrying conditions, have not yet become a routine, there is room for model studies and analysis. Particularly attractive are methods, that combine a tight-binding-based description of the electronic structure with advanced time-propagation algorithms for real-time simulations of spin dynamics [231]. It is also highly desirable that the electronic open-boundary conditions are incorporated into the time-dependent scheme in a conceptually clear and efficient way, allowing for the investigations of time-dependent transport phenomena. Methods that satisfy these requirements have the advantage of a fully atomistic approach, combined with computational feasibility, and can be invaluable tools for modeling spin dynamics in isolated and current carrying systems.

1.4 Thesis Outline

This Thesis concerns time-dependent simulations of spin and charge dynamics in reduced-dimensional atomic-scale systems, both in isolation and in the presence of electric currents. We will introduce the theoretical and computational framework for our approach, which will then be used to investigate time-dependent phenomena in the systems of interest. Special attention will be devoted to the discussion of relevant experimental advances and theoretical developments in the areas of magneto-dynamics and electron transport at the nanoscale.

The Thesis is organized in the following way. Apart from this introductory chapter and conclusions (Chapter 7), there are five main chapters. The first three (Chapters 2–4) discuss the theory and modeling of spin dynamics in finite isolated systems. The last two (Chapters 5–6) deal with dynamical simulations of systems with open-boundary conditions. Each chapter is preceded by an extensive introduction, where we discuss the background and motivation for the work presented in a particular chapter.

In Chapter 2 we begin with a brief overview of the current state-of-the-art experimental techniques for probing spin dynamics at the atomic scale. We then discuss several approaches to the theoretical description of spin-dynamic phenomena, from macroscopic models to fully atomistic formulations. The main focus of the chapter is to introduce the method behind the time-dependent atomistic simulations of spin dynamics, performed in this Thesis. The method is based on the integration of the equations of motion for the density matrix of the system. The main electronic structure tool in this

and the following two chapters is the tight-binding model (in later chapters we will make clear when our description departs from this simple model). We also describe the mixed quantum-classical (Ehrenfest) scheme for spin dynamics, which is the basis for dynamical simulations of atomic wires with magnetic impurities, carried out in Chapter 4. At the end of the chapter we discuss the numerical implementation of the time-integration algorithm, which is the common core in all closed- and open-boundary simulations, presented in this Thesis.

In Chapter 3 we use time-dependent simulations to calculate the dynamical response to external excitations of itinerant electrons in atomic chains. The purpose of the chapter is twofold. On the one hand, here we illustrate how the output of the real-time dynamical simulations can be analyzed and interpreted. In certain cases we also compare the numerical results to those obtained from analytical calculations. On the other hand the investigations presented in this chapter provide an insight into the dynamical properties of electronic degrees of freedom in atomic chains, described by a tight-binding Hamiltonian. We find that the excitation spectra, calculated from long-time dynamical simulations, exhibit features characteristic of one-dimensional fermionic systems and closely resemble the excitation spectra of quantum spin chains.

In Chapter 4 we discuss the possibility of electrostatic gate control of spin dynamics in a finite monoatomic wire linking two localized spin-carrying impurities (local spins). This is described as a quantum-classical dynamical system at the Ehrenfest level, where the itinerant electrons of the wire are described quantum-mechanically and the local spins are treated as classical angular momenta. The interaction between the two subsystems is described by the *s-d* model. We use the following strategy to induce and probe the spin dynamics in this system. One of the local spins, excited externally, acts as a spin-pump, generating a disturbance in the itinerant spin density along the wire. The effectiveness of the spin-pumping communication between the two spins is measured by the dynamical response of the second local spin (the probe) in the form of transverse oscillations. We show that by applying an electrostatic gate to the interconnecting wire, the propagation of the spin-signal and, as a consequence, the dynamical communication between the two spin-centers can be enhanced, leading to a large swing of the probe spin for a certain range of gate voltages.

Chapter 5 is concerned with theoretical and computational aspects of time-dependent simulations of electron transport in nanoscale junctions. We start with a description

of the Landauer approach to steady-state transport in systems of non-interacting electrons, where the key concepts of the electron transport theory are introduced. We then present a detailed discussion of the nonequilibrium Green's function formalism (NEGF), which allows one to treat interacting systems. In the rest of the chapter we describe our implementation of the recently proposed multiple-probe battery (MPB) approach to electron transport. This approach is based on the NEGF formalism but it formulates the electronic transport problem using a novel geometry: the semi-infinite electrodes in the conventional transport setup are replaced by finite electrodes attached to a sea of *probes*, or reservoirs, which play the role of an external battery. The main advantage of the method is that, under certain approximations, one can derive an effective equation of motion, which describes the evolution of the system in contact with the battery. We conclude the chapter by presenting a number of test simulations performed with the MPB method, including a time-resolved study of spin-excitations in an atomic chain with open boundaries.

In Chapter 6 we use the MPB method to study time-dependent electron transport in a strongly correlated quantum dot. Although here we do not specifically investigate any spin-dependent effects, this is an opportunity to test our approach against the results available in the literature. In addition, this system has been the center of a number of recent theoretical studies, concerning the fundamental aspects of *ab initio* transport theory for strongly correlated systems. Our theoretical framework is the adiabatic lattice density functional theory, equipped with a novel exchange-correlation functional, specifically tailored to treat electron correlations in one-dimensional systems. In agreement with earlier findings, we show that Coulomb blockade manifests itself in the time-dependent transport as a dynamical state with rapidly oscillating currents and charge densities. Furthermore, we investigate the effect of electron-electron interaction on the steady-state transport properties. In particular, we find negative differential conductance in some transport regimes. We relate this effect to both the electron-electron interaction and the finite bandwidth of the electrodes.

In addition to the standard chapters, this Thesis has three appendices, in which we clarify certain concepts and present the details of the calculations that were not included in the main text.

In Appendix A we illustrate the concept of avoided crossings, which is used in Chapter 4. We consider a dimer, described by a simple tight-binding Hamiltonian, with an electrostatic potential applied to one of the sites. We show that in the case of a non-zero

hopping between the sites an avoided crossing is formed between the two eigenvalues of the Hamiltonian, calculated as functions of the applied potential.

In Appendix B we present the derivations that were omitted in the discussion of the multiple-probe battery method in Chapter 5. In particular, we elaborate on the perturbation expansion for the time-evolution operator and on the exact expression for the open-boundary terms in the equations of motion.

In Appendix C we calculate the gate-voltage dependence of the linear-response conductance and charge density of a quantum dot, described by the Anderson impurity model. For this we use an approximate expression for the Green's function of the dot in the presence of tunneling between the dot and the electrodes.

Finally, we summarize the work presented in this Thesis. We also highlight some remaining issues and topics that might be considered for further investigation.

Chapter 2

Atomistic simulations of spin dynamics: theoretical framework

2.1 Introduction

The rapid development of the field of spintronics [59] over the past two decades has uncovered exciting and novel phenomena related to the dynamics of the electron spin in a wide variety of systems, ranging from bulk materials to spatially-confined structures [95]. These phenomena include current-induced domain-wall motion [244], spin-wave confinement effects [54], spin-transfer-torque-induced magnetization switching [184], microwave oscillations [132], spin-pumping [218], femtosecond magnetization reversal [131], just to name a few. The lower limit for the length scales at which one could observe the dynamics of the spin degrees of freedom is shifting towards the atomic scale. Fueled by recent advances in newly-emerging fields of research, such as single-electron spintronics and spin-based quantum information processing and computing, the investigation of dynamics of single spins in solid state environment has indeed become possible [87]. The characteristic time scales of spin dynamics, accessible in experiments, also span many orders of magnitude, with the corresponding dynamical phenomena ranging from slow magnetization processes ($t \gtrsim 1$ s), that can be detected using conventional magnetometers, to ultrafast ($t \sim 1$ fs) response of magnetic materials following intense laser excitations.

The increasing ability to probe the spin dynamics with extremely high spatial and temporal resolution stimulates the development of new theoretical approaches, capable

of adequately describing the dynamics of electrons and their spins at ultrashort time and length scales. At these dimensions, where quantum effects become unavoidable, the use of classical phenomenological models is inappropriate and there is a need for quantum atomistic approaches. Considerable efforts have been put into the development of *ab initio* based methods for spin dynamics [8, 9, 37, 39, 215] which potentially offer a very accurate description of dynamical properties of magnetic materials. These efforts are currently focused on the extension of the density functional theory to time-dependent phenomena involving spins. Although the theoretical foundations of such approach have been already laid out, it would not be an overstatement to say that this field is in its infancy. In particular, applications to large-scale simulations of realistic systems are still out of reach. Clearly, there is a demand for methods that fill the intermediate gap between semi-classical and *ab initio* approaches. One alternative is offered by time-dependent schemes based on model Hamiltonians, in particular of tight-binding type, which have the advantage of a fully-atomistic description combined with computational feasibility. In this Thesis we use an implementation of such time-dependent tight-binding based scheme, which provides a conceptually clear framework for simulations of spin dynamics in atomic-scale systems.

In this chapter we will review the existing experimental techniques that can be used to probe the dynamical behavior of spin systems. We will then discuss in more detail the relevant advances in the theoretical description of spin-dynamic phenomena, with an emphasis on atomistic approaches. An introduction to the computational scheme for modeling the spin dynamics employed in this Thesis will be given, with additional discussion of few technical details of the numerical implementation.

2.2 Probing spin dynamics at the atomic scale

There exist a wide range of experimental methods, including magnetic, electrical and optical techniques, which can be used to probe the magnetic state of the system at different time and length scales [95].

One of the most commonly used techniques to study magneto-dynamics is magneto-optical spectroscopy. This group of methods is based on magneto-optical effects, in which the polarization of light interacting with a magnetic material changes in a magnetization-dependent way. The Faraday effect and the magneto-optical Kerr effect (MOKE) belong to this class of phenomena. Usually magneto-optics has a limited

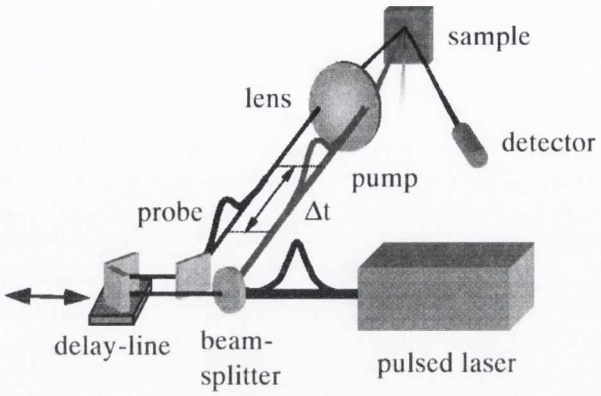

FIGURE 2.1: Schematic of an optical pump-probe scheme. A laser pulse is divided in a pump- and a probe-part by a beam splitter. The time delay Δt between the pump- and the probe-pulse is controlled by a delay line which changes the optical path of the probe-beam. Both beams are focused on the same spot of the sample. After reflection (for MOKE) the probe beam is analyzed by a detector to obtain information on the state of the system at a specific (delay) time after the excitation produced by the pump pulse. Image is from M. van Kampen [259].

spatial resolution ($\approx$ 100 nm) and it is rather a "collective" than atom-specific technique. However, it has the unique advantage in terms of time resolution. In general, optics studies visible, ultraviolet, and infrared light. This is characterized approximately by photon energies of $10^{-2} - 10^{2}$ eV, wavelengths in the range of 10 nm – 300 μm, frequencies ranging from THz to 10 PHz, which corresponds to time scales of the order of ps and fs.

The development of modern pulsed lasers with power densities larger than 10^{16} Wcm^{-2} and with very short pulse duration in the femtosecond and even attosecond regime [223] have brought the imaging of magneto-dynamics to the next level. The so called pump-probe (stroboscopic) techniques performed with fs-lasers allow one to address the dynamics on ultrafast time scales. In a pump-probe experiment (see Fig. 2.1) the system under study is brought out of equilibrium by a pump-pulse, and after a certain time delay the state of the system, for instance its magnetization, is measured by a probe pulse. For optical measurement of the magnetization one can use MOKE, in which the polarization of the reflected probe pulse carries information about the magnetization of the material. In fact, the development of magneto-optical pump-probe techniques has lead to the first observation of magnetization dynamics on the ps and later on the sub-ps scale [19]. Recently, the X-ray magnetic circular dichroism (XMCD) spectroscopy, which has an important advantage of chemical element selectivity, was combined with

fs-laser pulses to study ultrafast demagnetization of Ni [232]. This was realized by using a fs-laser pulse to separate an ultrashort "slice" from an approximately 50-ps long X-ray pulse produced on the synchrotron.

The results of numerous experiments on ultrafast magnetization dynamics over the last decade have generated a number of interesting questions that are still heavily debated. It is not entirely clear, for instance, what are the microscopic mechanisms that govern the changes in magnetization on such ultrafast time scales, in particular, the quenching of the magnetic moment after the interaction with a fs-laser pulse [131]. In fact, the research aimed at understanding the fundamental limits of magnetization dynamics at fs scale has merged into a new sub-discipline named *femtomagnetism* [277]. This field is attracting significant attention at the moment since the ability to control the magnetization at such time scales would open up new possibilities for fast switching mechanisms in novel memory devices.

Other types of time-resolved magnetometry measurements include, for instance, spin polarized photoemission electron spectroscopy (SP-PEEM), measured on X-ray synchrotrons. This technique has high spatial resolution (10 nm) and can probe magnetic systems at a relatively small time scale since it benefits directly from the pulsed nature of the light emission of X-ray synchrotrons with characteristic pulse-times of 20–100 ps.

Spin-resolved spectroscopy performed with a scanning tunneling microscope (STM) [see a cartoon in Fig. 2.2], which has sub-nanometer spatial resolution, can be classified as an electrical measurement.[1] Recently, inelastic electron tunneling spectroscopy (IETS) with STM[2] was used to measure the spin-excitation spectra of various atomic-scale magnetic structures, such as individual magnetic atoms from transition-metal group (Fe, Co, Mn), dimers and chains of atoms absorbed on surfaces [91, 97]. These are truly remarkable experiments, in which the *in situ* imaging, manipulation and spectroscopic

[1]Scanning tunneling microscopy is usually performed in two modes. The first mode, in which the STM tip is kept at a constant height while scanning the sample, provides a fast characterization of the surface. In the second mode, the height of the tip is adjusted at each lateral position on the surface in order to give a constant value of the current. This provides a high-resolution topography of the surface. Scanning tunneling spectroscopy (STS) can be performed at a given lateral position by sweeping the bias voltage and measuring the current, which allows one to construct an I-V characteristic. The differential conductance (dI/dV) can be obtained either by differentiating the I-V curve or by directly applying a voltage pulse and measuring the corresponding variation of the current (this can be done "on the fly" in the constant-current mode).

[2]The second derivative of the I-V curve obtained with an STM provides information about the vibrations of the sample just as in inelastic electron tunneling spectroscopy (IETS), this is why the technique is commonly called STM-IETS.

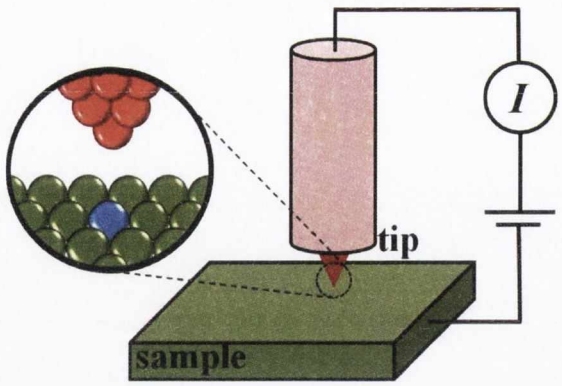

FIGURE 2.2: A cartoon illustrating a basic STM experiment. An STM tip with an atomically sharp point can be positioned precisely (with sub-nanometer resolution) above the surface of the sample with the help of a piezoelectric scanner. A bias voltage is applied between the sample and the tip, which for sufficiently small tip-sample distances results in the tunneling current.

capabilities of STM serve as a tool to probe the magnetic response of the system with atomic resolution.

The idea of a pump-probe measurement was recently implemented in the STM geometry and was used to measure electron spin relaxation times in a Fe-Cu dimer with nanosecond time resolution [163]. In such all-electronic pump-probe scheme, a strong voltage pulse (the pump pulse) creates a spin-excitation of the surface atom and a weaker voltage pulse (the probe pulse) is then applied to read-out the spin state of the atom at time Δt after the pump pulse. Integrating the pump-probe current over many pump-probe cycles and varying Δt allows one to map out the dynamical evolution of the expectation value of the atom's spin.

We note that there is a number of other experimental methods which may not provide the same high resolution as those mentioned above but are very well suited to study certain spin-dynamic processes. For instance, two complementary techniques, namely, ferromagnetic resonance and Brillouin light scattering (BLS) are commonly used to investigate small amplitude magneto-dynamics. In particular, BLS which can provide the resolution up to 30-50 μm and 1 ns has become a powerful tool for the observation of spin waves.

Another group of state-of-the-art techniques that have merged into a discipline on its own deals with single-spin dynamics in quantum dots and atomic impurities such as nitrogen-vacancy (N-V) centers in diamond. Although the fabrication of such systems

has long become a routine, the problem of the initialization, manipulation and measurement (read out) of their spin state is technically very demanding and has been fully solved only recently. It is worth discussing in more details some of the recent achievements in this field.

The characteristic feature of single-spin systems is the discreteness of their energy levels. The existence of spin-dependent transitions between the levels allows the implementation of several spin read-out techniques in which the spin information is transferred to quantities that are more easily measured, such as an electric charge or the polarization of light, thus allowing for electrical or optical measurements. For instance, the optical pump-probe scheme based on the Faraday effect was recently used to detect the time-averaged spin state of a single electron spin in a quantum dot [12]. N-V centers also have a discrete energy spectrum and strong transitions in the optical range, which provide the possibility of optical initialization and measurement [71].

The ability to manipulate the spin, combined with the spin read-out scheme, provides a full control over the spin state. Rotations of the single spin can be achieved by magnetic, electrical or optical means. The general principle for all methods is to drive coherent transitions between two spin states by applying an appropriate excitation. The energy of this excitation determines the period of the rotation or, in other words, the time scale of the spin dynamics.

The most well-known approach is electron spin resonance (ESR). Generally speaking, ESR [205], also known as electron paramagnetic resonance (EPR), is a spectroscopic technique based on the absorption of electromagnetic radiation by a paramagnetic sample placed in a magnetic field. In a typical experiment an oscillating magnetic field B_{ac} is applied perpendicular to the static magnetic field B. When the frequency of B_{ac} matches the Zeeman splitting between the spin-up and spin-down levels, induced by B, e.g. $f_{ac} = g\mu_{\mathrm{B}}B/\hbar$, the spin is effectively rotated. The practical realization of this idea have been demonstrated in both quantum dots [137] and N-V centers [88, 114]. The coherently driven oscillations of the electron-spin are called Rabi oscillations, and their frequency is defined by the amplitude of the alternating magnetic field, $f_{\mathrm{Rabi}} = g\mu_{\mathrm{B}}B_{\mathrm{ac}}/2\hbar$. Due to the limitations to the strength of an applied magnetic field, the corresponding period of single-spin rotations performed with ESR is typically limited to the nanosecond range. For applications in quantum information processing much faster operation times are required.

Using an oscillating electric field instead of a magnetic field was proposed as an alternative to ESR. An electric field can be coupled to the spin through mediating mechanisms, such as spin-orbit interaction or magnetic field gradient [146, 190]. In comparison to magnetic resonance, such all-electrical control has the important advantage that it allows spins to be easily addressed locally, because electric fields are easier to confine to small regions of space than the magnetic ones. However, in terms of time resolution, the technique is also limited to the nanosecond scale.

Optical techniques also allow the coherent manipulation of spins and several experimental scheme have been proposed [20, 85, 109]. For example, in Ref. [20] the a.c. Stark effect[3] was used to manipulate a single electron spin in a quantum dot. Short laser pulses with high instantaneous density were shown to induce rotations of the spin in a time interval as short as 30 ps, which is about three orders of magnitude faster than any magnetic or electrical manipulation of single spins.

2.3 Theoretical approaches to spin dynamics – different levels of description

In the previous section we described several experimental techniques which can be used to probe a magnetic state of a system with different spatial and temporal resolution. In a similar way, one can distinguish between theoretical approaches to spin dynamics based on their ability to capture the prevailing physical mechanisms that govern the spin-dynamic phenomena at particular time and length scales. Starting at the macroscopic level, several methods and their range of applicability will be discussed below.

2.3.1 Landau-Lifshitz-Gilbert equation

On the long time scale of 100 ps–1 ns the main driving forces for magnetization dynamics are external fields, magnetic dipole-dipole and spin-lattice interactions [277].

[3]In the presence of an electromagnetic wave, the energy of electronic transitions changes. In analogy to the effect first observed in static electric fields (Stark effect), this is called the optical or a.c. (dynamical) Stark effect.

In this regime, the dynamics of the magnetization is mainly characterized by its precessional motion, which is opposed to the damping that tends to align the magnetization in the direction of the effective magnetic field. The theoretical description of such precessional motion including the effect of damping goes back to the phenomenological Landau-Lifshitz-Gilbert (LLG) equation [77, 148]. This is the basic classical equation of motion for the magnetization, which enters the majority of models for magneto-dynamics, including large-scale micromagnetic implementations. The macroscopic LLG equation has been very successful in describing precessional magnetization reversal in small magnetic particles and thin films [181]. The addition of terms due to the spin-transfer torque [21, 227] effect allows one to model experimentally observed current-induced oscillations of magnetization in spin-valve structures [63, 103]. Theoretical developments aimed at describing adiabatic and non-adiabatic effects in the domain wall motion driven by the spin-transfer torque are also largely based on the LLG equation [239, 243, 278].

We will now recall a heuristic derivation [181] of the equation describing the precessional motion of the magnetization based on simple considerations of classical mechanics. We will then discuss how the dissipative processes can be introduced in the equation through an additional phenomenological term.

Heuristic derivation of LLG equation

The classical angular momentum $\boldsymbol{L}$ [see Fig. 2.3(a)] of a particle[4] with respect to some point of origin is defined as

$$\boldsymbol{L} = m\left(\boldsymbol{r} \times \boldsymbol{v}\right), \tag{2.1}$$

where m is the mass, $\boldsymbol{r}$ is the position and $\boldsymbol{v}$ is the velocity of the particle.

For any force $\boldsymbol{F}$ acting on the particle equation of motion for the angular momentum reads

$$\frac{d\boldsymbol{L}}{dt} = m\left(\frac{d\boldsymbol{r}}{dt} \times \boldsymbol{v}\right) + m\left(\boldsymbol{r} \times \frac{d\boldsymbol{v}}{dt}\right) = 0 + \boldsymbol{r} \times \boldsymbol{F} \equiv \boldsymbol{\tau}, \tag{2.2}$$

where $\boldsymbol{\tau} = \boldsymbol{r} \times \boldsymbol{F}$ is the torque.

The classical angular momentum can be related to a magnetic dipole moment of a closed planar loop in a uniform magnetic field $\boldsymbol{B}$. The force $d\boldsymbol{F}$ acting on a current

[4]Hereafter vectors are denoted by bold characters.

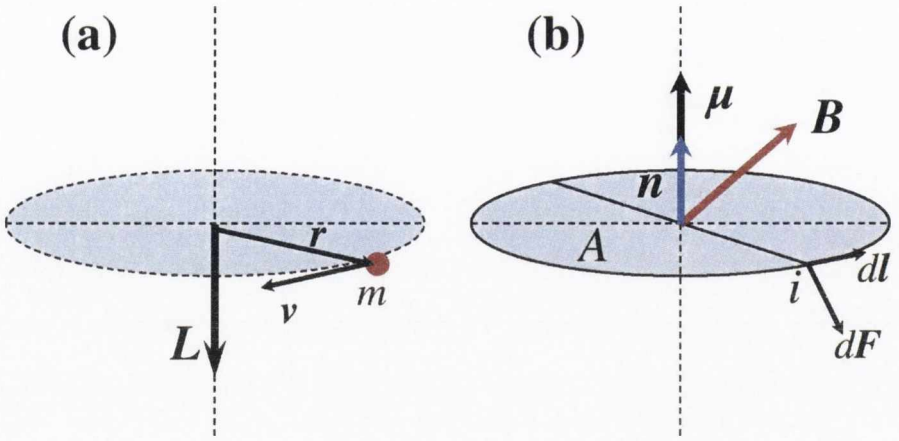

FIGURE 2.3: Vector representation of the angular momentum (a) and of the magnetic dipole moment of a current loop (b).

element of length $d\boldsymbol{l}$ and current density i reads

$$d\boldsymbol{F} = id\boldsymbol{l} \times \boldsymbol{B}. \tag{2.3}$$

After integration, we obtain the total torque exerted by the magnetic field on the current loop

$$\boldsymbol{\tau} = i\boldsymbol{A} \times \boldsymbol{B}, \tag{2.4}$$

where $\boldsymbol{A} = A\boldsymbol{n}$ is a vector area, $\boldsymbol{n}$ being the unit vector perpendicular to the plane of the loop and A being the area of the surface enclosed by the loop. The magnetic dipole moment of the current loop [see Fig. 2.3(b)] can be then defined as

$$\boldsymbol{\mu} = i\boldsymbol{A}. \tag{2.5}$$

The current density, i, of a loop which has a radius r and carries a charge e moving with velocity v is given by

$$i = \frac{ev}{2\pi r}. \tag{2.6}$$

This leads to the following relation between the magnetic dipole moment and the angular momentum

$$\boldsymbol{\mu} = \frac{e}{2m}\boldsymbol{L} = \gamma_{\mathrm{g}}\boldsymbol{L}, \tag{2.7}$$

where $\gamma_{\mathrm{g}} = \dfrac{e}{2m}(< 0)$ is the gyromagnetic ratio (here e and m are, respectively, the charge and the mass of an electron). The equation of motion for the magnetic moment

thus reads

$$\frac{d\boldsymbol{\mu}}{dt} = \gamma_{\mathrm{g}}\boldsymbol{\mu} \times \boldsymbol{B}. \tag{2.8}$$

Although we have derived Eq. (2.8) by using solely the notions of classical mechanics, there is a deep analogy between the equation of motion for the magnetic dipole moment and its quantum mechanical counterpart for a free electron spin. In fact, using Ehrenfest's theorem, the equation of motion for the expectation value $\langle \hat{\boldsymbol{s}} \rangle$ of the quantum mechanical spin operator $\hat{\boldsymbol{s}}$ can be written as

$$\frac{d\left\langle \hat{\boldsymbol{s}} \right\rangle (t)}{dt} = \frac{1}{\imath\hbar} \left\langle \left[\hat{\boldsymbol{s}}, \hat{H}(t) \right] \right\rangle, \tag{2.9}$$

For an isolated spin, subject to a magnetic field $\boldsymbol{B}(t)$, the Hamiltonian is $\hat{H} = \frac{g\mu_{\mathrm{B}}}{\hbar}\hat{\boldsymbol{s}}(t) \cdot \boldsymbol{B}(t)$, where $\mu_{\mathrm{B}} = \frac{|e|\hbar}{2m} = 5.788\,10^{-5}$ eV/T is the Bohr magneton. By using the commutation relations for the spin operator

$$[\hat{s}_\alpha, \hat{s}_\beta] = \imath\hbar\epsilon_{\alpha\beta\gamma}\hat{s}_\gamma, \tag{2.10}$$

where $\epsilon_{\alpha\beta\gamma}$ is the totally anti-symmetric Levi-Civita tensor with $\epsilon_{xyz} = 1$, we obtain the following expression for the commutator in Eq. (2.9) for one of the projections of $\hat{\boldsymbol{s}}$

$$\begin{aligned} [\hat{s}_x, H(t)] &= \frac{g\mu_{\mathrm{B}}}{\hbar} \left[\hat{s}_x, \hat{s}_x B_x(t) + \hat{s}_y B_y(t) + \hat{s}_z B_z(t) \right] = \\ &= \frac{g\mu_{\mathrm{B}}}{\hbar} \left\{ B_y(t) \left[\hat{s}_x, \hat{s}_y \right] + B_z(t) \left[\hat{s}_x, \hat{s}_z \right] \right\} = \\ &= \frac{g\mu_{\mathrm{B}}}{\hbar} \imath\hbar \left\{ B_y(t)\hat{s}_z - B_z(t)\hat{s}_y \right\}. \end{aligned} \tag{2.11}$$

Furthermore we obtain the equation of motion for $\langle \hat{\boldsymbol{s}} \rangle$ in the final form

$$\frac{d\left\langle \hat{\boldsymbol{s}} \right\rangle (t)}{dt} = -\frac{g\mu_{\mathrm{B}}}{\hbar} \left\langle \hat{\boldsymbol{s}} \right\rangle (t) \times \boldsymbol{B}(t), \tag{2.12}$$

which is, clearly, similar to Eq. (2.8).

Going back to the classical equation of motion [Eq. (2.8)], one can define the macroscopic magnetization as the total dipole moment, or the sum of all the individual magnetic moments, per unit volume. This is essentially the *macrospin* approximation, where the magnetization of the system is represented by a single vector $\boldsymbol{M}$. By taking into account that $\boldsymbol{B} = \mu_0 \boldsymbol{H}$ (μ_0 is magnetic permeability of vacuum) and by

introducing a new parameter $\gamma_0 \equiv \mu_0|\gamma_g| = -\mu_0\gamma_g$, we obtain the following equation

$$\frac{d\boldsymbol{M}(t)}{dt} = -\gamma_0 \boldsymbol{M}(t) \times \boldsymbol{H}(t). \tag{2.13}$$

It immediately follows from Eq. (2.13) that

$$\frac{d|\boldsymbol{M}(t)|^2}{dt} = 0. \tag{2.14}$$

and, for time-independent magnetic field $\boldsymbol{H}$,

$$\frac{d\left(\boldsymbol{M}(t) \cdot \boldsymbol{H}\right)}{dt} = 0. \tag{2.15}$$

This means that the amplitude of vector $\boldsymbol{M}$ is constant and the angle between the magnetization and the applied magnetic field is unchanged. Such conditions corresponds to the perfect Larmor precession (with frequency $\omega_L = \gamma_0 H$, where H is the magnitude of the magnetic field), of the macroscopic magnetization $\boldsymbol{M}$ around the magnetic field [see Fig. 2.4(a)].

However, the precessional motion alone can not describe the behavior of the magnetization observed experimentally, for example, the saturation of the magnetization with applied magnetic field. The simplest way to account for this behavior is to introduce an additional term on the right-hand side of equation Eq. (2.13) that will tend to align the magnetization in the direction of the field

$$\frac{d\boldsymbol{M}(t)}{dt} = -\gamma_0 \boldsymbol{M}(t) \times \boldsymbol{H}(t) - \frac{\alpha_L}{M_S} \boldsymbol{M}(t) \times \left[\boldsymbol{M}(t) \times \boldsymbol{H}(t)\right], \tag{2.16}$$

where M_S is the saturation magnetization and α_L is the Landau-Lifshitz damping constant. The above equation was proposed by Landau and Lifshitz [148] in 1935. It was later modified by Gilbert [76] in 1955, in order to overcome the unphysical solution for large damping parameters ($\alpha_L \geq 1$) [167]. The so-called Landau-Lifshitz-Gilbert (LLG) equation reads

$$\frac{d\boldsymbol{M}(t)}{dt} = -\gamma_0 \boldsymbol{M}(t) \times \boldsymbol{H}(t) + \frac{\alpha_G}{M_S} \boldsymbol{M}(t) \times \frac{d\boldsymbol{M}(t)}{dt}, \tag{2.17}$$

where α_G is the Gilbert damping parameter. It can be shown that the LLG equation [Eq. (2.17)] can be transformed back into the Landau-Lifshitz equation [Eq. (2.16)] by introducing new parameters $\gamma_0' = \frac{\gamma_0}{1+\alpha_G^2}$ and $\alpha_L' = \frac{\gamma_0 \alpha_G}{1+\alpha_G^2}$ [167].

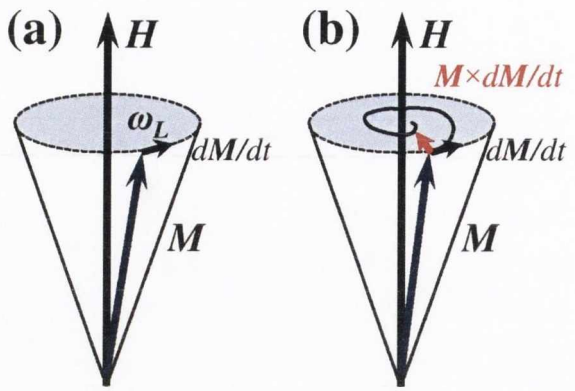

FIGURE 2.4: (a) Larmor precession of the magnetization vector $\boldsymbol{M}$ around the magnetic field $\boldsymbol{H}$ as described by the equation of motion without the damping term [Eq. (2.13)]. In this case the magnetization rotates about the magnetic field direction with $|\boldsymbol{M}| = const$ and a fixed angle between $\boldsymbol{M}$ and $\boldsymbol{H}$. (b) Schematic representation of the magnetization dynamics under combined action of the magnetic field and the damping [Eq. (2.16)-(2.17)]. In this case the magnetization rotates about the magnetic field direction but tends to align with $\boldsymbol{H}$.

The first term in the LLG equation still represents the precession of the magnetization around the magnetic field while the second term describes the dissipation in the system. Due to this last term, the direction of the magnetization deviates from the precessional trajectory and spirals down with time until it becomes aligned with the direction of the magnetic field as shown schematically on Fig. 2.4(b). Note also that $\boldsymbol{H}(t)$ in Eq. (2.16) and Eq. (2.17) represents the effective magnetic field, which comprises all external and internal (anisotropy and demagnetizing fields) magnetic field, acting on the magnetization.

The damping constant α_{G} is essentially a phenomenological parameter which does not contain any details on the physical mechanisms leading to dissipation. In fact understanding the microscopic origin of the damping is a notorious problem and it is currently a very active area of research since tailoring the damping constant is a key factor in the operation of memory devices. Possible mechanisms include spin-orbit interaction, magnon scattering processes, relaxation due to the presence of impurities and Eddy currents in the case of conductors. There have been several attempts to determine the damping from first-principles calculations [23, 78]. A new scheme for spin-dynamics simulations based on a modified LLG equation with additional inertia terms was proposed in Ref. [23]. The inertia effect is incorporated into the equation of motion through a term proportional to the second derivative of the magnetization over time, e.g. of the form $\boldsymbol{I}\frac{d\boldsymbol{M}^2}{dt^2}$, where $\boldsymbol{I}$ is the moment of inertia. This leads to

nutations of the magnetization vector, a new type of motion compared to precession and damping. It is argued that the inclusion of such dynamical term combined with the first-principles-based calculations of the damping constant and the moment inertia may provide a suitable framework for investigation of ultrafast dynamics.

When electric current flows through a ferromagnetic material, the transfer of angular momentum occurs from conduction electrons to the local magnetization, a mechanism known as spin-transfer torque [21, 227]. In order to account for this current-induced effect, additional terms can be added to the phenomenological LLG equation. Since the motion of conduction electrons is typically much faster than that of the magnetization, the spins of the electrons tend to align with the direction of the local magnetization, leading to the *adiabatic* torque. Deviations from the adiabatic process are also possible, when the adiabatic approximation breaks down and the electrons essentially can not adapt to the local magnetization. This results in the *non-adiabatic* torque that can appear, for instance, in narrow inhomogeneous structures [168]. Understanding of the microscopic mechanisms of the non-adiabatic effect is still not complete [239, 243, 278]. Following the formulation of nonequilibrium current-induced effects in magnetization dynamics proposed by Zhang and Li [278], the torque can be introduced into the LLG equation through the following terms

$$T_{\mathrm{a}} = -\frac{1}{M_{\mathrm{S}}}\boldsymbol{M}(t) \times \left[\boldsymbol{M}(t) \times (\boldsymbol{u} \cdot \bigtriangledown)\, \boldsymbol{M}(t)\right], \tag{2.18}$$

$$T_{\mathrm{na}} = -\frac{\beta}{M_{\mathrm{S}}}\boldsymbol{M}(t) \times (\boldsymbol{u} \cdot \bigtriangledown)\, \boldsymbol{M}(t), \tag{2.19}$$

where $\boldsymbol{u} = \frac{IPg\mu_B}{2|e|M_{\mathrm{S}}} \cdot \boldsymbol{j_e}$ is usually interpreted as the velocity of the electron flow, with $\boldsymbol{j_e}$ being the direction of the current flow, I the current density, P the spin-current polarization of the system and M_{S} the saturation magnetization. The first term describes the adiabatic process, while the second one represents the non-adiabatic contribution to the torque, where a dimensionless parameter β expresses the strength of the non-adiabaticity. Recently, the non-adiabatic torque, and, in particular, the parameter β, has been measured experimentally in different types of domain walls in permalloy nanowires [64].

The extensions of the basic LLG equation beyond the macrospin approximation can be used to construct theoretical models that provide a higher level of description of magnetically ordered systems compared to the macroscopic one. This has been achieved in

the *micromagnetic* theory which is widely used for modeling magnetic domain structures of various shapes and even for simulations of magnetic switching in memory elements [281].

2.3.2 Micromagnetics

The micromagnetic theory, or micromagnetics [30], essentially adopts a macroscopic view on the magnetic configuration of the system. However, usually the magnetic state is no longer represented by a single uniform magnetization vector $\boldsymbol{M}$ as in the macrospin approximation. Instead, the magnetization of the system $\boldsymbol{M}(\mathbf{r})$ and the effective field $\boldsymbol{H}(\mathbf{r})$ are considered to be continuous functions of the spatial variable $\mathbf{r}$. The effective magnetic field can be calculated by minimizing the total energy of the system with respect to the magnetization

$$\boldsymbol{H}(\boldsymbol{r}) = -\frac{\partial E(\boldsymbol{r})}{\partial \boldsymbol{M}(\mathbf{r})} = -\frac{1}{M}\frac{\partial E(\boldsymbol{r})}{\partial \boldsymbol{m}(\mathbf{r})}, \tag{2.20}$$

where $\boldsymbol{m}(\mathbf{r})$ represents the unit vector of the magnetization, M is the magnitude of the magnetization vector and $E(\boldsymbol{r})$ is the total energy density. For a typical ferromagnet $E(\boldsymbol{r})$ consists of several contribution, corresponding to different interactions that are present in the system

$$E(\boldsymbol{r}) = E_{\text{an}}(\boldsymbol{r}) + E_{\text{ex}}(\boldsymbol{r}) + E_{\text{mag}}(\boldsymbol{r}) + E_{\text{Zeeman}}(\boldsymbol{r}), \tag{2.21}$$

where E_{an} is the anisotropy energy density, E_{ex} is the exchange energy density, E_{mag} is the magnetostatic energy density and E_{Zeeman} is the energy density due to the presence of external magnetic field (Zeeman energy density). The evaluation of these terms and the minimization of the total energy is the main part of the micromagnetic simulation. The temporal evolution of the magnetization is governed by the LLG equation. In practice, the system is spatially divided into a mesh of fine elements, or cells, and within each cell the magnetization $\boldsymbol{M}_i$ is assumed to be uniform. Vectors $\boldsymbol{M}_i$ evolve according to the discretized LLG equation which reads

$$\frac{d\boldsymbol{M}_i(t)}{dt} = -\gamma_0 \boldsymbol{M}_i(t) \times \boldsymbol{H}_i(t) + \frac{\alpha_{\text{G}}}{M_{\text{S}i}} \boldsymbol{M}_i(t) \times \frac{d\boldsymbol{M}_i(t)}{dt}, \tag{2.22}$$

where $\boldsymbol{H}_i(t)$ represents an effective field acting on the magnetization of each cell and $M_{\mathrm{S}i}$ is the saturation magnetization of i-th cell. The dynamics of the magnetic configuration, represented by a discrete mesh $\{\boldsymbol{M}_i\}_{i=1}^{N_M}$ with N_M being the number of cells, can be calculated by integrating the set of equations given by Eq. (2.22). Such approach provides a description of the dynamical response of a magnetic system on the sub-μm length scales, thus acting as a bridge between macroscopic and atomistic models.

The effect of thermal fluctuations can be included into the LLG equation through an additional stochastic term in the effective field $\boldsymbol{H}(t)$. This can be done in analogy with the Langevin equation, which is well-known from statistical mechanics and, in its original form, describes the Brownian motion of particles in a fluid. Such stochastic Langevin dynamics can be incorporated into the micromagnetic simulations to study thermally activated processes.

Despite the successes of the LLG-based models in describing the time-dependent properties of magnetic systems, in particular, the precessional motion of the magnetization, the range of their applicability is limited to relatively slow processes and large length scales. In addition to the use of phenomenological parameters that are difficult to justify on fundamental grounds, a major intrinsic weakness of the LLG equation is the assumption that the properties of the magnetic system vary slowly on the atomic scale and that one can adopt an essentially macroscopic view on the magnetization. Such view gradually becomes invalid as one approaches the atomic scale, where quantum effects and interactions prevail. It is at dimensions below $\sim$ 1 nm and at times lower than $\sim$ 100 ps, that the concepts of the LLG equation, such as the magnetization itself, start to break down and one eventually needs to resort to quantum-mechanical models and analysis.

2.3.3 Atomistic approaches

Atomistic approaches based on a quantum-mechanical treatment of the electronic structure of the system are capable of giving a much more accurate description of magnetization dynamics compared to classical and semi-classical models that rely on the macroscopic approximation and ad hoc parameters. Such approaches would provide a suitable framework for including different physical mechanisms involved in the magnetization dynamics and, ultimately, for constructing a first-principles based description of spin dynamics that enables the investigation of realistic systems. Although several

computational schemes capable of describing the time evolution of the spin degrees of freedom in atomic-scale systems have been proposed [72, 144, 191, 225, 231, 254], atomistic simulations of spin dynamics, in particular, explicitly time-dependent schemes, form an area of research in magneto-dynamics that is still not fully explored.

A natural platform for developing an *ab initio* spin dynamics method is the density functional theory (DFT). In a nutshell, DFT provides an efficient way of determining the ground-state properties of a many-electron system by calculating its equilibrium electron density. A theoretical foundation of DFT is provided by the Hohenberg-Kohn (HK) theorems [98] which are formulated for any system which consists of electrons moving in an external potential $v_{\text{ext}}(\mathbf{r})$. Stated simply, the main conclusions of the two theorems can be summarized as follows:

(1) the external potential $v_{\text{ext}}(\mathbf{r})$, and hence the total energy E of the system, is a unique functional of the electron density $n(\mathbf{r})$, which depends only on three spatial coordinates;

(2) the ground-state energy can be obtained variationally, e.g. the density that minimizes the total energy functional is the exact ground-state density.

A practical implementation of DFT is based on the Kohn-Sham scheme [134] which provides a recipe for calculating the ground-state electron density by mapping the interacting system to a system of non-interacting quasi-particles moving in an effective potential, which produces the same electron density, e.g. the one corresponding to the original interacting system. Although the DFT formalism is in principle exact, the effective potential in the Kohn-Sham DFT includes the exchange-correlation (XC) part, which contains information about all electron-electron interactions beyond the Hartree level. This XC functional is unknown and must be approximated. The most widely used approximation is the local density approximation (LDA), where the XC functional depends only on the electron density at the position, at which the functional is evaluated, and it takes the value corresponding to that of the homogeneous electron gas.

The generalization of DFT for a first-principles treatment of the spin degrees of freedom, offered by spin-density functional theory (SDFT), provides a powerful tool for the calculation of spin-dependent properties of the system such as spin-densities and spin-resolved single-particle band structures. However, it is applicable only in the static regime since DFT itself is a ground-state theory by construction. The situation

has changed with the development of time-dependent DFT (TDDFT) [170] which has brought the dynamical phenomena within the reach of DFT. The general formalism of TDDFT is based on the Runge-Gross (RG) theorem [215] which can be viewed as an extension of HK theorem to time-dependent systems. The RG theorem demonstrates that, for a given initial state (wave function), there is a unique mapping between the time-dependent external potential of a system $v_{\text{ext}}(\boldsymbol{r}, t)$ and its time-dependent electron density $n(\boldsymbol{r}, t)$. Similarly to the static case, one can use the time-dependent version of the Kohn-Sham scheme, where an auxiliary system of non-interacting electrons is constructed and the corresponding time-dependent equations of motion are solved. The first explicitly spin-dependent version of TDDFT was proposed by Liu and Vosko [160]. Since then the foundations of time-dependent SDFT (TD-SDFT) has been laid out. The general equations of motion for the spin-density, which can also provide information on the spin-currents, have been derived from TD-SDFT by Capelle *et al.* [39]. Note that the spin-resolved version of LDA is the local spin-density approximation (LSDA).

Although TDDFT provides a more suitable framework for investigating dynamical processes, for instance, for the calculation of the energies of excited states of the system, it inherits some of the limitations which are intrinsic to DFT. One of the long-standing problems in DFT is the difficulty in treating strongly-correlated systems. This is attributed to the shortcomings of the typically used approximations to the XC functional, such as the LDA, which do not fully account for electron-electron interaction. The same problem persists in TDDFT as it also requires the knowledge of the time-dependent XC functional for practical applications. The most natural approximation to the time-dependent XC functional is the adiabatic local density approximation (ALDA), where the ground-state LDA functional is calculated for the instantaneous time-dependent density distribution. Clearly, such local (in space and time) approximation will suffer from the same limitations as its static counterpart.[5] Moreover, it appears that the non-locality problem affects TDDFT even in a more severe form. Additional complications arise from the time-dependence: if the non-locality in time is taken into account, e.g. the XC potential at time t depends on the density at an earlier time t', then at this earlier time a small volume element of the system, which is now located at position $\boldsymbol{r}$, was located at a different position $\boldsymbol{r}'$. In other words, the non-locality in time leads to the non-locality in space. An attempt to deal with this problem on a fundamental level is undertaken by time-dependent current density functional theory (TD-CDFT) [261],

[5] As we will see in Chapter 6 time-dependent approaches to electronic transport combined with novel exchange-correlation functionals, carrying a derivative discontinuity, may provide insight into new dynamical phenomena originating from electron correlation.

where the current density is considered as the primary independent variable together with the electron density.

A well-known practical scheme for *ab initio* spin dynamics was proposed by Antropov *et al.* in the mid 1990s [8, 9]. The authors introduced general equations of motion which describe spin dynamics in magnetic materials in the adiabatic approximation. The latter allows one to adopt a mixed quantum-classical description of the spin degrees of freedom in magnetic materials containing atoms with localized magnetic moments. Because of the difference in the characteristic energies of the itinerant and the localized spins [the intersite exchange integrals are typically much smaller (< 100 meV) than the characteristic band energies], the orientations of the local magnetic moments are considered to be slowly varying in time compared to their magnitudes, and the angles of the magnetization are introduced as collective variables within DFT. These variables are represented by vectors and are essentially treated as classical degrees of freedom, analogously to the nuclear coordinates in a Born-Oppenheimer approximation (BOA) [27]. Such separation of the spin degrees of freedom is, in fact, justified in many systems with localized magnetic moments and has been used successfully to calculate experimentally verifiable quantities like spin-wave stiffness in transition metals [7, 156, 157]. Antropov's scheme provides the theoretical footing for some large-scale numerical implementations of atomistic spin dynamics, as the one described in Ref. [225].

To conclude this section, we note that although methodological and computational schemes for *ab initio* simulations of spin dynamics have been developed, such simulations are usually computationally demanding. Alternative to that are model Hamiltonian based approaches that provide a suitable framework for atomistic simulations of spin dynamics and can be, in principle, extended to *ab initio* schemes.

2.4 Spin dynamics in finite atomic-scale systems

In this section we describe the simulation method for spin dynamics used in this Thesis. The original formulation of the method can be found in Refs. [229, 231]. We start with the description of a general scheme for spin dynamics based on the Liouville-von Neumann equation and then discuss applications to the systems of interest. In particular, we consider an implementation of the tight-binding model within the proposed time-dependent formalism. We also discuss the Ehrenfest approach which will be used

to simulate the mixed quantum-classical dynamics in a system consisting of a number of localized magnetic impurities embedded in a low-dimensional atomic lattice.

2.4.1 General scheme for spin dynamics

The time evolution of any quantum-mechanical system, described by a Hamiltonian $\hat{H}_{\mathrm{S}}$, is governed by the Schrödinger equation

$$\imath\hbar \frac{\partial \left|\Psi_{\mathrm{S}}(t)\right\rangle}{\partial t} = \hat{H}_{\mathrm{S}} \left|\Psi_{\mathrm{S}}(t)\right\rangle , \tag{2.23}$$

where $\left|\Psi_{\mathrm{S}}(t)\right\rangle$ is a state vector[6] of the system, which is represented, according to Dirac notation, by a ket-vector in the Hilbert space ($\left|\Psi_{\mathrm{S}}(t)\right\rangle \in \mathcal{H}$).

In the case of the time-independent Hamiltonian, we can make the following ansatz for a special class of solutions of Eq. (2.23) using the method of separation of variables

$$\left|\Psi_{\mathrm{S}}(t)\right\rangle = f(t) \left|\psi\right\rangle , \tag{2.24}$$

where the function $f(t)$ only depends on time while $\left|\psi\right\rangle$ is a time-independent part of the wave function. By inserting Eq. (2.24) into the time-dependent Schrödinger equation, we find

$$f(t) = const \cdot e^{-\imath Et/\hbar}, \tag{2.25}$$

where E is the energy. The wave function $\left|\psi\right\rangle$ thus satisfies the following equation

$$\hat{H}_{\mathrm{S}} \left|\psi\right\rangle = E \left|\psi\right\rangle . \tag{2.26}$$

This is the time-independent, or stationary, Schrödinger equation, which essentially describes the stationary solutions of the time-dependent Schrödinger equation with the Hamiltonian $\hat{H}_{\mathrm{S}}$. The stationary solutions are represented by wave functions in the form $\left|\Psi_{\mathrm{S}}(t)\right\rangle = e^{-\imath Et/\hbar} \left|\psi\right\rangle$, where the time dependence enters only through a phase factor $e^{-\imath Et/\hbar}$, meaning that during the time evolution the wave function only

[6]The state vector can be specified in some representation with respect to a basis of orthogonal states $\left|x_1, ..., x_f\right\rangle$ defined by a complete set of simultaneously measurable physical observables $\{X\} = \{X_i, ..., X_f\}$

$$\left\langle x_1, ..., x_f | \Psi_{\mathrm{S}}(t)\right\rangle = \Psi_{\mathrm{S}}(x_1, ..., x_f, t),$$

where the function $\Psi_{\mathrm{S}}(x,t) \equiv \Psi_{\mathrm{S}}(x_1, ..., x_f, t)$ is called a wave function in the X-representation. In this chapter we will use "state vector" and "wave function" as interchangeable notions.

accumulates a phase. Equation (2.26) can be considered as an eigenvalue problem for a Hermitian operator $\hat{H}_{\mathrm{S}}$, for which the eigenvalues E are real and the eigenvectors $|\psi\rangle$, corresponding to different eigenvalues, are orthogonal. Although Eq. (2.26) is formally solvable, in reality, an exact solution can be found only for a limited range of models and systems of small size. In condensed matter physics, however, the systems of interest usually consist of a large number of interacting electrons and nuclei, which makes the Hamiltonian in Eq. (2.26) rather complicated and the associated wave function $|\psi\rangle$ practically impossible to calculate. This is the reason why one needs to resort to alternative methods such as DFT, which was discussed in the previous section.

In the general case of time-dependent Hamiltonian $\hat{H}_{\mathrm{S}}(t)$, one must solve Eq. (2.23). In principle, the formal solution of the time-dependent Schrödinger equation is known. By introducing the unitary time-evolution operator $\hat{U}_{\mathrm{S}}$, the solution can be written as

$$|\Psi_{\mathrm{S}}(t)\rangle = \hat{U}_{\mathrm{S}}(t, t_0)\,|\Psi_{\mathrm{S}}(t_0)\rangle\,, \tag{2.27}$$

where t_0 is an arbitrary initial time. By inserting the above expression into equation Eq. (2.23) and integrating over time we obtain [46, p. 19]

$$\hat{U}_{\mathrm{S}}(t) \equiv \hat{U}_{\mathrm{S}}(t, t_0) = 1 - \frac{\imath}{\hbar}\int_{t_0}^{t} \hat{H}_{\mathrm{S}}(t_1)\hat{U}_{\mathrm{S}}(t_1, t_0)dt_1. \tag{2.28}$$

Iterating Eq. (2.28) further we find

$$\hat{U}_{\mathrm{S}}(t, t_0) = 1 - \frac{\imath}{\hbar}\int_{t_0}^{t} \hat{H}_{\mathrm{S}}(t_1)dt_1 + \left(-\frac{\imath}{\hbar}\right)^2 \int_{t_0}^{t}\int_{t_0}^{t_1} \hat{H}_{\mathrm{S}}(t_1)\hat{H}_{\mathrm{S}}(t_2)dt_1\,dt_2 + ..., \tag{2.29}$$

which leads to the following nested integral

$$\mathcal{I}_n(t) = \left(-\frac{\imath}{\hbar}\right)^n \int_{t_0}^{t} dt_1 \int_{t_0}^{t_1} dt_2 ... \int_{t_0}^{t_{n-1}} dt_n \hat{H}_{\mathrm{S}}(t_1)...\hat{H}_{\mathrm{S}}(t_n), \tag{2.30}$$

where $t > t_1 > ... > t_n > t_0$. If one performs a permutation of any of the time variables $t_1, ..., t_n$ in $\mathcal{I}_n(t)$, in the new ordering the earlier times will still be on the right to the later ones, while the value of the integral remains the same. Therefore, one can sum over all identical integrals obtained by the permutations. In order to do that, we can introduce the time-ordering operator P, which, in the case of two operators, reads

$$P[\hat{H}_{\mathrm{S}}(t_1)\hat{H}_{\mathrm{S}}(t_2)] = \hat{H}_{\mathrm{S}}(t_1)\hat{H}_{\mathrm{S}}(t_2)\theta(t_1 - t_2) - \hat{H}_{\mathrm{S}}(t_2)\hat{H}_{\mathrm{S}}(t_1)\theta(t_2 - t_1), \tag{2.31}$$

where θ is the Heaviside step function. The definition can be generalized to n operators as follows

$$P[\hat{H}_{\mathrm{S}}(t_1)\hat{H}_{\mathrm{S}}(t_2)...\hat{H}_{\mathrm{S}}(t_n)] = \sum_{Q} \hat{H}_{\mathrm{S}}(t_{Q_1})\hat{H}_{\mathrm{S}}(t_{Q_2})...\hat{H}_{\mathrm{S}}(t_{Q_n}) \prod_{n} \theta(t_{Q_{n-1}} - t_{Q_n}). \quad (2.32)$$

Note that in the case of fermionic operators one uses Wick's time ordering operator T, which is defined similarly to P in Eq. (2.31) but with a minus sign instead of a plus.

Finally, after summing over all permutations, we obtain

$$\mathcal{I}_n = \frac{1}{n!}\left(-\frac{\imath}{\hbar}\right)^n \int_{t_0}^{t} dt_1 ... \int_{t_0}^{t_{n-1}} dt_n \, T[\hat{H}_{\mathrm{S}}(t_1)...\hat{H}_{\mathrm{S}}(t_n)], \quad (2.33)$$

and

$$\hat{U}_S(t, t_0) = Texp\left[-\frac{\imath}{\hbar}\int_{t_0}^{t} d\tau \hat{H}_{\mathrm{S}}(\tau)\right], \quad (2.34)$$

where $Texp$ denotes the exponential series of time-ordered products. The above equation is a formal solution of the time-dependent Schrödinger equation for any Hamiltonian $\hat{H}_{\mathrm{S}}(t)$. Clearly, if $\hat{H}_{\mathrm{S}}(t)$ is known as a simple function of time, the integral in Eq. (2.34) can be easily calculated. Another advantage of having an explicit expression for the time-evolution operator becomes clear if we look at the evolution of the system in the *interaction picture*, in which the Schrödinger picture Hamiltonian $\hat{H}_{\mathrm{S}}(t)$ is divided into two parts

$$\hat{H}_{\mathrm{S}}(t) = \hat{H}_0 + \hat{V}(t), \quad (2.35)$$

where $\hat{H}_0$ is usually time-independent while $\hat{V}(t)$ represents a time-dependent perturbation. A state vector in the interaction picture is defined as

$$|\Psi_{\mathrm{I}}(t)\rangle = e^{\imath \hat{H}_0 t/\hbar} |\Psi_{\mathrm{S}}(t)\rangle, \quad (2.36)$$

where $|\Psi_{\mathrm{S}}(t)\rangle$ is the state vector in the Schrödinger picture. The evolution of $|\Psi_{\mathrm{I}}(t)\rangle$ is given by

$$\imath\hbar \frac{\partial |\Psi_{\mathrm{I}}(t)\rangle}{\partial t} = \hat{V}_{\mathrm{I}}(t) |\Psi_{\mathrm{I}}(t)\rangle, \quad (2.37)$$

where $\hat{V}_{\mathrm{I}}(t) = e^{\imath \hat{H}_0 t/\hbar} \hat{V}(t) e^{-\imath \hat{H}_0 t/\hbar}$ and the formal solution for the time-evolution operator in the interaction picture reads

$$\hat{U}_{\mathrm{I}}(t, \tau) = Texp\left[-\frac{\imath}{\hbar}\int_{\tau}^{t} dt' \hat{V}_{\mathrm{I}}(t')\right]. \quad (2.38)$$

This expression can be expanded in powers of V_{I} and it is the basis of the time-dependent perturbation theory.

Since we do not intend to use a perturbative approximation and, in general, the Hamiltonian $\hat{H}_{\mathrm{S}}(t)$ is a complicated function of time, we go back to the original time-dependent Schrödinger equation. The vector $|\Psi_{\mathrm{S}}(t)\rangle$ in Eq. (2.23) describes a quantum-mechanical state of the system and can be expanded in the basis of eigenvectors of any Hermitian operator $\hat{A}$ corresponding to an observable A so that

$$|\Psi_{\mathrm{S}}(t)\rangle = \sum_k c_k(t)\,|\phi_k\rangle\,, \tag{2.39}$$

where $|\phi_k\rangle$ are eigenvectors of $\hat{A}$, which form a complete set of orthogonal basis states in the Hilbert space, with corresponding eigenvalues a_k ($\hat{A}\,|\phi_k\rangle = a_k\,|\phi_k\rangle$). The expectation value of $\hat{A}$ in a state $|\Psi_{\mathrm{S}}(t)\rangle$ is given by

$$\left\langle \hat{A} \right\rangle = \left\langle \Psi_{\mathrm{S}}(t)|\hat{A}|\Psi_{\mathrm{S}}(t) \right\rangle = \sum_k a_k |\,\langle\phi_k|\Psi_{\mathrm{S}}(t)\rangle\,|^2, \tag{2.40}$$

where $\omega_k(t) = |\,\langle\phi_k|\Psi_{\mathrm{S}}(t)\rangle\,|^2$ represents the probability of finding the system in the quatum state $|\phi_k\rangle$. The statistical aspects of quantum mechanics can be represented by the notion of an ensemble of noninteracting "replicas" of the system, which are in the same quantum state $|\Psi_{\mathrm{S}}(t)\rangle$, and each replica can be found in one of the states $|\phi_k\rangle$ with the probability $\omega_k(t)$. An ensemble introduced in such a way is called a *pure* quantum ensemble. Physically, however, the realization of a pure ensemble is practically impossible and, therefore, one has to deal with ensembles of a more general type, namely, with *mixed* ensembles, where a state of the system is represented by a statistical "mixture" of several quantum-mechanical states. Such mixed states can be conveniently described by using the concept of the *density matrix*, which is defined as[7]

$$\hat{\rho}(t) = \sum_r \omega_r\,|\Psi_r(t)\rangle\,\langle\Psi_r(t)|\,, \tag{2.41}$$

[7] In temperature-dependent problems ($T \neq 0$), one needs to define $\hat{\rho}$ as a statistical operator: 1) $\hat{\rho} = e^{-\beta\hat{H}}/\mathcal{Z}_C$ in the case of the canonical ensemble, in which the system is allowed to exchange heat with the environment at fixed temperature, volume and number of particles; 2) $\hat{\rho} = e^{-\beta\left(\hat{H}-\mu\hat{N}\right)}/\mathcal{Z}$ for the grand-canonical ensemble, in which the system exchanges both heat and particles with the environment at fixed temperature, volume and chemical potential (μ). The corresponding partition functions are defined as $\mathcal{Z}_C = Tre^{-\beta\hat{H}}$ and $\mathcal{Z} = Tre^{-\beta\left(\hat{H}-\mu\hat{N}\right)}$, where $\beta = 1/k_{\mathrm{B}}T$ and $\hat{N}$ the electron number operator.

where $\{|\Psi_r(t)\rangle\}$ is a set of arbitrary normalized quantum states and $\omega_r \geq 0$ is the probability of finding the system of the ensemble in the state $|\Psi_r(t)\rangle$ with $\sum_r \omega_r = 1$. The density matrix is a Hermitian and positive-definite operator with $Tr\hat{\rho} = 1$, where Tr denotes the sum over all diagonal elements, independent of the basis.

Importantly, the expectation value of an operator $\hat{A}$, corresponding to a quantum-mechanical observable A, is now given by

$$\left\langle \hat{A} \right\rangle = \sum_r \omega_r \left\langle \Psi_r(t)|\hat{A}|\Psi_r(t) \right\rangle = Tr\left[\hat{\rho}\,\hat{A}\right]. \tag{2.42}$$

Thus in a mixed ensemble a state of the system is not a superposition of quantum states as in the pure ensemble [see Eq. (2.39)], but is a statistical "mixture" of different quantum states, which do not interfere for any observable A.

It follows from the time-dependent Schrödinger equation [Eq. (2.23)] and from the definition of $\hat{\rho}(t)$ [Eq. (2.41)] that the evolution of the density matrix is given by

$$\frac{\partial \hat{\rho}}{\partial t} = \frac{\imath}{\hbar}\left[\hat{\rho}, \hat{H}\right]. \tag{2.43}$$

This is known as the Liouville-von Neumann, or quantum Liouville equation.

Finally, any operator $\hat{A}$ evolves according to the following equation in the Heisenberg picture

$$\frac{d\hat{A}_{\mathrm{H}}(t)}{dt} = \frac{\partial \hat{A}_{\mathrm{H}}(t)}{\partial t} + \frac{\imath}{\hbar}\left[\hat{H}(t), \hat{A}_{\mathrm{H}}(t)\right]. \tag{2.44}$$

The density matrix is the quantum-mechanical analogue of the phase-space distribution function as it is defined in classical nonequilibrium statistical mechanics [283, p. 11]. In order to illustrate this analogy, we recall some of the basic concepts of statistical mechanics.

In Hamiltonian mechanics a dynamical state, or a microscopic state, of a system with f degrees of freedom is characterized by the set of generalized coordinates $(q) = (q_1, ..., q_f)$ and conjugate momenta $(p) = (p_1, ..., p_f)$, or by a point $(q, p) = (q_1, ..., q_f; p_1, ..., p_f)$ in a $2f$-dimensional phase-space Γ. The evolution of the microscopic state is given by a trajectory $\{(q), (p)\}$ in Γ space while the phase variables $q_i(t)$ and $p_i(t)$ vary according

to the Hamilton equations

$$\frac{dq_i(t)}{dt} = \frac{\partial H(q,p,t)}{\partial p_i}, \tag{2.45}$$

$$\frac{dp_i(t)}{dt} = -\frac{\partial H(q,p,t)}{\partial q_i}, \tag{2.46}$$

where $i = 1, ..., f$ and $H(q,p,t)$ is the Hamiltonian, or the Hamiltonian function, of the system. For macroscopic systems, consisting of many particles, it is difficult to determine the microscopic state and its exact trajectory. Therefore, it is convenient to use a probabilistic interpretation of the dynamical processes, where one considers a statistical ensemble described by the distribution function $\rho(q,p,t)$ which satisfies

$$\int \rho(q,p,t)d\Gamma = 1. \tag{2.47}$$

The quantity $d\omega = \rho(q,p,t)d\Gamma$ is the probability of finding the system of the ensemble in the element $d\Gamma$ of the phase space, close to the point (q,p) at time t.

The result of the measurement of the physical quantity $\mathcal{A}$ can be taken as an average value $\langle\mathcal{A}\rangle$ of the corresponding dynamical variable $\mathcal{A}(q,p,t)$ which reads

$$\langle\mathcal{A}\rangle = \int \mathcal{A}(q,p,t)\rho(q,p,t)d\Gamma. \tag{2.48}$$

The distribution function satisfies the classical Louville equation, a classical analogue of the Liouville-von Neumann equation

$$\frac{\partial\rho}{\partial t} = \{H,\rho\}, \tag{2.49}$$

where $\{,\}$ denotes the Poisson bracket, which for any two functions $\varphi_1(q,p,t)$ and $\varphi_2(q,p,t)$ is defined as

$$\{\varphi_1,\varphi_2\} = -\{\varphi_2,\varphi_1\} = \sum_{i=1}^{f} \frac{\partial\varphi_1}{\partial q_i}\frac{\partial\varphi_2}{\partial p_i} - \frac{\partial\varphi_1}{\partial p_i}\frac{\partial\varphi_2}{\partial q_i}. \tag{2.50}$$

The Liouville equation is a direct consequence of the Liouville's theorem, which states that the volume of the phase space is conserved during the dynamical evolution of the system.

By differentiating a dynamical variable $\mathcal{A}(q,p,t)$ over time and by taking into account

that the derivatives $\dot{q}$ and $\dot{p}$ are given by the Hamilton equations [see Eq. (2.46)], we obtain the equation of motion for $\mathcal{A}(q, p, t)$

$$\frac{d\mathcal{A}}{dt} = \frac{\partial \mathcal{A}}{\partial t} + \{\mathcal{A}, H\}, \tag{2.51}$$

which is, indeed, very similar to the quantum-mechanical equation for the operator $\hat{A}$, corresponding to an observable A.

The above discussion clearly demonstrates a deep analogy between classical and quantum statistical mechanics and provides an intuitive understanding of the concept of the density matrix using a simple probability language. In particular, the most important common concept in both theories is the Liouville equation [see Eq. (2.43) and Eq. (2.49)]. We will further explore the analogy between quantum and classical equations of motion when dealing with mixed quantum-classical simulations of spin dynamics within the Ehrenfest approximation (see Section 2.4.3).

The quantum Liouville equation provides a convenient and compact description of the time evolution of a quantum-mechanical system and it is the central equation in our method for atomistic simulations of spin dynamics. As it is a first order differential equation,[8] it can be integrated using a reliable time-integration method. Once the density matrix is calculated, all the physical quantities of interest, including spin observables such as spin-densities, can be obtained straightforwardly.

So far we considered Eq. (2.43) in its most general form without specifying the Hamiltonian $\hat{H}(t)$. In the next two subsections we will discuss some particular cases of the model Hamiltonian, which are most suitable for the description of the systems of interest such as atomic chains. We emphasize, however, that the time-dependent scheme based on Eq. (2.43) is applicable to a wide range of Hamiltonians, including *ab initio* ones. In the simplest case of LSDA, the evaluation of the Kohn-Sham Hamiltonian at each time step, following the modifications in the electronic density, can be incorporated into the time-integration loop for Eq. (2.43).

[8] More precisely, it is a system of $(2N)^2$ equations if the operator $\hat{\rho}(t)$ is expressed in some spin-resolved basis $\{\phi_k\}_{k=1}^{2N}$ (2 is for spin) and one considers an equation for each density matrix element $\rho_{kk'}(t) = \langle \phi_k | \hat{\rho}(t) | \phi_{k'} \rangle$ in this basis. The number of equations can be further reduced down to $2N(2N+1)/2$ if we take advantage of the hermicity of $\hat{\rho}$ and only consider the elements in the upper triangular part of the density matrix.

2.4.2 Tight-binding model

The tight-binding (TB) model [10, p. 175] is a quantum-mechanical model that provides a simple and yet physically motivated description of electronic states in materials. The name "tight binding" suggests that this electronic structure model describes the properties of tightly bound electrons. This implies that the overlap of atomic orbitals is small enough to consider the wave function of the electron to be rather similar to the atomic orbital of the atom it belongs to. In the practical electronic structure calculations within the TB approximation, one uses an approximate set of wave functions based on the superposition of wave functions of isolated atoms located at each atomic site. This concept goes back to the linear combination of atomic orbitals (LCAO) method [226], which was first used for approximating molecular orbitals and was extended to the case of solids by Bloch. TB models are currently applied to a wide variety of problems in physics and chemistry. In many cases they give qualitatively accurate results for electronic properties of realistic materials, a well known example being graphene, a two-dimensional honey-comb lattice of carbon atoms. We also note that most of the celebrated models in condensed matter physics, such as the Hubbard model, are essentially based on the TB Hamiltonian.

As the capabilities of accurate *ab initio* simulations of materials are constantly increasing, so does the demand for methods that are able to capture the important physics while still being fast enough to simulate large systems. This is particularly relevant for time-dependent simulations as in spin and molecular dynamics where *ab initio* based approaches are still limited to relatively small sizes and short times. The TB model offers an alternative to accurate but computationally demanding first-principles calculations. Within the TB approximation one approaches the electronic structure problem by constructing a one-body Hamiltonian of the system and by solving the eigenvalue problem. In contrast to DFT, the TB model assumes only a minimal local basis of atomic orbitals and it is usually non-self-consistent. These approximations reduce the accuracy of the method but enable much faster calculations, a feature which is particularly useful for large systems. The parameters entering the TB Hamiltonian, such as the overlap integrals, can be determined by fitting either to a set of experimental data (empirical TB) or to band structures and total energies obtained with advanced electronic structure methods (semi-empirical TB). A large number of semi-empirical TB-based models have been developed for a variety of crystalline metals, semiconductors and insulators [194]. The simplest and still widely used method of parametrization

of the TB model, based on the two-center approximation for the TB Hamiltonian matrix elements, goes back to the work of Slater and Koster [226].

TB model for quasi-1D nanostructures on Si(100) surface

Just as a practical example, which illustrates the usefulness of the TB model, we will consider one particular system, for which even a very simple TB Hamiltonian produces quite reasonable results, namely, quasi one-dimensional (1D) nanostructures on Si(100) surface. In fact, this surface has been one of the most intensively studied structures in the past decades due to its complexity and technological importance. Recently, this system has gained renewed attention from both experimental and theoretical communities due to the possibility of creating quasi 1D confinement on this surface, thus allowing to construct and explore real quantum wells [186].

The Si atoms terminating the Si(100) surface pair up to form dimers in order to reduce the number of dangling bonds per atom. The dimers are arranged in rows along the [110] direction and essentially form quasi-1D nanostructures, or nanowires, as shown schematically in Fig. 2.5(b). The remaining dangling bonds have been shown to give the main contribution to the surface states near the Fermi level. The tilting (buckling) of the dimers results in the redistribution of charge in the dimers and to the formation of the surface band gap between occupied π and empty π^* dangling bond states. The latter (the empty π^* band) exhibits quasi-1D character leading to quantum confinement effects.

Notably, there exist several possibilities of the surface reconstruction for Si(100) surface, such as (c4 $\times$ 2), where the dimers are tilted in anti-phase both along and across the dimer rows, and (p2 $\times$ 2), where the buckling is alternating along the rows but is in-phase in the perpendicular direction. It is still not entirely clear which of the two reconstructions is the most stable. Recent theoretical works, based on the DFT calculation of the total energy of the surface configuration, demonstrate that the energy difference between the two possible reconstructions is indeed quite small ($\sim$ 0.5 meV per Si-Si dimer) with (c4$\times$2) being the most energetically favorable [169]. In our model calculations we consider a simpler case of the (p2 $\times$ 2)-reconstruction [see Fig. 2.5(b)], which requires a smaller unit cell.

The band structure of the 10-layer slab of the Si(100) surface in p2 $\times$ 2-reconstruction from Ref. [169] is presented in Fig. 2.5(a) [black lines]. The figure shows only the first two bands above the Fermi level which are effectively decoupled from the bulk states.

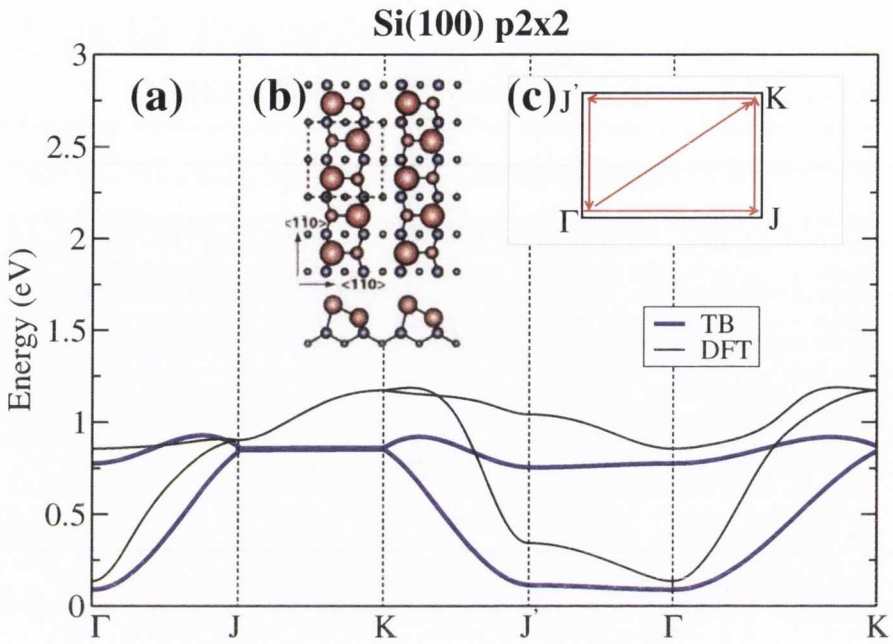

FIGURE 2.5: (a) The black lines show the electronic band structure of a 10-layer cut of the Si(100) surface in (p2 × 2)-reconstruction reported in Ref. [169] (the calculation was performed for a relaxed structure and a 2 × 2 supercell using OpenMX[2] simulation package, based on DFT with norm-conserving pseudopotential and linear combination of pseudo-atomic localized basis set). Only the two bands originating from the surface states are shown. The thick purple lines show the fit of the two bands obtained from a tight-binding model for a nanowire formed by the dimer rows. The following parameters have been used: $\mathcal{E}_t = 0.87$ eV, $\mathcal{E}_b = 5.0$ eV, $|\gamma_{tb}| = 0.24$ eV, $|\gamma'_{tb}| = 0.7$ eV, $|\gamma_{tt}| = 0.1$ eV, $|\gamma_{bb}| = 0.09$ eV. (b) Ball-and-stick representation of the first three layers of the investigated surface (top view). The Si-Si dimers are shown in red and the top atoms of the dimers are represented by larger balls compared to the neighboring bottom atoms (from Ref. [237]). The square marks the basis for the TB calculation, consisting of two top and two bottom atoms. (c) Brillouin zone path used for electronic band structure calculation.

One immediately notices that the bands exhibit dispersion only along the dimer rows direction (ΓJ and KJ′) which, indeed, indicates a quasi-1D character.

It is quite natural to build a TB Hamiltonian on the basis of a quasi-1D lattice formed by the Si-Si dimers, in order to model the surface band structure. The unit cell for our TB calculation consists of four atoms, which constitute two neighboring dimers as shown in Fig. 2.5(b). We use the periodic conditions along the dimer rows in order to simulate an infinite nanowire and include only the nearest-neighbors interactions. Thus the parameters of the TB Hamiltonian are the on-site energies of the top ($\mathcal{E}_t$) and bottom ($\mathcal{E}_b$) atoms, the hopping integrals between the top atoms (γ_{tt}) and the bottom atoms (γ_{bb}), the hopping integrals between the top atom and the bottom atom across

the dimer rows ($\gamma_{\rm tb}$) and along the dimer rows ($\gamma'_{\rm tb}$). These parameters have been fitted to reproduce the main features of the bands calculated using DFT and the results are shown in Fig. 2.5(a) [purple lines]. Although the agreement between TB and DFT is not perfect, mainly due to the fact that the coupling to the underlying layers is not taken into account in the TB Hamiltonian, the character of the bands is well captured by the TB model, in particular the absence of dispersion along the direction perpendicular to the dimer rows (JK). This essentially means that our quasi-1D model, with parameters fitted to DFT, can be used to investigate the properties of the nanostructures formed on the Si(100) surface. If one is interested in the dynamical properties, for instance, in the presence of magnetic impurities on the surface, the time-dependent scheme for spin dynamics simulations, discussed in the previous section, can be readily applied to this system.

Since the TB model provides a natural framework for the model Hamiltonian based description of atomistic systems, we will use it as a main electronic structure tool throughout this Thesis. In Chapter 3 and Chapter 4 we will consider systems in which the main components are 1D chains of atoms. An isolated atomic chain consisting of N sites will be typically described by a spin-polarized single-band nearest-neighbors TB Hamiltonian, which can be conveniently written in the second quantization form as

$$\hat{H}_{\rm TB} = \sum_{\substack{i,j\,=\,1,N \\ \alpha\,=\uparrow,\downarrow}} H_{ij}^{\rm TB}\, \hat{c}_i^{\alpha\dagger}\, \hat{c}_j^{\alpha}, \tag{2.52}$$

where $H_{ij}^{\rm TB} = \varepsilon_i\, \delta_{ij} + \gamma_{ij}\, \delta_{i,j\pm1}$ with on-site energies ε_i and the hopping integral γ_{ij} between sites i and j (most of the time we will consider a single uniform hopping γ, which is the same for all sites); $\hat{c}_i^{\alpha\dagger}(\hat{c}_i^{\alpha})$ is the creation (annihilation) operator for an electron with spin-up ($\alpha =\uparrow$) or spin-down ($\alpha =\downarrow$) at the atomic site i. In order to work with concise expressions, we will sometimes omit the limits of summation, for example the sum in Eq. (2.52) will be substituted by $\sum_{i,j,\alpha}$. The wave functions of the Hamiltonian will be constructed in the basis of the spin-resolved atomic orbitals $|i\,\sigma\rangle \equiv |i\rangle \otimes |\sigma\rangle$ where $i = 1, ..., N$ is atomic site index and $\sigma =\uparrow,\downarrow$ denotes the spin component.

To conclude the discussion on the TB model, we will derive the explicit expressions for the spin-currents, or spin-resolved bond currents, which arise from the dynamical evolution of the spin degrees of freedom in a system described by a TB Hamiltonian. This is particularly useful for Chapter 6, where we will use the definition of the bond

current to construct the *I-V* characteristics of a nanojunction, consisting of a single quantum dot attached to two 1D leads described by a TB Hamiltonian.

Spin-currents in TB model

In the basis of spin-resolved atomic orbitals $|i\,\sigma\rangle$, the equation of motion for each density matrix element $\rho_{ii}^{\sigma\sigma} = \langle\sigma\, i|\hat{\rho}|i\,\sigma\rangle$ can be written as

$$\frac{\partial\rho_{ii}^{\sigma\sigma}(t)}{\partial t} = \frac{1}{\imath\hbar}\left[\hat{H}(t),\hat{\rho}(t)\right]_{ii}^{\sigma\sigma} = \frac{1}{\imath\hbar}\sum_{k}\sum_{\gamma}\left\{H_{ik}^{\sigma\gamma}(t)\rho_{ki}^{\gamma\sigma}(t) - \rho_{ik}^{\sigma\gamma}(t)H_{ki}^{\gamma\sigma}(t)\right\}. \tag{2.53}$$

Here we consider a Hamiltonian of a more general type than the one in Eq. (2.52), namely

$$\hat{H}(t) = \sum_{i,j,\alpha} H_{ij}^{\mathrm{TB}}\,\hat{c}_i^{\alpha\dagger}\,\hat{c}_j^{\alpha} + \sum_{i}\sum_{\alpha,\beta}\hat{c}_i^{\alpha\dagger}\hat{\boldsymbol{\sigma}}^{\alpha\beta}\hat{c}_i^{\beta}\cdot\boldsymbol{\mathcal{B}}_i(t), \tag{2.54}$$

where $\hat{H}_{ij}^{\mathrm{TB}}$ is the same as in Eq. (2.52) and $\hat{\boldsymbol{\sigma}} = \frac{1}{2}(\sigma_x,\sigma_y,\sigma_z)$ is the electron spin operator, $\{\sigma_l\}_{l=x,y,z}$ being the set of Pauli matrices. In the second term we have introduced a local coupling to an effective field $\boldsymbol{\mathcal{B}}_i(t)$. This can represent the interaction with a magnetic field $\boldsymbol{B}(t)$, e.g $\boldsymbol{\mathcal{B}}_i(t) \equiv g\mu_B\boldsymbol{B}(t)$, or a Heisenberg-type interaction with the spin of a magnetic impurity $\boldsymbol{S}$, e.g. $\boldsymbol{\mathcal{B}}_i(t) \equiv J\boldsymbol{S}(t)$ with J being the strength of the interaction (in the units of energy). Note that in the basis of localized atomic orbitals $e\rho_{ii}^{\sigma\sigma}$ is essentially the electron population on site i in a spin state σ (e is the electron charge).

We will define the current, or the charge flux, $I_n(t)$ as the amount of change of the on-site electron density in the time interval dt, e.g. $I_n(t) = e\sum_\sigma \dot{\rho}_{nn}^{\sigma\sigma}(t)$. One can then distinguish partial contributions to the current, namely, $I_n^\sigma(t) = e\dot{\rho}_{nn}^{\sigma\sigma}(t)$. For the spin-up case ($\sigma =\uparrow$) we have

$$\begin{aligned} I_n^{\uparrow}(t) \equiv e\dot{\rho}_{nn}^{\uparrow\uparrow}(t) &= \frac{e}{\imath\hbar}\sum_{k\neq n}(H_{nk}^{\uparrow\uparrow}\rho_{kn}^{\uparrow\uparrow} - \rho_{nk}^{\uparrow\uparrow}H_{kn}^{\uparrow\uparrow}) + \frac{e}{\imath\hbar}(H_{nn}^{\uparrow\downarrow}\rho_{nn}^{\downarrow\uparrow} - \rho_{nn}^{\uparrow\downarrow}H_{nn}^{\downarrow\uparrow}) + \\ &+ \frac{e}{\imath\hbar}\sum_{k\neq n}(H_{nk}^{\uparrow\downarrow}\rho_{kn}^{\downarrow\uparrow} - \rho_{nk}^{\uparrow\downarrow}H_{kn}^{\downarrow\uparrow}), \end{aligned} \tag{2.55}$$

where we have decomposed the sum over the site-index into parts with $k = n$ and $k \neq n$. Using the property of hermicity of the operators $\hat{H}$ and $\hat{\rho}$ we obtain a more

concise expression

$$I_n^{\uparrow}(t) = \underbrace{\frac{2e}{\hbar}\sum_{k\neq n}\Im\left(H_{nk}^{\uparrow\uparrow}\rho_{kn}^{\uparrow\uparrow}\right)}_{\sum_k I_{nk}^{\uparrow\uparrow}} + \underbrace{\frac{2e}{\hbar}\Im\left(H_{nn}^{\uparrow\downarrow}\rho_{nn}^{\downarrow\uparrow}\right)}_{I_{nn}^{\uparrow\downarrow}} + \underbrace{\frac{2e}{\hbar}\sum_{k\neq n}\Im\left(H_{nk}^{\uparrow\downarrow}\rho_{kn}^{\downarrow\uparrow}\right)}_{\sum_k I_{nk}^{\uparrow\downarrow}}, \tag{2.56}$$

where $I_{nk}^{\uparrow\uparrow}$ arises from the transfer of spin between sites n and k, $I_{nn}^{\uparrow\downarrow}$ represents the process which involves the change of spin at site n and $I_{nk}^{\uparrow\downarrow}$ describes the nonlocal contribution, which is due to the change of spin on different sites. Hereafter $\Im$ denotes the imaginary part. Note that the first term, $I_{nk}^{\uparrow\uparrow}$, is similar to the *bond current*, defined by Todorov [245, 246] in a non spin-polarized case as $I_{n,n+1} = \frac{2e}{\hbar}\Im\left(H_{n,n+1}\rho_{n+1,n}\right)$, which essentially describes the charge transport between sites n and $n+1$.

A similar expression can be written for the spin-down case ($\sigma = \downarrow$)

$$I_n^{\downarrow}(t) \equiv e\dot{\rho}_{nn}^{\downarrow\downarrow}(t) = \sum_{k\neq n} I_{nk}^{\downarrow\downarrow} + I_{nn}^{\downarrow\uparrow} + \sum_{k\neq n} I_{nk}^{\downarrow\uparrow}, \tag{2.57}$$

where the three contributions have the same meaning as those for the spin-up case.

In the presence of spin-mixing terms in the Hamiltonian, which act locally at site i [see the second term in Eq. (2.54)], the matrix elements of the form $H_{ij}^{\alpha\beta}$ for $i \neq j$ and $\alpha \neq \beta$ are zero. Thus the terms $I_{nk}^{\sigma\sigma'}$ vanish and one remains only with two contributions: one is $I_{nk}^{\sigma\sigma}$ and is related to the spin-transfer process which preserves the orientation of the spin, while the other, $I_{nn}^{\sigma\sigma'}$, represents the mixing of the spin-up and spin-down channels locally at site n. Clearly, the latter is zero in the absence of the spin-mixing terms as in the Hamiltonian given by Eq. (2.52).

By taking into account only the nearest-neighbors interactions, we obtain

$$I_n^{\uparrow}(t) = \frac{2e}{\hbar}\Im\left(H_{n,n-1}^{\uparrow\uparrow}\rho_{n-1,n}^{\uparrow\uparrow}\right) + \frac{2e}{\hbar}\Im\left(H_{n,n+1}^{\uparrow\uparrow}\rho_{n+1,n}^{\uparrow\uparrow}\right) + \frac{2e}{\hbar}\Im\left(H_{nn}^{\uparrow\downarrow}\rho_{nn}^{\downarrow\uparrow}\right), \tag{2.58}$$

$$I_n^{\downarrow}(t) = \frac{2e}{\hbar}\Im\left(H_{n,n-1}^{\downarrow\downarrow}\rho_{n-1,n}^{\downarrow\downarrow}\right) + \frac{2e}{\hbar}\Im\left(H_{n,n+1}^{\downarrow\downarrow}\rho_{n+1,n}^{\downarrow\downarrow}\right) + \frac{2e}{\hbar}\Im\left(H_{nn}^{\downarrow\uparrow}\rho_{nn}^{\uparrow\downarrow}\right). \tag{2.59}$$

The first two terms on the right-hand sides of both equations account for the transfer of spin from site $n-1$ to n and from n to $n+1$, respectively. We can then define a spin-resolved bond current

$$I_{n,n+1}^{\sigma} = \frac{2}{\hbar}\Im\left(H_{n,n+1}^{\sigma\sigma}\rho_{n+1,n}^{\sigma\sigma}\right), \tag{2.60}$$

which will be taken as the actual electric current through the bond $(n, n+1)$. The total charge bond current through the bond $(n, n+1)$ can be calculated as $I_{n,n+1} = \sum_\sigma I^\sigma_{n,n+1}$ and the spin-polarized bond current as $\Delta I_{n,n+1} = I^\uparrow_{n,n+1} - I^\downarrow_{n,n+1}$.

2.4.3 Ehrenfest spin dynamics

In this section we set out the theoretical framework for Chapter 4, where we investigate the possibility of the electrical control of spin transfer in monoatomic chains incorporating spin impurities. This is a brief introduction to the basic concepts and equations. Some specific issues, such as the relevance of our model system to realistic materials, will be discussed in Chapter 4.

We employ the mixed quantum-classical Ehrenfest description of the spin dynamics [229, 231], in the spirit of the *s-d* model, where the itinerant electrons are described by a TB Hamiltonian while the spins of the localized magnetic impurities are treated classically. The main assumptions underlying such quantum-classical description can be summarized as follows:

(1) At the fundamental level, the system is described by means of the *s-d* model [275, p. 221], where the magnetic moments of the impurities, originating from the deeply localized *d*-electrons, are coupled to the conduction *s*-electrons via an effective exchange interaction.[9]

(2) At the next level of approximation, in the limit of a strongly localized impurity, one assumes that the magnitude of the local magnetic moment is conserved and can thus be treated as an effective classical angular momentum, or *local spin*, at the impurity site.

Similarly to the quantum-mechanical spin operators [see Eq. (2.10)], these local spins obey the following commutation relations [273]

$$\left\{\mathcal{S}_i^\alpha, \mathcal{S}_i^\beta\right\} = \epsilon_{\alpha\beta\gamma}\mathcal{S}_i^\gamma, \tag{2.61}$$

[9]The *s-d* model has been designed for dilute magnetic alloys [136], e.g. non-magnetic metals incorporating magnetic impurity atoms. The calculation of the resistivity in the third-order perturbation theory by using the *s-d* model leads to the logarithmic terms, diverging at $T = 0$ [135]. This is an indication of the resistance minimum observed at low temperatures, a signature of the Kondo effect. Another important result of the *s-d* model is the RKKY [123, 214, 274] interaction between localized spins. Note also that an extension of the *s-d* model to include a quantum treatment of the local spins has been proved very successful in describing inelastic spin-excitations for magnetic adatoms on metallic surfaces [107].

where $\mathcal{S}_i^\alpha$ with $\alpha = x, y, z$ is the α-th Cartesian projection of the local spin $\boldsymbol{\mathcal{S}}_i$ and $\epsilon_{\alpha\beta\gamma}$ is the totally anti-symmetric permutation tensor ($\epsilon_{xyz} = 1$). Hereafter we will represent the local spins by the dimensionless unit vectors $\boldsymbol{S}_i$ defined as

$$\boldsymbol{S}_i = \frac{1}{\mathcal{S}} \boldsymbol{\mathcal{S}}_i, \tag{2.62}$$

where $\mathcal{S}$ is the magnitude of the local spin and we will consider $\mathcal{S} = \hbar$ in analogy with the quantum-mechanical equations of motion. Substituting $\boldsymbol{\mathcal{S}}_i$ in Eq. (2.61) by $\boldsymbol{\mathcal{S}}_i = \mathcal{S} \cdot \boldsymbol{S}_i$, we obtain the commutation relations for vectors $\boldsymbol{S}_i$

$$\left\{ S_i^\alpha, S_i^\beta \right\} = \frac{1}{\mathcal{S}} \epsilon_{\alpha\beta\gamma} S_i^\gamma, \tag{2.63}$$

where S_i^α are the Cartesian components of the dimensionless unit vector $\boldsymbol{S}_i$ in the direction of the i-th local spin.

Hamiltonian and equations of motion

For a system consisting of a N-sites long atomic chain and N (in general) spin impurities, exchange-coupled to the itinerant spin-density on site i, the time-dependent Hamiltonians read

$$\hat{H}_{\mathrm{el}}(t) = \sum_{i,j,\alpha} H_{ij}^{\mathrm{TB}} \hat{c}_i^{\alpha\dagger} \hat{c}_j^{\alpha} - J \sum_{i,\alpha,\beta} \hat{c}_i^{\alpha\dagger} \hat{\boldsymbol{\sigma}}^{\alpha\beta} \hat{c}_i^{\beta} \cdot \boldsymbol{S}_i(t), \tag{2.64}$$

$$H_{\mathrm{S}}(t) = \sum_i \boldsymbol{S}_i(t) \cdot \boldsymbol{\Theta}_i(t). \tag{2.65}$$

The top expression is for the electronic subsystem. Here the notation is the same as in Eq. (2.52) and Eq. (2.54) and H_{ij}^{TB} describes the matrix elements of a single-orbital nearest-neighbors Hamiltonian with on-site energies ε_i and hopping integral γ; $J > 0$ is the exchange coupling strength.

The Hamiltonian $H_{\mathrm{S}}(t)$ of the classical spins describes the interaction of $\boldsymbol{S}_i$ with the local effective field $\boldsymbol{\Theta}_i(t)$, which reads

$$\boldsymbol{\Theta}_i(t) = -J\boldsymbol{s}_i(t) - \frac{g\mu_{\mathrm{B}}}{\hbar} \mathcal{S} \boldsymbol{B}_i(t). \tag{2.66}$$

Here the first term described the coupling of the local spin $\boldsymbol{S}_i$ to the electron spin-density, taken as the instantaneous expectation value of the conduction-electron spin at site i, e.g. $\boldsymbol{s}_i(t) \equiv \langle \hat{\boldsymbol{\sigma}} \rangle_i (t)$. The second term describes the interaction with the

external magnetic field $\boldsymbol{B}_i$, which can be applied locally to $\boldsymbol{S}_i$. We assume $g = 2$ for the localized spins.

The equations of motions for the two subsystems then read

$$\frac{\partial \hat{\rho}(t)}{\partial t} = \frac{i}{\hbar}\left[\hat{\rho}(t), \hat{H}_{\mathrm{el}}(t)\right], \tag{2.67}$$

$$\frac{d\boldsymbol{S}_i(t)}{dt} = \{\boldsymbol{S}_i(t), H_{\mathrm{S}}(t)\}. \tag{2.68}$$

The first equation is the Liouville-von Neumann equation for the density matrix $\hat{\rho}$, which describes the quantum-mechanical system of itinerant electrons [see Eq. (2.43)]. The second one is the classical equation of motion for a dynamical variable $\boldsymbol{S}_i(t)$, which was derived earlier and is given in the general form by Eq. (2.51). The commutation relations for the local spin [see Eq. (2.63)] allow us to calculate the Poisson bracket in Eq. (2.68) so that the classical equation of motion now reads

$$\frac{d\boldsymbol{S}_i(t)}{dt} = -\frac{1}{\mathcal{S}}\boldsymbol{S}_i(t) \times \boldsymbol{\Theta}_i(t). \tag{2.69}$$

The classical Liouville equation is formally equivalent to its quantum mechanical counterpart [see Eq. (2.12)], if one assumes that vector $\boldsymbol{S}_i$ in Eq. (2.69) represents the expectation value of the quantum-mechanical spin and that its modulus remains constant.

Such mixed quantum-classical dynamics can be seen as a mapping onto the spin-space of the Ehrenfest approach to molecular dynamics [100, 102]. In fact, a widely used method for decoupling the dynamics of the heavy and slow ions from the dynamics of the light and fast electrons is based on the Born-Oppenheimer approximation (BOA) [27]. In this adiabatic approximation, one assumes that as the ions move, the electronic subsystem remains in the thermodynamic state, which minimizes its free energy for the given instantaneous ionic positions. A second method, which deals with some of the drawbacks of BOA, is the Ehrenfest approach, in which both electrons and ions are allowed to evolve according to their equations of motion. In these equations the two subsystems experience each other as external time-evolving classical fields. The ions are treated as classical particles, while the electrons are treated quantum-mechanically.

The separation of dynamical variables that leads to the system of quantum-classical equations of motion given by Eqs. (2.67)-(2.68) is, in principal, similar to Antropov's adiabatic approximation to spin dynamics, which we briefly discussed in Section 2.3.3.

Such adiabatic spin-dynamics (ASD) model is an approximation of the *ab initio* treatment of spin dynamics for materials with localized magnetic moments. The important difference between our model and the ASD is in the choice of the single-electron Hamiltonian. While in Antropov's ASD one uses the Kohn-Sham Hamiltonian, our model is based, in the present form, on a much simpler single-band non-interacting tight-binding Hamiltonian. This, however, allows us to benefit from the computational feasibility of the tight-binding approximation and to go beyond the BOA. In fact, our model can be used to simulate the dynamics of relatively large systems (of the order of 1000 atoms) at the Ehrenfest level.

2.4.4 Computational scheme – time integrator

In order to obtain the electronic density matrix and the Cartesian components of the local spins as functions of time, the coupled quantum-classical equations of motion [Eqs. (2.67)-(2.68)] can be integrated numerically using a *time integrator*.

A time integrator is the core of any dynamical simulation, and it is basically the scheme which replaces a differential equation in continuous time by a difference equation defining approximate snapshots of the solution at discrete time steps. Long time interval simulations require the integrator to be iterated a large number of times. In the case of our Ehrenfest dynamical system the number of time steps is of the order of 10^4. In such situations a reliable integrator is needed to ensure a successful simulation.

The system of equations of motion described by Eqs. (2.67)-(2.68) falls into the category of initial value problems for a set of $\mathcal{N}$ coupled first-order differential equations[10] for the functions g_i, $i = 1, 2, ..., \mathcal{N}$, having a general form

$$\frac{dg_i(t)}{dt} = f_i(t, g_1, ..., g_{\mathcal{N}}), \qquad i = 1, ..., \mathcal{N}, \tag{2.70}$$

where the functions f_i on the right-hand side are known. These equations need to be integrated simultaneously over time, starting from the initial time $t = t_0$, given the initial conditions $g_i(t_0)$. In the Ehrenfest system the initial conditions include the local spin configuration $\{\boldsymbol{S}_i(t_0)\}$ and the electron density matrix $\hat{\rho}(t_0)$ at the initial time.

[10]For the Ehrenfest system containing N_S local spins embedded in an N-sites long spin-polarized chain, $\mathcal{N} = 3N_S + 2N(2N+1)/2$. See also the footnote on page 34.

A number of numerical algorithms have been developed for the solution of this type of equations. The simplest implementation of the discretization procedure applied to Eqs. (2.70) results in the elementary one-step Euler's method, given by the formula[11]

$$g_{n+1} = g_n + hf(t_n, g_n), \tag{2.71}$$

which advances a solution from t_n to $t_{n+1} \equiv t_n + h$, where h is the time step and $g_n(g_{n+1})$ is the value of the function $g(t)$ at the moment of time $t_n(t_{n+1})$. This method itself is rarely used in practice due to low accuracy and numerical instability, however it is conceptually important for many practical integration methods.

The Runge-Kutta methods [206, p. 704] is a class of the most frequently used integrators. A typical Runge-Kutta scheme propagates a solution over the time step h by performing several Euler-type steps, each involving an evaluation of the right-hand side functions f_i, and then using the obtained information to match a Taylor series expansion up to some higher order. We use the classical fourth-order Runge-Kutta (RK4) method, given by the following rule

$$\begin{aligned}
k_1 &= hf(t_n, g_n), \\
k_2 &= hf(t_n + \frac{h}{2}, g_n + \frac{k_1}{2}), \\
k_3 &= hf(t_n + \frac{h}{2}, g_n + \frac{k_2}{2}), \\
k_4 &= hf(t_n + h, g_n + k_3), \\
g_{n+1} &= g_n + \frac{1}{6}(k_1 + 2k_2 + 2k_3 + k_4) + O(h^5),
\end{aligned} \tag{2.72}$$

where $O(h^5)$ is an error term, which means that the deviation of the exact solution from the numerical one, given by g_{n+1} in Eq. (2.72) at time step $n + 1$, is smaller in absolute value than a constant times h^5 for $h \to 0$. This term, representing the intrinsic accuracy of the RK4 algorithm, essentially determines the accuracy of the entire numerical scheme, since the numerical round-off errors are usually much smaller than the errors due to the time-integration algorithm.

As a prior step to launching the time integrator, one needs to determine the initial conditions. This is done by performing a *ground-state* calculation, which gives the equilibrium electron density distribution for a given local configuration of the classical spins. At t_0 for a given orientation of $\boldsymbol{S}_i(t_0)$ the electron density matrix $\hat{\rho}$ is constructed

[11] The difference equation is given for $\mathcal{N} = 1$, i.e, in a 1D case, for simplicity.

as

$$\hat{\rho}(t_0) = \sum_{\nu} f_\nu |\varphi_\nu\rangle\langle\varphi_\nu|, \tag{2.73}$$

where $\{|\varphi_\nu\rangle\}_{\nu=1}^{2N}$ are the eigenstates of the spin-polarized electron Hamiltonian $\hat{H}_{\mathrm{el}}(t_0)$ and $f_\nu = f(\epsilon_\nu)$ are the occupation numbers distributed according to the Fermi-Dirac statistics.[12]

The dynamical evolution is triggered by applying an excitation to the system. Note, that the substitution of the ground state values of $\boldsymbol{S}_i(t_0)$ and $\hat{\rho}(t_0)$ into the equations of motion leads to $\{\boldsymbol{S}_i(t_0), H_S(t_0)\} = 0$ and $\left[\hat{\rho}(t_0), \hat{H}_{\mathrm{el}}(t_0)\right] = 0$ so that no evolution can be obtained without perturbation. From mathematical point of view, such perturbation can be realized in several ways, for instance, by deviating the electron density matrix from its equilibrium at $t = t_1$ so that $\rho(t_1) = \rho(t_0) + \delta\rho$. This is, however, a rather artificial procedure unless the density $\rho(t_1)$, constructed in such a way, is the ground-state density of the electron Hamiltonian, that has been perturbed in some physical way, for example, if $\hat{H}_{\mathrm{el}}(t_1)$ corresponds to some other configuration of the local spins, different from the initial one. Another possibility is, at $t = t_1$, to tilt one of the local spins with respect to its initial orientation, $\boldsymbol{S}_i(t_1) = \boldsymbol{S}_i(t_0) + \delta\boldsymbol{S}_i$. One can also change the local spin Hamiltonian H_{S} directly by applying a transverse magnetic field to one of the local spins, which leads to $\boldsymbol{\Theta}_i(t_1) = \boldsymbol{\Theta}_i(t_0) + \frac{g_S \mu_B}{\hbar} \mathcal{S}\boldsymbol{B}_i(t)$. This results in the precession of $\boldsymbol{S}_i$, which, in turn, induces the evolution of the electronic spins. A general technical procedure behind the time-dependent simulation, which combines the ground-state calculation, the excitation and the time propagation, is illustrated in Fig. 2.6.

Information about the actual accuracy of the numerical scheme is extracted from the deviation of a conserved quantity from a constant value for a given time step over a typical duration of the simulation. The conserved quantities for the Ehrenfest dynamical system are

- The total energy of the system $E_{\mathrm{tot}}(t)$, which contains the contribution from the electronic subsystem, e.g. $E_{\mathrm{el}}(t) = Tr\left[\hat{\rho}(t)\hat{H}_{\mathrm{el}}(t)\right]$, and from the subsystem of the local spins in the presence of an applied magnetic field, e.g. $E_{\mathrm{S}}(t) = g\mu_{\mathrm{B}} \sum_i \boldsymbol{S}_i(t) \cdot \boldsymbol{B}_i(t)$.

[12] Hereafter $f(E)$ denotes the Fermi-Dirac distribution and $f(E) = 1/\left[e^{(E-\mu)/k_{\mathrm{B}}T} + 1\right]$, where $k_{\mathrm{B}} \approx 8.617\ \mathrm{eV\,K^{-1}}$ is the Boltzmann constant, T is the temperature and μ is the chemical potential, which in this case is equal to the Fermi energy E_{F} [159, p. 23]. The latter is determined so that $\sum_i \rho_{ii}(t_0) = N_{\mathrm{el}}$ (N_{el} is the number of electrons in the system).

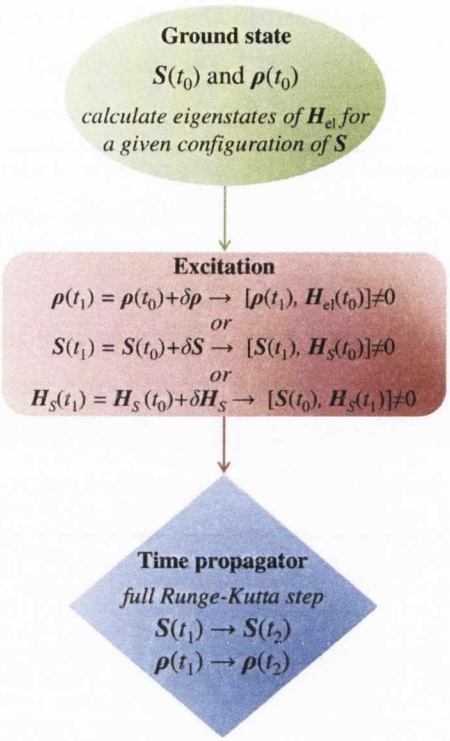

FIGURE 2.6: Scheme of the time-dependent algorithm.

- The number of electrons in the system $N_{\mathrm{el}}(t)$ which can be calculated as $N_{\mathrm{el}}(t) = \sum_i \rho_{ii}(t)$.
- The absolute value of each of the vectors $\boldsymbol{S}_i(t)$, e.g. $|\boldsymbol{S}_i|^2(t)$ since $\boldsymbol{S}_i(t)$ is considered as a vector with constant magnitude.
- The total spin $\boldsymbol{S}_{\mathrm{tot}}(t) = \sum_i \boldsymbol{s}_i(t) + \sum_i \boldsymbol{S}_i$.

The conservation of these quantities has been verified within a relative error of $10^{-7}\%$ for a typical time step $h = 0.01$ fs and a typical total time of the simulation $T_{tot} \approx 1$ ps.

The main and most computationally demanding part of the time-integration procedure is the multiplication of $\hat{\rho}$ and $\hat{H}_{\mathrm{el}}$ (expressed in the atomic-orbitals basis), which is performed in order to calculate the value of $\left[\hat{\rho}, \hat{H}_{\mathrm{el}}\right]$ at each step inside one full RK4 cycle. Each of the $2N \times 2N$ elements of the matrix multiplication product is calculated as

$$\left(\hat{\rho} \cdot \hat{H}_{\mathrm{el}}\right)_{mn} = \sum_{k=1}^{2N} \rho_{mk} \cdot (H_{\mathrm{el}})_{kn} \,. \tag{2.74}$$

Thus the total number of operations involved in the matrix multiplication is $(2N)^3$. This can be significantly reduced if one takes advantage of the sparse nature of the

Hamiltonian matrix. Indeed, since only the nearest-neighbors interactions are taken into account, the maximum number of non-zero elements in each column (or row) of the Hamiltonian matrix is equal to 4 (1 diagonal and 2 off-diagonal elements and one additional element in each row due to the interaction with the local spin[13]). This gives $2N \cdot 2N \cdot 4 = 16N^2$ operations and reduces the computational cost by $\approx \frac{N}{2}$.

Finally, we note that the same numerical time-evolution algorithm will be used to solve the quantum-mechanical equations of motion [similar to Eq. (2.67) but with additional open-boundary terms] describing the time-dependent transport in Chapter 5 and Chapter 6.

2.5 Summary

In this chapter we discussed the general motivation for atomistic spin dynamics and set out the theoretical and computational framework for practical simulations. We started with an overview of current state-of-art experimental techniques used to probe the dynamics of the spin degrees of freedom with very high resolution, reaching sub-nanometer length scale and femtosecond time regime. We then presented a brief assessment of the theoretical approaches capable of providing an adequate description of spin dynamics at dimensions comparable to those accessible in experiments. As purely empirical macroscopic models are unlikely to capture the relevant physics, the search for more appropriate models has been set in the realm of quantum atomistic simulations. A natural framework for such simulations is provided by the time-dependent density functional theory. However, in practice such simulations are computationally very demanding.

As a first step before an *ab initio* description is put forward, we considered a tight-binding based Ehrenfest scheme for spin dynamics, which can be applied to systems

[13] In the basis of spin-polarized atomic orbitals $|i\,\sigma\rangle$, the electron Hamiltonian, as well as the density matrix, is composed of 4 blocks of dimension $N \times N$, two of which contain the matrix elements of the form $\left\langle \uparrow\, i|\hat{H}_{\rm el}|i'\,\uparrow \right\rangle$ and $\left\langle \downarrow\, i|\hat{H}_{\rm el}|i'\,\downarrow \right\rangle$ while the other two correspond to $\left\langle \uparrow\, i|\hat{H}_{\rm el}|i'\,\downarrow \right\rangle$ and $\left\langle \downarrow\, i|\hat{H}_{\rm el}|i'\,\uparrow \right\rangle$. This can be written schematically as

$$H_{\rm el} = \begin{pmatrix} H_{\rm el}^{\uparrow\uparrow} & H_{\rm el}^{\uparrow\downarrow} \\ H_{\rm el}^{\downarrow\uparrow} & H_{\rm el}^{\downarrow\downarrow} \end{pmatrix}.$$

The exchange interaction with each local spin brings two off-diagonal complex elements, one in the $H_{\rm el}^{\uparrow\downarrow}$-block and the other in the ${H_{\rm el}}^{\downarrow\uparrow}$-block.

comprising localized magnetic moments and band-like electrons. In the Ehrenfest picture, two subsystems are considered. One comprises itinerant electrons, whose evolution is governed by the Liouville-von Neumann equation, and the other - localized spins - represented by classical variables (vectors), evolving according to the classical equation of motion, formally equivalent to its quantum-mechanical counterpart. The interaction between the two subsystems is introduced in the framework of the *s-d* model. All the components of the scheme, such as the model Hamiltonian, the Ehrenfest approximation and the time-integration method, have been discussed in details. Some practical applications will be presented in the following two chapters.

Chapter 3

Itinerant electron dynamics in atomic chains

3.1 Introduction

The term *low-dimensional* [111] refers to systems, which have at least one dimension smaller than the Fermi wavelength λ_F, or to systems, which consist of a small number of atoms or molecules. At these length scales quantum effects dominate the elementary physical processes that determine the behavior of the system as a whole. As a result, the properties of low-dimensional systems, including optical, electronic, and magnetic ones, are often very different from those of their bulk counterparts.

From a theoretical point of view, low-dimensional systems are incredibly useful models to study. The main reason for this is their greater mathematical simplicity compared to that of systems in higher dimensions. This allows one to find solutions to some problems which are difficult, or impossible, to solve otherwise. At the same time even seemingly simple models often contain very rich physics. Perhaps, one of the most famous examples are one-dimensional (1D) systems of interacting particles. The progress in theoretical understating of their properties has lead to new concepts in physics, such as the Tomonaga-Luttinger liquid [75, p. 1].

Several examples of quasi-1D systems, for instance, linear polymer chains like polyethylene, have been available for a long time. However, the last decades have witnessed a real explosion in the realization of low-dimensional systems. As materials research has

made great progress, new bulk materials with low-dimensional structure embedded inside have been discovered. These include spin-ladders [25] and other similar compounds which behave like arrays of 1D spin chains [147]. Further advances in nanofabrication techniques have lead to realizations of isolated low-dimensional systems, such as quantum wires [268], nanotubes [53] and quantum dots [140], just to name a few.

In recent years, a seemingly ultimate limit of miniaturization has been achieved: atomic-scale magnetic structures can now be assembled literally one atom at a time by using a scanning tunneling microscope (STM) [97]. Spin-excitation spectra of individual magnetic atoms and 1D chains of atoms absorbed on surfaces can be studied with inelastic electron tunneling spectroscopy (IETS) [91]. Moreover, the time-resolved analysis of magnetic properties of individual atoms can be carried out by using a recently proposed all-electron pump-probe scheme for spin-polarized STM [163].

Thanks to these remarkable experimental advances, the investigation of low - dimensional systems has evolved from being merely a theoretical curiosity to one of the most important and rich fields in physics. This field is driven not only by the interest in fundamental science but also by the growing demand of information an communication technology for the further miniaturization of devices down to the ultimate atomic scale [161, 197]. However, apart from the size, the key factor, which determines the performance of any realistic device, is the speed at which the information can be read and stored. This is ultimately related to a general question of how the system responds to external stimuli, such as electric current, magnetic field or optical excitation. Such response is essentially a dynamical process and it is intrinsically connected to the dynamical evolution of charge and spin degrees of freedom in the system. Theoretical models that can accurately describe the dynamics of electrons and their spins at the atomic scale are becoming valuable tools for understanding materials behavior.

In this chapter we use the computational scheme for atomistic simulations of spin dynamics, introduced in the previous chapter (see Section 2.4), to probe the dynamical response to external excitations of itinerant electrons in atomic chains. On the one hand, this serves as an introduction to the next chapter, where the dynamics of a more complex system incorporating magnetic impurities is investigated. On the other hand, we take here the opportunity to illustrate the functionality of our time-dependent scheme using a simple tight-binding chain as a test platform and to introduce some basic concepts. In the next chapter, due to the complexity of the system considered, we will largely rely on numerical simulations since no exact solutions are available. In

contrast to this, in the present chapter we take advantage of the relative simplicity of the model and perform a useful analytical calculation, which will allow us not only to test our numerical approach against exact results but also to derive some general conclusions about the dynamics of the system.

The results presented in this chapter can be also viewed as an independent study of the dynamical properties of itinerant electrons in atomic chains subject to external excitations. We start with a brief discussion of the linear response method, which is an invaluable tool for calculating the dynamical response of the system in the case when the perturbation is weak. Although our method does not rely on the linear approximation and is therefore applicable to excitations of arbitrary strength, it is instructive to compare the results obtained from the time-dependent simulations with the linear response results. Throughout this chapter we mostly consider small external perturbations and, as we will demonstrate in the following sections, our results indeed show a good agreement with the linear response calculations. We will also make it clear when our method can provide insight beyond what is accessible by the linear response approach.

Going into more details, we use the computational scheme for time-dependent atomistic simulations to calculate the real-time propagation of a locally produced excitation in the chain. The dynamics triggered by such excitation is then analyzed in the frequency domain. Next, the excitation spectra, calculated as the two-dimensional Fourier transforms of the nonequilibrium charge density distribution along the chain, are investigated. These spectra reveal some characteristic features of excitations in 1D systems and are particularly similar to the ones obtained for quantum spin chains. We resort to analytical analysis in order to explain these similarities. Finally, as a link to the next chapter, where we will be dealing with magnetic impurities embedded in atomic chains, we consider a classical Heisenberg model [117] for a system consisting of two coupled spins of the unit length. One of them represents the spin of the impurity and is set into the Larmor precession around a locally applied magnetic field, while the other represents the spin of the itinerant electron. Surprisingly, this simple problem has a rather complex solution, which can be also found analytically.

3.2 Dynamics upon weak perturbation: linear response

Linear response theory [276, p. 110] provides a general procedure to describe, in an approximate way, the nonequilibrium evolution of the system subject to an external perturbation, provided the latter is small enough. The main idea is to calculate the response of the system to the first order in the perturbation (hence the term "linear response") by neglecting higher order non-linear contributions. This is indeed justified if the perturbation is weak. Within the linear response framework one can derive an explicit expression for the *response function*, a quantity that measures a nonequilibrium response of the system to a weak perturbation, in terms of equilibrium dynamical quantities.

Consider a system subject to an external perturbation and described by the following Hamiltonian

$$\hat{H}(t) = \hat{H}_0 + \hat{V}(t), \tag{3.1}$$

where $\hat{H}_0$ corresponds to the unperturbed system in equilibrium while $\hat{V}(t)$ is the perturbation.[1] One can determine the response of the system to the perturbation in terms of some physical observable A, for instance electric current or magnetization, by calculating the expectation value of the corresponding operator $\hat{A}$, e.g. $\left\langle \hat{A} \right\rangle_t \equiv Tr\left\{ \hat{\rho}(t)\, \hat{A} \right\}$ [see Eq. (2.42)]. Here $\hat{\rho}(t)$ denotes the density matrix of the perturbed system described by the Hamiltonian $\hat{H}(t)$ in Eq. (3.1).

In the interaction picture (see Section 2.4.1 of Chapter 2) the density matrix is written as

$$\hat{\rho}_{\mathrm{I}}(t) = e^{\imath \hat{H}_0 t/\hbar}\, \hat{\rho}(t)\, e^{-\imath \hat{H}_0 t/\hbar}, \tag{3.2}$$

and its time evolution is given by the Liouville equation [Eq. (2.43)]

$$\frac{\partial \hat{\rho}_{\mathrm{I}}(t)}{\partial t} = -\frac{\imath}{\hbar} \left[\hat{V}_{\mathrm{I}}(t), \hat{\rho}_{\mathrm{I}}(t) \right], \tag{3.3}$$

where $\hat{V}_{\mathrm{I}}(t) = e^{\imath \hat{H}_0 t/\hbar}\, \hat{V}(t)\, e^{-\imath \hat{H}_0 t/\hbar}$. The solution of Eq. (3.3) in the integral form reads

$$\hat{\rho}_{\mathrm{I}}(t) = -\frac{\imath}{\hbar} \int_{-\infty}^{t} \left[\hat{V}_{\mathrm{I}}(t'), \hat{\rho}_{\mathrm{I}}(t') \right] dt' + \hat{\rho}_{\mathrm{I}}(-\infty). \tag{3.4}$$

[1] Such perturbation can represent, for instance, an electromagnetic field.

Furthermore, we assume that in the remote past, e.g. at $t \to -\infty$, the system is in equilibrium and is described by the Hamiltonian $\hat{H}_0$ so that $\hat{\rho}_{\rm I}(-\infty) = \hat{\rho}_0$, where $\hat{\rho}_0$ is constructed from the eigenvectors of $\hat{H}_0$.[2] Next, by using the first-order perturbation theory in V one can write

$$\Delta\hat{\rho}_{\rm I}(t) \equiv \hat{\rho}_{\rm I}(t) - \hat{\rho}_0 = -\frac{\imath}{\hbar}\int_{-\infty}^{t} \left[\hat{V}_{\rm I}(t'), \hat{\rho}_0\right] dt' + O(V^2). \tag{3.5}$$

The quantity $\Delta\hat{\rho}_{\rm I}(t)$ describes the deviation of the system from equilibrium due to the external perturbation $\hat{V}(t)$ in the linear response regime. The corresponding deviation of the expectation value of the operator $\hat{A}$ is given by

$$\Delta A(t) \equiv Tr\left\{\Delta\hat{\rho}_{\rm I}(t)\,\hat{A}_{\rm I}(t)\right\} = -\frac{\imath}{\hbar}\int_{-\infty}^{t} Tr\left\{\left[\hat{V}_{\rm I}(t'), \hat{\rho}_0\right]\,\hat{A}_{\rm I}(t)\right\} dt'. \tag{3.6}$$

By using the cyclic property of the trace, we obtain

$$\Delta A(t) = -\frac{\imath}{\hbar}\int_{-\infty}^{t} \left\langle\left[\hat{A}_{\rm I}(t), \hat{V}_{\rm I}(t')\right]\right\rangle dt', \tag{3.7}$$

where $\langle\,\cdot\,\rangle \equiv Tr\,\{\hat{\rho}_0\,\cdot\}$.

One can usually express the perturbation $\hat{V}(t)$ in terms of a *generalized force* $f(t)$ and an operator $\hat{B}$, corresponding to a *conjugate* observable B

$$\hat{V}(t) = -f(t)\hat{B}. \tag{3.8}$$

We can now rewrite Eq. (3.7) as follows

$$\Delta A(t) = -\int_{-\infty}^{+\infty} \chi(t-t')f(t')\,dt', \tag{3.9}$$

where we have introduced the *response function*[3]

$$\chi(t-t') = -\frac{\imath}{\hbar}\theta(t-t')\left\langle\left[\hat{A}(t-t'), \hat{B}(0)\right]\right\rangle. \tag{3.10}$$

[2] At finite temperature $\hat{\rho}_0$ has to be constructed as an equilibrium statistical operator [see footnote in Eq. (2.41)].

[3] In general, we can define a two point response function $\chi(t,t') \equiv -\frac{\imath}{\hbar}\theta(t-t')\left\langle\left[\hat{A}(t), \hat{B}(t')\right]\right\rangle$. However, in equilibrium the evolution of the system should only depend on the time interval between the perturbation and the measurement (observation) so that $\left\langle\left[\hat{A}(t), \hat{B}(t')\right]\right\rangle = \left\langle\left[\hat{A}(t-t'), \hat{B}(0)\right]\right\rangle = \left\langle\left[\hat{A}(0), \hat{B}(t'-t)\right]\right\rangle$.

Note that in the final formula we omitted the "I" subscript, which indicates the interaction picture with respect to the external perturbation $\hat{V}(t)$. Indeed, since the only term not included in $\hat{H}_0$ is $\hat{V}(t)$ [see Eq. (3.1)], we can assume that the operators are expressed in the Heisenberg picture while the expectation values are calculated using the perturbation theory in the interaction term V [276, p. 113].

The presence of the Heaviside step function $\theta(t-t')$ reflects the property of *causality* of the response function: one measures the response of the system at time t to a perturbation introduced earlier at time t' so that $\chi = 0$ for $t < t'$. Note that the Fourier transform of the response function, $\chi(\omega)$, is usually referred to as the *dynamical susceptibility*. One can also notice that the response function can be written as

$$\chi(\tau) = -\frac{\imath}{\hbar}\theta(\tau)\left\{\left\langle \hat{A}(\tau)\,\hat{B}(0)\right\rangle - \left\langle \hat{B}(0)\,\hat{A}(\tau)\right\rangle\right\}, \tag{3.11}$$

where $\tau = t - t'$. By introducing the correlation function $C_{AB}(\tau) \equiv \left\langle \hat{A}(\tau)\,\hat{B}(0)\right\rangle$, we obtain

$$\chi(\tau) = -\frac{\imath}{\hbar}\theta(\tau)\left\{C_{AB}(\tau) - C^{*}_{AB}(\tau)\right\} = \frac{2}{\hbar}\theta(\tau)\,\Im C_{AB}(\tau). \tag{3.12}$$

The physical meaning of Eq. (3.10) and Eq. (3.12) can be understood as follows: the nonequilibrium response of the system to a weak external perturbation is determined entirely by its equilibrium fluctuations. This is the essence of the fluctuation-dissipation theorem [143].

We will use the concept of the dynamical susceptibility in Section 3.4 in order to calculate the response of an atomic chain to a small localized excitation in terms of the nonequilibrium charge density distribution along the chain. This will be compared to the frequency portrait of dynamics, obtained directly from the time-dependent simulations.

In the following section we will introduce the model system considered throughout this chapter. We will also demonstrate how the dynamical simulations can be used to analyze the evolution of electronic degrees of freedom in atomic chains upon external perturbation.

3.3 Excitations in atomic chains: time-domain analysis

Throughout this section we consider a 1D atomic chain described by a single-band nearest-neighbors tight-binding Hamiltonian H_{TB} [see Eq. (2.52) in Chapter 2]. In all simulations, if not specified otherwise, we use a chain of $N = 100$ atoms, inter-site hopping $\gamma = -1.0$ eV, and the half-filling, $\rho_0 = 0.5$, or one-electron per site for a spin-polarized chain. We start by looking at local excitations, and by studying how these evolve in time along the chain. The excitation is produced on the first site ($i = 1$) by applying a Gaussian perturbation of the on-site potential ε_1, given by

$$\delta\varepsilon_1(t) = \delta\bar{\varepsilon}_1 \, e^{-\frac{(t-\bar{t})^2}{2c^2}}, \tag{3.13}$$

where $\delta\bar{\varepsilon}_1 = 0.1|\gamma|$ is the amplitude of the perturbation, $\bar{t} = 5$ fs is the time at which the perturbation is produced, and $c^2 = 0.07\bar{t}$ is the Gaussian variance, which determines the width of $\delta\varepsilon_1(t)$. This procedure is illustrated schematically in Fig. 3.1. Note that we intentionally use a very general form of an external perturbation since it is merely a tool used to drive the system out of equilibrium, thus allowing us to observe the dynamics on the electronic (fs) time scale.

The initial perturbation generates a nonequilibrium charge distribution along the chain which can be described by the deviation of the charge density on site i from its ground-state value at $t = t_0$, e.g. $\delta\rho_i(t) = \sum_\sigma \rho_{ii}^{\sigma\sigma}(t_0) - \rho_{ii}^{\sigma\sigma}(t)$. The two spin channels evolve independently, as there is no spin-mixing term in the Hamiltonian H_{TB}, and their dynamics is identical. For this reason we only look at the evolution of the total nonequilibrium charge density $\delta\rho_i$, thus restricting ourselves to the case of charge-excitations. Our study, however, is general and it is as well valid for spin-excitations, as we will illustrate further in the next chapter.

The quantity $\delta\rho_i(t)$ is obtained from the integration of the equations of motion using the time-propagation algorithm, which was presented in the previous chapter (we use the same procedure that was described in Section 2.4.4, with the only difference that there are no local spins and only one equation of motion needs to be integrated, namely the quantum Liouville equation for the electronic density matrix). The time evolution of $\delta\rho_i$ for the first 300 fs of the total time of the simulation $T_{\mathrm{tot}} = 2$ ps is displayed in Fig. 3.2. The first three panels of the figure [Fig. 3.2(a)-(c)] show three different

snapshots of the time evolution of $\delta\rho_i(t)$ along the chain, namely, at both ends ($i = 1$ and $i = N$) and in the middle of the chain ($i = N/2$).

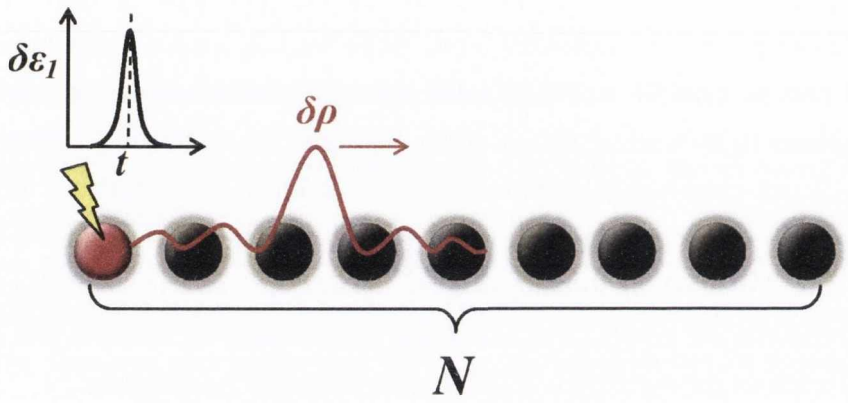

FIGURE 3.1: Cartoon of the model system: an excitation is produced on the first site ($i = 1$) of the N-sites long chain by applying a perturbation $\delta\varepsilon_1(t)$ to the on-site potential. This leads to the dynamics of the charge density $\delta\rho$.

Let us focus on the dynamics of the charge density on the first site [see Fig. 3.2(c)]. The first sharp peak in $\delta\rho_1(t)$ represents the disturbance, or excitation, introduced by the external perturbation $\delta\varepsilon_1(t)$. This initial disturbance is then transferred to the next sites along the chain. Once the incident excitation arrives at the last site, it gets reflected back, as the system considered here has perfectly reflecting boundaries. After the reflection, the excitation returns to the first site, resulting in the second peak in the charge density at $t = 2\tau$, where τ is the time needed for the excitation to reach the last site (the traveling time).

The space and time evolution of the charge density, which is presented in Fig. 3.2(d), can be qualitatively characterized as the propagation of a spatially localized wave packet. The atomic chain itself can then be considered as a *waveguide* for propagating excitations, similarly to classical wave mechanics. Since the chain is finite and we assume perfect reflection at the boundaries, the wave packet essentially bounces between the two boundaries, gradually loosing its definition due to the interference of propagating and reflected "waves" which constitute the packet. Although the width of the wave packet naturally broadens with time, it travels along the chain with a practically uniform group velocity. Figure 3.3 shows the calculated group velocity, v_g, as a function of the hopping integral γ. Such a dependence is obtained from our time-dependent simulations by calculating $v_g = L/\tau$, where $L = N \cdot a$ is the length of the chain, a is the

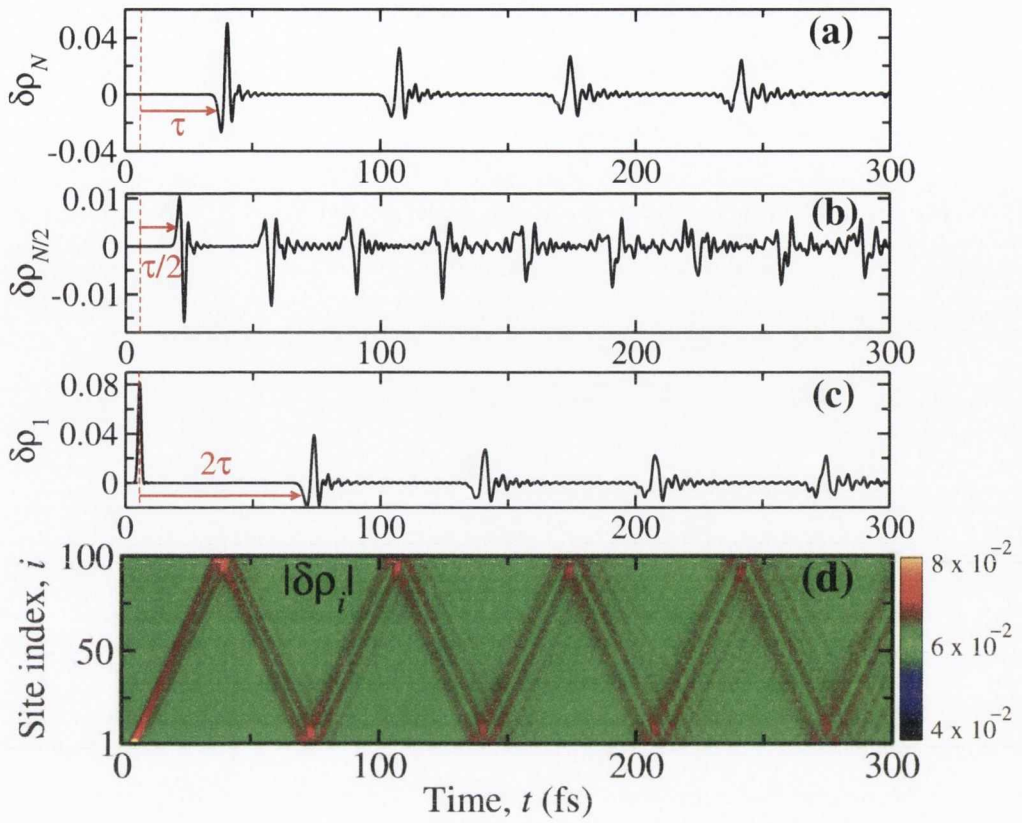

FIGURE 3.2: Time evolution of $\delta\rho_i(t) = \sum_\sigma \rho_{ii}^{\sigma\sigma}(t_0) - \rho_{ii}^{\sigma\sigma}(t)$ for (a) $i = N$, (b) $i = N/2$ and (c) $i = 1$. (d) Spatially-resolved time evolution of the charge density: $\delta\rho_i(t)$ as a function of time and position along the chain. The color shade represents the absolute value of $\delta\rho_i(t)$.

inter-site distance[4] and τ is the "one-way" traveling time [see Fig. 3.2(a)]. The linear dependence in Fig. 3.3 agrees very well with the simple analytical expression for the electron group velocity at the Fermi level, calculated for a 1D tight-binding chain at half-filling

$$v_{\mathrm{g}}^{\mathrm{TB}} = \frac{1}{\hbar}\frac{\partial E(k)}{\partial k}\bigg|_{k=k_{\mathrm{F}}} \approx \frac{2\gamma\, a}{\hbar}, \tag{3.14}$$

where k is the wave-vector and k_{F} is its value at the Fermi level.

3.4 Analysis of dynamics in the frequency domain

One can often get a better insight into the dynamics of the system by looking at its frequency portrait. In order to investigate the dynamics of the itinerant electrons in the

[4]In our model a is arbitrary and we set $a = 1$.

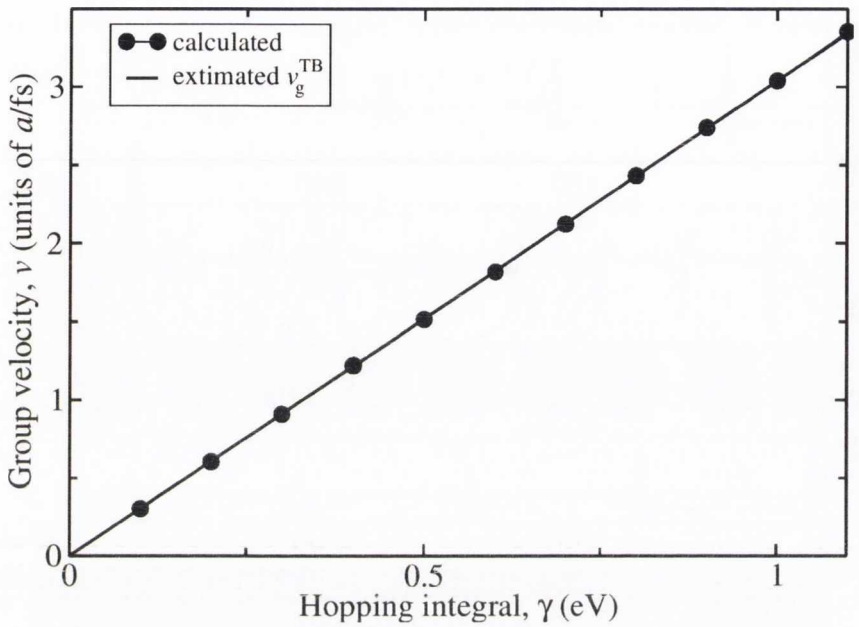

FIGURE 3.3: The group velocity v_g of the wave packet as a function of the hopping integral γ, obtained from the time-dependent simulation for each γ (full circles). Solid line shows, for comparison, the analytical estimate v_g^{TB}, given by Eq. (3.14).

frequency domain, we calculate the Fourier transforms of $\delta\rho_i(t)$ for $i = 1$ and $i = N$. In fact, $\delta\rho_i(t)$ is not a continuous function of time but it is sampled at evenly spaced time intervals h. Therefore, one needs to use the discrete version of the Fourier transform (dFT)[5]

$$\begin{aligned} \mathrm{dFT}[\delta\rho_i(t)](\nu_n) = \int_{-\infty}^{+\infty} \delta\rho_i(t)\, e^{2\pi\imath\nu_n t}\, dt &\approx \sum_{l=1}^{N_s} \delta\rho_i(t_l)\, e^{2\pi\imath\nu_n t_l} h = \\ &= h \sum_{l=1}^{N_s} \delta\rho_i(t_l)\, e^{2\pi\imath nl/N_s}, \end{aligned} \tag{3.15}$$

where $\{t_l \equiv lh\}_{l=1}^{N_s}$ is a set of discrete points in time at which the function $\delta\rho_i(t)$ is sampled, N_s is the total number of time steps and $\left\{\nu_n \equiv \frac{n}{N_s h}\right\}_{n=1}^{N_s}$ is the set of the corresponding frequencies (the angular frequencies are given by $\omega_n = 2\pi\nu_n$). The

[5]We use a numerical implementation of the Fast Fourier Transform (FFT) algorithm [206, p. 490],which is based on the idea of decomposing the discrete Fourier transform of length N_s into the sum of two transforms of length $N_s/2$ each, one over the even elements of the original transform and the other over the odd ones. The recursive application of this procedure leads to a significant reduction of the number of operations needed to compute a transform of length N_s: FFT needs $O(N_s \log_2 N_s)$ operations compared to $O(N_s^2)$ in the case of straightforward matrix multiplication.

positive frequencies are contained in the interval $1 \leq n \leq N_s/2 - 1$, the negative ones in the interval $N_s/2 + 1 \leq n \leq N_s - 1$ and $n = 0$ gives the zero frequency. The mode with index $n = N_s/2$ corresponds to the critical Nyquist frequency, $\nu_c = \pm\frac{1}{2h}$, and one has to make sure that the function of interest is within the bandwidth given by the interval $\{-\nu_c, \nu_c\}$, in order to avoid aliasing effects in the Fourier transform. In practice, we construct the dFT power portraits, where the x-axis displays angular frequencies $\omega_n \geq 0$ ($n = 0, ..., N_s/2-1$) and the y-axis the quantity $\left\{|\mathrm{dFT}[\delta\rho_i(t)](\omega_n)|^2 + |\mathrm{dFT}[\delta\rho_i(t)](\omega_{n+N_s/2})|^2\right\}/2$, where we have simply folded the spectrum at the symmetry point $n = N_s/2$.

The spectra obtained, denoted as $\mathrm{dFT}[\delta\rho_i(t)](\omega)$ for $i = 1$ and $i = N$, are shown in Fig. 3.4. What is immediately noticeable is the large number of discrete modes, which constitute the frequency portraits. In order to understand this result we perform the linear response calculation using the method described in Section 3.2. By taking the definition of the response function in Eq. (3.10) and by setting $A \equiv \rho_j$ and $B \equiv \rho_1$, we calculate the response of the system to a perturbation, applied to site 1 at time $t = 0$, in terms of the charge density, measured on site j at time t

$$\chi_{1,j}(t) = -\frac{\imath}{\hbar}\langle[\hat{\rho}_j(t), \hat{\rho}_1(0)]\rangle = -\frac{\imath}{\hbar}Tr\left\{\hat{\rho}_1(0)\left[\hat{\rho}(0), \hat{\rho}_j(t)\right]\right\}, \quad t \geq 0 \tag{3.16}$$

where the density matrix $\hat{\rho}(0)$ corresponds to the unperturbed Hamiltonian $\hat{H}_{\mathrm{TB}}$ (here we consider a non spin-polarized Hamiltonian for simplicity); $\hat{\rho}_i$ is the projection of the density matrix operator on the local atomic orbitals basis $|i\rangle$, where i represents the atomic site. The final expression for the response function reads

$$\chi_{1,j}(t) = -\frac{\imath}{\hbar}\sum_{n,m=1}^{N}\langle\varphi_n|\hat{\rho}_1(0)|\varphi_m\rangle \cdot \langle\varphi_m|\hat{\rho}_j(0)|\varphi_n\rangle \cdot (f_m - f_n) \cdot e^{-\imath(\omega_m - \omega_n)t}, \tag{3.17}$$

where $\omega_n = e_n/\hbar$, e_n being the eigenvalues of $\hat{H}_{\mathrm{TB}}$, and f_n are the eigenvalues of the density matrix operator, e.g. $\hat{\rho}|\varphi_n\rangle = f_n|\varphi_n\rangle$.[6] By taking the Fourier transform of the response function, we obtain

$$\chi_{1,j}(\omega) = \sum_{n,m=1}^{N}\tilde{\chi}_{1,j}^{n,m}\,\delta(\omega - \omega_{nm}), \tag{3.18}$$

[6]In fact, f_n are the occupation numbers, distributed according to Fermi-Dirac statistics [see Eq. (2.73)].

where $\omega_{nm} \equiv \omega_n - \omega_m$ and

$$\begin{aligned} \tilde{\chi}_{1,j}^{n,m} &= -\frac{\imath}{\hbar} \langle \varphi_n | \hat{\rho}_1(0) | \varphi_m \rangle \cdot \langle \varphi_m | \hat{\rho}_j(0) | \varphi_n \rangle \cdot (f_m - f_n) = \\ &= -\frac{\imath}{\hbar} c_{1n}^* \, c_{1m} \, c_{jm}^* \, c_{jn} \, (f_m - f_n). \end{aligned} \tag{3.19}$$

Here the coefficients $c_{in} \equiv \langle i | \varphi_n \rangle$ are defined as projections of the eigenvectors $|\varphi_n\rangle$ on the atomic orbitals $|i\rangle$.

As one can see from Eq. (3.18), the response of the system in the frequency domain is given by a set of discrete modes with frequencies ω_{nm} and amplitudes $\tilde{\chi}_{1,j}^{n,m}$. The absolute value of the dynamical susceptibility $\chi_{1,j}(\omega)$ for $j = N$ is shown in Fig. 3.4 (black line) and is in good agreement with the calculated Fourier transform of $\rho_N(t)$.[7] This is expected since in our time-dependent simulations the dynamics is triggered by a weak perturbation in the on-site potential of the first site, which generates only a small disturbance in the charge density distribution along the chain.

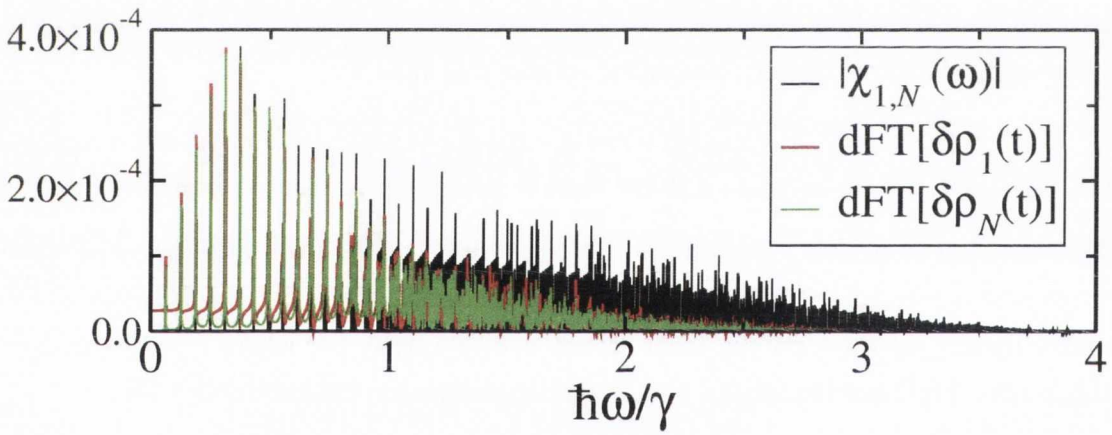

FIGURE 3.4: The absolute value of the dynamical susceptibility $|\chi_{1,N}(\omega)|$ [Eq. (3.19)], representing the response of the charge density on site N to a weak excitation produced earlier on site 1 (black line). Calculated Fourier spectra of $\delta\rho_1(t)$ (red line) and $\delta\rho_N(t)$ (green line), denoted as $\mathrm{dFT}[\delta\rho_1(t)](\omega)$ and $\mathrm{dFT}[\delta\rho_N(t)](\omega)$, respectively. The frequency domain is represented by the dimensionless quantity $\hbar\omega/\gamma$ (for this we always take the module of γ so that $\hbar\omega/\gamma > 0$ for $\omega > 0$).

In addition to the linear response analysis, we propose an alternative method for calculating the dynamics of the system considered here, which can be carried out analytically without resorting to a linear approximation. We elaborate the details of such calculation below.

[7] In the limit $N \to \infty$ the discrete modes in the spectra presented in Fig. 3.4 will merges into a smooth "bell-shape" curve.

In the previous section we used a Gaussian perturbation to drive the system out of equilibrium. This perturbation effectively represents an additional time-dependent term in the Hamiltonian, e.g. $\delta\hat{H}(t) = \delta\varepsilon_i(t)$. However, after a short time t_p from the start of the simulation ($t_p \approx 10$ fs for the perturbation considered here), the term $\delta\hat{H}(t)$ dies out and the dynamics is driven only by the time-independent Hamiltonian $\hat{H}_{\mathrm{TB}}$. For times $t > t_p$ we can then write down the formal solution of the Liouville-von Neumann equation [see Eq. (2.43)] for the density matrix

$$\hat{\rho}(t) = e^{-\imath\hat{H}_{\mathrm{TB}}t/\hbar}\hat{\rho}(t_i)\, e^{\imath\hat{H}_{\mathrm{TB}}t/\hbar}, \tag{3.20}$$

where $\hat{\rho}(t_i)$ is the density matrix at time $t_i > t_p$. The same equation describes the evolution of the system, if we simply introduce a modification of the density matrix at the time t_i so that $\hat{\rho}(t_i)$ is different from $\hat{\rho}(t_0)$, which is obtained from the ground-state calculation. This would lead to a dynamics, very similar to the one described in the previous section. Although such an ad hoc perturbation of the density matrix seems more straightforward, we chose a more physical way of driving the system out of equilibrium, e.g. by applying an external perturbation, which may represent, for instance, a laser field.

In order to calculate the matrix elements of $\hat{\rho}(t)$ in Eq. (3.20), we introduce the basis formed by the eigenvectors $\{|\varphi_n\rangle\}_{n=1}^{2N}$ of the Hamiltonian $\hat{H}_{\mathrm{TB}}$, where the composite index $n = \{i, \sigma\}$ labels the set of $2N$ spin-polarized eigenstates with i representing the site index and $\sigma = \uparrow, \downarrow$ the spin component. The density matrix elements in this basis read

$$\rho_{mn}(t) = e^{-\imath\omega_{mn}t}\langle\varphi_m|\hat{\rho}(t_i)|\varphi_n\rangle \equiv e^{-\imath\omega_{mn}t}\rho_{mn}(t_i), \tag{3.21}$$

where the frequencies ω_{mn} are defined as $\omega_{mn} \equiv (e_m - e_n)/\hbar$ with e_n being the eigenvalues of $\hat{H}_{\mathrm{TB}}$; $\rho_{mn}(t_i)$ are the density matrix elements in the basis of the eigenvectors at $t = t_i$.

As we are interested in the propagation of the excitation along the chain, we project the expression given by Eq. (3.21) onto the basis that has a clear spatial meaning, namely, the basis of the spin-polarized local atomic orbitals $|i\,\sigma\rangle$, where i represents the atomic site and $\sigma = \uparrow, \downarrow$ is the spin component. The coefficients $c_{in}^{\sigma} \equiv \langle i\,\sigma|\varphi_n\rangle$ are defined as projections of the eigenvectors $|\varphi_n\rangle$ on the spin-resolved atomic orbitals $|i\,\sigma\rangle$. Note that in c_{in}^{σ} the first subscript index and the superscript index always correspond to the atomic orbital, while the second subscript index labels the corresponding eigenvector.

We start by substituting the initial density matrix elements, i.e. $\rho_{mn}(t_i)$ in Eq. (3.21), by their projections on $|i\,\sigma\rangle$-basis

$$\begin{aligned}\rho_{mn}(t) &= e^{-\imath\omega_{mn}t}\sum_{i\alpha}\sum_{j\beta}\langle\phi_m|\ i\,\alpha\rangle\,\langle\alpha\,i|\,\hat{\rho}(t_i)\,|j\,\beta\rangle\,\langle\beta\,j|\ \phi_n\rangle = \\ &= e^{-\imath\omega_{mn}t}\sum_{i\alpha}\sum_{j\beta}c_{im}^{\alpha *}\,c_{jn}^{\beta}\,\rho_{ij}^{\alpha\beta}(t_i).\end{aligned} \tag{3.22}$$

Note that this is equivalent to inserting $\sum_{i\alpha}|\alpha\,i\,\rangle\langle\,i\,\alpha|=\hat{I}$ and $\sum_{i\beta}|\beta\,i\,\rangle\langle\,i\,\beta|=\hat{I}$ into Eq. (3.21), where $\hat{I}$ is the identity operator for a complete orthogonal basis $|i\,\alpha\rangle$.

The expression for the time-dependent density matrix in the $|i\,\sigma\,\rangle$-basis reads

$$\begin{aligned}\rho_{kl}^{\sigma\sigma'}(t) &= \langle\sigma\,k|\,\hat{\rho}(t)\,|l\,\sigma'\rangle = \\ &= \sum_{mn}\langle\sigma\,k|\ \phi_m\rangle\,\langle\phi_m|\,\hat{\rho}(t)\,|\phi_n\rangle\,\langle\phi_n|\ l\,\sigma'\rangle = \\ &= \sum_{mn}c_{km}^{\sigma}\,c_{ln}^{\sigma' *}\,\rho_{mn}(t).\end{aligned} \tag{3.23}$$

By inserting Eq. (3.22) into Esq. (3.23), we arrive at the final expression for the density matrix elements in the basis of the spin-resolved atomic orbitals $|i\,\sigma\rangle$

$$\rho_{kl}^{\sigma\sigma\prime}(t)=\sum_{mn}e^{-\imath\omega_{mn}t}\,c_{km}^{\sigma}\,c_{ln}^{\sigma' *}\sum_{i\alpha}\sum_{j\beta}c_{im}^{\alpha *}\,c_{jn}^{\beta}\,\rho_{ij}^{\alpha\beta}(t_i). \tag{3.24}$$

The above expression essentially means that the time evolution of the density matrix is governed by the energy spectrum of the time-independent Hamiltonian $\hat{H}_{\mathrm{TB}}$ and, of course, the initial conditions $\rho_{ij}^{\alpha\beta}(t_i)$.

Equation (3.24) can be also written in a compact form

$$\rho_{kl}^{\sigma\sigma'}(t)=\sum_{mn}e^{-\imath\omega_{mn}t}\,A_{kl,mn}^{\sigma\sigma'}, \tag{3.25}$$

with the amplitudes $A_{kl,mn}^{\sigma\sigma'}$ defined as

$$A_{kl,mn}^{\sigma\sigma'}=c_{km}^{\sigma}\,c_{ln}^{\sigma' *}\sum_{i\alpha}\sum_{j\beta}c_{im}^{\alpha *}\,c_{jn}^{\beta}\,\rho_{ij}^{\alpha\beta}(t_i). \tag{3.26}$$

Importantly, Esq. (3.25) and Esq. (3.26) give the frequencies and amplitudes of the Fourier transform of the time-dependent density matrix.

We note that for the uniform tight-binding Hamiltonian $\hat{H}_{\mathrm{TB}}$ with $\varepsilon_i = \varepsilon_0$ the eigenstates can be calculated exactly, in particular, the eigenvalues read

$$e_n = \varepsilon_0 + 2\gamma \cos\left(\frac{\pi\, n}{N+1}\right), \tag{3.27}$$

where $n = 1, ..., N$ and each e_n is doubly degenerate (because of spin) so that we have $2N$ eigenvalues in total.

By using Esq. (3.27) we can calculate the frequencies ω_{mn}

$$\omega_{mn} = \frac{\epsilon_m - \epsilon_n}{\hbar} = \frac{4\,|\gamma|}{\hbar} \sin\left[\frac{\pi(m-n)}{2(N+1)}\right] \cdot \sin\left[\frac{\pi(m+n)}{2(N+1)}\right], \tag{3.28}$$

where $\{\omega_{mn}\}^{N}_{\substack{m,n=1 \\ m>n}}$ forms a set of $N \cdot (N-1)$ positive frequencies.

For consistency with the notations used in the formula for the Fourier transform, we can, in principle, introduce a new index p, $p = 1, ..., N \cdot (N-1)$, labeling the frequencies as ω_p. By calculating the extrema of the function $F(m,n) = \omega_{mn}$, we estimate the smallest (ω_{min}) and the largest (ω_{max}) frequencies in the spectrum, which are given by

$$\omega_{min} \approx \frac{3\pi^2|\gamma|}{(N+1)^2\hbar}, \tag{3.29}$$

$$\omega_{max} \approx \frac{4|\gamma|}{\hbar}. \tag{3.30}$$

The frequency ω_{max} is calculated in the limit of $N \to \infty$ and corresponds to the edge of the tight-binding energy-spectrum, which spans the eigenvalues in the interval $[-2|\gamma|, 2|\gamma|]$. For the parameters typically used in our simulations the corresponding maximum period $T_{max} = \frac{2\pi}{\omega_{min}} \lesssim 1$ ps is within the total time of the simulation while the corresponding minimum period $T_{min} = \frac{2\pi}{\omega_{max}} \approx 1$ fs is much larger than the typical time step $h = 0.01$ fs.

We have verified that the analytical spectrum and the functions $\rho^{\sigma\sigma'}_{kl}(t)$, constructed from Eq. (3.24), match perfectly the ones obtained from the time-dependent simulations, which confirms the reliability of our time-integrator for the typical duration of the simulations.

We would also like to point out that the result presented in Eq. (3.24) is general and not limited to the tight-binding Hamiltonian $\hat{H}_{\mathrm{TB}}$. In fact, it is valid for any

time-independent Hamiltonian. In Chapter 4 we will use such a result in the situation when a number of local spins, represented by vectors oriented along a fixed direction, is introduced. In this case, the Hamiltonian, which contains, in addition to a tight-binding term, a local exchange interaction to static impurity spins, is again time-independent and, therefore, Eq. (3.24) can be used to calculate the Fourier transforms of the spin observables. The analysis of the combined dynamics of itinerant electrons and spin impurities will be also largely based on the information about the dynamical spectrum of the itinerant electrons, already contained in Eq. (3.24).

Finally, we note that similar analytical calculations for a time-independent Hamiltonian has been carried out in a pedagogical study reported in Ref. [263]. The authors used the wave function representation and provided a description of the propagation of an initial localized state in a finite tight-binding chain in terms of the probability amplitudes. Such description was then used to investigate the dynamics of a tight-binding chain with a local defect and with a random disorder.

3.5 Calculated excitation spectra

A further insight into the dynamics can be obtained by looking at the full excitation spectra. These are calculated as two-dimensional discrete Fourier transforms of $\delta\rho_i(t)$. For that we use the generalization of Eq. (3.15) to two dimensions

$$\begin{aligned} \mathrm{dFT}[\delta\rho_i(t)](k_s,\nu_n) &\approx h\sum_{j=1}^{N}\sum_{l=1}^{N_s}\delta\rho_j(t_l)\,e^{2\pi\imath k_s r_j}\,e^{2\pi\imath\nu_n t_l} = \\ &= h\sum_{j=1}^{N}\sum_{l=1}^{N_s}\delta\rho_j(t_l)\,e^{2\pi\imath sj/N}\,e^{2\pi\imath nl/N_s}, \end{aligned} \tag{3.31}$$

where $r_j \equiv \{j\cdot a\}_{j=1}^{N}$ is the set of discrete points in space, corresponding to the positions of the atoms in the chain, and $k_s \equiv \left\{\frac{s}{N\cdot a}\right\}_{s=1}^{N}$ is the set of discrete points in the reciprocal space ($a = 1$). The other notations are the same as in Eq. (3.15). The calculated excitation spectrum, denoted as $\mathrm{dFT}[\delta\rho_i(t)](k,\omega)$, is shown in Fig. 3.5.

This excitation spectrum reveals the key features of 1D fermionic systems [75, p. 12], in particular a near-continuum of allowed modes in a certain region of (k,ω)-space, defined by a low- and a high-energy dispersion functions. We discuss these features in more detail below.

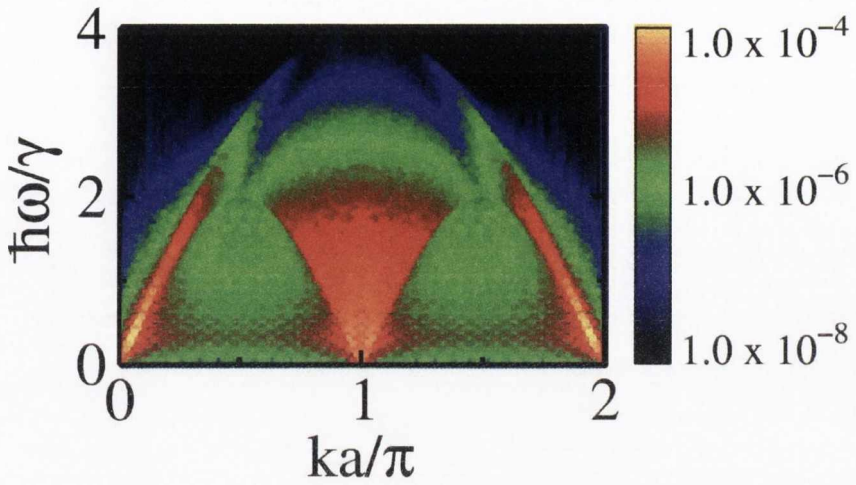

FIGURE 3.5: Two-dimensional Fourier transform of $\delta\rho_i(t)$. The color shade represents the absolute value of $\mathrm{dFT}[\delta\rho_i(t)](k,\omega)$ and is logarithmically scaled for better contrast. The frequency domain is represented by the dimensionless quantity $\hbar\omega/\gamma$ while the k-space is represented by ka/π. Note that $ka/\pi = 1$ corresponds to $k = 2k_{\mathrm{F}}$, where $k_{\mathrm{F}} = \frac{\pi}{2a}$.

The excitations in a 1D electron system considered here can be viewed as particle-hole excitations, or a process where an electron is taken from below the Fermi level and is excited into a state with a higher energy, above the Fermi level. In other words, during this process a particle with momentum k_i is destroyed and a particle with momentum $k_f \equiv k_i + k$ is created. The momentum of the excitation is thus equal to k. Importantly, the energy of the excitation, $\mathcal{E}_{k_i}(k)$, depends on both k_i and k, therefore, if one looks at the energy (frequency) of the excitation as a function of momentum, one, indeed, has a *continuum* of states. Of course, for a finite system considered here, we have a large but finite number of states.

In higher dimensions, the continuum extends to zero energy (frequency) for all $k \in [0, 2k_F]$, because one can always create an excitation of arbitrary low energy. In 1D systems, the Fermi surface is represented by just one point, therefore the energy of the electron-hole excitation can approach zero only for $k \to 0$ and $k \to 2k_{\mathrm{F}}$. This is a general property of excitations in electron systems in 1D and it is independent of the dispersion relation. Figure 3.5 essentially demonstrates this property in a special case of excitations in a 1D tight-binding chain.

We will now look at some characteristic features of the excitation spectrum which are determined by the tight-binding dispersion relation, e.g. by the specific form of the eigenvalues $\{e_n\}_{n=1}^{N}$ of the electronic Hamiltonian $\hat{H}_{\mathrm{TB}}$.

In the previous section, we have already established the analytical expression for the frequencies ω_{mn}, which contribute to the frequency portrait of the dynamics in atomic chains [see Eq. (3.28)]. We will now rewrite this expression in a more convenient form, by denoting $k_i = \frac{\pi m}{N+1}$ and $k_f = \frac{\pi n}{N+1}$ (for $m, n = 1, ..., N$ and $N \to \infty$ the k-vectors approximately lie in the region $[0, \pi]$). The near-continuum of allowed excitations is thus defined as

$$\omega(k) = \frac{4|\gamma|}{\hbar} \sin\left(\frac{k}{2}\right) \sin\left(\frac{k}{2} + k_i\right), \tag{3.32}$$

given the following conditions are satisfied

$$e(k_i) = \varepsilon_0 + 2\gamma \cos k_i < E_F, \tag{3.33}$$

$$e(k_i + k) = \varepsilon_0 + 2\gamma \cos(k_i + k) > E_F, \tag{3.34}$$

or, in other words, the initial state with energy $e(k_i)$ is occupied while the finite state with energy $e(k_i + k)$ is empty; E_F is the Fermi energy.

Based on equations Eq. (3.32)-(3.34), one can introduce a parameter α, given by

$$\alpha = \arccos\left(|E_F - \varepsilon_0|/2|\gamma|\right), \tag{3.35}$$

and the following characteristic lines in (k, ω)-plane

$$\omega_1(k) = \frac{4|\gamma|}{\hbar} \sin\left(\frac{k}{2}\right) \sin\left(\frac{|k|}{2} - \alpha\right), \tag{3.36}$$

$$\omega_2(k) = \frac{4|\gamma|}{\hbar} \sin\left(\frac{k}{2}\right) \sin\left(\frac{|k|}{2} + \alpha\right), \tag{3.37}$$

$$\omega_3(k) = \frac{4|\gamma|}{\hbar} \sin\left(\frac{k}{2}\right), \tag{3.38}$$

The lower boundary of the excitation spectrum is given by $\omega_1(k)$. The upper boundary is given by $\omega_2(k)$ for $|k| \leq \pi - 2\alpha$ and by $\omega_3(k)$ for $|k| \geq \pi - 2\alpha$. One can immediately notice that $\omega_3(k)$ does not depend on any other system parameters except the hopping γ. The other two lines, however, strongly depend on the parameter α which, in addition to γ, is controlled by ε_0 and by E_F, or in other words by the band filling.[8]

[8]Here the on-site energy does not play a role since we only consider the trivial case when $\varepsilon_0 = 0$. However, according to Eq. (3.35) the modification of ε_0 can act in a way similar to the variation of E_F, or the band filling. We will use this similarity in the next chapter, where an electrostatic gate is introduced as a shift of the on-site energies of the atoms of a section of the chain, leading to a strong gate-dependence of the excitation spectrum.

The variation of the excitation spectrum with the band filling is presented in Fig. 3.6, where in addition to $\rho_0 = 0.5$ (the same as in Fig. 3.5) we considered two other cases, namely, $\rho_0 = 0.6$ and $\rho_0 = 0.8$. Indeed, one can observe significant differences in the spectra for different ρ_0. In the case of the half-filling, $E_{\mathrm{F}} = 0$ and, for $\varepsilon_0 = 0$, $\alpha = \arccos(0) = \frac{\pi}{2}$. This leads to $\omega_1(q) = \omega_2(q) = \frac{2|\gamma|}{\hbar}\sin(k)$, which gives the lower limit of the spectrum, while the upper limit is given by $\omega_3(k) = \frac{4|\gamma|}{\hbar}\sin\left(\frac{k}{2}\right)$ [see Fig. 3.6(a)]. However, away from the half-filling [see Fig. 3.6(b) and (c)] this symmetry is distorted, and, clearly, all three characteristic lines are different. The most pronounced feature of the spectra for $\rho_0 \neq 0.5$ is the shift of the zero-frequency point $k = 2k_F$ (marked by an arrow in Fig. 3.6) away from $k = \pi/a$ due to fact that the value of k_F varies with E_{F}. As a result, we observe the apparent folding of the spectrum at $k = 2k_F$, compared to $\rho_0 = 0.5$ case.

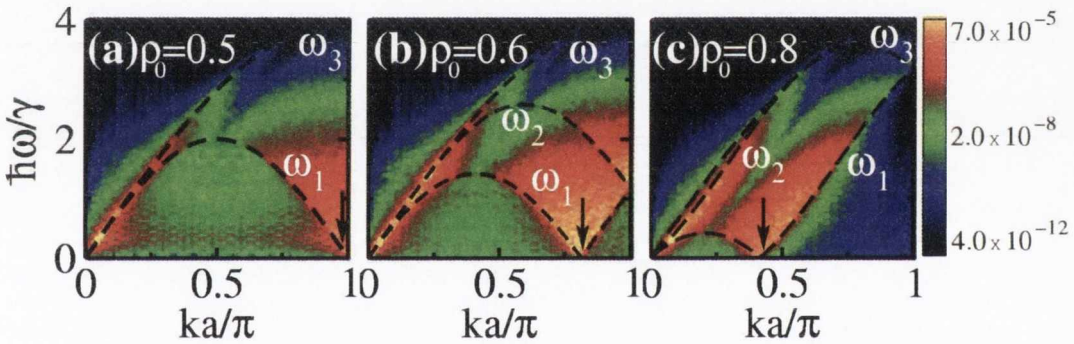

FIGURE 3.6: Two-dimensional Fourier transform of $\delta\rho_i(t)$ for (a) $\rho_0 = 0.5$, (b) $\rho_0 = 0.6$ and (c) $\rho_0 = 0.8$. The color shade represents the absolute value of $\mathrm{dFT}[\delta\rho_i(t)](k,\omega)$ and is logarithmically scaled for better contrast. Three dashed black lines on each graph show $\omega_1(k)$, $\omega_2(k)$ and $\omega_3(k)$ calculated using Eqs. (3.36)-(3.38) for each value of ρ_0.

Interestingly, the mode-occupation patterns analogous to the ones presented in Fig. 3.6 can be encountered in the analysis of dynamical properties of low-dimensional quantum spin models. The systems described by these models are, in fact, the true hallmarks of quantum magnetism and have been rigorously studied in the literature [185]. It is worth discussing in more detail the similarities between the excitation spectra of quantum spin chains and the ones obtained for the electronic tight-binding model.

3.6 Similarities to quantum spin chains

The Hamiltonian, describing an ensemble of quantum spins coupled via Heisenberg exchange interaction in the presence of magnetic field $\boldsymbol{h} = h\hat{\boldsymbol{z}}$, reads

$$\hat{H}_{XYZ} = \sum_{<ij>} \left(J^x \hat{s}_i^x \hat{s}_j^x + J^y \hat{s}_i^y \hat{s}_j^y + J^z \hat{s}_i^z \hat{s}_j^z \right) + h \sum_i \hat{s}_i^z, \tag{3.39}$$

where the spin operators $\hat{s}^\alpha$ are defined as $\hat{s}^\alpha = \hat{\sigma}^\alpha/2$, with $\{\sigma^\alpha\}_{\alpha=x,y,z}$ being the set of Pauli matrices (in the following $\hbar$ is set to 1 in order to simplify the notations), and $\boldsymbol{J} = \{J^x, J^y, J^z\}$ represents the strength of the exchange interaction along the x-, y- and z-direction. The sum in the first term is over the nearest neighbors. The quantum spin operators satisfy the commutation relation $\left[\hat{s}_i^\alpha, \hat{s}_j^\beta\right] = \imath \delta_{ij} \epsilon_{\alpha\beta\gamma} \hat{s}_i^\gamma$, where $\epsilon_{\alpha\beta\gamma}$ is the totally anti-symmetric Levi-Civita tensor with $\epsilon_{xyz} = 1$.

The general Hamiltonian in Eq. (3.39) corresponds to the anisotropic XYZ Heisenberg model which covers in the limiting cases some well-known specific models, such as the Ising model ($J^x = J^y = 0$), isotropic XY model ($J^x = J^y$, $J^z = 0$), antiferromagnetic Heisenberg spin-1/2 model ($J^x = J^y = J^z = J > 0$) etc.

For example, the Hamiltonian of the isotropic XY model can be written as

$$\hat{H}_{XY} = \sum_i J(\hat{s}_i^x \hat{s}_{i+1}^x + \hat{s}_i^y \hat{s}_{i+1}^y) + h \sum_i \hat{s}_i^z \equiv \sum_i \frac{J}{2}(\hat{s}_i^+ \hat{s}_{i+1}^- + \hat{s}_i^- \hat{s}_{i+1}^+) + h \sum_i \hat{s}_i^z, \tag{3.40}$$

where $\hat{s}^\pm = \hat{s}^x \pm \imath \hat{s}^y$ are the spin raising and lowering operators (ladder operators), which satisfy fermionic commutation relations on the same site[9]

$$\left\{\hat{s}_n^-, \hat{s}_n^+\right\} = 1, \quad \left\{\hat{s}_n^-, \hat{s}_n^-\right\} = \left\{\hat{s}_n^+, \hat{s}_n^+\right\} = 0 \tag{3.41}$$

and bosonic commutation relations on different sites

$$\left[\hat{s}_n^-, \hat{s}_m^+\right] = \left[\hat{s}_n^-, \hat{s}_m^-\right] = \left[\hat{s}_n^+, \hat{s}_m^+\right] = 0, \tag{3.42}$$

where $n \neq m$.

[9]It is also easy to show that $[\hat{s}_n^+, \hat{s}_m^-] = 2\hat{s}_n^z \delta_{mn}$, $[\hat{s}_n^z, \hat{s}_m^+] = \hat{s}_n^+ \delta_{mn}$ and $[\hat{s}_n^z, \hat{s}_m^-] = -\hat{s}_n^- \delta_{mn}$ (see for example Ref. [166, p. 37]), where the commutator of two operators A and B is given by $[A, B] = AB - BA$. However for the derivation presented here we need extra fermionic commutation relations for the ladder operators, for which we use the anti-commutator $\{A, B\} = AB + BA$.

Using the Jordan-Wigner transformation [55], which maps the Pauli spin-operators to fermionic operators, one can formally map the Hamiltonian of a spin-1/2 chain to a tight-binding Hamiltonian. The logic behind the Jordan-Wigner fermionization approach is essentially the same as that of the bosonization approaches, such as the well-known Holstein-Primakoff transformation [99] which, in its original form, is a mapping of the angular momentum operators to boson creation and annihilation operators. The Jordan-Wigner fermionization was originally suggested as a rigorous framework for the description of spin-1/2 XY model [Eq. (3.40)]. It is an alternative to other well-known approaches to quantum spin models, such as the famous Bethe ansatz,[10] exact diagonalization and other numerical methods. Here we follow Ref. [55] and perform the Jordan-Wigner transformation for the Hamiltonian given by Eq. (3.40).

We introduce the following fermionic operators

$$\hat{c}_1 = \hat{s}_1^-, \quad \hat{c}_n = (-2\hat{s}_1^z)(-2\hat{s}_2^z)\dots\left(-2\hat{s}_{n-1}^z\right)\hat{s}_n^-, \quad n = 2, \dots, N, \tag{3.43}$$

$$\hat{c}_1^\dagger = \hat{s}_1^+, \quad \hat{c}_n^\dagger = (-2\hat{s}_1^z)(-2\hat{s}_2^z)\dots\left(-2\hat{s}_{n-1}^z\right)\hat{s}_n^+, \quad n = 2, \dots, N. \tag{3.44}$$

By using the fact that $(-2\hat{s}^z)^2 = 1$ and $\hat{s}^z\,\hat{s}^\pm = -\hat{s}^\pm\,\hat{s}^z$, it can be shown that, indeed, the introduced operators satisfy the commutation relations of Fermi type

$$\left\{\hat{c}_n, \hat{c}_m^\dagger\right\} = \delta_{nm}, \quad \left\{\hat{c}_n, \hat{c}_m\right\} = \left\{\hat{c}_n^\dagger, \hat{c}_m^\dagger\right\} = 0. \tag{3.45}$$

The inverse transformation reads

$$\hat{s}_1^- = \hat{c}_1, \quad \hat{s}_n^- = e^{\pm\imath\pi\sum_{j=1}^{n-1}\hat{c}_j^\dagger\hat{c}_j}\,\hat{c}_n, \quad n = 1, \dots, N, \tag{3.46}$$

$$\hat{s}_1^+ = \hat{c}_1^\dagger, \quad \hat{s}_n^+ = e^{\pm\imath\pi\sum_{j=1}^{n-1}\hat{c}_j^\dagger\hat{c}_j}\,\hat{c}_n^\dagger, \quad n = 1, \dots, N. \tag{3.47}$$

[10] The Bethe ansatz [18, 121] was originally developed by H. Bethe in 1931 to solve the antiferromagnetic Heisenberg spin-1/2 model. It is based on a "guess" about the exact form of the eigenstates of the Heisenberg Hamiltonian which can be written as a linear combination of the basis states having the same number of down-spins

$$|\psi\rangle = \sum_{1\le x_1<\dots<x_n\le L} a(x_1, \dots, x_n)|x_1, \dots, x_n\rangle,$$

where $|x_1, \dots, x_n\rangle$ is the state in which n spins are flipped and L is the number of spins. Bethe's idea was to deduce the form of the amplitudes $a(x_1, \dots, x_n)$, which eventually yield the exact eigenstates of the ground state in terms of the solution of a system of coupled nonlinear equations. Since Bethe's original proposal, the method has been generalized to a large variety of models. As we will see in Chapter 6, the exact Bethe ansatz solutions of the Hubbard model in certain limits provide the basis for constructing an approximate exchange-correlation functional, which can accurately describe strongly-correlated systems in 1D within the lattice density functional theory framework.

By noticing that $\hat{c}_j^\dagger \hat{c}_{j+1}^\dagger = \hat{s}_j^+ (-2\hat{s}_j^z) \hat{s}_{j+1}^+ = \hat{s}_j^+ \hat{s}_{j+1}^+$, we finally write down the Hamiltonian of the spin-1/2 XY model in the Jordan-Wigner picture

$$\hat{H}_{XY}^{\mathrm{TB}} = \sum_i \frac{J}{2}(\hat{c}_i^\dagger \hat{c}_{i+1} + \hat{c}_{i+1}^\dagger \hat{c}_i) + h \sum_i \left(\hat{c}_i^\dagger \hat{c}_i - \frac{1}{2} \right). \tag{3.48}$$

This is essentially a spinless tight-binding nearest-neighbors Hamiltonian[11] with the intersite hopping $\gamma = \frac{J}{2}$ and the on-site energies $\epsilon_0 = h$. The spectra of the two-particle excitations of such Hamiltonian, calculated by Derzhko [55] and shown in Fig. 3.7 (the figures have been taken from Ref. [55]), are very similar to the ones we investigated in the case of charge dynamics of the atomic chain. The characteristic lines $\omega_1(k)$, $\omega_2(k)$ and $\omega_3(k)$, which define the excitation continuum in (k, ω)-space, are now controlled by the strength of the exchange interaction J and the value of magnetic field h (see Fig. 3.7).

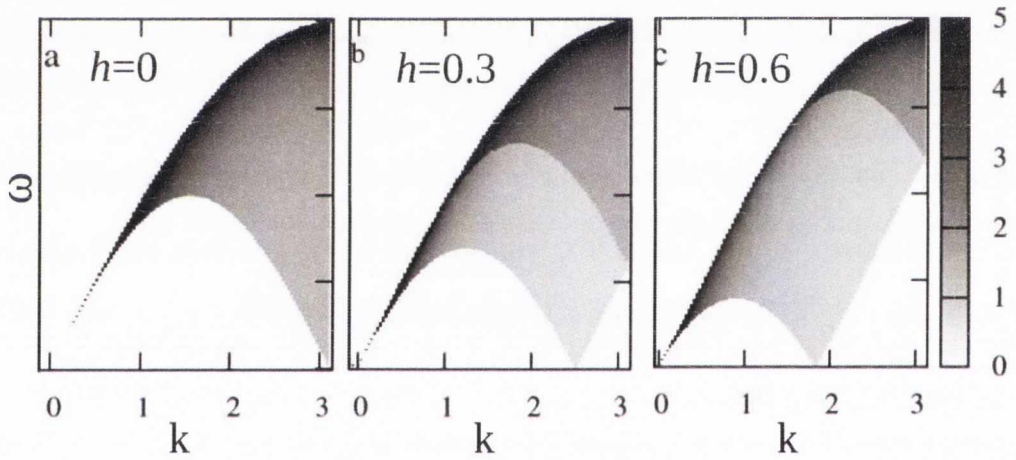

FIGURE 3.7: The transverse dynamic structure factor, representing the two-fermion excitation spectrum of the spin-1/2 XY model in transverse magnetic field [Eq. (3.48)], for $J = -1$ and (a) h=0, (b) h=0.3 and (c) h=0.6. The figures are from Ref. [55].

The dynamical quantities of interest in quantum spin models are the spin-spin correlation functions $\langle \hat{s}_m^\alpha(t) \hat{s}_n^\beta(0) \rangle$. In the linear response regime, the Fourier transform of $\langle \hat{s}_m^\alpha(t) \hat{s}_n^\beta(0) \rangle$, which can be written as $\hat{s}^{\alpha\beta}(q,\omega) = \frac{1}{2\pi} \int dt\, e^{\imath\omega t} \frac{1}{N} \sum_{mn} \langle \hat{s}_m^\alpha(t) \hat{s}_n^\beta(0) \rangle e^{-\imath q(m-n)}$,

[11] In contract to the XY model, the general Heisenberg Hamiltonian given by Eq. (3.39) can not be transformed into a non-interacting tight-binding Hamiltonian. The Jordan-Wigner transformation in this case yields an interaction term of the form $\left(\hat{c}_i^\dagger \hat{c}_i - \frac{1}{2} \right) \left(\hat{c}_{i+1}^\dagger \hat{c}_{i+1} - \frac{1}{2} \right)$. Hence, the simple analysis that can be performed for the XY model is not possible in this case. However, some of the low-energy properties of the antiferromagnetic Heisenberg model, in particular the presence of gapless excitations and the absence of the long range order, are similar to those of the simpler XY model.

is related, through the fluctuation-dissipation theorem [143], to the imaginary part of the Fourier transform of the dynamical susceptibility $\chi''(q,\omega)$, a quantity that can be measured experimentally. In fact, the neutron scattering cross-section is proportional to $\chi''(q,\omega)$ and, therefore, can be used as a tool to directly probe excitations in quantum spin systems.

The striking resemblance between Fig. 3.7 and Fig. 3.6 confirms that the excitation spectra, calculated from time-dependent simulations in the previous section, are indeed the linear response spectra. Note, however, that the agreement only holds in the case of weak external perturbations. As we will show in the next chapter (see Section 4.4 of Chapter 4), where we make full use of our time-dependent method, in the case of strong perturbations the dynamical evolution of the system deviates significantly from the linear response scenario.

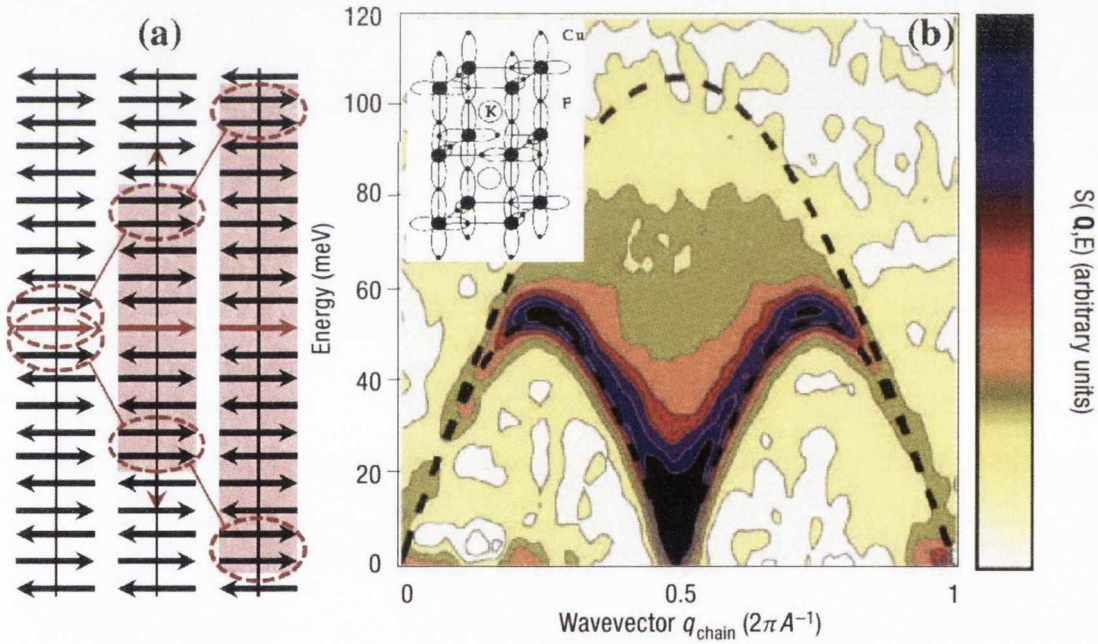

FIGURE 3.8: (a) Cartoon of spinon excitations: a spin-flip in a perfectly ordered antiferromagnetic spin chain splits into two domain wall boundaries, illustrating two spinons, each carrying half of a spin-flip. (b) Inelastic neutron scattering data for $KCuF_3$, plotted as a function of energy (E) and momentum (q) parallel to the chains of Cu^{2+} ions for $T = 6K$. The color indicates the size of the neutron scattering cross-section $S(q,E)$ and the superimposed black dashed lines indicate the boundaries of excitation continuum, predicted at $T = 0$ K by analytical calculations. Picture is taken from Ref. [147]. The inset shows the structure of $KCuF_3$ (from Ref. [75]).

Remarkably, in nature there exist a number of materials that behave like 1D spin chains. One well-known example is $KCuF_3$ [147]. This is a three-dimensional material, which due to its geometrical and molecular structure behaves like an array of weakly coupled spin-1/2 chains. The magnetic Cu^{2+} ions in $KCuF_3$ carry a spin $S = 1/2$ due to one unpaired electron and are coupled into linear chains by a strong antiferromagnetic interaction ($J = 34$ meV) through F^- ions. The chains are formed along c-axis [see inset in Fig. 3.8(b)] and the interaction between them is significantly smaller ($J = -1.6$ meV) than the intra-chain interaction. At first glance, such a spin chain could be the simplest possible realization of an antiferromagnet, however, in reality the system fails to develop the long-range Néel ordering, where neighboring spins are aligned antiparallel to each other. This is consistent with the Mermin-Wagner theorem [178, 179] which essentially states the absence of long-range ordered phases in one- and two-dimensional systems.[12] In relation to this point, one can mention the well-known failure of the classical spin-wave theory, which assumes small fluctuations around a classical ordered ground state, to describe excitations in antiferromagnetic Heisenberg model. In particular, an antiferromagnetic Heisenberg spin-1/2 chain appears to be a unique correlated spin system with peculiar dynamical properties. The basic two-particle excitations in this model are *spinons* [67]. These are topological excitations that can be visualized as a twist of π in the spin order [see Fig. 3.8(a)] and can be represented by quasiparticles with spin equal 1/2.

An example of inelastic neutron scattering data for $KCuF_3$ is presented in Fig. 3.8. The figure reveals a multi-spinon excitation spectrum which forms a continuum over an extended region of energy (E) and wave-vector (q) space. The lower and upper boundaries of the continuum are given, respectively, by functions $E_1(q) \propto J|\sin(qa)|$ and $E_2(q) \propto J|\sin(\frac{qa}{2})|$ (marked as black dashed lines on the graph), where a is the lattice parameter. These functions have been predicted by analytical calculations based on the Bethe ansatz [183] and belong to the same class of characteristic lines as the ones we have encountered in the excitation spectra of monoatomic tight-binding chains.

[12] In a more rigorous form, the theorem states that a continuous symmetry cannot be spontaneously broken at finite temperature in one- and two-dimensional systems. This can be intuitively understood as the absence of spontaneous magnetization and long-range order. The paper of Mermin and Wagner [179], for instance, contains a proof that at any nonzero temperature, one- or two-dimensional isotropic Heisenberg models with finite-range exchange interaction can be neither ferromagnetic nor antiferromagnetic. Interestingly, this result was already predicted in the work of Bloch (1930), where the foundations of the classical spin-wave theory were laid out.

3.7 Introducing a single spin-impurity

In the last section of this chapter we will look at another analytically solvable model. As a first step towards modeling the combined dynamics of itinerant electrons and spin impurities, we consider a simple system, presented in Fig. 3.9, where the spin of the impurity and the spin of the itinerant electron are treated as classical angular momentum vectors, $\boldsymbol{S}$ and $\boldsymbol{s}$, respectively. The two vectors are coupled via the exchange interaction $J > 0$. This is essentially a classical Heisenberg model for two spins, which can be formally obtained from the fully quantum Heisenberg model [see, for example, Eq. (3.39)] in the limit of infinite magnitude of the quantum spin [117]. In addition to the exchange interaction, $\boldsymbol{S}$ is subject to a constant homogeneous magnetic field $\boldsymbol{B} = B\hat{\boldsymbol{z}}$. The equations of motion for the two vectors read

$$\frac{d\boldsymbol{S}}{dt} = J\boldsymbol{S} \times \boldsymbol{s} + \gamma_{\mathrm{g}} \boldsymbol{S} \times \boldsymbol{B}, \tag{3.49}$$

$$\frac{d\boldsymbol{s}}{dt} = J\boldsymbol{s} \times \boldsymbol{S}. \tag{3.50}$$

where γ_{g} is the gyromagnetic ratio.[13] Hereafter, we will denote the magnitude of magnetic field as $B \equiv B\gamma_{\mathrm{g}}$.

Equations (3.49) and (3.50) form a system of nonlinear first-order differential equations where the unknown functions are represented by vectors with three components in the Cartesian coordinate system, e.g. $\boldsymbol{s} = \{s_x, s_y, s_z\}$ and $\boldsymbol{S} = \{S_x, S_y, S_z\}$. In order to find the solution of the system of equations, we perform a transformation to the spherical coordinate system, characterized by the following unit vectors (see the inset in Fig. 3.9)

$$\boldsymbol{u_r} = \begin{pmatrix} \cos\varphi \sin\theta \\ \sin\varphi \sin\theta \\ \cos\theta \end{pmatrix}, \; \boldsymbol{u_\theta} = \begin{pmatrix} \cos\varphi \cos\theta \\ \sin\varphi \cos\theta \\ -\sin\theta \end{pmatrix}, \; \boldsymbol{u_\varphi} = \begin{pmatrix} -\sin\varphi \\ \cos\varphi \\ 0 \end{pmatrix},$$

[13] According to the laws of classical physics, a charged body rotating about an axis of symmetry, has a magnetic dipole moment $\boldsymbol{\mu}$ and an angular momentum $\boldsymbol{L}$. Both $\boldsymbol{\mu}$ and $\boldsymbol{L}$ can be considered as vectors with certain module (magnitude) and direction. In the classical picture, presented in Fig. 3.9 we assume vectors $\boldsymbol{S}$ and $\boldsymbol{s}$ equivalent to angular momentum $\boldsymbol{L}$ (in units of eV·s). The corresponding magnetic moment is related to the angular momentum through a gyromagnetic ratio, which for a classical spinning charged solid or particle with a uniform charge (e) and mass (m) distributions, is given by $\gamma_{\mathrm{g}} = \frac{e}{2m}$ (in units of $\mathrm{s}^{-1}\mathrm{T}^{-1}$). Here, for simplicity, we take e and m as being the value of the electron charge and the electron mass, respectively. See also the discussion in Section 2.3.1 of Chapter 2.

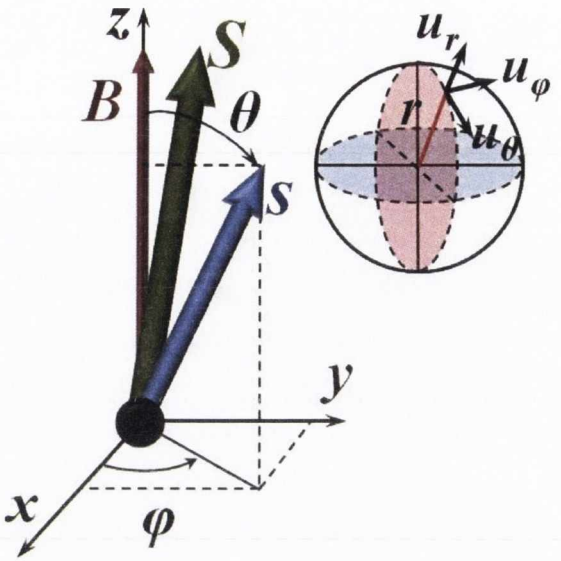

FIGURE 3.9: Model system: two classical vectors, representing the itinerant spin $\boldsymbol{s}$ and the spin of the impurity $\boldsymbol{S}$ coupled via the exchange interaction. The local spin is set to precess around a magnetic field $\boldsymbol{B}$, applied along the z-direction. The inset shows the unit vectors $\{\boldsymbol{u}_r, \boldsymbol{u}_\theta, \boldsymbol{u}_\varphi\}$ of the spherical coordinate system. Here r is the radial coordinate, θ is the polar, or inclination, angle and φ is the azimuthal angle.

where r is the radial coordinate, θ is the polar angle and φ is the azimuthal angle. The unit vectors satisfy the following relations

$$\begin{aligned} \boldsymbol{u}_r \times \boldsymbol{u}_\theta &= \boldsymbol{u}_\varphi, \\ \boldsymbol{u}_\theta \times \boldsymbol{u}_\varphi &= \boldsymbol{u}_r, \\ \boldsymbol{u}_\varphi \times \boldsymbol{u}_r &= \boldsymbol{u}_\theta. \end{aligned} \tag{3.51}$$

Starting with $\boldsymbol{B} = B\hat{\boldsymbol{z}} = \{0, 0, B\}$, we obtain

$$B_r = B\,\cos\theta, \quad B_\theta = -B\,\sin\theta, \quad B_\varphi = 0, \tag{3.52}$$

or

$$\boldsymbol{B} = B\left(\cos\theta\,\boldsymbol{u}_r - \sin\theta\,\boldsymbol{u}_\theta\right). \tag{3.53}$$

For simplicity, we assume that the magnitudes of vectors $\boldsymbol{S}$ and $\boldsymbol{s}$ are equal to unity and that

$$\boldsymbol{s} = \boldsymbol{u}_r. \tag{3.54}$$

The impurity spin is also expressed through the unit vectors of the spherical coordinate system

$$\boldsymbol{S} = \alpha\, \boldsymbol{u_r} + \beta\, \boldsymbol{u_\theta} + \gamma\, \boldsymbol{u_\varphi}, \tag{3.55}$$

where α, β and γ are unknown time-dependent coefficients which satisfy the following relation

$$\alpha^2 + \beta^2 + \gamma^2 = 1. \tag{3.56}$$

By substituting Eqs. (3.53)-(3.55) into the equations of motion and by using Eq. (3.56), after some algebraic manipulations, we obtain the following equations of motion for the angles φ and θ

$$\dot{\varphi} + B = 0, \tag{3.57}$$

$$\ddot{\theta} + J \cdot B \cdot \sin\theta = 0. \tag{3.58}$$

The first equation immediately leads to

$$\varphi(t) = -B\, t + \varphi(0), \tag{3.59}$$

The second equation is a nonlinear second-order differential equation. Interestingly, it is identical to the equation of motion of a simple gravity pendulum

$$\ddot{\theta} + \frac{g}{l} \sin\theta = 0, \tag{3.60}$$

where angle θ describes the deviation of the pendulum from the direction of the force of gravity, g is the acceleration due to gravity and l is the length of the pendulum rode. It is known that in the linear approximation, e.g. for small angle θ, $\sin\theta \approx \theta$ and Eq. (3.60) has a simple periodic solution given by $\cos(\sqrt{g/l}t)$. In the case of a linearized equation Eq. (3.58) the frequency is $\sqrt{J\,B}$, which clearly confirms the existence of two driving forces in the system, namely the exchange interaction (J) and the locally applied magnetic field (B). However, in general, the solution of Eq. (3.58) is not trivial but it can be obtained by using Jacobi elliptic functions formalism[2, p. 567]

$$\theta(t) = \pm 2\, Am\left(\frac{1}{2}\sqrt{(2\,J\,B + c_1)(t + c_2)^2}\,|\, -\frac{4\,J\,B}{2\,J\,B + c_1}\right), \tag{3.61}$$

where c_1 and c_2 are arbitrary constants and $Am(x|m)$ denotes the Jacobi amplitude function. The latter is an inverse function of the elliptic integral of the first kind $F(x|m) = \int_0^x \frac{dt}{\sqrt{1-m^2\,sin^2 t}}$ and is also given by $Am(x|m) = \int_0^x dn(x'|m)dx'$, where

$dn(x'|m)$ is the Jacobi elliptic function with elliptic modulus m. Naturally, the arbitrary constants c_1 and c_2 can be found from the initial conditions for the angles θ and φ.

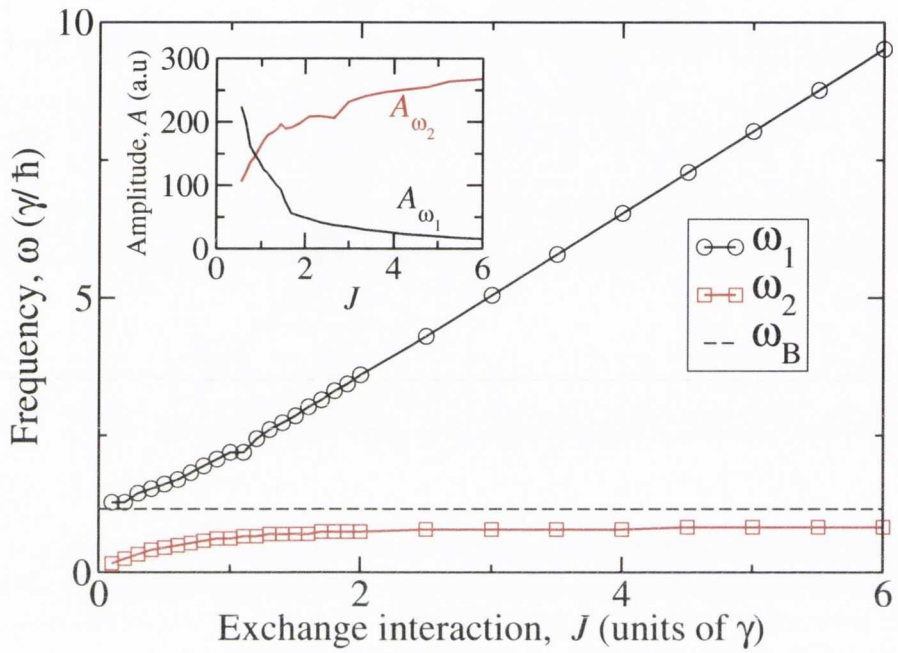

FIGURE 3.10: Two leading frequencies in the Fourier spectra of $S_x(t)$ and $s_x(t)$ as functions of the exchange interaction J. Note that J is in the units of γ and ω is in the units of $\frac{\gamma}{\hbar}$. The inset shows the corresponding amplitudes of ω_1 and ω_2 in the Fourier transform as functions of J. In the initial state, $\boldsymbol{S}$ is parallel to $\boldsymbol{B}$ and $\boldsymbol{s}$ is slightly tilted from the z-axis by angles $\theta(0) = \varphi(0) < 5^{\circ}$.

Once $\theta(t)$ and $\varphi(t)$ are calculated, we can determine the position of the vector $\boldsymbol{S}$ in the spherical coordinate system by using the following relations for β and γ, obtained from Eq. (3.50)

$$\beta = \dot{\varphi} \cdot \sin\theta / J, \tag{3.62}$$

$$\gamma = -\dot{\theta}/J, \tag{3.63}$$

and, finally, $\alpha = \sqrt{1 - \beta^2 - \gamma^2}$.

In order to investigate the dynamics of $\boldsymbol{S}$ and $\boldsymbol{s}$ in a wide range of parameters, we resort to the numerical solution of Eqs. (3.57) and (3.58) and calculate the time-dependent Cartesian components of $\boldsymbol{S}$ and $\boldsymbol{s}$. By computing the Fourier spectra of the transverse (x-) components of the impurity and itinerant spins as functions of time, we are able to identify two leading frequencies in the spectrum (these are the same for $\boldsymbol{S}$ and $\boldsymbol{s}$ since

the motion of the two spins is synchronized). The dependence of these two frequencies on the strength of the exchange interaction J, for a fixed value of B, is shown in Fig. 3.10. Note that we scaled the units to match those we use in the fully quantum mechanical treatment of dynamics in atomic chain, e.g. we use the units of $\gamma/\hbar$ for the frequencies and γ for J, where γ is the typical value of the hopping parameter in the chain.

As one can see from Fig. 3.10 , one of the frequencies, ω_1, increases dramatically with increasing J, while the second one, ω_2, saturates with J to a value close to the Larmor frequency $\omega_B = \frac{eB}{2m}$. The amplitudes of ω_1 and ω_2, which measure the contribution of each mode to the dynamical spectrum, behave differently: the amplitude A_{ω_1} decreases with J while the amplitude A_{ω_2} increases with J (see the inset in Fig 3.10). The trajectories of the two vectors and the corresponding Fourier transforms, calculated by using the exact solution are in agreement with those obtained from the time-dependent simulations for an isolated site with a fully quantum itinerant spin coupled to the spin of the impurity (represented by the angular momentum vector $\boldsymbol{S}$). The physical meaning of the result presented in Fig. 3.10 is the following: (i) when the two driving forces $\boldsymbol{J}$ and $\boldsymbol{B}$ are comparable in magnitude, the dynamics of the system is determined by two competing frequencies ω_1 and ω_2, which give comparable contribution to the dynamical spectrum; (ii) when the strength of the exchange interaction increases, the two vectors are almost perfectly aligned (however, they rapidly precess around each other with the large frequency $\omega_1 \propto J$) and the system as a whole precesses around the magnetic filed $\boldsymbol{B}$ with the frequency ω_2 close to the Larmor frequency.

The calculation presented here clearly demonstrates that even the simplest classical problem shown in Fig. 3.9 has a rather complex solution. For a system of several magnetic impurities embedded in an atomic chain, consisting of N atoms, the number of degrees of freedom is significantly larger. One should expect high complexity and nonlinearity in the possible solutions, especially if the system is subject to external time-dependent perturbations.

3.8 Summary

In this chapter we have investigated the time evolution of itinerant electrons in one-dimensional atomic chains upon an external perturbation. We have calculated, both

analytically and numerically, the frequency portraits of the dynamics. The excitation spectrum, calculated as the two-dimensional Fourier transform of the nonequilibrium charge density distribution along the chain, has been also studied. We found that the spectrum exhibits a number of interesting properties, characteristic of one-dimensional fermionic systems. Importantly, it forms a continuum in a certain region of energy and momentum space, and the shape of this region varies systematically with the system parameters. Finally, we have looked at the simple system, where the spin of the magnetic impurity is coupled to the itinerant spin and to the magnetic field on an isolated site. This problem was treated classically and the exact solution of the system of equations of motion was found. The calculated frequency portraits of the dynamics of the impurity spin demonstrate the deviation from simple Larmor precession due to the exchange coupling to the itinerant electron spin. In conclusion, the study carried out in this chapter, gives insight into the dynamical properties of itinerant electrons in atomic chains. This provides a part of the solution to the problem considered in the next chapter, where an atomic chain is used as a medium for the transfer of spin-excitations between two well separated localized spin centers.

Chapter 4

Electrical control of spin dynamics in a one-dimensional device

4.1 Introduction

In magnetic memory devices, the magnetization vectors of individual magnetic elements, which can be set either "up" or "down", play the role of logical bits. A conventional way of recording a magnetic bit is by switching its magnetization from one orientation to another with an applied magnetic field. In fact, this is the basic working principle of magnetic hard disks. However, with electronic industry successfully entering the nanoworld, the conventional approaches to manipulating a magnetic state using magnetic fields alone, face serious limitations.

One of the problems arising from the continuous miniaturization of electronic devices is known as the scalability issue: in contrast to electric fields, magnetic fields are difficult to confine at the nanoscale and the magnitudes of the fields required for field-induced switching do not scale down with device dimensions. This presents a great challenge for obtaining high-density memory storage. Moreover, magnetic fields used for magnetization switching are typically produced by electric current lines [173], which is not very efficient due to unavoidable energy losses associated with Joule heating. These problems are experienced not only in conventional devices but also in novel spintronic applications such as Magnetoresistive Random Access Memory (MRAM) since the first concept of a working MRAM cell is indeed based on field-induced switching [4].

In addition to that, it appears that fundamental limitations exist to the speed at which magnetic switching can be realized. In fact, the most efficient mechanism involved in magnetic recording is precessional magnetization switching: when a magnetic field $\boldsymbol{B}$ is applied to a magnetic bit over a period of time τ, the magnetization vector precesses around the direction of the field until the quantity $|\boldsymbol{B}| \cdot \tau$ reaches a threshold value and the magnetization changes its orientation. Thus the pulse duration τ essentially determines the switching time and, ultimately, the speed of the memory storage. Intuitively, one could assume that the switching speed can be significantly increased if strong enough fields and very short pulses are used. However, recent experiments demonstrated that this intuitive picture does not hold and there is a physical limit to the speed of magnetic recording. In the work of Tudosa *et al.* [256] ultrashort and intense magnetic field pulses ($|\boldsymbol{B}| \approx$ few Tesla and $\tau \approx 2$ ps), generated by relativistic electron beams, were applied to magnetic granular recording media (14-nm-thick films of CoCrPt). It was observed that at such extreme conditions precessional switching no longer takes place at well-defined field strengths. Instead, the behavior of magnetic grains becomes stochastic and the switching occurs randomly within a wide range of magnetic fields. These findings indicate that at time scales of 2 ps one reaches a fundamental limit for deterministic magnetization switching.

In view of these limitations, considerable effort has been devoted to finding new ways to manipulate the magnetization. Since conventional semiconductor technology relies on electric fields to control the conductivity, it is also highly desirable to become able to control the magnetization and, in general, the spin state of a magnetic medium using electric fields [44]. It is anticipated that the new generation of magnetic information storage technology with high density and low power consumption would be possibly based on such electric-field control.

One way to manipulate spins by purely electrical means relies on the spin-transfer torque mechanism [21, 227]. This approach uses spin-polarized currents to control the direction of the magnetization and has been realized in various nanoscale materials ranging from magnetic multilayers [184] to, more recently, individual superparamagnetic nanoislands [141] and single atoms in STM-type geometry [164]. Spin-Transfer-Torque-based Random Access Memory (STT-RAM) has been considered as a promising candidate for a new type of devices, which could solve energy-consumption and scalability issues of MRAM. For practical STT-RAM implementations, however, it is crucial to reduce the critical current density needed to switch the magnetization, which at the moment is still quite high ($\approx 10^6$ A/cm^2 [62]).

Alternative to electric-current control is the optical control, such as that in the laser-driven ultrafast magnetization switching [131]. Although, the first experiments on ultrafast spin dynamics demonstrated a rather destructive and uncontrollable effect of an intense thermal excitation produced by a laser pulse in a magnetic medium, new observations suggest that it is indeed possible to manipulate the magnetization at these time scales by using optical excitations. Recently, it was reported that circularly polarized fs-laser pulses can be used to non-thermally excite and coherently control the spin dynamics in magnetic materials, such as rare-earth orthoferrites [130]. In a somewhat different context, the optical manipulation of single spins in bulk media, such as N-V centers in diamond [88], is at the heart of the most promising candidates for solid-state quantum computing [13, 252].

Another alternative is based on the idea of an electrostatic control of the spin-density, i.e. of the construction of spin-transistor type devices [113, 284]. Recently, the concept of gate-modulated spin-pumping transistors has been studied theoretically in infinite graphene strips with patterned magnetic implantations [82, 83]. Importantly, such devices rely on the efficient transport of spin information between two points in space and time, and require the possibility to actively tune the spin-signal during its propagation.

In this Chapter we explore the possibility of electrical control of spin transfer in atomistic spin-conductors. We consider a finite monoatomic wire linking two localized spin-carrying impurities, e.g. local spins. When one of the local spins is set into precession, it generates a perturbation in the itinerant spin-density. This perturbation is carried through the wire by conduction electrons and can be detected in the dynamical response of the second spin. We show that the propagation of the spin-signal and, consequently, the dynamical communication between the two spin-centers, can be tuned by means of an electrostatic gate applied to the interconnecting wire. Our main finding is an enhancement of the spin-pumping communication for a certain range of gate voltages. Importantly, the resonant feature in the transmission of the spin-signal between the two local spins can be directly linked to the modification of the electronic structure of the wire induced by the applied electrostatic gate. The theoretical framework for the investigations reported in this chapter is that of the quantum-classical Ehrenfest dynamics, which was discussed in Section 2.4.3.

4.2 Model system

A cartoon of the device considered in this chapter is presented in Fig. 4.1. This consists of an N-sites long atomic wire (typically N=100) interconnecting two magnetic centers. The latter, represented in the figure by two vectors, $\boldsymbol{S}_1$ and $\boldsymbol{S}_2$, enter our model as substitutional magnetic impurities positioned at the two ends of the wire, with their spins originating from the deeply localized d-electrons. One of them, say the left-hand side local spin $\boldsymbol{S}_1$, is labeled as "driven", as its precession is induced by an external perturbation. The other local spin, $\boldsymbol{S}_2$, located at the opposite end of the chain acts as a "probe". This local spin does not interact with any external fields and only couples to the itinerant electrons of the chain. Hence $\boldsymbol{S}_2$ probes the magnetic excitations produced by the driven spin $\boldsymbol{S}_1$ as these propagate through the interconnecting wire. The device is described as a mixed quantum-classical system in the spirit of the s-d model and its dynamics is modeled at the Ehrenfest level. Since the theoretical framework of such spin dynamics was discussed in detail in Section 2.4.3, here we only write the explicit expressions for the Hamiltonians of the quantum electrons and the classical local spins together with their corresponding equations of motion (EOMs). The time-dependent Hamiltonians of the two subsystems read

$$\hat{H}_{\rm el}(t) = \sum_{\substack{i,j=1,N \\ \alpha=\uparrow,\downarrow}} H_{ij}^{\rm TB}\, \hat{c}_i^{\alpha\dagger}\, \hat{c}_j^{\alpha} - \tag{4.1}$$

$$-J \sum_{\alpha,\beta=\uparrow\downarrow} \left[\boldsymbol{S}_1(t) \hat{c}_1^{\alpha\dagger}\, \hat{c}_1^{\beta} + \boldsymbol{S}_2(t)\, \hat{c}_N^{\alpha\dagger}\, \hat{c}_N^{\beta} \right] \cdot \hat{\boldsymbol{\sigma}}^{\alpha\beta} , \tag{4.2}$$

$$H_{\rm S}(t) = -\boldsymbol{S}_1(t) \cdot [J\boldsymbol{s}_1(t) + g\mu_{\rm B}\boldsymbol{B}] - J\boldsymbol{S}_2(t) \cdot \boldsymbol{s}_N(t) . \tag{4.3}$$

The notations are the same as in Eq. (2.64) and Eq. (2.65) with $\boldsymbol{S}_1$ and $\boldsymbol{S}_2$ representing the unit vectors in the directions of the two local spins. The only difference compared to a more general Ehrenfest system, discussed in Section 2.4.3, is that only two local spins are considered. Thus the equations of motion [see Eq. (2.67) and Eq. (2.68)] can be conveniently written as

$$\frac{\partial \hat{\rho}}{\partial t} = \frac{i}{\hbar} \left[\hat{\rho}, \hat{H}_{\rm el} \right] , \tag{4.4}$$

$$\frac{d\boldsymbol{S}_n}{dt} = \{ \boldsymbol{S}_n, H_{\rm S} \} = \frac{\boldsymbol{S}_n}{\mathcal{S}} \times \begin{cases} J\boldsymbol{s}_1 + g\mu_{\rm B}\boldsymbol{B} & \text{for } n = 1 \\ J\boldsymbol{s}_N & \text{for } n = 2 \end{cases} . \tag{4.5}$$

The instantaneous on-site spin-density $\boldsymbol{s}_i(t)$ entering Eq. (4.5) is generated as

$$\boldsymbol{s}_i(t) \equiv \langle \boldsymbol{\sigma} \rangle_i (t) = \mathrm{Tr}\left[\rho(t)\boldsymbol{\sigma}\right]_i = \sum_{\alpha\beta} \rho_{ii}^{\alpha\beta}(t)\boldsymbol{\sigma}^{\beta\alpha} , \tag{4.6}$$

i.e. it is the expectation value of the electronic spin at site i and time t.

The coupled EOMs are integrated numerically using the RK4 algorithm as discussed in Section 2.4.4. As a result the set of trajectories for the electronic spin-densities $\boldsymbol{s}_i(t)$ and for the two classical spins $\boldsymbol{S}_1(t)$ and $\boldsymbol{S}_2(t)$ are obtained.

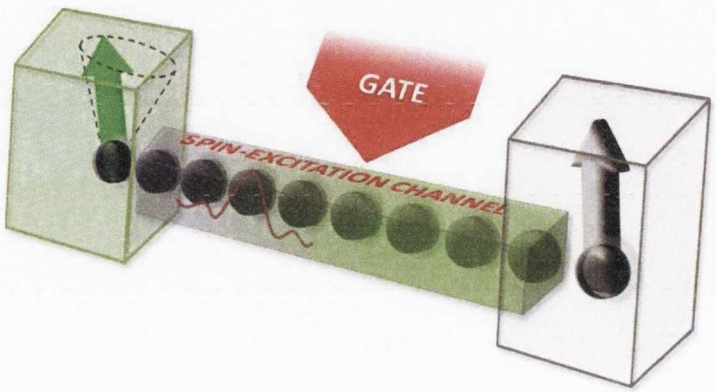

FIGURE 4.1: Model system: two localized spin-impurities are electronically connected by a monoatomic wire, where electrons can flow. An electrostatic gate is applied to some of the interconnecting sites.

Note that the Hamiltonian of the local spins [see Eq. (4.3)] describes the interaction of the local spins with the conduction electrons (through instantaneous electron spin-density) and with the external magnetic field $\boldsymbol{B} = B\hat{\boldsymbol{z}} = \{0, 0, B\}$, which is applied locally to $\boldsymbol{S}_1$ only, in order to drive its precession. This does not imply any true physical meaning of an extremely localized external magnetic field and is only an instrumental variable that we use to drive the precession of $\boldsymbol{S}_1$ which gives rise to the spin-pumping in the system.

We restrict our treatment to the present form of the classical Hamiltonian since we are mainly concerned with the dynamical exchange interaction between the spins of the impurities mediated by the itinerant electrons (similarly to RKKY interaction [123, 214, 274] in the static regime). Any additional non-conservative terms, such as those describing Gilbert damping, are explicitly omitted in this work, e.g. our system is conservative. We mention, however, that an almost identical set of equations, except

for a phenomenological damping term added to the equation of motion for the local spins (along the lines of the LLG equation) has been used in Ref. [138] to study the real-time relaxation dynamics of the electron-spin coupled systems.

The effect of an electrostatic gate is incorporated in our model as a rigid shift of the on-site energies $\varepsilon_i \rightarrow \varepsilon_i + V_g$, where $i \in [i_1, i_2]$ is a certain range of sites located in the middle of the chain and V_g is the gate voltage. This region can also be re-interpreted as a part of a different material so that the same model system also describes a one-dimensional (1D) tri-layered heterostructure (tunnel junction or quantum well), in which the two peripheral layers are identical.

Since the existence of the localized spins is an essential requirement for the coupled quantum-classical spin dynamics, our model is most suitable for describing systems containing magnetic impurities embedded in non-magnetic hosts. A number of relevant experimental set-ups comprising a noble metal surface with adsorbed transition metal atoms (or rare earths) [177] or individual (and chains of) magnetic adatoms on insulating surfaces [96, 97] can be found in the literature.

Although our model can be easily extended to higher dimensions, here we have focused on spin dynamics in a 1D structure. A possible realization of such a model system are metallic carbon nanotubes doped with single substitutional magnetic impurities, which have been recently proposed as promising candidates for spintronics applications [82]. In a broader context, our model system is as a schematic representation of two (or several) magnetic devices (impurity atoms, adatoms or magnetic molecules) dynamically coupled through a low-dimensional atomic lattice.

An essential advantage of the approach is the ability to model the effects of arbitrary excitations. In fact, in contrast to linear-response methods, our simulations are not limited to small gate voltages, spatially-continuous electrostatic potentials or small-angle spin precession. This becomes particularly important for calculations with an applied electrostatic gate when the value of the gate voltage is comparable or larger than the typical energy scale of the system (this is defined by the hopping parameter γ). In this case the application of the perturbation theory is not justified since the external perturbation is significant and, therefore, one can expect deviations from the linear response result. Indeed, as we will see in Section 4.4, the time-dependent simulations of spin dynamics in the presence of an electrostatic gate for large gate voltages reveal a dynamical picture qualitatively different from that obtained in the case of small gate voltages, e.g. in the limit of weak perturbation.

4.3 Dynamics of the itinerant spins with frozen impurities

4.3.1 No external gate

As a preliminary step towards the combined quantum-classical dynamics, we first address the dynamics of the spin-density of the itinerant electrons in the presence of the two local spins, whose directions are fixed, e.g. $\boldsymbol{S}_{1,2}||\hat{\boldsymbol{z}}$. A spin-excitation is produced by a small but finite spatially-localized perturbation in the spin-density. As initial density matrix at t_0 we use the one that corresponds to a perturbed Hamiltonian $\hat{H}_{\rm el}(t_0-\delta t)$ in which one of the localized spins is slightly tilted in the $x-z$ plane, such that $\boldsymbol{S}_1(t_0-\delta t)\times\hat{\boldsymbol{z}}\approx d\theta\lesssim 5^{\rm o}$. However, at t_0 we bring $\boldsymbol{S}_1$ back to its original direction ($\boldsymbol{S}_1||\hat{\boldsymbol{z}}$) where it stays throughout the simulation. In other words we study the time evolution of the system with the two local spins parallel to each other starting from the ground state electronic charge density of the system where one of the two spins is tilted by a small angle.

As we showed in the previous chapter, the evolution of the density matrix for $t>t_0$ is given by $\hat{\rho}(t)=e^{-i\hat{H}_{\rm el}t/\hbar}\hat{\rho}(t_0)e^{i\hat{H}_{\rm el}t/\hbar}$ (in the case of the frozen local spins $\hat{H}_{\rm el}$ is time-independent). When projected onto the basis of the spin-resolved atomic orbitals $|i\sigma\rangle$, this expression describes the time evolution of the density matrix elements and also provides complete information about the dynamical spectrum in terms of frequencies and amplitudes [see Eq. (3.24)]. Using this result we can derive similar expressions for the spin-densities $\boldsymbol{s}_i(t)$. Following the definition of the spin-density given in Eq. (4.6), the l-th Cartesian component ($l=x,y,z$) of the expectation value of the electron spin on a particular site k can be calculated as

$$\begin{aligned} s_k^l(t) &= \sum_{\alpha\beta}\rho_{kk}^{\alpha\beta}\,\sigma_l^{\beta\alpha}= \\ &= \sum_{\alpha\beta}\left(\sum_{mn}e^{-i\omega_{mn}t}c_{km}^{\alpha}\,c_{kn}^{\beta *}\sum_{i\gamma}\sum_{j\delta}c_{im}^{\gamma *}\,c_{jn}^{\delta}\,\rho_{ij}^{\gamma\delta}(t_0)\right)\sigma_l^{\alpha\beta}, \end{aligned} \tag{4.7}$$

or

$$s_k^l(t)=\sum_{\alpha\beta}\left(\sum_{mn}e^{-i\omega_{mm}t}\,A_{kk,mn}^{\alpha\beta}\right)\sigma_l^{\alpha\beta}, \tag{4.8}$$

where

$$A^{\alpha\beta}_{kk,mn} = c^{\alpha}_{km}\, c^{\beta *}_{kn} \sum_{i\gamma} \sum_{j\delta} c^{\gamma *}_{im}\, c^{\delta}_{jn}\, \rho^{\gamma\delta}_{ij}(t_0), \tag{4.9}$$

and the frequencies $\omega_{mn} \equiv (e_m - e_n)/\hbar$ correspond to the differences between the eigenvalues e_m of $\hat{H}_{\rm el}(t_0)$.

The typical evolution of the spin-density of the itinerant electrons, resulting from the spin-excitation described above, is presented in Fig. 4.2. The trajectories of the on-site spin polarization $\Delta s^z_i(t) = s^z_i(t) - s^z_i(t_0)$ calculated using Eq. (4.7) are identical (on the scale of the graph) to those obtained by the numerical integration of the EOMs [i.e. from Eq. (4.4)-(4.5)].

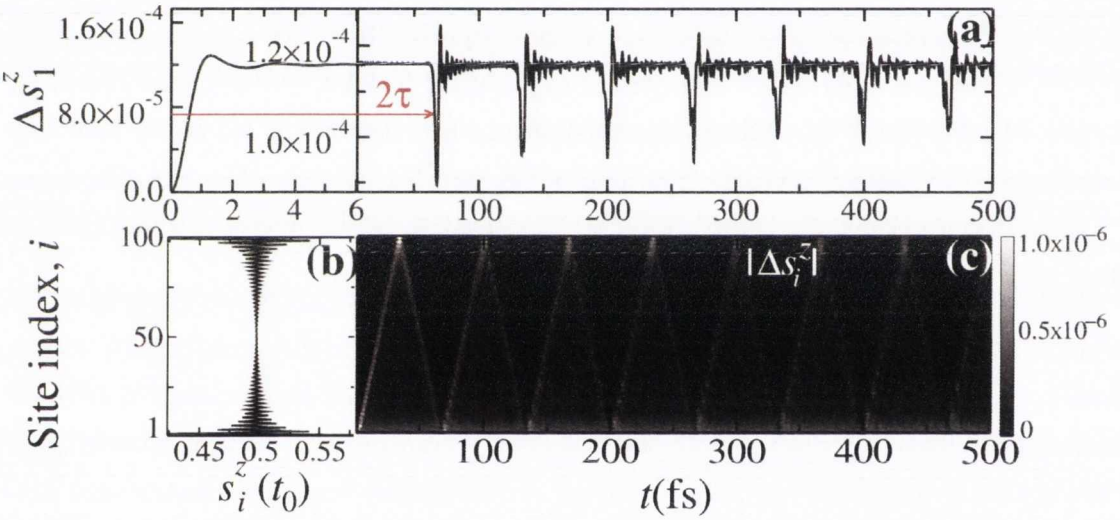

FIGURE 4.2: Spin-excitation in a one-dimensional wire. (a) Time-dependence of the spin-polarization on the first site (Δs^z_1) as obtained from the numerical integration of the EOMs and directly from Eq. (4.7). (b) Initial spin-polarization $s^z(t_0)$ as a function of the site index. (c) Time and space evolution of Δs^z_i with the color shade representing the absolute value of $\Delta s^z_i(t)$. Note that 2τ is the spin wave-packet round-trip time as also seen in the bottom panel.

The spatial distribution of the initial spin polarization, $s^z_i(t_0)$, is shown in Fig. 4.2(b) and its subsequent evolution is presented in Fig. 4.2(c). Similarly to the charge-only case discussed in the previous chapter, the spatially-resolved temporal portrait of the spin dynamics can be viewed as the propagation of a spin wave-packet. This travels along the wire with a practically uniform velocity very close to the Fermi level group velocity, as expected in view of the rather small overall local spin-polarization of the chain. The backbone of the packet is detectable even after a few tens of reflections at the ends of the wire. Such a feature demonstrates that this finite 1D model atomic

system is an efficient waveguide for spin wave-packets of femtosecond duration, at least over the investigated time scales of a few picoseconds.

Equation (4.8) can be used to calculate directly the dynamical spectra of particular spin-observables. These match perfectly those calculated by performing the discrete Fourier transform of the time-dependent spin-densities obtained over the finite duration of the simulation. Clearly, in the absence of the localized impurities the frequencies ω_{mn} (and their corresponding amplitudes) are identical to those calculated for a finite homogeneous tight-binding chain [see Section 3.4]. However, the interaction with the two frozen local impurities for $J = |\gamma|$ has a minor effect on the electron Hamiltonian, and, therefore, all frequencies are contained approximately in the interval $[\omega_{min}, \omega_{max}]$ with $\omega_{\min} \approx 3\pi^2|\gamma|/(N+1)^2\hbar$ and $\omega_{\max} \approx 4|\gamma|/\hbar$ [see Eq. (3.29)-(3.30)].

4.3.2 Electrostatic gate applied

The dynamics of the itinerant spins, as described by Eq. (4.7), in the case of an electrostatic gate applied to a section of sites in the middle of the wire cannot be expressed in a closed form as a function of $V_{\rm g}$ for arbitrarily big systems. Therefore we resort to our numerical integration scheme in order to investigate the spin dynamics in the presence of the gate. Before addressing the dynamics, however, we first analyze the ground-state electronic structure of the gated wire for different values of the gate potential $V_{\rm g}$. Figure 4.3 shows the adiabatic variation of the eigenvalues for a non spin-polarized 30-sites long chain without localized spins as a function of the gate potential $V_{\rm g}$. The gate is applied to 10 sites in the middle of the chain, i.e. at the sites with indices going from i_1=11 to i_2=20. Note that the energy-related quantities on all the figures are in units of the hopping integral γ, which sets the energy scale for the entire system. According to their weights at the three subsections of the chain, calculated as $\Omega_{\rm L,M,R} = \sum_{i\in{\rm L,M,R}} |c_{in}|^2$, we distinguish three types of states depending on which of the three partial weights is the greatest (here $c_{in} = \langle i|\varphi_n\rangle$ is the projection of the eigenvector φ_n of $\hat{H}_{\rm el}$ on the non-spin-polarized atomic orbital $|i\rangle$). The eigenstates corresponding to the two peripheral un-gated regions ($\Omega_{\rm L}$ and $\Omega_{\rm R}$) are degenerate by symmetry, as the gate is applied in the geometric center of the wire.

For $V_{\rm g}$ close to 0, the discrete energy spectrum consists of the eigenvalues in the range $[-2|\gamma|, 2|\gamma|]$. With the increase of $V_{\rm g}$ the level-spacing distorts as the eigenvalues are affected differently by the gate. Certain eigenvalues grow nearly linearly with increasing

V_g (these are shown as red squares in Fig. 4.3). The spatial distribution of these eigenvalues is predominantly concentrated in the gated region, i.e. they correspond to the region where the local on-site potentials have been modified.

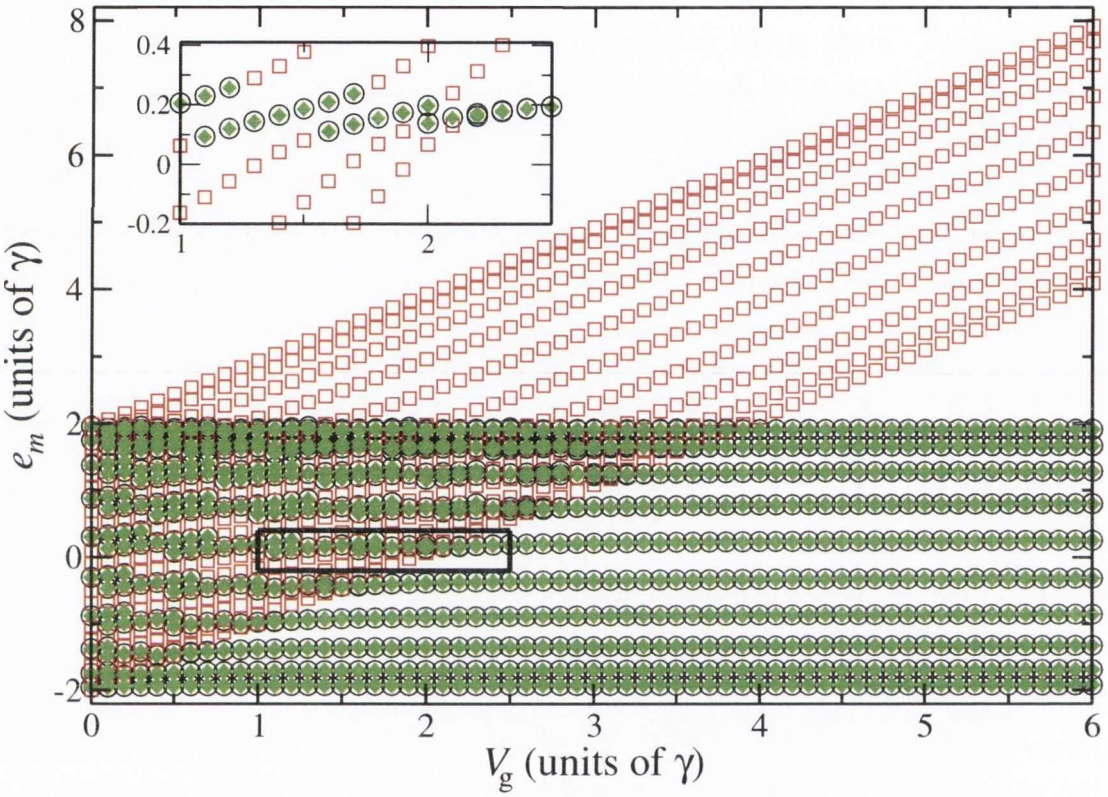

FIGURE 4.3: Schematic of the gate-dependence of the ground-state energy spectrum of $\hat{H}_{el}$, e.g. $\{e_m\}_{m=1}^{2N}$. The eigenvalues associated with the left-hand side of the wire (Ω_L) are marked with black circles, those originating from the states in the gated middle (Ω_M) - with red squares and those corresponding to the right-hand side (Ω_R) - with green diamonds. The inset shows a magnification of a region corresponding to intermediate values of V_g, illustrating the situation of avoided crossings.

For extremely large values of V_g ($V_g > 4|\gamma|$) the chain is effectively split into three energetically-decoupled parts, the gated middle and the two identical un-biased parts (the left-hand side and the right-hand side of the chain). Most interesting, however, is the range of intermediate gate voltages, for which the three parts of the wire are substantially affected but not yet decoupled by the gate voltage. For such V_g avoided crossings occur between states localized in the gated and the non-gated regions.

Avoided crossings [149, p. 302] is an important and widely used concept in quantum mechanics, which is closely related to the adiabatic theorem [242, p. 6]. In the original Born and Fock formulation, the theorem essentially states that a quantum-mechanical

system will remain in its instantaneous eigenstate if it is perturbed slowly enough by a Hamiltonian with a nonzero spectral gap.[1] This condition has been removed, however, in later formulations. One can therefore distinguish between *adiabatic* and *diabatic* processes. In the first case (adiabatic process), the perturbation[2] is applied slowly (compared to the characteristic time scale) so that the system has enough time to adapt to it. In such situations the adiabatic theorem holds and, if the initial state of the system at $t = t_0$ was, for instance, one of the eigenstates of the initial Hamiltonian $\hat{H}(t_0)$, at each subsequent moment of time t the system will be found in the corresponding eigenstate of the Hamiltonian $\hat{H}(t)$. The process described in Fig. 4.3 is an example of the adiabatic process since the gate potential was applied in the distant past ($t \to -\infty$) and at $t = t_0$ we simply calculated the ground state of the system in the presence of the gate. In contrast to this, a rapid change in the external conditions (diabatic process) prevents the system from adapting to it. In this case, the final state, or the eigenstate of the perturbed Hamiltonian $\hat{H}(t)$, does not necessarily correspond to any of the eigenstates of the initial Hamiltonian $\hat{H}(t_0)$. Importantly, in the case of a non-zero coupling term in the Hamiltonian (the hopping γ in the case of the tight-binding chain) the eigenvalues of $\hat{H}(t)$ can not be degenerate and therefore will form an avoided crossing with the variation of the perturbation parameter (the gate voltage $V_{\rm g}$ for the system considered here). In order to illustrate how exactly an avoided crossing occurs, we considered the effect of the gate potential on a simple two-level system (the calculations are presented in Appendix A).

Going back to Fig. 4.3, one immediately notices that when the system is parametrically driven towards the avoided crossing of two eigenvalues, this gives rise to additional low-frequency lines in the dynamical spectrum, described by Eq. (4.7) and Eq. (3.24). Intuitively, this comes from the fact that two eigenvalues e_{m_0} and e_{n_0}, for which $(e_{m_0} - e_{n_0}) \to 0$, produce the frequency $\omega_{m_0 n_0} \equiv (e_{m_0} - e_{n_0})/\hbar \to 0$. As we will demonstrate in the last section of this chapter the presence of the avoided crossings around the Fermi level for certain intermediate $V_{\rm g}$ directly yields an enhanced transmission through the gated wire at low frequencies.

A more detailed spectral analysis is obtained by the two-dimensional discrete Fourier transform (dFT) power portraits of Δs_i^z (see Fig. 4.4) denoted as dFT$[\Delta s_i^z(t)]$ (k, ω). In the top three panels of the figure [Fig. 4.4(a)-(c)], we show the excitation spectra

[1] This means that the energy spectrum of the Hamiltonian is discrete so that there is a gap between the eigenvalue and the rest of the spectrum.

[2] Note that this is an arbitrary perturbation, e.g. it does not necessarily represent small external disturbances in the system as in perturbation theory.

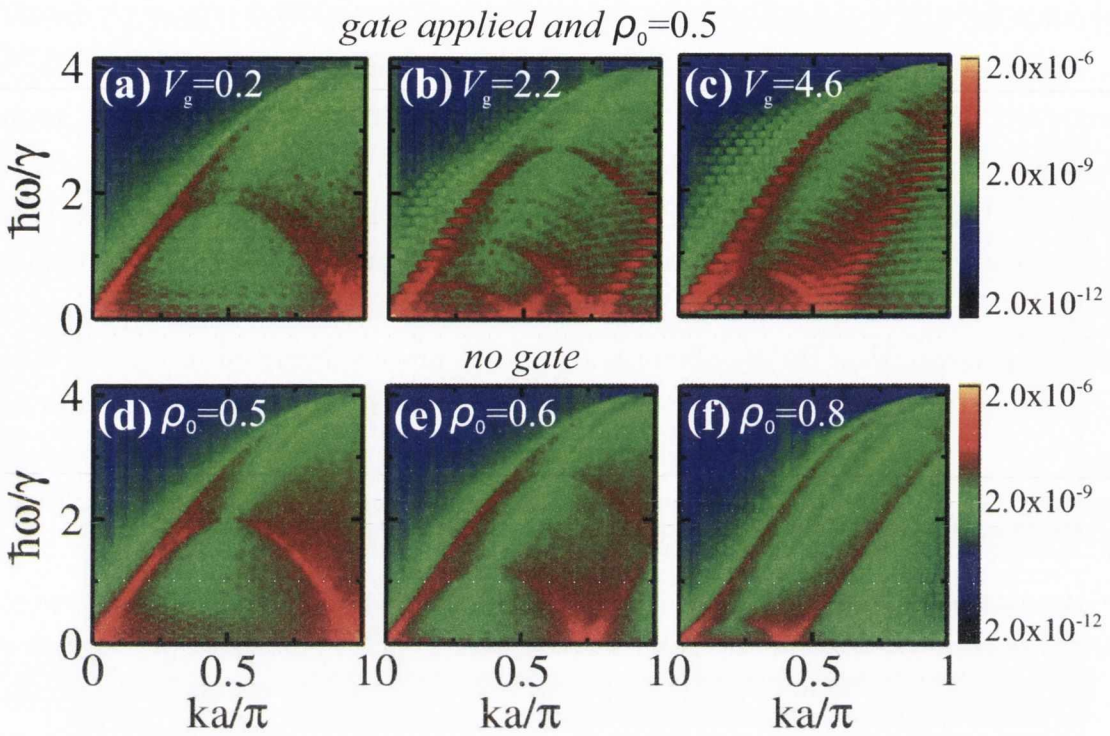

FIGURE 4.4: Top panels: $\mathrm{dFT}[\Delta s_i^z(t)]\,(k,\omega)$ for a fixed band filling, $\rho_0 = 0.5$, and different values of the gate potential, (a) $V_\mathrm{g} = 0.2|\gamma|$, (b) $V_\mathrm{g} = 2.2|\gamma|$ and (c) $V_\mathrm{g} = 4.6|\gamma|$. Bottom panels: $\mathrm{dFT}[\Delta s_i^z(t)]\,(k,\omega)$ for $V_\mathrm{g} = 0$ and different values of the band filling, (d) $\rho_0 = 0.5$, (e) $\rho_0 = 0.6$ and (f) $\rho_0 = 0.8$. The inter-site distance a is arbitrary. The color shade represents the absolute value of $\mathrm{dFT}[\Delta s_i^z(t)]\,(k,\omega)$ and is logarithmically scaled for better contrast.

resulting from spin dynamics in the presence of the gate. The gate potential has been applied to the middle of the chain in the ground state, i.e. $V_\mathrm{g} \sum_{\alpha, i\in[i_1,i_2]} \hat{c}_i^{\alpha\dagger} \hat{c}_i^{\alpha}$ has been added to $\hat{H}_\mathrm{el}$ at $t < t_0$. We use the half-filling case, $\rho_0 = 0.5$, or one electron per atom. The three panels in the bottom of the figure [Fig. 4.4(d)-(f)] show, for comparison, the two-dimensional dFT portraits of spin dynamics in the un-gated chain with frozen impurities for three different values of the band filling (these spectra are practically identical to the ones stemming from the charge-only dynamics, considered in the previous chapter and presented in Fig. 3.6).

As we already discussed in the case of charge-excitations in homogeneous atomic chains, the excitation spectra presented in Fig. 4.4(d)-(f) reveal key feature of 1D fermionic systems that vary systematically with the band filling, in particular, they display a

near-continuum of allowed modes in a certain (k, ω)-space region defined by a low- and a high-energy dispersion functions. Moreover, it is clear from Fig. 4.4 that the effect of the variation of V_g on the excitation spectra is quite similar to the effect of the band filling in the non-gated case. Due to the gate potential, the relative electron populations of the gated and gate-free parts of the chain change as the gated region is depopulated. For intermediate values of V_g [see Fig. 4.4(b)] the excitation spectrum is rather a superposition of two spectra with band fillings below and above 0.5 (approximately 0.2 and 0.6). Furthermore, we find a substantially increased population of the low-frequency modes for all k-vectors, i.e. of the states that are forbidden for $V_g = 0$. For large V_g [see Fig. 4.4(c)] the middle part of the wire becomes almost completely depleted and the (k, ω)-portrait corresponds effectively to the excitation spectrum of a single chain with a band filling $\rho_0 \approx 0.75$, which is similar to the non-gated case presented in Fig. 4.4(f).

4.4 Combined quantum-classical spin dynamics in the presence of a gate

The inclusion of dynamic local spin-impurities in the model requires the numerical integration of the set of coupled non-linear EOMs [see Eq. (4.4)-(4.5)]. For a small number of classical spins the dynamics of the itinerant spin-density is qualitatively very similar to what is described by Eq. (4.7). The frequency-domain analysis of the classical spin trajectories by means of dFT reveals the characteristic signature of the discrete electronic spectrum with only additional modulations in the amplitudes around the Larmor frequency due to precession of the driven local spin, $\boldsymbol{S}_1$. The latter essentially acts as a spin-pump in the system (see cartoon of the model system in Fig. 4.1). We consider now the following situation: the quantum-classical spin system is in its ground state with $\boldsymbol{S}_{1,2} || \hat{\boldsymbol{z}}$ until $t = t_0$, when the first local spin $\boldsymbol{S}_1$ starts fluctuating to form a small misalignment with $\boldsymbol{B} = B\hat{\boldsymbol{z}} = \{0, 0, B\}$, such that $\boldsymbol{S}_1(t_0) \times \hat{\boldsymbol{z}} \approx d\theta \lesssim 5^{\circ}$. This sets the entire quantum-classical spin system into motion. The typical trajectories of the transverse components $S_1^x(t)$ and $S_2^x(t)$ and their frequency-domain dFT images for different values of the gate voltage are presented in Fig. 4.5.

In this case the excitation of a transverse spin-density at $t = t_0$ by the initiation of the Larmor precession is very similar in nature to the excitation induced by tilting one

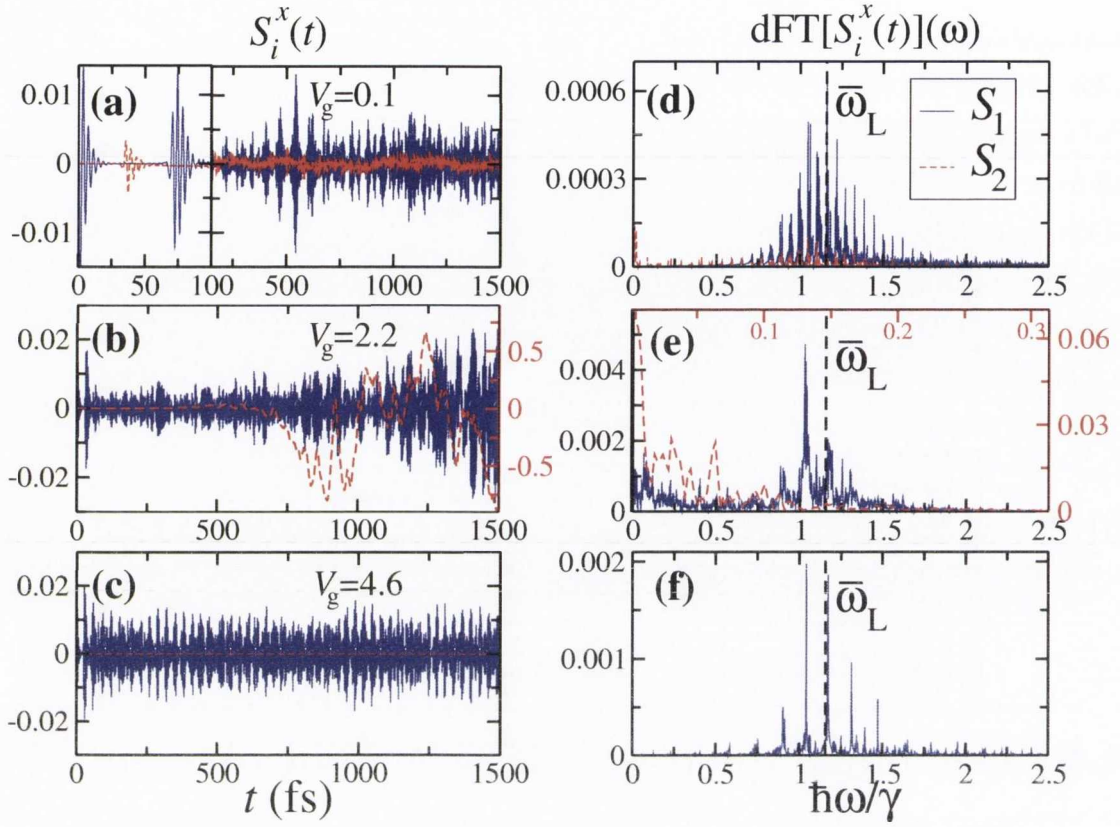

FIGURE 4.5: Time evolution of the x-components of the localized spins, $S_1^x(t)$ (blue) and $S_2^x(t)$ (red) [left] and the corresponding Fourier spectra, dFT$[S_i^x(t)](\omega)$, [right] for three different gate voltages (a, d) $V_g = 0.1|\gamma|$, (b, e) $V_g = 2.2|\gamma|$ and (c, f) $V_g = 4.6|\gamma|$. The frequency-domain is represented by the dimensionless quantity $\hbar\omega/|\gamma|$ and $\bar{\omega}_L = \hbar\omega_L/|\gamma| = 1.16$ for $|\gamma| = 1\ eV$. Note that in the case of $V_g = 2.2|\gamma|$ different scales are used for the magnitudes of $S_1^x(t)$ and $S_2^x(t)$ and their spectra (axes corresponding to $S_2^x(t)$ are marked in red).

local spin investigated before in Section 4.3. In fact, it develops in a very similar way in the early stages of the time evolution. Just like in Fig. 4.2 a non-equilibrium transverse spin-density wave-packet is sent along the wire and both localized spins respond each time the packet reaches them. Figure 4.5(a) displays the case of a very small gate voltage $V_g \ll |\gamma|$. The frequency-domain image of the precessional motion of $S_1^x(t)$ has the signature of the discrete electronic spectrum with an amplitude envelope that peaks at the Larmor frequency $\omega_L = 2\mu_B B/\hbar$. The dFT-portrait of the probe spin $S_2^x(t)$ is very similar to that of $S_1^x(t)$. Although significantly down-scaled in amplitude, it has the electronic-structure modes imprinted in its classical motion in the same way as it is for the driven spin. This qualitative behavior is observed for $V_g = 0$ and a range of small voltages $V_g \leq |\gamma|$ but it changes dramatically for gate voltages $V_g > |\gamma|$ [see Fig.

4.5(b) and (c)]. The case of extremely big voltages $V_g > 4|\gamma|$ (depicted in the bottom panel) is a trivial one for which the electrostatic barrier V_g is completely opaque to the electrons and the probe spin $\boldsymbol{S}_2$ does not respond to the Larmor precession of $\boldsymbol{S}_1$. Note also the rarefaction of modes in the S_1^x spectrum due to the effective shortening of the chain by 2/3.

Special attention must be devoted to the intermediate V_g regime in which the dynamics of the probe spin is qualitatively different and uncorrelated to that of the driven one [see Fig. 4.5(b)]. The typical outcome of the real-time dynamics at such intermediate voltages $|\gamma| < V_g < 4|\gamma|$ is that the probe spin starts accumulating very big transverse deflections. This is then fed back into the pumping spin which also deflects more but still preserves, to a great extent, its precession about the magnetic field.

It is worth noting that this self-amplification of the spin dynamics does not come at a total energy cost, as the model system described by Eq. (4.2)-(4.3) is completely conservative. As such we simply observe a conversion of electrostatic energy into "spin-energy" in the form of transverse (to the driving magnetic field) oscillations in the spin-density. This accumulation is related to the increasing energy transfer from the itinerant electrons to the localized moments, as illustrated in Fig. 4.6(a). Such an energy transfer is defined as $\Delta E(t) = |\Delta E_{\rm el}(t) - \Delta E_{\rm S}(t)|$, where $\Delta E_{\rm el/S}(t) = E_{\rm el/S}(t) - E_{\rm el/S}(t_0)$, $E_{\rm el}(t) = {\rm Tr}[\hat{\rho}(t) \cdot \hat{H}_{\rm el}(t)]$ and $E_{\rm S}(t) = -g\mu_B \boldsymbol{S}_1(t) \cdot \boldsymbol{B}$. The total energy conservation $\Delta E_{el}(t) = -\Delta E_S(t)$ has been verified within a relative error of 10^{-7} %. The amplification of the energy transfer is characteristic of this V_g range ($|\gamma| < V_g < 4|\gamma|$) [see the inset of Fig. 4.6(a)]. This effect can appear as a particular form of "heating" for the local spins, at the expense of electron gas, as within the time covered by the simulation ($\approx$ 10 ps) the energy transfer seems to be irreversible. It is well-known that the typical Ehrenfest molecular dynamics (EMD) suffers from the inability to account for Joule heating processes [101] due to the lack of dynamical correlations between the electrons and the ions. It is not clear, however, whether this is the case for spin dynamics. Our simulations are limited to picosecond times and by no means imply a possible qualitative difference of the EMD and its spin counterpart.

The frequency-domain image of the localized spin trajectories [see Fig. 4.5(e)] for $|\gamma| < V_g < 4|\gamma|$ shows a substantial qualitative difference for the driven and the probe spins. While around $\omega_{\rm L}$ the shape of the spectrum of $\boldsymbol{S}_1$ is similar to the two extreme V_g cases, a significant amplitude is accumulated now at low frequencies. The main difference from the small V_g case, however, is in the spectrum of $\boldsymbol{S}_2$ which shows practically no

response at the Larmor frequency but has very large amplitudes in the low frequency range.

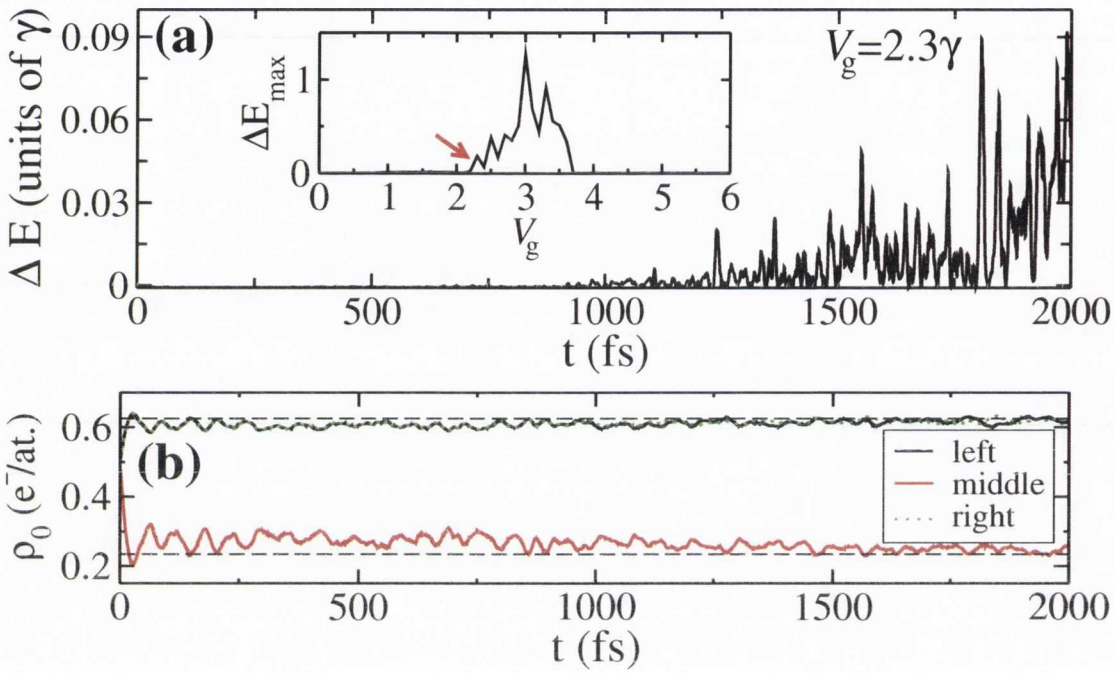

FIGURE 4.6: (a) Time evolution of the energy transfer, $\Delta E(t)$, between electronic and localized spins for $V_g = 2.2|\gamma|$. The inset shows the maximum value of the energy transfer, ΔE_{max}, for a fixed duration of simulation (2 ps) as a function of V_g. A red arrow indicates the particular voltage for which $\Delta E(t)$ is plotted. (b) Evolution of the electron populations of different parts of the chain for $V_g = 2.2|\gamma|$. The two black dashed lines show the equilibrium populations of the gate-free parts (upper line) and of the gated middle section (lower line), i.e. the populations corresponding to the case when the gate is applied in the ground state.

This behavior in the classical spin dynamics, characteristic of certain gate voltages, stems from the dominance of the low frequency modes in the electron dynamics at those V_g. The effect can be seen also in the much simpler case of a non-spin-polarized uniform atomic wire subjected to an electrostatic gate applied in the middle. In the next section we will consider the charge dynamics associated with this situation and analyze the lowest frequency components entering Eq. (3.24) [see previous chapter]. The initial charge excitation, similarly to the transverse spin polarization in the model above, is triggered by a local electrostatic perturbation at the first site. It follows from Eq. (3.24) that, for certain values of V_g for which two adjacent adiabatic eigenvalues (e_m, e_{m+1}) around the Fermi level come closer to each other in an avoided crossing, the dynamical charge amplitude at the opposite end of the wire exhibits a peak at that particular very low frequency $(e_m - e_{m+1})/\hbar$. In other words, at a certain gate voltage

a condition is created for resonant charge transfer between the three parts of the chain at low frequencies. This, in the case of itinerant transverse spin-polarization, promotes the enhanced reaction of the probe spin to the spin pumping produced on the other side of the gate.

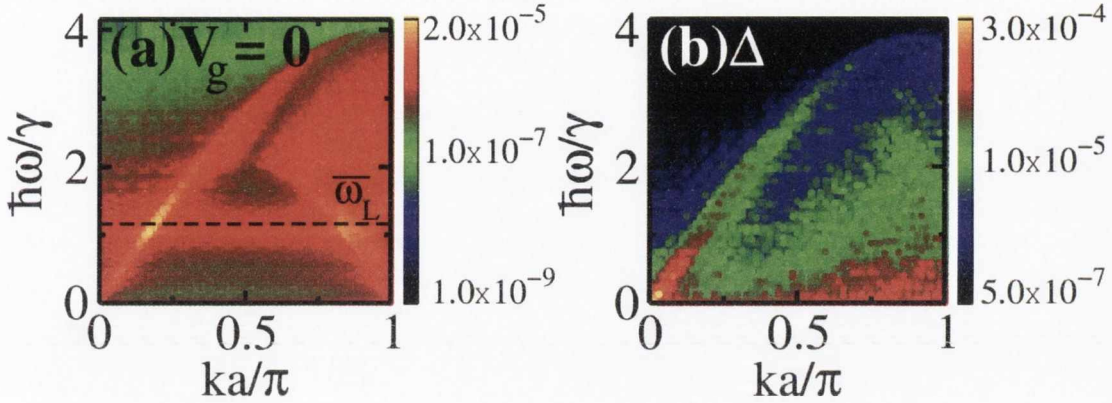

FIGURE 4.7: (a) $\mathrm{dFT}[\Delta s_i^x(t)](k,\omega)$ for V_g=0. (b) The difference between $\mathrm{dFT}[\Delta s_i^x(t)](k,\omega)$ for V_g=2.2$|\gamma|$ and for V_g=0, defined as $\Delta = |\mathrm{dFT}[s_i^x(t)](k,\omega)_{V_g=2.2|\gamma|} - \mathrm{dFT}[s_i^x(t)](k,\omega)_{V_g=0}|$. The color shade represents the absolute value of $\mathrm{dFT}[\Delta s_i^x(t)](k,\omega)$ and Δ, respectively, and is logarithmically scaled for better contrast.

The electronic part of full quantum-classical spin dynamics in the presence of the gate is shown in Fig. 4.7. As before we construct the two-dimensional dFT portraits of the spin-density evolution. Providing additional k-resolved information, these give another perspective for interpreting the dramatic increase of the low-frequency oscillations of the probe spin at certain gate voltages, when compared to the case of the frozen local spins and electrons relaxed at $t = t_0 - \delta t$ to the external gate potential (Fig. 4.4). In the latter case, the increased low-frequency occupations (with respect to the non-gated case) were attributed to the split of the 1D system into subsystems with different average electron densities. Here we find a similar pattern, now in the presence of dynamically-coupled local spins and a gate abruptly introduced at $t = t_0$. Those two additional time-dependent factors result in a significant variation in time of the electron distributions in the gated and non-gated segments of the chain [see Fig. 4.6(b)]. The dFT image in this case can be interpreted as a superposition of spectra corresponding to different ρ_0, resulting in a smearing of the low-frequency structure previously present in the (k,ω)-space image. A comparison of the results for $V_g = 0$ and $V_g = 2.2|\gamma|$ is presented in Fig. 4.7. We find that the full dynamical portrait in the case of $V_g = 0$ is rather similar to the results obtained for frozen-impurities (see Fig. 4.4), the only

additional feature being the excitations at the Larmor frequency [see the bright feature corresponding to $\bar{\omega}_{\mathrm{L}}$ in Fig. 4.7(a)]. The difference (point-by-point subtraction of the contour plots) with the corresponding gated case, depicted in Fig. 4.7(b) shows that it is indeed mainly the lower frequency band of the spectrum, for any wave-vector, that gains occupation in the gated case.

4.5 Analysis of dynamical amplitudes

In this section we further illustrate the direct link between the modification of the energy-spectrum of the itinerant electrons Hamiltonian due to the applied gate potential and the enhanced spin transfer along the chain for particular range of gate voltages. We consider the eigenstate-resolved dynamical amplitude A^i_{mn} corresponding to a mode with frequency ω_{mn}, associated to the transitions between the eigenstates e_m and e_n. The system is the simplified wire used for the spectroscopic analysis presented in Fig. 4.3, i.e. it is a non-spin-polarized 30-sites long chain. The excitation is applied at $t = t_0$ simply as a potential shift at the first atomic site. From Eq. (3.24) the dynamical amplitude at site i is defined as

$$A^i_{mn} = c_{im} c^*_{in} \sum_{kl} c^*_{km} c_{ln} \rho_{kl}(t_0) \,, \tag{4.10}$$

such that

$$\rho_{ii}(t) = \sum_{mn} e^{-i\omega_{mn} t} A^i_{mn} \tag{4.11}$$

is the electron occupation at site i. This quantity is calculated at the last site, $i = N$, i.e. at the opposite side of the chain with respect to the perturbation. In Eq. (4.10) $c_{in} = \langle i|\varphi_n\rangle$ are on-site projections of the eigenvectors $|\varphi_n\rangle$ of the non-spin-polarized Hamiltonian $\hat{H}_{\mathrm{el}}(V_{\mathrm{g}})$ for which the gate voltage V_{g} is applied between the sites i=11 and i=21. Note that, in contrast to the spin-polarized case, there is no need for additional spin-indices in the expression for dynamical amplitudes, and we now use the upper index to denote a particular site along the chain at which the corresponding electron charge-density is calculated [see Eq. (4.10)].

From all the pairs of adjacent eigenstates (e_m, e_{m+1}), which give rise to the lowest frequency modes $\omega_{m,m+1} = (e_m - e_{m+1})/\hbar$ in the dynamics, we identify in Fig. 4.8 those which have the highest (in absolute value) amplitude $A^N_{m,m+1}$. For small gate

voltages these are the eigenstates around the Fermi level but as V_g increases the modes with the largest amplitudes tend to arise where avoided crossings of eigenstates occur. These are also the modes with frequencies close to the lowest possible frequency for that particular gate voltage.

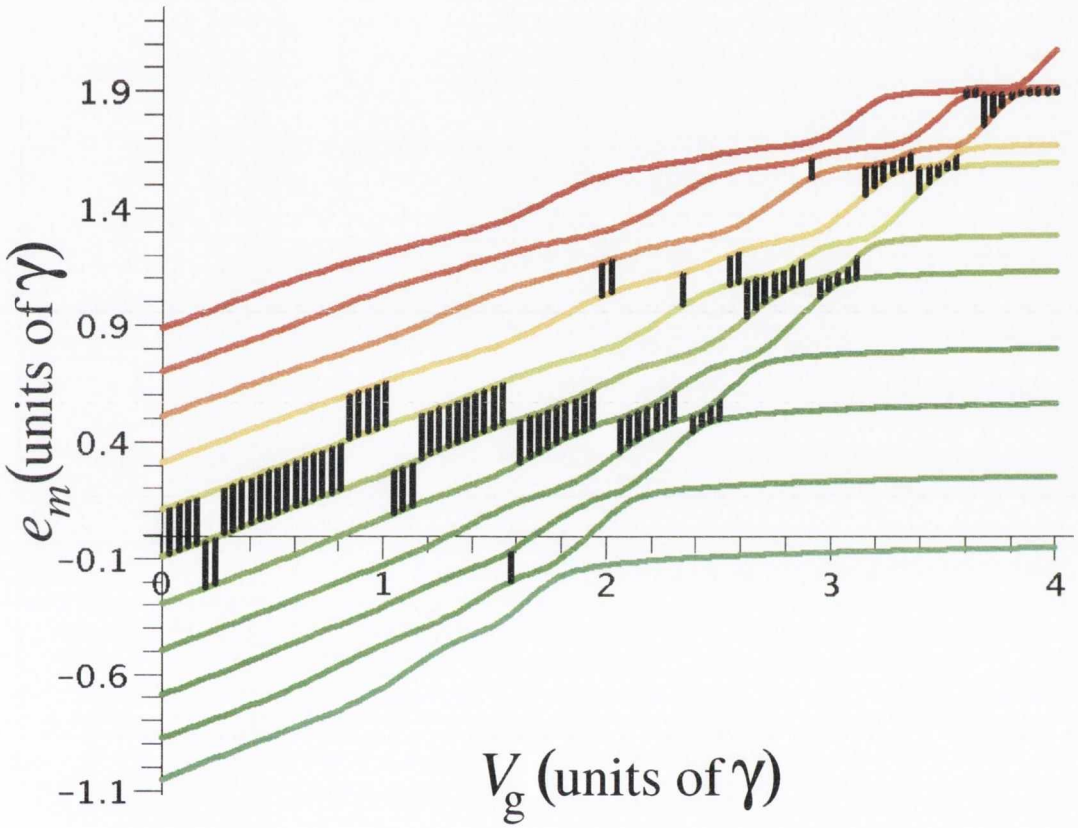

FIGURE 4.8: Adiabatic variation with the gate voltage of a few eigenvalues around the Fermi level (we have used $\varepsilon_0 = 0$ and $|\gamma| = 1\,\text{eV}$, hence $E_F = 0$ at $V_g = 0$). Marked with black lines are the pairs of eigenstates (e_m, e_{m+1}) which give rise to the highest (in absolute value) dynamical amplitude $A^N_{m,m+1}$ at the last site N.

The actual highest amplitude at the last site, corresponding to the highlighted modes in Fig. 4.8, are depicted as a function of V_g in Fig. 4.9(a), together with the quantity $A^N_{\text{sum}} \equiv \sqrt{\sum_m (A^N_{m,m+1})^2}$. This represents the pessimistic estimate (considering all modes orthogonal in phase) of the total low-frequency amplitude corresponding to all pairs of adjacent eigenvalues. Such curves demonstrate the resonant nature of the dynamical site-occupation as a function of the gate voltage. Figure 4.9(a) also shows that the low frequency charge excitation peaks for intermediate gate voltages (for this case $V_g \sim 2.5\ |\gamma|$) can be related to the observed enhanced low-frequency coupling between

the itinerant and localized spins for the intermediate V_g range. Interestingly, the two $A(V_g)$ curves coincide for very low and very high voltages, showing that in this case the entire dynamics is practically due to just one mode (marked in black in Fig. 4.8). In the intermediate regime it is clear that there are more than one low-frequency modes which have a significant amplitude, although the one marked in Fig. 4.8 gives the leading contribution.

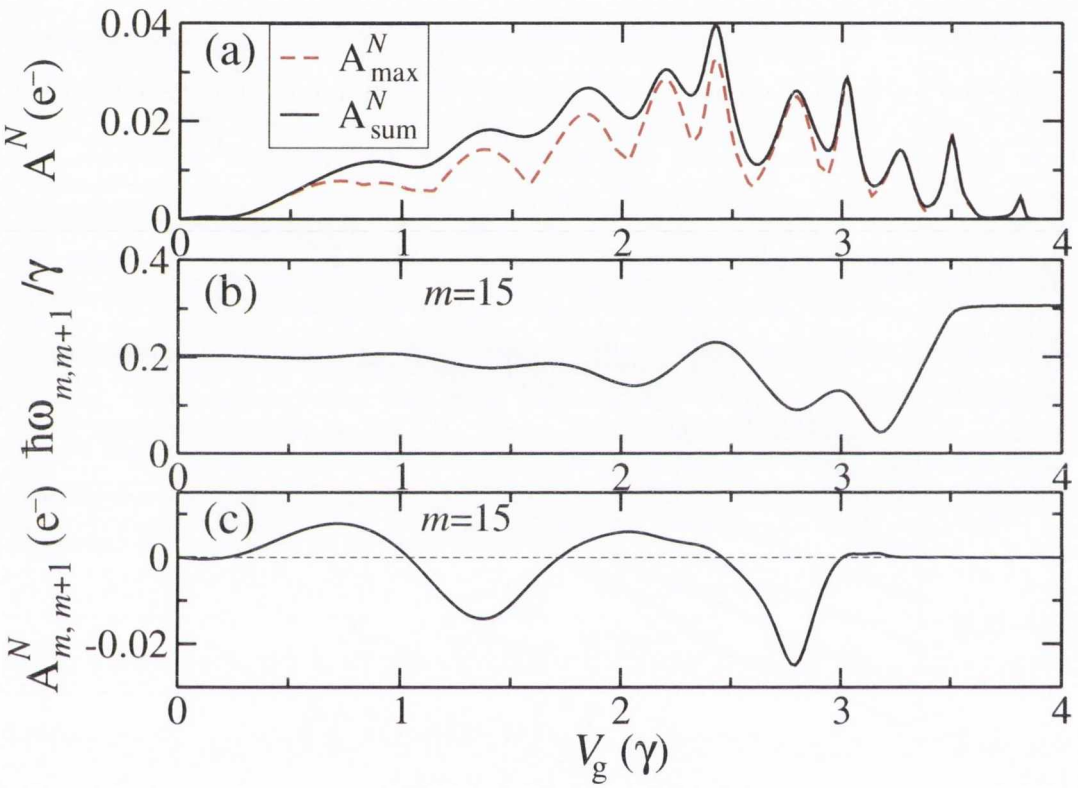

FIGURE 4.9: (a) The maximum single-mode amplitude A^N_{max} and an estimate for the total low-frequency amplitude A^N_{sum} (see text for details) as a function of the applied gate voltage. (b) The frequency of the mode related to the pair of eigenstates ($m = 15$) around the Fermi level, adiabatically evolved with the gate voltage, and (c) its corresponding amplitude as defined in Eq. (4.10).

For a particular pair of adjacent eigenstates there are a few instances where the adiabatic eigenvalues come closer together as a function of the gate voltage. In Fig. 4.9(b,c) we analyze the dependence of the frequency and the amplitude corresponding to the pair of eigenvalues just below and above the Fermi level in the ground state ($m = 15$ for the 30-sites long chain at half-filling). We find that the dynamical charge amplitude on the last site peaks (as absolute value) every time the frequency passes through a minimum.

4.6 Summary

In this chapter we have employed atomistic simulations of spin-dynamics (quantum-classical Ehrenfest dynamics) to investigate the effect of an electrostatic gate as a mean for controlling the indirect coupling between two distant localized spin-impurities in a finite one-dimensional wire comprising one hundred atoms. One of the impurities, precessing in external magnetic field, plays the role of a spin-pump and the response of the second (probe) spin was analyzed as a function of the gate potential applied to the interconnecting wire. We identified a range of external gate potentials for which the spin-pumping is extremely efficient and leads to a substantial excitation of transversely-polarized itinerant spin-density in the non-gated parts of the chain. This, in turn, produces a massive low-frequency swing of the probe spin. Such a resonant effect has been related to gate-induced avoided crossings in the electronic structure of the interconnect. For certain gate voltages these occur in the vicinity of the Fermi level and assist the enhanced transfer of charge/spin across the barrier. Evidences for this effect are also identified in the Fourier portraits of the calculated time-dependent spin-distributions.

Chapter 5

Time-dependent electron transport at the atomic scale: theoretical framework

5.1 Introduction

In the first part of this Thesis (Chapters 2–4) we focused on the investigation of spin dynamics in finite atomic-scale systems. The electronic structure of our model systems was described by a tight-binding (TB) Hamiltonian while the information about the dynamics was obtained by integrating the Liouville-von Neumann equation. This scheme has the basic ingredients of a fully atomistic approach and is capable of adequately describing the time evolution of a spin system at the atomic scale. However, in its present form it describes perfectly conservative dynamics and, therefore, is only applicable to *closed* systems.[1] An interaction with the environment was incorporated in the model in the form of an external perturbation, introduced simply as an initial condition for the time-dependent equations of motion and used to drive the system out of equilibrium.

[1] According to the thermodynamic definition, a closed system does not exchange particles with the environment but is allowed to exchange energy and, therefore, it can be subject to deterministic external forces. Systems which do not exchange particles nor energy with their surroundings are called *isolated*. In this sense, the systems we considered in the previous chapters are closed but not isolated since we included interaction with an external magnetic field.

Physical systems, however, are never truly closed and in reality one deals with *open* systems, which exchange energy and particles with their surroundings. An example of a physical process, in which the system interacts dynamically with the environment, is the *electronic transport*. In fact, investigation of various properties of materials and structures in the presence of electric currents is of great practical importance.

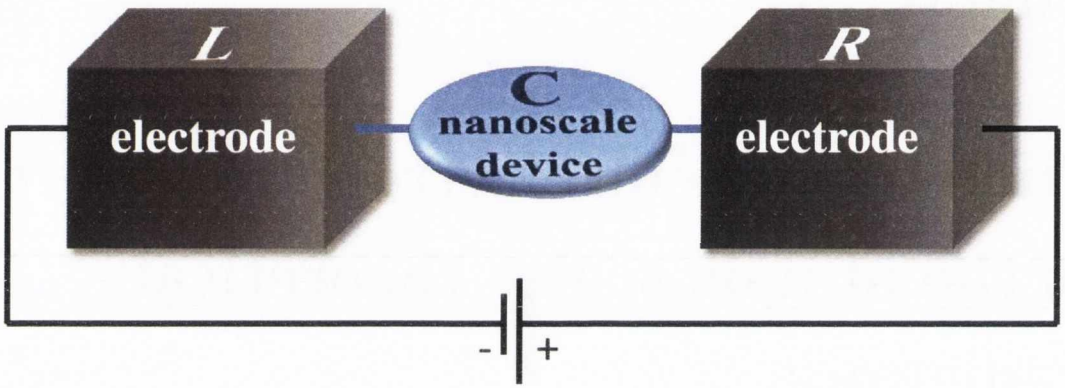

FIGURE 5.1: Schematic of a typical electronic transport setup: a central region, representing a nanoscale object, is sandwiched between two macroscopic electrodes attached to a battery.

The ever improving ability to fabricate and manipulate nanoscale systems with unprecedented level of control, has enabled the study of electronic transport at the nanometer and sub-nanometer length scale. A typical experimental setup consists of a central nanoscopic region attached to two or more macroscopic electrodes (leads), as shown schematically in Fig. 5.1. Examples of structures, which can represent the central region and have been studied experimentally, include quantum point contacts [260], nanowires [51], quantum dots and multi-dot systems [11], nanotubes [36] and molecules [188]. With the advance of a new field of molecular electronics [50], the latter are envisioned as active components in novel electronic devices.

Investigations of electronic transport through nanoscale objects have led to the discovery of a variety of new phenomena. At a fundamental level, the physical properties of such reduced-dimensional systems are dominated by quantum effects, among them electron correlations, which strongly affect the electronic transport. This is reflected in the term *quantum transport*, which is typically used to describe the motion of electrons through constrictions with transverse dimensions smaller than the electron wavelength. One of the hallmarks of quantum transport is single-electron charging which has been observed, for example, in tunnel spectroscopy of few-electron quantum dots [140]. Novel

topics, which are attracting particular attention at the moment, include STM studies of few-atom clusters [97], Coulomb blockade and Kondo-type physics, manifesting themselves in transport properties of quantum dots and single molecules [49, 79, 154].

The experimental advances have been accompanied by significant progress in theoretical understanding of electronic transport at the nanoscale [217, 220]. Apart from the fundamental interest in the fascinatingly rich physics that occurs at this length scale, the main objective here is to develop theoretical methods capable of accurately describing and, ultimately, predicting the properties of realistic current carrying devices. This is, however, a remarkable theoretical challenge. In order to build efficient computational tools for calculating electronic transport in real devices, one needs to combine advanced algorithms for modeling quantum transport with state-of-the-art electronic structure methods [209]. Ideally, such tools should be able to describe inelastic effects and treat systems with strong electron-electron interactions as these are now intensively studied experimentally [89, 97]. The ability to deal with spin-dependent problems is also crucial in view of the great interest in electronic transport through magnetic materials [211]. Another important requirement is computational feasibility which is necessary to simulate large systems.

5.2 Formulation of the electronic transport problem

In general, electronic transport is a nonequilibrium many-body problem, which is practically impossible to solve exactly even for simplest models [187]. Over the years, many approaches to the electronic transport problem have been proposed, based on a certain number of approximations and assumptions [217]. Typically, one is interested in the situation sketched in Fig. 5.1, where the central region is bridging two metallic electrodes attached to an external battery. The generation of electric current in such a structure relies on the battery, a device that continuously charges the surfaces of the electrodes by means of some alternative, for instance internal chemical, process. Hence a potential difference can be applied at the contacts between the electrodes and the battery, enabling the electric current to flow across the structure, from one electrode to the other.

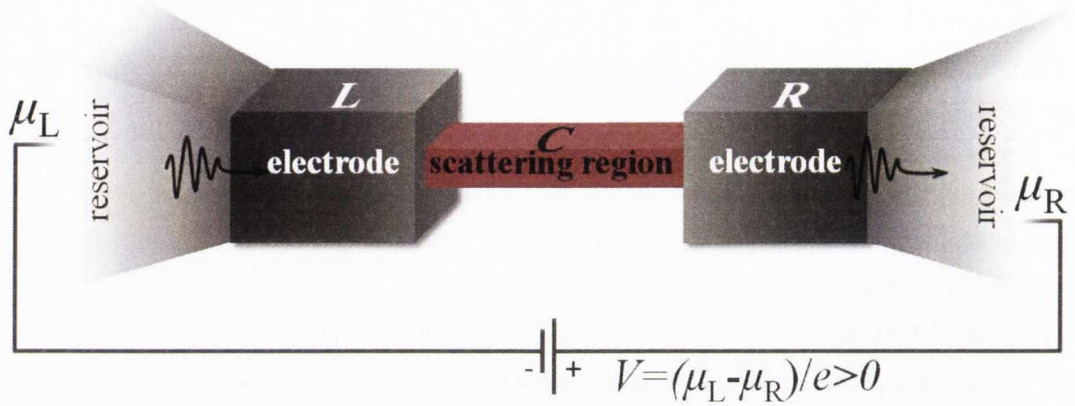

FIGURE 5.2: Typical interpretation of the electronic transport problem: an *open* system consisting of a scattering region bridging two electrodes, which are connected to external reservoirs. Each reservoir is kept at a fixed chemical potential ($\mu_L > \mu_R$ for the sake of definiteness), thus acting as an external battery. A positive bias voltage arises from the difference in the chemical potentials, e.g. $V = (\mu_L - \mu_R)/e$.

The majority of currently used theoretical approaches to electronic transport are based on the assumption that the battery can be considered as a *reservoir* of electrons (see Fig. 5.2), i.e. it is an ideal system that can supply and receive carriers and energy without the change of its internal state [57].[2] The concept of a reservoir is similar to that of a thermostat in statistical physics. One further assumes that the reservoirs connected to the right and to the left electrode, representing the negative and the positive poles of the battery, are kept at different chemical potentials, μ_L and μ_R, respectively.[3] Thus the potential difference between the electrodes (bias), giving rise to the charge flow across the device, can be defined as $V = (\mu_L - \mu_R)/e$. This idea is typically attributed to Landauer [110, 150, 151].

Furthermore, one can divide the methods dealing with the generic problem depicted in Fig. 5.2 into two main categories, namely, steady-state approaches and time-dependent schemes. The methods which belong to the first class are based on the assumption that the system, driven out of equilibrium by applied bias voltage, always evolves towards the steady state. The steady-state current can be then calculated as a balance

[2] Another possibility to model a current flow through the device depicted in Fig. 5.1 is to consider the electrodes as oppositely charged plates of a capacitor [57, 219]. As the capacitor discharges, the electric current flows through the device. However, in the limit of infinitely long plates (electrodes) one can expect the steady-state current to be established.

[3] Note that, in principle, the chemical potential is defined strictly in thermal equilibrium. The applicability of this concept to the nonequilibrium situations is not straightforward and has been discussed in the literature [32, 57, 120].

of currents entering and leaving the central (scattering) region using different techniques [220]. One of the most popular among the many others is the nonquilibrium Green's function (NEGF) technique. NEGF, combined with *ab initio* electronic structure methods, provides a theoretical foundation for the majority of state-of-the-art electronic transport codes [210].

A well-known conceptual framework for establishing the steady-state transport has been proposed by Caroli *et al.* [40, 41, 42, 48]. In this so-called "contacting approach" the electrodes are disconnected from the scattering region in the remote past and are in equilibrium at two different chemical potentials. The coupling between the electrodes and the device is then switched on adiabatically, allowing the system to evolve towards the steady state. This formal approach has been used in the formulation suggested by Jauho, Wingreen and Meir [174, 271]. The authors derived a general and, in principle, exact expression for the nonequilibrium current through an interacting system attached to semi-infinite non-interacting reservoirs in terms of nonequilibrium Green's functions (we will recall this result in Section 5.4). An alternative scheme, which can be used for time-dependent simulations of transport [144], has been introduced by Cini [45], who considered the electrodes and the scattering region as being connected and in equilibrium in the remote past. The system is then driven out of equilibrium by a perturbation in the form of an external scalar potential. It has been shown in Ref. [233] that for non-interacting systems, the "contacting approach" and the Cini scheme lead to the same steady state and that in the case of time-independent (dc) potentials the steady-state current does not depend on the history of the applied bias.

The second group of methods, e.g. methods that use explicitly time-dependent equations to describe the evolution of current carrying systems, is much more restricted. The main difficulty in approaching the time-dependent electronic transport problem stems from the fact that the steady-state techniques are not easily transferable to time-dependent situations and essentially new concepts and theoretical formulations must be developed. These, however, have been attracting increasing attention due to their ability to provide information about the behavior of open systems, which is not accessible by standard steady-state approaches [219]. This includes the description of transient regimes, i.e. the dynamical paths leading to the steady state, and response to time-dependent perturbation, for instance, to applied ac bias voltage. Time-dependent approaches also appear to be the only appropriate tools in situations when the establishment of the steady-state regime itself is questionable [145].

From a more formal point of view, dynamical simulations provide a natural platform for investigating electronic transport. In fact, the application of steady-state methods, such as those combining static DFT with the NEGF approach, to intrinsically time-dependent phenomena have been criticized on fundamental grounds [133]. To date, several schemes for time-dependent simulations of transport in nanoscale conductors have been proposed. These include model studies [58, 192, 196, 219, 282] and *ab initio* based formulations, such as TDDFT for open systems [15, 233, 280].

In this chapter we present an implementation of a recently proposed *multiple-probe battery* (MPB) approach [171] to electronic transport, which offers an explicit realization of an external battery. In practice, this is achieved by introducing the coupling between the electrodes and a large number of external *probes*, or reservoirs, which are in equilibrium at fixed chemical potentials. This setup provides the possibility of constructing a steady-state formalism, which gives a controllable approximation to the results obtained within the NEGF framework with semi-infinite electrodes. However, the main advantage of the MPB method is that it allows one to derive an effective quantum Liouville equation with explicit open-boundary terms, which account for the exchange of charge carries and energy between the system and the external reservoirs (battery).

Before setting up a theoretical framework for this approach, we will discuss, in the following sections, some of the relevant topics of general transport theory. In particular, a brief overview of the main results of the Landauer approach [35], a cornerstone of quantum transport theory, and the basic concepts of the NEGF formalism [90] will be given.

5.3 Landauer approach to steady-state transport

A traditional viewpoint on the electric current as a response of a conductor to an applied electric field is shared by many approaches, starting from the classical Drude model [10, p. 7] and the semi-classical Boltzman equation (see Chapter 1 in Ref. [90]) to the famous linear-response Kubo formula [143]. An alternative way of looking at the electronic transport problem, formulated by Landauer [150], is to consider electron conduction as a scattering process that the indecent carrier flow undergoes inside the sample (device). Hence the conductance is associated with the quantum-mechanical

probability for charge carriers to be transmitted across the device. The main advantage of this approach is that the problem of nonequilibrium electronic transport is essentially mapped onto a time-independent scattering problem.

The system considered in the Landauer approach is similar to the one depicted in Fig. 5.2. The reservoirs, connected to the electrodes L and R, are in equilibrium with chemical potentials μ_{L} and μ_{R}, respectively, and are populated according to the corresponding Fermi-Dirac distributions. The latter are given by the following expression for $\alpha = \mathrm{L}, \mathrm{R}$

$$f_\alpha(E) = \frac{1}{e^{(E-\mu_\alpha)/k_{\mathrm{B}}T} + 1} \ , \tag{5.1}$$

where $k_{\mathrm{B}} \approx 8.617 \ \mathrm{eV\,K^{-1}}$ is the Boltzmann constant. Importantly, the reservoirs are assumed to be totally reflectionless and phase-breaking. This means that they supply electrons into the leads according to the distributions $f_\alpha(E)$ and absorb electrons, completely destroying their quantum-mechanical phases, while being unaffected by both processes. Thus the reservoirs simply act as sources of right- and left-going electrons, which are injected *infinitely* far into L and R at local equilibrium distributions $f_{\mathrm{L}}(E)$ and $f_{\mathrm{R}}(E)$, respectively.

The electrodes are modeled as *ballistic*, e.g. scattering-free, conductors by assuming that their characteristic length l is much smaller than the electron mean free path l_{mfp} ($l << l_{\mathrm{mfp}}$). Another important assumption of the Landauer approach is that of the non-interacting electrons. This allows one to formulate the conduction problem in terms of incoming and outgoing single-electron wave functions, which propagate in the electrodes and are scattered elastically by the potential in the central region. In the simplest case of a one-dimensional system one can consider the wave functions as Bloch waves propagating along a one-dimensional wire, or a *scattering channel*. In the absence of a scattering potential and of spin polarization the conductance of such system is given by

$$G_0 = \frac{2e^2}{h}, \tag{5.2}$$

where G_0 is usually called *the conductance quantum*. This is one of the fundamental results of the Landauer approach, which means that the finite conductance emerges even in the case of ballistic electrodes and perfectly transmitting device.

In systems of higher dimensions one faces a multi-channel problem since several possible waves with the same energy can propagate in the electrodes. In principle, each scattering state i originating from the left electrode can be transmitted into a state j in

the right electrode and vice versa. By calculating the total current through the system as a balance between currents originating from the left and from the right electrode, we obtain

$$I = \frac{2e}{h} \int_{-\infty}^{+\infty} [T_{\mathrm{LR}}(E) f_{\mathrm{L}}(E) - T_{\mathrm{RL}}(E) f_{\mathrm{R}}(E)] \, dE, \tag{5.3}$$

where T_{LR} and T_{RL} are the total transmission probabilities for the right-going and the left-going electrons, respectively. These are defined as

$$T_{\mathrm{LR}}(E) = \sum_{i=1}^{M_{\mathrm{L}}} \sum_{j=1}^{M_{\mathrm{R}}} T_{ij}(E), \tag{5.4}$$

$$T_{\mathrm{RL}}(E) = \sum_{i=1}^{M_{\mathrm{R}}} \sum_{j=1}^{M_{\mathrm{L}}} T_{ij}(E), \tag{5.5}$$

where the summation is performed over all available scattering channels in the left and in the right electrodes (M_{L} and M_{R}, respectively) and $T_{ij}(E)$ denotes the probability for the wave with initial momentum k_i to be transmitted across the central region into the final state with momentum k_j at the same energy E. Assuming that $T_{\mathrm{LR}}(E) = T_{\mathrm{RL}}(E) = \mathcal{T}(E)$ (a condition for the conservation of the carrier flux[4]) we arrive at the final expression for the current

$$I = \frac{2e}{h} \int_{-\infty}^{+\infty} \mathcal{T}(E) \, [f_{\mathrm{L}}(E) - f_{\mathrm{R}}(E)] \, dE. \tag{5.6}$$

In the linear response regime, e.g. for $(\mu_{\mathrm{L}} - \mu_{\mathrm{R}}) \to 0$, and in the zero-temperature limit, we find that $I = GV$ with conductance $G = 2e^2\mathcal{T}/h = G_0\mathcal{T}$, where $\mathcal{T}$ is evaluated at the Fermi energy of the electrodes (E_{F}) at equilibrium since the two chemical potentials differ negligibly from each other and from E_{F}, e.g. $\mu_{\mathrm{L}} = E_{\mathrm{F}} + \epsilon$ and $\mu_{\mathrm{R}} = E_{\mathrm{F}} - \epsilon$ with $\epsilon \to 0$.[5]

The Landauer approach has been very successful in describing many fundamental phenomena in nanoscale transport, such as conductance quantization. As was demonstrated, for instance, in the well-known experiment by van Wees *et al.* [260], the conductance of a quantum point contact, created by confining a two-dimensional electron gas with the help of local gate-electrodes, exhibits steps which are nearly perfect integer-multiples of G_0. The fact that one can use the Landauer formula to describe the electronic transport in this quantum system suggests that it indeed behaves like

[4] This is always satisfied if the system possesses time-reversal symmetry.

[5] Note that for non spin-degenerate systems the expression for conductance G will contain an additional factor 1/2.

a ballistic conductor and that the scattering events take place mainly at the potential barriers created by the local gates.

However, this single-particle scattering approach has its limitations. First of all, the Landauer formula does not offer an explicit expression for the transmission coefficient but only suggests that there is a direct link between current and transmission. Moreover, the Landauer approach is, in principle, applicable only to non-interacting systems, or effectively to interacting systems described at the mean-field level. In order to include the interactions in a systematic way, advanced approached such as NEGF are needed.

Note that a phenomenological way of describing inelastic (phase-breaking) effects in the electron conduction within the scattering theory was suggested by Büttiker [34]. In his approach the inelastic scattering events are simulated by attaching extra electrodes (voltage-probes) to the central region, in addition to a pair of electrodes between which the current flows (current-probes). These voltage-probes are connected to the corresponding reservoirs, kept at fixed chemical potentials. Although the voltage-probes do not affect the total current, they introduce some randomness in the phases of the electron wave functions, which tends to break the phase coherence. Hence the current through the entire structure will have a coherent component, corresponding to the current generated by the current-probes, and the incoherent component due to the interaction with the voltage-probes.

5.4 Nonequilibrium Green's function formalism

In classical physics and mathematics Green's functions is a tool for solving inhomogeneous linear differential equations of the form $\mathcal{L}f(x) = s(x)$, where $\mathcal{L}$ is a linear differential operator, $s(x)$ is an inhomogeneity, or a source term, $f(x)$ is an unknown function with x representing a variable or a set of variables. The Green's function (GF), $\mathcal{G}(x, x')$, of a linear operator, $\mathcal{L}$, satisfies, at a point x', a differential equation with a singular inhomogeneity, which reads

$$\mathcal{L}\mathcal{G}(x, x') = \delta(x - x'), \tag{5.7}$$

where δ is a Dirac delta function. The solution for the function $f(x)$ can be then written in terms of the GF and the source term, namely

$$f(x) = \int \mathcal{G}(x, x')s(x')dx'. \tag{5.8}$$

The GF defined in this way allows one to calculate the response of the system at a point x to a perturbation produced at a point x'. Since each operator $\mathcal{L}$ admits a GF, one can also think of the GF as the inverse of $\mathcal{L}$, e.g. $\mathcal{G} = \mathcal{L}^{-1}$.

Similarly, one can introduce the Green's functions in quantum mechanics as an alternative way of solving the Schrödinger equation [Eq. (2.23)]. These Green's functions provide a versatile tool for evaluating the properties of generally interacting systems both in thermal equilibrium and under nonequilibrium conditions. The nonequilibrium version of the formalism (NEGF) [119, 125] has become a popular method for calculations of quantum transport, in particular for system such as the one depicted in Fig. 5.2. One major advantage, offered by the NEGF method, is the possibility of mapping the infinitely long electrodes in the Landauer setup onto a finite sub-space of the system. Moreover, many-body effects such as electron-electron and electron-phonon interactions, may be included in a systematic way within the NEGF formalism via perturbative techniques [187].

We note, however, that the rigorous definition of the equilibrium GFs and their extension to out-of-equilibrium situations is a subtle and mathematically complex subject [165]. For this reason in the following sections we will only introduce the basic concepts of the NEGF formalism (omitting some important derivations) and its application to the steady-state transport problem [209].

5.4.1 Definitions

Following Ref. [166, p. 71] and [90, p. 38], we start with the formal definition of a time-ordered (causal) single-particle GF

$$G(\boldsymbol{r}, t; \boldsymbol{r}', t') = -\frac{\imath}{\hbar} \left\langle |T[\psi(\boldsymbol{r}, t)\psi^{\dagger}(\boldsymbol{r}', t')]| \right\rangle , \tag{5.9}$$

where $\psi^\dagger(x,t)(\psi(x,t))$ is a field operator[6] which creates (destroys) a particle at the position $\boldsymbol{r}$ and time t, and T is the time-ordering operator, or Wick's operator for fermions [see the definition in Eq. (2.31)]. For $t' > t$ the GF, defined by Eq. (5.9), gives the probability amplitude that at time t' a particle is created at position $\boldsymbol{r}'$ while at time t a particle is destroyed at position $\boldsymbol{r}$, or in other words that the system is propagated from the point $(\boldsymbol{r}, t)$ to the point $(\boldsymbol{r}', t')$. We will now clarify the meaning of the bra- and ket-vectors in Eq. (5.9).

In equilibrium and at zero-temperature $|\rangle$ represents the exact ground state $|\Psi_0\rangle$ of a fully interacting system described by the Hamiltonian $\hat{H}$, e.g. $\hat{H}\,|\Psi_0\rangle = E\,|\Psi_0\rangle$. At finite temperature one needs to express the GF in terms of the density matrix operator $\hat{\rho}$, defined as a statistical operator in the canonical or the grand canonical ensemble [see footnote in Eq. (2.41)]. In this case $\langle|\cdot|\rangle$ represents the quantum-mechanical average, e.g. $\langle|\cdot|\rangle \equiv Tr\{\hat{\rho}, \cdot\}$. We note that in truly nonequilibrium situations the density matrix is, in principle, unknown [165, 166], in particular, at finite temperature it does not have the form of a statistical operator.

In addition to the time-ordered GF one can introduce retarded/advanced and "lesser than"/"greater than"[7] GFs as follows

$$G^+(\boldsymbol{r},t;\boldsymbol{r}',t') = -\frac{\imath}{\hbar}\,\theta(t-t')\left\langle\left|\left[\psi(\boldsymbol{r},t)\psi^\dagger(\boldsymbol{r}',t')\right]\right|\right\rangle, \text{ retarded,} \tag{5.10}$$

$$G^-(\boldsymbol{r},t;\boldsymbol{r}',t') = \frac{\imath}{\hbar}\,\theta(t'-t)\left\langle\left|\left[\psi(\boldsymbol{r},t)\psi^\dagger(\boldsymbol{r}',t')\right]\right|\right\rangle, \text{ advanced,} \tag{5.11}$$

$$G^<(\boldsymbol{r},t;\boldsymbol{r}',t') = \frac{\imath}{\hbar}\left\langle\left|\psi^\dagger(\boldsymbol{r}',t')\psi(\boldsymbol{r},t)\right|\right\rangle, \text{ "lesser than",} \tag{5.12}$$

$$G^>(\boldsymbol{r},t;\boldsymbol{r}',t') = -\frac{\imath}{\hbar}\left\langle\left|\psi(\boldsymbol{r},t)\psi^\dagger(\boldsymbol{r}',t')\right|\right\rangle, \text{ "greater than",} \tag{5.13}$$

[6] The field operators are defined through creation and annihilation operators such as

$$\psi^\dagger(\boldsymbol{r}) = \sum_k u_k^*(\boldsymbol{r})\hat{c}_k^\dagger, \quad \psi(\boldsymbol{r}) = \sum_k u_k(\boldsymbol{r})\hat{c}_k,$$

where $\{u_k(\boldsymbol{r})\}$ is any complete set of single-particle eigenvectors.

[7] The "lesser than" and the "greater than" GFs are also sometimes called *correlation functions*. For simplicity we will refer to these functions simply as "lesser" and "greater".

where [ ] in the definition of $G^{\pm}$ denotes the commutator (anti-commutator for fermions). Note that these functions are not independent from each other, for instance

$$G^{-} = G^{+\dagger}, \tag{5.14}$$

$$G^{<} = G^{>\dagger}, \tag{5.15}$$

$$G^{+} - G^{-} = G^{>} - G^{<}. \tag{5.16}$$

The retarded GF is very well suited for calculating the physical response of the system: G^{+} is different from zero only for $t \geq t'$ and can be used to calculate the response at time t to an earlier excitation produced at time t'. The "lesser" and the "greater" GFs are directly linked to the physical observables such as the particle density

$$n(\boldsymbol{r}, t) = \left\langle |\psi^{\dagger}(\boldsymbol{r}, t)\psi(\boldsymbol{r}, t)| \right\rangle = -\imath\hbar \lim_{\epsilon \to 0^{+}} G^{<}(\boldsymbol{r}, t; \boldsymbol{r}, t + \epsilon). \tag{5.17}$$

Similarly, one can define the single-particle density matrix

$$\rho(\boldsymbol{r}, \boldsymbol{r}', t) = -\imath\hbar \lim_{\epsilon \to 0^{+}} G^{<}(\boldsymbol{r}, t; \boldsymbol{r}', t + \epsilon). \tag{5.18}$$

Note, that in the localized orbital basis $|i\rangle \equiv |i\,\sigma\rangle$, which is the usual choice of the basis throughout this Thesis, the operators $\psi^{\dagger}(\psi)$ will be substituted by the creation(annihilation) operators $\hat{c}_i^{\dagger}(\hat{c}_i)$ and the GF can be conveniently described by an operator $\hat{G}$ with the corresponding matrix G expanded over the basis. Hereafter we will use both the spatial form of the Green's function given by Eq. (5.9) and its operator form.

5.4.2 Equilibrium Green's functions

5.4.2.1 Perturbation expansion at zero and non-zero temperature

We will now briefly review the well-known techniques for calculating the GFs of interacting systems at both zero and finite temperature in equilibrium. We will start from the zero-temperature case.

Since, in general, the ground state of an interacting system $|\Psi_0\rangle$ is unknown, it is desirable to express it in terms of quantities that are known or can be easily calculated, such as the ground state of a non-interacting system. In the interaction picture, the

total Hamiltonian $\hat{H}$ is divided into a "simple", in this case non-interacting, part $\hat{H}_0$ and the perturbation $\hat{V}$, which contains all the interactions. Let us denote the ground state of the non-interacting system described by the Hamiltonian $\hat{H}_0$ as $|\Phi_0\rangle$. The main idea, which will allow us to relate $|\Psi_0\rangle$ to $|\Phi_0\rangle$, is to assume that the system was in the non-interacting ground state $|\Phi_0\rangle$ in the asymptotic past ($t \to -\infty$) and that it returns to the same non-interacting ground state in the asymptotic future ($t \to +\infty$). Technically, this idea can be implemented by writing the total interacting Hamiltonian as

$$\hat{H} = \hat{H}_0 + e^{-\epsilon|t|}\hat{V}, \tag{5.19}$$

where ϵ is an infinitesimally small positive number, e.g. $\epsilon \to 0^+$. Equation (5.19) essentially means that the interactions, contained in $\hat{V}$, are adiabatically switched on at $t \to -\infty$ and adiabatically switched off at $t \to +\infty$, which insures that at these limits $\hat{H} \to \hat{H}_0$ and, therefore, $|\Psi_0(\pm\infty)\rangle \to |\Phi_0\rangle$. The interacting ground state $|\Psi_0\rangle$ at time t_0 can be expressed in terms of $|\Phi_0\rangle$ with the help of the time-evolutions operator [see the definition in Eq. (2.27) in Section 2.4.1 of Chapter 2]

$$|\Psi_0(t_0)\rangle = U(t_0, -\infty)\,|\Phi_0\rangle\,, \tag{5.20}$$

and

$$\langle\Psi_0(t_0)| = U(+\infty, t_0)\,\langle\Phi_0|\,. \tag{5.21}$$

By substituting Eqs. (5.20) and (5.21) into the definition of the time-ordered GF [see Eq. (5.9)], we obtain the expression $U(+\infty, t_0)U(t_0, -\infty)$ inside $\langle|\cdot|\rangle$. One can define an object, called the S-matrix, such as $S(t,t') = \hat{U}(t,t'')\hat{U}^\dagger(t',t'')$. Thus we have

$$S(+\infty, -\infty) = U(+\infty, t_0)U(t_0, -\infty), \tag{5.22}$$

and

$$G(\boldsymbol{r}, t; \boldsymbol{r}', t') = -\frac{\imath}{\hbar}\frac{\langle\Phi_0|T[S(+\infty,-\infty)\psi(\boldsymbol{r},t)\psi^\dagger(\boldsymbol{r}',t')]|\Phi_0\rangle}{\langle\Phi_0|S(+\infty,-\infty)|\Phi_0\rangle}\,, \tag{5.23}$$

where $S(+\infty,-\infty) = Texp\left[\int_{-\infty}^{+\infty}\hat{V}(t_1)dt_1\right]$ and can be conveniently expanded in terms of the perturbation $\hat{V}$ as we have already discussed in Section 2.4.1 of Chapter 2 [see Eq. (2.38)]. This is usually referred to as the perturbation expansion on the *Feynman contour*, formed by the real-time axis $(-\infty, +\infty)$.

At finite temperature, one has to evaluate the GF (and, in fact, the expectation value of any operator) in terms of the density matrix $\rho = e^{-\beta\hat{H}}/\mathcal{Z}_C$ (here we chose the

canonical ensemble for simplicity). One immediately notices that the factor $e^{-\beta\hat{H}}$ is formally equivalent to the time-evolution operator $\hat{U}$, if we assume that the system "evolves" from some moment of time t to the complex time $t - \imath\hbar\beta$

$$\hat{U}(t_0, t_0 - \imath\hbar\beta) = e^{-\beta\hat{H}}. \tag{5.24}$$

Using this result, one can set up the perturbation expansion of the time-evolution operator in imaginary time $\tau = \imath t$ on the segment $(t_0, t_0 - \imath\hbar\beta)$ of the imaginary-time axis, or the *Matsubara contour*. The time-ordered GFs can be also redefined as imaginary-time, or Matsubara, GFs. Similarly to the zero-temperature case, the use of the adiabatic approximation allows one to evaluate the quantum-mechanical averages over the non-interacting density matrix $\rho_0 = e^{-\beta\hat{H}_0}/\mathcal{Z}_C$.

Alternatively, the whole perturbation expansion of the GF can be summarized in the form the integral Dyson equation. In the case of the real-time GFs the Dyson equation reads

$$\begin{aligned} G(\boldsymbol{r}, t; \boldsymbol{r}', t') = G_0(\boldsymbol{r}, t; \boldsymbol{r}', t') \quad + \quad & \int d\boldsymbol{r}_1 d\boldsymbol{r}_2 dt_1 dt_2 \, G_0(\boldsymbol{r}, t; \boldsymbol{r}_1, t_1) \times \\ & \times \Sigma(\boldsymbol{r}_1, t_1; \boldsymbol{r}_2, t_2) \, G(\boldsymbol{r}_2, t_2; \boldsymbol{r}', t'), \end{aligned} \tag{5.25}$$

where G_0 is the GF of a non-interacting system. We have also introduced the self-energy Σ, a quantity which contains all the information about the effects of interactions on the single-particle dynamics. As we will see later, in the Landauer setup with semi-infinite electrodes the self-energy accounts for the "interaction" (coupling) between the central region and the leads.

5.4.2.2 Green's functions in the energy domain

If the system is in equilibrium, the GF should depend only on the difference $t - t'$. Assuming that the system is also homogeneous, we can define $G(x - x', t - t') \equiv G(x, t)$, where we introduced new variables $t \equiv t - t'$ and $x \equiv x - x'$. By taking for definiteness the zero-temperature definition of the GF in Eq. (5.9) and by differentiating it with respect to time, we find

$$\left(\imath\hbar\frac{\partial}{\partial t} - \hat{H}\right) G(x, t) = \delta(x)\delta(t). \tag{5.26}$$

where we also assumed that $\hat{H}$ is a single-particle Hamiltonian. One can see from the above equation, that similarly to the general function $\mathcal{G}$ in Eq. (5.7), the GF satisfies the Schrödinger equation with a singular inhomogeneity.

We can convert Eq. (5.26) into the energy (frequency) domain by performing the Fourier transform over time. Assuming that the Hamiltonian $\hat{H}$ is time-independent, we get

$$\left(E - \hat{H}\right) G(x, E) = \delta(x), \tag{5.27}$$

where we defined the Fourier transform of $G(x,t)$ as $\mathrm{FT}\left[G(x,t)\right](E) \equiv G(x,E) = \int_{-\infty}^{\infty} e^{-iEt/\hbar} G(x,t)\, dt$ and used the fact that the Fourier transform of the Dirac delta function gives a unity. Equation (5.27) can be written in the operator form as

$$\left(E\hat{I} - \hat{H}\right) \hat{G}(E) = \hat{I}, \tag{5.28}$$

where $\hat{I}$ is the identity operator with the same dimensions as $\hat{H}$. Solving equation (5.28) is equivalent to solving the time-independent Schrödinger equation and one can, indeed, think of $\hat{G}(E)$ as the inverse of the operator $\left(E\hat{I} - \hat{H}\right)$, e.g. $\hat{G}(E) = \left(E\hat{I} - \hat{H}\right)^{-1}$, similarly to the definition of a *resolvent*. This definition as it is, however, does not take into account the causality of the GF: if we perform the inverse Fourier transform of $G(x,E)$ we will not be able to recover the time-ordered GF $G(x,t)$. We can correct the definition by introducing the retarded GF in the energy-domain such as

$$\hat{G}^{+}(E) = lim_{\epsilon \to 0^{+}} \left[(E + \imath\epsilon)\, \hat{I} - \hat{H}\right]^{-1}. \tag{5.29}$$

This is, in fact, a rather general result. It can be shown, using for instance the Titchmarsh's theorem [266], that for a general response function $\mathcal{G}(t)$ the causality condition ($\mathcal{G}(t)$ is non-zero only for $t \geq 0$) implies that the Fourier transform $\mathrm{FT}\left[\mathcal{G}(t)\right](\omega) \equiv \mathcal{G}(\omega)$ is analytic in the upper half-plane, which is equivalent to setting $\mathcal{G}(\omega) = \lim_{\epsilon \to 0^{+}} \mathcal{G}(\omega + \imath\epsilon)$.

The Fourier transform of the GF $G(\boldsymbol{r}, t)$ over both space- and time-coordinates can be calculated as

$$\mathrm{FT}\left[G(\boldsymbol{r},t)\right](\boldsymbol{k},E) \equiv G(\boldsymbol{k},E) = \int dE \int d\boldsymbol{r} e^{-iEt/\hbar} e^{-i\boldsymbol{k}\boldsymbol{r}} G(\boldsymbol{r},t). \tag{5.30}$$

With the assumptions of temporal and spatial homogeneity, we can take the two-dimensional Fourier transform of the Dyson equation [Eq. (5.25)], which reads

$$G(\boldsymbol{k}, E) = G_0(\boldsymbol{k}, E) + G_0(\boldsymbol{k}, E)\Sigma(\boldsymbol{k}, E)G(\boldsymbol{k}, E). \tag{5.31}$$

5.4.2.3 Spectral function

The *spectral function* of the system is defined as

$$\begin{aligned} A(\boldsymbol{k}, E) = \frac{\imath}{2\pi}\left[G^{+}(\boldsymbol{k}, E) - G^{-}(\boldsymbol{k}, E)\right] &= \frac{\imath}{2\pi}\left[G^{>}(\boldsymbol{k}, E) - G^{<}(\boldsymbol{k}, E)\right] = \\ &= -\frac{1}{\pi}\Im\left[G^{+}(\boldsymbol{k}, E)\right], \end{aligned} \tag{5.32}$$

where we used the relation between $G^{\pm}$ and $G^{<(>)}$ [Eq. (5.16)] and the fact that $G^{-} = G^{+\dagger}$. Note that $\Im$ denotes the imaginary and $\Re$ the real part.

With the help of the Fourier-transformed version of the Dyson equation [see Eq. (5.31)] we can rewrite the expression for the spectral function such as

$$\begin{aligned} 2\pi A(\boldsymbol{k}, E) &= \imath G^{+}(\boldsymbol{k}, E)\left[\Sigma^{+}(\boldsymbol{k}, E) - \Sigma^{-}(\boldsymbol{k}, E)\right] G^{-}(\boldsymbol{k}, E) = \\ &= G^{+}(\boldsymbol{k}, E)\Gamma(\boldsymbol{k}, E)G^{-}(\boldsymbol{k}, E), \end{aligned} \tag{5.33}$$

where $\hat{\Sigma}^{+}(\hat{\Sigma}^{-})$ is (retarded) advanced self-energy and we have introduced

$$\Gamma(\boldsymbol{k}, E) = \imath\left[\Sigma^{+}(\boldsymbol{k}, E) - \Sigma^{-}(\boldsymbol{k}, E)\right] = -2\Im\Sigma^{+}(\boldsymbol{k}, E). \tag{5.34}$$

The spectral function satisfies

$$\int dE A(\boldsymbol{k}, E) = 1, \tag{5.35}$$

and the density of states, in general, can be evaluated as

$$D(E) = \int \frac{d\boldsymbol{k}}{(2\pi)^3} A(\boldsymbol{k}, E). \tag{5.36}$$

Note that for a non-interacting system $A(\boldsymbol{k}, E) = \delta(E - e_k)$, where $\{e_k\}$ are the eigenvalues of the single-particle non-interacting Hamiltonian. The density of states is then given by $D(E) = Tr\left[A(\boldsymbol{k}, E)\right] = \sum_{e_k} \delta(E - e_k)$.

One can show, that for the system, which is in equilibrium with an external reservoir at temperature T and chemical potential μ, the following relations between $G^<$, $G^>$ and A can be established[8]

$$G^>(\boldsymbol{k}, E) = -e^{\beta(E-\mu)} G^<(\boldsymbol{k}, E), \tag{5.37}$$

$$G^<(\boldsymbol{k}, E) = 2\pi\imath f(E) A(\boldsymbol{k}, E), \tag{5.38}$$

$$G^>(\boldsymbol{k}, E) = -2\pi\imath \left[1 - f(E)\right] A(\boldsymbol{k}, E). \tag{5.39}$$

By using Eq. (5.32), we immediately obtain

$$G^<(\boldsymbol{k}, E) = -2\imath f(E) \Im \left[G^+(\boldsymbol{k}, E)\right]. \tag{5.40}$$

The above expressions suggest an intuitive interpretation of the "lesser" and the "greater" GFs as occupations of single-particle states due to the Fermi distribution.

The physical meaning of the spectral function can be further clarified by using the concept of quasi-particles. It follows from the Dyson equation [Eq. (5.31)] that the retarded GF can be written as

$$G^+(\boldsymbol{k}, E) = \frac{1}{E - e_k - \Re\Sigma^+(\boldsymbol{k}, E) - \imath\Im\Sigma^+(\boldsymbol{k}, E)}, \tag{5.41}$$

where e_k are the eigenvalues of the non-interacting Hamiltonian $\hat{H}_0$. Note that $E \equiv \lim_{\epsilon \to 0^+}(E + \imath\epsilon)$ for the retarded GF. The poles of G^+ correspond to the values of E for which the denominator on the right-hand side of Eq. (5.41) is zero. In the absence of interactions, e.g. for $\Re\Sigma^+ = \Im\Sigma^+ = 0$, the poles would occur at $E = e_k$. In the first-order approximation we can write the poles in the interacting case as

$$E = e_k + \Re\Sigma^+(\boldsymbol{k}, e_k) + \imath\Im\Sigma^+(\boldsymbol{k}, e_k). \tag{5.42}$$

By inserting the expression for the GF with poles defined by Eq. (5.42) into the definition of the spectral function [Eq. (5.32)] we obtain

$$A(\boldsymbol{k}, E) = -\frac{1}{\pi} \frac{\Im\Sigma^+(\boldsymbol{k}, e_k)}{\left[E - e_k - \Re\Sigma^+(\boldsymbol{k}, e_k)\right]^2 + \left[\Im\Sigma^+(\boldsymbol{k}, e_k)\right]^2}. \tag{5.43}$$

[8]The relations between $G^<$, $G^>$ and A are the manifestation of the fluctuation-dissipation theorem [143]. The proof of these relations involves a formal derivation using the exact eigenstates of the fully interacting Hamiltonian (see [90, p. 41] and [57, p. 227]).

Therefore the spectral function contains the information on how the eigenstates of the unperturbed Hamiltonian $\hat{H}_0$ change in the presence of the interactions: the states are shifted by $\Re\Sigma^+$ and are broadened into a Lorentzian with the width defined by $2\Im\Sigma^+$. The latter, in fact, coincides with Γ [see Eq. (5.34)], which is usually referred to as the *broadening matrix*. The new states can be associated with quasi-particle states with energies $e_k \to e_k + \Re\Sigma^+$ and a finite lifetime $\tau \propto \hbar/\Gamma$.

Finally, the expressions for the self-energies, corresponding to the "lesser" and the "greater" GFs, are given by

$$\hat{\Sigma}^< = -2\imath f(E)\Im\hat{\Sigma}^+, \tag{5.44}$$

$$\hat{\Sigma}^> = 2\imath\left[1 - f(E)\right]\Im\hat{\Sigma}^+. \tag{5.45}$$

With the help of Eq. (5.34), we find the relation between $\hat{\Sigma}^{<(>)}$ and the broadening matrix $\hat{\Gamma}$

$$\imath\left(\hat{\Sigma}^> - \hat{\Sigma}^<\right) = \imath\left(\hat{\Sigma}^+ - \hat{\Sigma}^-\right) = \hat{\Gamma}. \tag{5.46}$$

The functions $\hat{\Sigma}^<$ and $\hat{\Sigma}^>$ are called the *in-scattering* and the *out-scattering* self-energies, respectively, since the quantity $\Sigma^{<(>)}/\hbar$ can be interpreted as a rate with which the particles are scattered in and out of the single-particle states due to interactions.

5.4.3 Nonequilibrium Green's functions – Keldysh formalism

Although the equilibrium techniques provide a convenient way of calculating the time-ordered GFs, they can not be straightforwardly applied to the nonequilibrium situation. Let us consider, for example, a nonequilibrium system at zero temperature. In this case, the density matrix should be written as a statistical "mixture" of quantum states $|\Psi\rangle$, e.g. $\hat{\rho} = \sum_\Psi p_\Psi |\Psi\rangle\langle\Psi|$, where p_Ψ is the probability to find the system in the state $|\Psi\rangle$. The full GF can be then calculated as $G = \sum_\Psi p_\Psi G_\Psi$, where G_Ψ is evaluated using Eq. (5.9) for each state $|\Psi\rangle$. In the interaction picture, we can again re-write the total Hamiltonian $\hat{\mathcal{H}}$, describing the system in nonequilibrium, as

$$\hat{\mathcal{H}} = \hat{H} + \hat{H}'(t), \tag{5.47}$$

where $\hat{H}$ now represents the unperturbed (equilibrium) part of $\hat{\mathcal{H}}$, which can in principal contain interactions, and $\hat{H}'(t)$ is the nonequilibrium perturbation, which drives

the system out of equilibrium. By using the same strategy that we employed in the equilibrium case, we obtain the following expression for G_Ψ

$$G_\Psi(\boldsymbol{r},t;\boldsymbol{r}',t') = -\frac{\imath}{\hbar}\left\langle \Psi(+\infty)|T[S(+\infty,-\infty)\psi(\boldsymbol{r},t)\psi^\dagger(\boldsymbol{r}',t')]|\Psi(-\infty)\right\rangle , \tag{5.48}$$

which is, indeed, very similar to Eq. (5.23) [for now we omit the normalization factor in the denominator]. One last step is required before one can proceed with the Feynman expansion, namely that the state of the system in the asymptotic future, $|\Psi(+\infty)\rangle$, is identical (down to a simple phase-factor) to the state in the asymptotic past, $|\Psi(-\infty)\rangle$. Such assumption, however, is not at all justified in nonequilibrium since we can not expect the system to return to the same ground state after it has been driven out of equilibrium via an external perturbation. On the contrary, we generally expect it to reach a new ground state, which is quite different from $|\Psi(-\infty)\rangle$.

The main purpose of the nonequilibrium techniques is essentially to avoid the reference to the unknown state $|\Psi(+\infty)\rangle$. One can do so by using once again the concept of the S-matrix

$$|\Psi(+\infty)\rangle = S(+\infty,-\infty)\,|\Psi(-\infty)\rangle\,. \tag{5.49}$$

Physically, this corresponds to reversing the time evolution of the system from the asymptotic future back to the asymptotic past. This leads to

$$\begin{aligned} G_\Psi(\boldsymbol{r},t;\boldsymbol{r}',t') \;=\; & -\frac{\imath}{\hbar}\left\langle \Psi(-\infty)S(-\infty,+\infty)\right| \\ & T\left[S(+\infty,-\infty)\psi(\boldsymbol{r},t)\psi^\dagger(\boldsymbol{r}',t')\right]|\Psi(-\infty)\rangle\,. \end{aligned} \tag{5.50}$$

Compared to the Feynman expansion (see Eq. 5.23), there is an additional S-matrix outside the time-ordering operator $T[\,]$. In order to push the S-matrix inside the T-product without allowing $S(-\infty,+\infty)\;S(+\infty,-\infty)$ to simply cancel each other, one can introduce the *Schwinger-Keldysh contour*, which is shown in Fig. 5.3, and redefine the time-ordering operator on this contour. Furthermore, similarly to the time-ordered GF, one can define the *contour-ordered* GFs such as

$$G(x,\tau_{\mathcal{C}};x',\tau'_{\mathcal{C}}) = -\frac{\imath}{\hbar}\left\langle |T_{\mathcal{C}}\left[\psi\left(x,\tau_{\mathcal{C}}\right)\psi^\dagger\left(x',\tau'_{\mathcal{C}}\right)\right]|\right\rangle , \tag{5.51}$$

where the new time-ordering operator T_c "orders" the field operators on the contour $\mathcal{C} = \mathcal{C}_1 \bigcup \mathcal{C}_2$ [see Fig. 5.3] which goes from $-\infty$ to $+\infty$ ($\mathcal{C}_1$ branch) and then back to $-\infty$ ($\mathcal{C}_2$ branch); $\tau_{\mathcal{C}} \in \mathcal{C}$ is the new time variable. Since the contour S-matrix is unity,

there is, in fact, no need in the normalization factor in the expression for the GF.

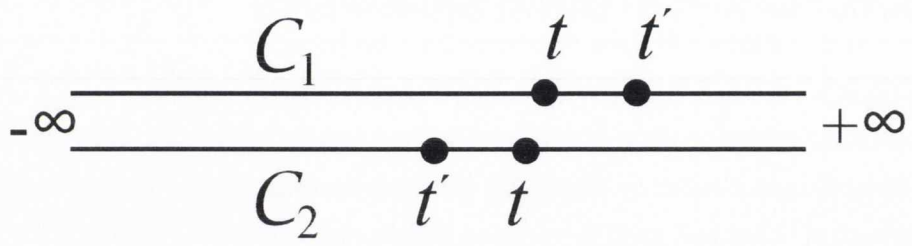

FIGURE 5.3: Schwinger-Keldysh contour which consists of two branches - the "forward" branch $\mathcal{C}_1$, which extends from $-\infty$ to $+\infty$, and the "backward" branch $\mathcal{C}_2$, which goes from $+\infty$ to $-\infty$. Along $\mathcal{C}_1$ the later time t' is located to the *right* from the earlier time t, along $\mathcal{C}_2$ the later time t' is located to the *left* from the earlier time t.

In the *Keldysh formalism*[9] one further employs the adiabatic approximation, e.g. one assumes that the nonequilibrium perturbation $\hat{H}'$ was switched on adiabatically from $t \to -\infty$ to the present time t. However, it is not switched off at $t \to +\infty$ as in the equilibrium case, but instead $\hat{\mathcal{H}} = \lim_{\epsilon \to 0^+} \hat{H} + e^{-\epsilon t}\hat{H}'$ (note that here we used the factor $e^{-\epsilon t}$ instead of $e^{-\epsilon|t|}$). This enables us to study nonequilibrium stationary states a long time after the perturbation has been switched on. The contour-ordered GFs can then be evaluated in the asymptotic state $|\Psi(-\infty)\rangle$, which corresponds to the equilibrium Hamiltonian $\hat{H}$, and the equilibrium density matrix can be constructed as $\hat{\rho} = \sum_\Psi p_\Psi |\Psi(-\infty)\rangle\langle\Psi(-\infty)|$.

If the density matrix can be somehow calculated at some initial time t_0, it is not necessary to refer to the asymptotic behavior of the system at $t \to -\infty$. Instead, the Schwinger-Keldysh contour can be generalized to the *closed time contour*, which goes from t_0 to the latest of t or t' and then back to t_0.

Usually, one can assume that in the asymptotic past the system is non-interacting ($\hat{H} = \hat{H}_0$). However, if one wishes to include the initial correlations, the equilibrium Hamiltonian $\hat{H}$ can be further partitioned into the non-interacting part $\hat{H}_0$ and the perturbation $\hat{V}$, which contains the interactions. It can be shown that the interacting and non-interacting density matrices can be related via $e^{-\beta\hat{H}} = e^{-\beta\hat{H}_0}S(t_0 - \imath\beta, t_0)$ [165]. Hence, it is possible to re-formulate the problem on the imaginary-time contour, known

[9] We note that a different but equivalent formalism has been developed by Kadanoff and Baym [119]. In their work a set of integro-differential equations of motion for the nonequilibrium GFs, known as *Kadanoff-Baym equations*, has been derived. These are equivalent to the integral quantum kinetic equations of the Keldysh formalism [125].

as *Kadanoff-Baym contour*, which contains, in addition to the two-branch contour $\mathcal{C}$, a segment $(t_0, t_0 - \imath\beta)$ of the imaginary-time axis (as in the Matsubara technique).

The GF in Eq. (5.51) can be further decomposed into four real-time GFs depending on which branch of the contour $\mathcal{C}$ the arguments $\tau_\mathcal{C}$ and $\tau'_\mathcal{C}$ belong to

$$G(\boldsymbol{r}, \tau_\mathcal{C}; \boldsymbol{r}', \tau'_\mathcal{C}) = \begin{cases} G^\mathcal{C}(\boldsymbol{r}, t; \boldsymbol{r}', t') = -\imath \left\langle |T[\psi(x,t)\psi^\dagger(x',t')]| \right\rangle, t, t' \in \mathcal{C}_1, \\ G^<(\boldsymbol{r}, t; \boldsymbol{r}', t') = \imath \left\langle |\psi^\dagger(x',t')\psi(x,t)| \right\rangle, t \in \mathcal{C}_1, t' \in \mathcal{C}_2, \\ G^>(\boldsymbol{r}, t; \boldsymbol{r}', t') = -\imath \left\langle |\psi(x,t)\psi^\dagger(x',t')| \right\rangle, t \in \mathcal{C}_2, t' \in \mathcal{C}_1, \\ G^{\bar{\mathcal{C}}}(\boldsymbol{r}, t; \boldsymbol{r}', t') = -\imath \left\langle |\bar{T}[\psi(x,t)\psi^\dagger(x',t')]| \right\rangle, t, t' \in \mathcal{C}_2 \end{cases} \tag{5.52}$$

where $G^\mathcal{C}$ is the time-ordered GF and $G^{\bar{\mathcal{C}}}$ is the anti-time-ordered GF with $\bar{T}$ being the anti-time-ordering operator, which orders operators in the opposite way compared to T; $G^{<(>)}$ is the lesser (greater) GF. The latter are not independent and can be related to the retarded (advanced) GFs. One then works with the object

$$\boldsymbol{G} = \begin{pmatrix} \hat{G}^\mathcal{C} & \hat{G}^< \\ \hat{G}^> & \hat{G}^{\bar{\mathcal{C}}} \end{pmatrix}, \tag{5.53}$$

and its corresponding self-energy.

With the nonequilibrium GFs, defined on the contour, each integral, which has the form

$$C(1,1') = \int d(2)\, A(1,2)\, B(2,1') \equiv (A, B) \tag{5.54}$$

or, as in the Dyson equation [see Eq. (5.25)]

$$C(1,1') = \int d(2)\, d(2')\, A(1,2)\, B(2,2')\, C(2',1') \equiv (A, B, C) \tag{5.55}$$

is the convolution integral on the two-branch contour $\mathcal{C}$. Here we used the shorthand notation $(1) = (x, \tau_\mathcal{C})$. Such integrals can be transformed into the real-time integrals according to the *Langreth rules* [90, p. 68]

$$(A, B)^{<(>)} = A^+ B^{<(>)} + A^{<(>)} B^-, \tag{5.56}$$

$$(A, B)^{\pm} = A^{\pm} B^{\pm}, \tag{5.57}$$

$$(A, B, C)^{<(>)} = A^+ B^+ C^{<(>)} + A^+ B^{<(>)} C^- + A^{<(>)} B^- C^-, \tag{5.58}$$

$$(A, B, C)^{\pm} = A^{\pm} B^{\pm} C^{\pm}, \tag{5.59}$$

where the matrix products on the left-hand sides of equations denote the convolution integrals on the contour $\mathcal{C}$, while the ones on the right-hand sides represent the integrals on the real-time axis from $-\infty$ to $+\infty$. With the help of the Langreth rules, the contour-ordered GFs in the Keldysh formalism can be treated in the same way as ordinary time-ordered GFs. By applying the set of rules, given by Eqs. (5.56)-(5.59), to the Dyson equation for the contour-ordered GFs, we obtain the central result of the Keldysh formalism, namely, the *kinetic equation* for the "lesser"("greater") GF

$$\hat{G}^{<(>)} = \left(\hat{I} + \hat{G}^{+}\hat{\Sigma}^{+}\right)\hat{G}_0^{<(>)}\left(\hat{I} + \hat{\Sigma}^{-}\hat{G}^{-}\right) + \hat{G}^{+}\hat{\Sigma}^{<(>)}\hat{G}^{-}, \tag{5.60}$$

where $\hat{G}_0^{<(>)}$ is the *free* GF, which corresponds to the non-interacting Hamiltonian $\hat{H}_0$. Note that this is an integral equation, in which the product of two operators denotes the integral over the space- and time-variables (the latter belong to the real-time axis). It can be shown that for finite systems [165], the first term on the right-hand side of Eq. (5.60) disappears and one is left with

$$\hat{G}^{<(>)} = \hat{G}^{+}\hat{\Sigma}^{<(>)}\hat{G}^{-}, \tag{5.61}$$

The above equation can be used for calculations of quantum transport.

5.4.4 Application to the steady-state transport

We will now demonstrate how some of the concepts of the NEGF formalism can be applied to the steady-state electronic transport problem. Our model system is the same as in the Landauer approach, namely, a nanostructure coupled to two external reservoirs via scattering-free non-interacting electrodes (see Fig. 5.4).

As before we assume that the reservoirs are in equilibrium at chemical potentials μ_α and that electrons are injected and absorbed without perturbing the reservoirs. Here we consider the problem with *open-boundary conditions*, where the semi-infinite electrodes are assumed to be in equilibrium and connected to the reservoirs infinitely far from the central region. The bias voltage is given by the difference in the chemical potentials, e.g. $V = (\mu_{\mathrm{L}} - \mu_{\mathrm{R}})/e$.

As was outlined in the introduction to this chapter, we can use the adiabatic approximation (Caroli's "contacting approach"), where one assumes that the equilibrium conditions described above were satisfied in the remote past ($t \to -\infty$), when the

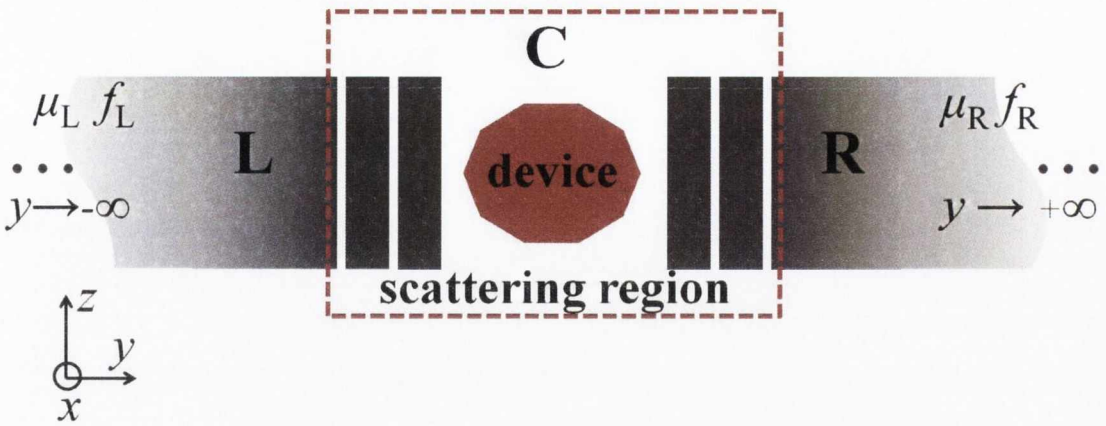

FIGURE 5.4: Electronic transport setup investigated within the NEGF framework: a scattering region bridging two semi-infinite electrodes, attached (at their infinite borders) to external reservoirs with chemical potentials μ_α, occupied according to Fermi-Dirac distributions f_α for $\alpha = \mathrm{L}, \mathrm{R}$. Note that, in addition to the nanoscale device, the scattering region contains few layers from both electrodes.

electrodes were disconnected from the central region and each of them was in equilibrium with the corresponding reservoir. The coupling is then switched on adiabatically, allowing the steady-state to develop.

We make the following partition of the total Hamiltonian $\hat{H}$ describing the entire system (electrodes+central region)

$$\hat{H} = \hat{H}_\mathrm{L} + \hat{H}_\mathrm{LC} + \hat{H}_\mathrm{CL} + \hat{H}_\mathrm{C} + \hat{H}_\mathrm{R} + \hat{H}_\mathrm{RC} + \hat{H}_\mathrm{CR}, \tag{5.62}$$

where $\hat{H}_\alpha$ for $\alpha = \mathrm{L}, \mathrm{R}$ is the Hamiltonian of the lead α, $\hat{H}_\mathrm{C}$ is the Hamiltonian of the central region, while other terms, namely $\hat{H}_{\mathrm{C}\alpha}$ (and its Hermitian conjugate $\hat{H}_{\alpha\mathrm{C}}$), denote the coupling between C and α. Importantly, there is no direct tunneling between L and R. Note also that in practical calculations the central region usually includes few slabs, or *principle layers*, from L and R, in order for the electrodes to be considered as bulk-like. The new scattering region, which now contains the device and the principal layers, is often referred to as the *extended molecule*.

The retarded GF of the isolated semi-infinite lead α is denoted as $\hat{g}_\alpha^+$ and satisfies

$$\left(z\hat{I} - \hat{H}_\alpha\right)\hat{g}_\alpha^+ = \hat{I}, \tag{5.63}$$

where we defined $z = \lim_{\epsilon \to 0^+} (E + \imath\epsilon)$.

The retarded GF of the entire system, denoted as $\hat{\mathcal{G}}^{+}$ in order to avoid confusion with the GF of C, can be determined from the following equation

$$\left(z\hat{I} - \hat{H}\right)\hat{\mathcal{G}}^{+} = \hat{I}. \tag{5.64}$$

By re-writing the above equation in the block-matrix form, it is easy to show that the retarded GF of the central region in the presence of the leads is given by

$$\hat{G}^{+} = \left[z - \hat{H}_{\mathrm{C}} - \hat{\Sigma}^{+}\right]^{-1}, \tag{5.65}$$

where

$$\hat{\Sigma}^{+} = \hat{\Sigma}_{\mathrm{L}}^{+} + \hat{\Sigma}_{\mathrm{R}}^{+}. \tag{5.66}$$

The self-energy $\hat{\Sigma}_{\alpha}^{+}$ due to the coupling between C and the lead α is given by

$$\hat{\Sigma}_{\alpha}^{+} = \hat{H}_{\mathrm{C}\alpha}\hat{g}_{\alpha}^{+}\hat{H}_{\alpha\mathrm{C}}. \tag{5.67}$$

$\hat{\Sigma}_{\alpha}^{+}$ is related to the corresponding broadening matrix $\hat{\Gamma}_{\alpha}$ via Eq. (5.46).

The strategy to calculate the steady-state current, flowing from the electrodes into the central region, is to define the current as the expectation value of the rate of change of the total particle number operator, e.g. $I_{\alpha} = e\left\langle \dot{\hat{N}}_{\alpha} \right\rangle$, where $\hat{N}_{\alpha} = \sum_{k\in\alpha} \hat{c}_{k}^{\dagger}\hat{c}_{k}$ is the particle number operator in the lead α (we employed a similar strategy for calculating the spin-currents in Section 2.4.2 of Chapter 2). Following Ref. [90, p. 162], the current originating from the electrode α is given by

$$I_{\alpha} = \frac{\imath e}{h}\int dE\, Tr\left[\hat{\Gamma}_{\alpha}(E)\cdot\left\{\hat{G}^{<}(E) + f_{\alpha}(E)\left(\hat{G}^{+}(E) - \hat{G}^{-}(E)\right)\right\}\right], \tag{5.68}$$

where $\hat{G}^{+}$, $\hat{G}^{-}$ and $\hat{G}^{<}$ are retarded, advanced and "lesser" GFs of the central region in the presence of the electrodes.

The total steady-state current calculated as a balance of currents originating from the left and from the right electrodes, e.g. $I = (I_{\mathrm{L}} - I_{\mathrm{R}})/2$, reads

$$\begin{aligned} I &= 2\frac{\imath e}{2h}\int dE\, Tr\left\{\left[\hat{\Gamma}_{\mathrm{L}}(E) - \hat{\Gamma}_{\mathrm{R}}(E)\right]\hat{G}^{<}(E) + \right. \\ &+ \left.\left[f_{\mathrm{L}}(E)\hat{\Gamma}_{\mathrm{L}}(E) - f_{\mathrm{R}}\hat{\Gamma}_{\mathrm{R}}(E)\right]\cdot\left[\hat{G}^{+}(E) - \hat{G}^{-}(E)\right]\right\}, \end{aligned} \tag{5.69}$$

where we have added a factor of 2 due to spin-degeneracy.

By using Eq. (5.44), the in-scattering self-energy of the central region can be written as

$$\hat{\Sigma}^{<} = \imath \left(f_{\mathrm{L}} \hat{\Gamma}_{\mathrm{L}} + f_{\mathrm{R}} \hat{\Gamma}_{\mathrm{R}} \right), \tag{5.70}$$

and from the kinetic equation for the "lesser" GF [Eq. (5.61)] we obtain[10]

$$\hat{G}^{<} = \hat{G}^{+} \hat{\Sigma}^{<} \hat{G}^{-} = \imath \hat{G}^{+} \left(f_{\mathrm{L}} \hat{\Gamma}_{\mathrm{L}} + f_{\mathrm{R}} \hat{\Gamma}_{\mathrm{R}} \right) \hat{G}^{-}. \tag{5.71}$$

With the help of the above equations and some algebraic manipulations [57, p. 244], we obtain the final expression for the current

$$I = \frac{2e}{h} \int dE \, Tr \left[\hat{\Gamma}_{\mathrm{R}}(E) \hat{G}^{+}(E) \hat{\Gamma}_{\mathrm{L}}(E) \hat{G}^{-}(E) \right] \cdot \left\{ f_{\mathrm{L}}(E) - f_{\mathrm{R}}(E) \right\}. \tag{5.72}$$

By introducing $\mathcal{T} = Tr \left[\hat{\Gamma}_{\mathrm{R}} \hat{G}^{+} \hat{\Gamma}_{\mathrm{L}} \hat{G}^{-} \right]$, we obtain an expression similar to the phenomenological Landauer formula [Eq. 5.6]. Note that the calculation of the current using Eq. (5.72) boils down to calculating the self-energies $\Sigma_{\alpha}^{\pm}$ for $\alpha = \mathrm{L}, \mathrm{R}$ since all the other quantities entering the equation ($G^{\pm}$ and $\hat{\Gamma}_{\alpha}$) can be expressed in terms of these self-energies. The latter can be calculated using Eq. (5.67), provided the GFs of the isolated semi-infinite leads are known (usually these can be determined through their corresponding surface GFs).

To summarize this section, we would like to point out that the NEGF-based approach to calculating the current through a nanostructure placed between two semi-infinite leads, discussed above, in its present form is limited to the steady state. In the following section we will present the MPB method, which can be used to describe time-dependent effects in electronic transport.

5.5 Multiple-probe battery approach to electronic open boundaries

One of the main objectives of this Thesis is to construct a computational scheme for solving the time-dependent spin-transport problem at the atomic scale. As a theoretical basis for such scheme we use the MPB approach proposed by Todorov and

[10] Note that we used the assumptions of spatial and temporal homogeneity to convert the kinetic equation into the energy-domain.

collaborators [171, 247]. This approach was initially developed in the context of correlated electron-ion dynamics and applied to problems related to current-induced heating effects in atomic wires [172].

We will start with a brief description of the steady-state MPB formalism, where we will use the results of the previous section on the NEGF approach to steady-state transport. The detailed discussion of the time-dependent formalism will be then presented and will serve as a theoretical foundation for the next chapter. At the end of this chapter a number of test simulations using the MPB method will be presented. These include the calculation of the *I-V* characteristics for a resonant dimer, following Ref. [171], and the time-resolved study of spin-excitations in an atomic chain with open boundaries.

5.5.1 Transport setup

Before we proceed, it is important to mention that we work in the basis of spin-resolved atomic orbitals $|i\,\sigma\rangle \equiv |i\rangle \otimes |\sigma\rangle$ and all operators are expanded in this basis. More precisely, each operator $\hat{A}$ is represented by a matrix A, consisting of four blocks of dimension $N_A \times N_A$, namely

$$A = \begin{pmatrix} A^{\uparrow\uparrow} & A^{\uparrow\downarrow} \\ A^{\downarrow\uparrow} & A^{\downarrow\downarrow} \end{pmatrix}, \tag{5.73}$$

where $A^{\sigma\sigma'} = \sum_{ii'} \left\langle \sigma i|\hat{A}|i'\sigma' \right\rangle$ for $\sigma = \uparrow, \downarrow$ (see also the discussion in Section 2.4.4).

The model system considered in the MPB method is shown schematically in Fig. 5.5. The system S consists of the central region C, or device, attached to two large but *finite* electrodes, denoted as L and R. In order to model the current flow through the system, we use the following strategy. In contrast to the Landauer setup, where the electrodes are attached to the external reservoirs at their infinite boundaries, in the MPB method each site i of the finite electrodes is attached to a probe P_i (see Fig. 5.5) through a Hamiltonian matrix element γ_i. The ensemble of probes is denoted as $\mathrm{P} = \{\mathrm{P}_i\}$ for $i \in \mathrm{L}, \mathrm{R}$. The retarded (advanced) GFs of each probe in isolation is denoted as $g^+_{\mathrm{P}_i}(g^-_{\mathrm{P}_i})$. The local density of states $d_{\mathrm{P}_i}(E)$ of the probe P_i is equivalent to the orbital-resolved spectral function and can be calculated by using Eq. (5.32) such that

$$d_{\mathrm{P}_i}(E) = -\frac{1}{\pi}\Im g^+_{\mathrm{P}_i}(E). \tag{5.74}$$

The probes attached to the electrode α have a chemical potential μ_α and the electrons

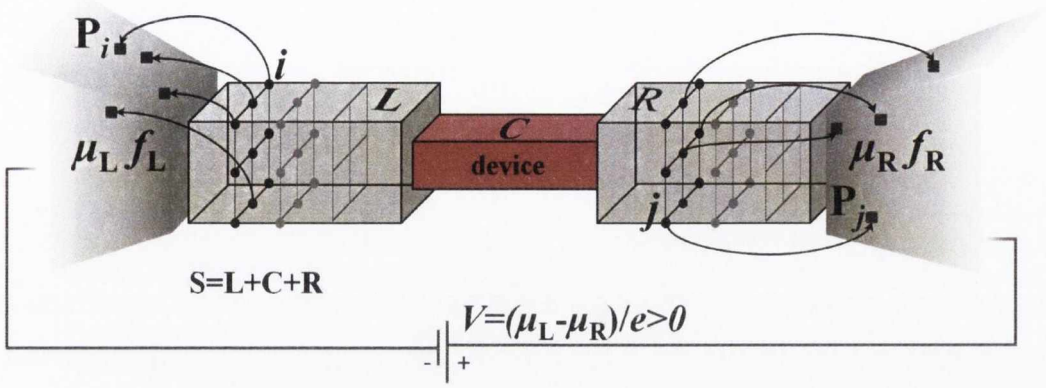

FIGURE 5.5: Transport setup in the MPB method: the central region C is sandwiched between two finite electrodes L and R. A probe P_i ($i \in \mathrm{L,R}$) is attached to each atom i in L and R electrode. The probes attached to L(R) are kept at a fixed chemical potential $\mu_{\mathrm{L}}(\mu_{\mathrm{R}})$ and have the Fermi-Dirac distribution $f_{\mathrm{L}}(f_{\mathrm{R}})$. The entire system, comprising the central region and the electrodes, is denoted as S. The bias voltage is introduced as the difference in the chemical potentials of the external probes.

are distributed according to the Fermi-Dirac distribution $f_\alpha(E)$. The bias is then introduced as the difference between the chemical potentials, e.g. $V = \mu_{\mathrm{L}} - \mu_{\mathrm{R}}$ (here V is in the units of eV). For symmetrically applied bias $\mu_{\mathrm{L(R)}} = \mu_0 \pm V/2$, while in the asymmetric case we set $\mu_{\mathrm{L}} = \mu_0 + V$ and $\mu_{\mathrm{L}} = \mu_0$, where μ_0 is a reference chemical potential, which coincides with the Fermi energy of the electrodes (unless specified, $\mu_0 = E_{\mathrm{F}} = 0$).

In the previous section we obtained an explicit expression for the self-energies of the central region in the presence of two semi-infinite electrodes [Eqs. (5.67)]. Similarly, the self-energy $\hat{\Sigma}_i$ of the system S due to the coupling to the i-th probe can be calculated as

$$\hat{\Sigma}_i(E) = \gamma_i \hat{g}^+_{\mathrm{P}_i}(E)\gamma_i^\dagger = \gamma_i^2 \hat{g}^+_{\mathrm{P}_i}(E). \tag{5.75}$$

In order to find the self-energy Σ_α of S due to the coupling to all probes attached to α, we need to sum up all the individual contributions Σ_i from the corresponding probes $\{\mathrm{P}_i\}_{i\in\alpha}$

$$\hat{\Sigma}^+_\alpha(E) = \sum_{i\in\alpha,\sigma} |i\,\sigma\rangle\, \gamma_i^2 g^+_{\mathrm{P}_i}(E)\, \langle\sigma\, i| \,. \tag{5.76}$$

The total self-energy due to the presence of the probes, attached to both electrodes, is given by

$$\hat{\Sigma}^\pm(E) = \hat{\Sigma}^\pm_{\mathrm{L}}(E) + \hat{\Sigma}^\pm_{\mathrm{R}}(E). \tag{5.77}$$

5.5.2 Steady-state formalism

We will now discuss the steady-state MPB formalism. The total Hamiltonian of the system S is partitioned in the same way as in Section 5.4.4, namely

$$\hat{H}_{\mathrm{S}} = \hat{H}_{\mathrm{L}} + \hat{H}_{\mathrm{LC}} + \hat{H}_{\mathrm{CL}} + \hat{H}_{\mathrm{C}} + \hat{H}_{\mathrm{CR}} + \hat{H}_{\mathrm{RC}} + \hat{H}_{\mathrm{R}}, \tag{5.78}$$

where the notation is the same as in Eq. (5.62). Here we assume that the Hamiltonian is time-independent. We also introduce the identity operator $\hat{I}_{\mathrm{M}} = \sum_{i\in\mathrm{M},\sigma} |i\,\sigma\rangle\langle\sigma\,i|$ for region M (M = L, C, R, P or S).

We assume that in the remote past the system S was in equilibrium and disconnected from the probes and that the coupling to the probes is switched on adiabatically, leading to the steady state. With these assumptions we can apply the steady-state NEGF formalism to the system depicted in Fig. 5.5. The only difference to our previous analysis (see Section 5.4.4) is that now the system S, which contains the finite electrodes and the device, is considered as a whole and the coupling to the probes plays a role of the external perturbation.

By using the kinetic equation [Eq. (5.61)], the "lesser" GF of S in the presence of the probes can be calculated as

$$\hat{G}_{\mathrm{S}}^{<} = \hat{G}_{\mathrm{S}}^{+}\hat{\Sigma}^{<}\hat{G}_{\mathrm{S}}^{-}, \tag{5.79}$$

where $\hat{G}_{\mathrm{S}}^{+}(\hat{G}_{\mathrm{S}}^{-})$ is the retarded (advanced) GF of S and is given by

$$\hat{G}_{\mathrm{S}}^{\pm}(E) = \left[\lim_{\epsilon\to 0^{+}} (E \pm \imath\epsilon)\,\hat{I}_{\mathrm{S}} - \hat{H}_{\mathrm{S}} - \hat{\Sigma}^{\pm}(E)\right]^{-1}. \tag{5.80}$$

The in-scattering self-energy $\hat{\Sigma}^{<}$ entering Eq. (5.79) reads

$$\hat{\Sigma}^{<}(E) = \imath\left[\hat{\Gamma}_{\mathrm{L}} f_{\mathrm{L}}(E) + \hat{\Gamma}_{\mathrm{R}} f_{\mathrm{R}}(E)\right], \tag{5.81}$$

where the broadening matrices $\hat{\Gamma}_{\mathrm{L(R)}}$, defined through their corresponding self-energies via Eq. (5.34), are written as

$$\begin{aligned}\hat{\Gamma}_{\mathrm{L(R)}}(E) = -2\Im\hat{\Sigma}^{+}_{\mathrm{L(R)}}(E) &= -2\Im\left[\sum_{i\in\mathrm{L(R)},\sigma} |i\,\sigma\rangle\gamma_i^2 g^{+}_{\mathrm{P}_i}(E)\langle\,\sigma\,i|\right] = \\ &= -2\sum_{i\in\mathrm{L(R)},\sigma} |i\,\sigma\rangle\gamma_i^2\Im g^{+}_{\mathrm{P}_i}(E)\langle\,\sigma\,i| = \\ &= 2\pi\sum_{i\in L(R)} |i\,\sigma\rangle\gamma_i^2\, d_{\mathrm{P}_i}(E)\langle\,\sigma\,i|. \end{aligned} \tag{5.82}$$

Next, using Eq. (5.18), in which the density matrix is expressed in terms of the "lesser" GF, and the kinetic equation [Eq. (5.79)], the density matrix of S reads

$$\begin{aligned}\hat{\rho}_{\mathrm{S}} &= \frac{1}{2\pi\imath}\int \hat{G}^{<}_{\mathrm{S}}(E)dE = \\ &= \frac{1}{2\pi\imath}\int \hat{G}^{+}_{\mathrm{S}}(E)\hat{\Sigma}^{<}(E)\hat{G}^{-}_{\mathrm{S}}(E)\,dE. \end{aligned} \tag{5.83}$$

Finally, by using Eq. (5.72), the steady-state current through the non spin-degenerate system S can be calculated as

$$I = \frac{e}{h}\int dE\, Tr\left[\hat{\Gamma}_{\mathrm{R}}(E)\hat{G}^{+}_{\mathrm{S}}(E)\hat{\Gamma}_{\mathrm{L}}(E)\hat{G}^{-}_{\mathrm{S}}(E)\right]\cdot\left\{f_{\mathrm{L}}(E) - f_{\mathrm{R}}(E)\right\}. \tag{5.84}$$

Hence the steady state of S under an applied bias voltage is completely determined by Eq. (5.83) and Eq. (5.84).

Further, we will make two assumptions that significantly simplify the formalism:

1. The coupling to the probes is identical for all sites in the leads and it is equal to γ_{P}.

2. The wideband approximation is used for the probes, e.g. the local density of states of the probes is an energy-independent constant, $d_{\mathrm{P}_i}(E) = d$ for all $i \in \mathrm{L,R}$ and $g^{+}_{\mathrm{P}_i} = -\pi\imath d$.

With these assumptions, the expressions for the retarded self-energy $\hat{\Sigma}^{+}$ [Eq. (5.77)], the broadening matrices $\hat{\Gamma}_{\mathrm{L(R)}}$ [Eq. (5.82)] and the in-scattering self-energy $\hat{\Sigma}^{<}_{\mathrm{S}}$ [Eq. (5.81)]

can be re-written as

$$\hat{\Sigma}^{+} = -\frac{\imath}{2}\Gamma\left[\sum_{i\in \mathrm{L},\sigma} |i\,\sigma\rangle\langle\sigma\, i| + \sum_{i\in \mathrm{R},\sigma} |i\,\sigma\rangle\langle\sigma\, i|\right] = -\imath\frac{\Gamma}{2}\hat{I}_{\mathrm{L}} - \imath\frac{\Gamma}{2}\hat{I}_{\mathrm{R}}, \quad (5.85)$$

$$\hat{\Gamma}_{\mathrm{L(R)}} = \Gamma \sum_{i\in L(R)} |i\,\sigma\rangle\langle\sigma\, i| = \Gamma\hat{I}_{\mathrm{L(R)}}, \quad (5.86)$$

$$\hat{\Sigma}^{<}(E) = \imath\left[\hat{\Gamma}_{\mathrm{L}} f_{\mathrm{L}}(E) + \hat{\Gamma}_{\mathrm{R}} f_{\mathrm{R}}(E)\right] = \imath\Gamma\left[f_{\mathrm{L}}(E)\hat{I}_{\mathrm{L}} + f_{\mathrm{R}}(E)\hat{I}_{\mathrm{R}}\right], \quad (5.87)$$

where we introduced a new parameter

$$\Gamma = 2\pi\gamma_{\mathrm{P}}^{2} d. \quad (5.88)$$

It can be shown that the steady-state current and the density, calculated using the MPB approach, tend to coincide with those obtained by the NEGF method with semi-infinite electrodes, in the limit of infinitely long leads, e.g. for $l_\alpha \to +\infty$ where l_α is the length of the lead α ($\alpha = \mathrm{L}, \mathrm{R}$), and weak coupling to the probes ($\gamma_{\mathrm{P}} \to 0$). In order to demonstrate this, let us consider the reduced density matrix $\hat{\rho}_{\mathrm{C}}$ of the central region. The expression for $\hat{\rho}_{\mathrm{C}}$ has the same functional form as the one for $\hat{\rho}_{\mathrm{S}}$ [Eq. (5.83)], namely

$$\hat{\rho}_{\mathrm{C}} = \frac{1}{2\pi\imath}\int \hat{G}_{\mathrm{C}}^{+}(E)\,\hat{\sigma}^{<}(E)\hat{G}_{\mathrm{C}}^{-}(E)dE, \quad (5.89)$$

where $\hat{G}_{\mathrm{C}}^{+}(\hat{G}_{\mathrm{C}}^{-})$ is the retarded (advanced) GF of C and $\hat{\sigma}^{<}$ is the in-scattering self-energy of C in the presence of the electrodes. By directly using the results obtained in Section 5.4.4, these quantities can be calculated as

$$\hat{G}_{\mathrm{C}}^{\pm}(E) = \left[\lim_{\epsilon\to 0^{+}} (E \pm \imath\epsilon)\,\hat{I}_{\mathrm{C}} - \hat{H}_{\mathrm{C}} - \hat{\sigma}^{\pm}(E)\right]^{-1}, \quad (5.90)$$

$$\hat{\sigma}^{<}(E) = \imath\left[-2\Im\sigma_{\mathrm{L}}^{+}(E) f_{\mathrm{L}}(E) - 2\Im\sigma_{\mathrm{R}}^{+}(E) f_{\mathrm{R}}(E)\right]. \quad (5.91)$$

Here $\hat{\sigma}^{\pm} = \hat{\sigma}_{\mathrm{L}}^{\pm} + \hat{\sigma}_{\mathrm{R}}^{\pm}$ represents the self-energy of C due to the coupling to both electrodes, with $\hat{\sigma}_{\alpha}^{\pm}$ given by

$$\hat{\sigma}_{\alpha}^{\pm}(E) = \hat{H}_{\mathrm{C}\alpha}\,\hat{g}_{\alpha}^{\pm}(E)\,\hat{H}_{\alpha C}, \quad (5.92)$$

where $\hat{g}_{\alpha}^{+}(\hat{g}_{\alpha}^{-})$ is the retarded (advanced) GF of the electrode α for $\alpha = \mathrm{L}, \mathrm{R}$. So far the expressions for the GFs and self-energies of C are formally equivalent to the ones obtained by the NEGF method with semi-infinite leads. The only difference is that in the above equations $\hat{g}_{\alpha}^{\pm}$ corresponds not to the semi-infinite electrodes in isolation but to finite electrodes coupled to the probes. Thus the retarded (advanced) GF of the

lead α reads

$$\begin{aligned} \hat{g}_{\alpha}^{\pm}(E) &= \left[\lim_{\epsilon\to 0^{+}} (E \pm \imath\epsilon)\,\hat{I}_{\alpha} - \hat{H}_{\alpha} - \hat{\Sigma}_{\alpha}^{\pm}(E)\right]^{-1} = \\ &= \left[\lim_{\epsilon\to 0^{+}} (E \pm \imath\epsilon)\,\hat{I}_{\alpha} - \hat{H}_{\alpha} \pm \imath\frac{\Gamma}{2}\hat{I}_{\alpha}\right]^{-1}. \end{aligned} \tag{5.93}$$

In the limit of $\gamma_{\mathrm{P}} \to 0$, Γ becomes infinitesimal [see Eq. (5.88)] and if, in addition, we set $l_{\alpha} \to +\infty$, $\hat{g}_{\alpha}^{\pm}(E)$ in the above equation tends to coincide with the retarded (advanced) GF of the semi-infinite electrode [see Eq. (5.63)] and the NEGF result is recovered. Note, however, that as Γ is decreased and l_{α} is increased, Γ should remain larger than the typical energy level spacing in the electrodes. For one-dimensional (1D) TB electrodes, we can roughly estimate the average level spacing for the lead α as $\Delta e_{\alpha} \approx 4|\gamma_{\alpha}|/N_{\alpha}$, where γ_{α} is the hopping and N_{α} is the number of sites in α.

We would like to point out that the MPB method does not depart conceptually from the Landauer approach, in which the opposite poles of the external battery are considered as ideal reservoirs for electrons. However, in the MPB scheme the practical realization of the battery is different from that in the Landauer approach: instead of a pair of infinitely long leads, attached to the reservoirs at their infinite boarders, a large number of probes, or reservoirs, kept at equilibrium with well-defined chemical potentials, is distributed over the finite electrodes. The coupling to the probes, effectively introduced through the self-energies $\{\Sigma_i\}_{i\in\mathrm{L,R}}$, broadens each discrete energy level in the spectra of the electrodes by an amount given by Γ, turning them into metallic leads with continuous density of states. By simultaneously decreasing Γ and increasing l_{α}, an arbitrary good approximation to the two-terminal setup with infinitely long leads can be obtained (this point will be illustrated further by a practical example in Section 5.6). In technical terms, in the MPB method the calculation of the self-energies due to the coupling to L and R and, therefore, of the energy-dependent surface GFs of the semi-infinite leads is no longer required, since the effect of the external battery on the central region is determined solely by the coupling to the probes [see Eq. (5.85)]. This makes the MPB method very tractable computationally. Another important advantage of the MPB method is the possibility of introducing the wideband limit in the probes while retaining the realistic band structure of the electrodes, in particular their finite bandwidth (the importance of this point has been discussed in Ref. [282]). Finally, by using the MPB transport setup, it is possible to construct a theoretical and computational framework for time-dependent simulations of transport. This will be

discussed in the next section.

5.5.3 Time-dependent formalism

5.5.3.1 General case

Let us consider the system S (electrodes+device) and the ensemble of probes P combined. This combined system, which we refer to as S + P, is described by the time-dependent Hamiltonian $\hat{H}(t)$, which reads

$$\hat{H}(t) = \hat{H}_{\mathrm{S}}(t) + \hat{H}_{\mathrm{SP}}(t) + \hat{H}_{\mathrm{PS}}(t) + \hat{H}_{\mathrm{P}}, \tag{5.94}$$

where $\hat{H}_{\mathrm{S}}(t)$ is the Hamiltonian of S given by Eq. (5.78), $\hat{H}_{\mathrm{SP}}(t)$ and $\hat{H}_{\mathrm{PS}}(t)$ describe the coupling between S and P with $\hat{H}_{\mathrm{SP}}(t) = \hat{H}^{\dagger}_{\mathrm{PS}}(t)$, and $\hat{H}_{\mathrm{P}}$ is the Hamiltonian of the probes, which is assumed to be time-independent.

Further, we can re-group the terms composing the Hamiltonian $\hat{H}(t)$ into two parts as follows

$$\hat{H}_0(t) = \hat{H}_{\mathrm{S}}(t) + \hat{H}_{\mathrm{P}}, \tag{5.95}$$

$$\hat{V}(t) = \hat{H}_{\mathrm{SP}}(t) + \hat{H}_{\mathrm{PS}}(t), \tag{5.96}$$

where $\hat{H}_0(t)$ describes S and P in isolation, while $\hat{V}(t)$ contains the interactions between the two subsystems, and $\hat{H}(t) = \hat{H}_0(t) + \hat{V}(t)$.

The total Hamiltonian $\hat{H}(t)$ and the partial Hamiltonians $\hat{H}_0(t)$ and $\hat{V}(t)$ can be expressed in a matrix form as

$$\hat{H}(t) = \begin{pmatrix} \hat{H}_{\mathrm{S}}(t) & \hat{H}_{\mathrm{SP}}(t) \\ \hat{H}_{\mathrm{PS}}(t) & \hat{H}_{\mathrm{P}} \end{pmatrix}. \tag{5.97}$$

$$\hat{H}_0(t) = \begin{pmatrix} \hat{H}_{\mathrm{S}}(t) & 0 \\ 0 & \hat{H}_{\mathrm{P}} \end{pmatrix}, \tag{5.98}$$

$$\hat{V}(t) = \begin{pmatrix} 0 & \hat{H}_{\mathrm{SP}}(t) \\ \hat{H}_{\mathrm{PS}}(t) & 0 \end{pmatrix}. \tag{5.99}$$

Similarly, the density matrix $\hat{\rho}(t)$ of S + P is given by

$$\hat{\rho}(t) = \begin{pmatrix} \hat{\rho}_{\mathrm{S}}(t) & \hat{\rho}_{\mathrm{SP}}(t) \\ \hat{\rho}_{\mathrm{PS}}(t) & \hat{\rho}_{\mathrm{P}} \end{pmatrix}. \tag{5.100}$$

The equation of motion for $\hat{\rho}(t)$ reads

$$\imath\hbar\,\dot{\hat{\rho}}(t) = \left[\hat{H}(t), \hat{\rho}(t)\right]. \tag{5.101}$$

By re-writing the above equation in matrix form, using Eq. (5.97) and Eq. (5.100), we immediately obtain the equation of motion for the reduced density matrix of S

$$\begin{aligned} \imath\hbar\,\dot{\hat{\rho}}_{\mathrm{S}}(t) &= \hat{H}_{\mathrm{S}}(t)\,\hat{\rho}_{\mathrm{S}}(t) + \hat{H}_{\mathrm{SP}}(t)\,\hat{\rho}_{\mathrm{PS}}(t) - \hat{\rho}_{\mathrm{S}}(t)\,\hat{H}_{\mathrm{S}}(t) - \hat{\rho}_{\mathrm{SP}}(t)\,\hat{H}_{\mathrm{PS}}(t) = \\ &= \left[\hat{H}_{\mathrm{S}}(t), \hat{\rho}_{\mathrm{S}}(t)\right] + \underbrace{\hat{H}_{\mathrm{SP}}(t)\,\hat{\rho}_{\mathrm{PS}}(t) - \hat{\rho}_{\mathrm{SP}}(t)\,\hat{H}_{\mathrm{PS}}(t)}_{\mathrm{OB}}, \end{aligned} \tag{5.102}$$

where the last two terms are the open boundary (OB) terms stemming from the interaction between S and P. In order to calculate the OB terms we will use the time-evolution operator, or *propagator*, formalism (see Section 2.4.1 of Chapter 2).

Similarly to the formal solution of the time-dependent Schrödinger equation [see Eq. (2.27)], the solution of Eq. (5.101) can be written in terms of the time-evolution operator

$$\hat{\rho}(t) = \hat{U}(t, t_0)\hat{\rho}(t_0)\hat{U}^{\dagger}(t, t_0), \tag{5.103}$$

where t_0 is the initial time. We can also formally introduce the two-times density matrix $\hat{\rho}(t, \tau)$ such as

$$\hat{\rho}(t, \tau) = \hat{U}(t, t_0)\hat{\rho}(t_0)\hat{U}^{\dagger}(\tau, t_0), \tag{5.104}$$

where

$$\hat{\rho}(t, t) \equiv \hat{\rho}(t). \tag{5.105}$$

The operator $U(t, \tau)$ satisfies the following equations

$$\imath\hbar\,\frac{\partial\hat{U}(t, \tau)}{\partial t} = \hat{H}(t)\hat{U}(t, \tau), \tag{5.106}$$

$$\hat{U}(\tau, \tau) = \hat{I}, \tag{5.107}$$

where $\hat{I} = \hat{I}_{\rm S} + \hat{I}_{\rm P}$ is the identity operator for S + P. Note that $\hat{U}$ can be also written in the matrix form as

$$\hat{U}(t,\tau) = \begin{pmatrix} \hat{U}_{\rm S}(t,\tau) & \hat{U}_{\rm SP}(t,\tau) \\ \hat{U}_{\rm PS}(t,\tau) & \hat{U}_{\rm P}(t,\tau) \end{pmatrix}. \tag{5.108}$$

Importantly, $\hat{U}$ is the total *effective* propagator and its component $\hat{U}_{\rm S}$, for instance, describes the evolution of S in the presence of the probes. In contrast to this, one can introduce the total *free* propagator $\hat{U}_0$ such as

$$\hat{U}_0(t,\tau) = \begin{pmatrix} \hat{U}_{0\rm S}(t,\tau) & 0 \\ 0 & \hat{U}_{0\rm P}(t,\tau) \end{pmatrix}, \tag{5.109}$$

where the propagators $\hat{U}_{0\rm S}$ and $\hat{U}_{0\rm P}$ describe, respectively, the evolution of the subsystems S and P in isolation. The equations of motion for operators $\hat{U}_0$, $\hat{U}_{0\rm S}$ and $\hat{U}_{0\rm P}$ read

$$\imath\hbar \frac{\partial \hat{U}_0(t,\tau)}{\partial t} = \hat{H}_0(t)\hat{U}_0(t,\tau), \quad \hat{U}_0(\tau,\tau) = \hat{I}, \tag{5.110}$$

$$\imath\hbar \frac{\partial \hat{U}_{0\rm S}(t,\tau)}{\partial t} = \hat{H}_{\rm S}(t)\hat{U}_{0\rm S}(t,\tau), \quad \hat{U}_{0\rm S}(\tau,\tau) = \hat{I}_{\rm S}, \tag{5.111}$$

$$\imath\hbar \frac{\partial \hat{U}_{0\rm P}(t,\tau)}{\partial t} = \hat{H}_{\rm P}\,\hat{U}_{0\rm P}(t,\tau), \quad \hat{U}_{0\rm P}(\tau,\tau) = \hat{I}_{\rm P}. \tag{5.112}$$

Since $\hat{H}_{\rm P}$ is time-independent, the solution of Eq. (5.112) can be found easily and it is given by

$$\hat{U}_{0\rm P}(t,\tau) = e^{-\imath\hat{H}_{\rm P}(t-\tau)/\hbar}. \tag{5.113}$$

The perturbative expansion of the effective propagator $\hat{U}$ around the free propagator $\hat{U}_0$ leads to the equation analogous to the Dyson equation for the GF [Eq. (5.25)]

$$\hat{U}(t,\tau) = \hat{U}_0(t,\tau) + \frac{1}{\imath\hbar}\int_\tau^t \hat{U}_0(t,\tau')\hat{V}(\tau')\hat{U}(\tau',\tau)d\tau' = \tag{5.114}$$

$$= \hat{U}_0(t,\tau) + \frac{1}{\imath\hbar}\int_\tau^t \hat{U}(t,\tau')\hat{V}(\tau')\hat{U}_0(\tau',\tau)d\tau'. \tag{5.115}$$

In Appendix B we provide the proof of Eq. (5.115) obtained by using the Leibniz integral rule. Similar equations can be written for the Hermitian conjugate of $\hat{U}$

$$\hat{U}^\dagger(t,\tau) = \hat{U}_0^\dagger(t,\tau) - \frac{1}{\imath\hbar}\int_\tau^t \hat{U}_0^\dagger(\tau',\tau)\hat{V}(\tau')\hat{U}^\dagger(t,\tau')d\tau' = \tag{5.116}$$

$$= \hat{U}_0^\dagger(t,\tau) - \frac{1}{\imath\hbar}\int_\tau^t \hat{U}^\dagger(\tau',\tau)\hat{V}(\tau')\hat{U}_0^\dagger(t,\tau')d\tau'. \tag{5.117}$$

Note that the above equations can be conveniently written in the matrix form by using the matrix representations of $\hat{U}$ and $\hat{U}_0$ [see Eq. (5.108) and Eq. (5.109)], leading to separate expressions for each of the propagators $\hat{U}_{\rm S}$, $\hat{U}_{\rm P}$, $\hat{U}_{\rm SP}$ and $\hat{U}_{\rm PS}$. By substituting these expressions into Eq. (5.103), one can derive the equation for $\hat{\rho}_{\rm SP}(t)$, which is necessary to calculate the OB terms in Eq. (5.102). The details of the derivation are presented in Appendix B and here we only show the final result

$$\hat{\rho}_{\rm SP}(t) = \hat{U}_{\rm SP}(t,t_0)\hat{\rho}_{\rm P}(t_0)\hat{U}_{0\rm P}(t,t_0) - \frac{1}{\imath\hbar}\int_{t_0}^{t}\hat{\rho}_{\rm S}(t,\tau)\hat{H}_{\rm SP}(\tau)\hat{U}_{0\rm P}(t,\tau)d\tau. \tag{5.118}$$

By multiplying the above equation by $\hat{H}_{\rm PS}(t)$ and by using the perturbation expansion for $\hat{U}_{\rm SP}$ [see Eq. (B.13) in Appendix B], we find

$$\begin{aligned}\hat{\rho}_{\rm SP}(t)\hat{H}_{\rm PS}(t) \;=\; & \frac{1}{\imath\hbar}\int_{t_0}^{t}\hat{U}_{\rm S}(t,\tau)\hat{H}_{\rm SP}(\tau)\hat{U}_{0\rm P}(\tau,t_0)\hat{\rho}_{\rm P}(t_0)\hat{U}_{0\rm P}^{\dagger}(t,t_0)\hat{H}_{\rm PS}(t)d\tau - \\ & -\frac{1}{\imath\hbar}\int_{t_0}^{t}\hat{\rho}_{\rm S}(t,\tau)\hat{H}_{\rm SP}(\tau)\hat{U}_{0\rm P}^{\dagger}(t,\tau)\hat{H}_{\rm PS}(t)d\tau.\end{aligned} \tag{5.119}$$

By using Eq. (5.114) one can also show that the propagator $\hat{U}_{\rm S}(t,\tau)$ satisfies

$$\hat{U}_{\rm S}(t,\tau) = \hat{U}_{0\rm S}(t,\tau) + \frac{1}{\imath\hbar}\int_{\tau}^{t}\hat{U}_{0\rm S}(t,\tau')\hat{H}_{\rm SP}(\tau')\hat{U}_{\rm PS}(\tau',\tau)d\tau'. \tag{5.120}$$

By using the expression for $\hat{U}_{\rm PS} = \hat{U}_{\rm SP}^{\dagger}$, we obtain

$$\begin{aligned}\hat{U}_{\rm S}(t,\tau) = \hat{U}_{0\rm S}(t,\tau) \;+\; & \left(\frac{1}{\imath\hbar}\right)^2\int_{\tau}^{t}d\tau'\int_{\tau}^{\tau'}d\tau''\hat{U}_{0\rm S}(t,\tau')\hat{H}_{\rm SP}(\tau')\times \\ & \times\hat{U}_{0\rm P}(\tau',\tau'')\hat{H}_{\rm PS}(\tau'')\hat{U}_{\rm S}(\tau'',\tau).\end{aligned} \tag{5.121}$$

Equation (5.119), with $\hat{U}_{\rm S}(t)$ given by Eq. (5.121), can be used to calculate the OB terms in the equation of motion for the density matrix S [see Eq. (5.102)]. We will further elaborate on these equations below.

5.5.3.2 Approximations

Wideband limit in the probes

We will now try to simplify Eq. (5.119) for the OB term $\hat{\rho}_{\mathrm{SP}}(t)\hat{H}_{\mathrm{PS}}(t)$ and Eq. (5.121) for the propagator $\hat{U}_{\mathrm{S}}$. Let us introduce

$$K_1(\tau,t) \equiv \hat{H}_{\mathrm{SP}}(\tau)\hat{U}_{0\mathrm{P}}(\tau,t_0)\hat{\rho}_{\mathrm{P}}(t_0)\hat{U}^{\dagger}_{0\mathrm{P}}(t,t_0)\hat{H}_{\mathrm{PS}}(t), \tag{5.122}$$

$$K_2(\tau,t) \equiv \hat{H}_{\mathrm{SP}}(\tau)\hat{U}^{\dagger}_{0\mathrm{P}}\hat{H}_{\mathrm{PS}}(t). \tag{5.123}$$

It follows from Eq. (5.113) that

$$\hat{U}^{\dagger}_{0\mathrm{P}}(t,\tau) = e^{\imath\hat{H}_{\mathrm{P}}(t-\tau)}. \tag{5.124}$$

Formally, the operator $e^{\imath\hat{H}_{\mathrm{P}}t/\hbar}$ is the inverse Fourier transform of the density of states operator of the probes, which is given by

$$\hat{d}_{\mathrm{P}}(E) = \delta(E-\hat{H}_{\mathrm{P}}) = \sum_{\mathrm{P}} |\mathrm{P}\rangle\delta(E-E_{\mathrm{P}})\langle P|, \tag{5.125}$$

where $|\mathrm{P}\rangle$ and E_{P} are the eigenvectors and the eigenvalues of $\hat{H}_{\mathrm{P}}$, respectively. Indeed, we can write

$$\begin{aligned}\int \hat{d}_{\mathrm{P}}(E)e^{\imath Et/\hbar}\,dE &\equiv \int \delta(E-\hat{H}_{\mathrm{P}})e^{\imath Et/\hbar}\,dE = \\ &= \int \delta(E-\hat{H}_{\mathrm{P}})e^{\imath(E-\hat{H}_{\mathrm{P}})t/\hbar}e^{\imath\hat{H}_{\mathrm{P}}t/\hbar}\,dE = \\ &= e^{\imath\hat{H}_{\mathrm{P}}t/\hbar},\end{aligned} \tag{5.126}$$

where we used the fact that the Fourier transform of the Dirac delta function is unity. The density of states operator of P can be also written as

$$\hat{d}_{\mathrm{P}}(E) = \sum_{i\in\mathrm{L(R)},\sigma} |i\,\sigma\rangle d_{\mathrm{P}_i}(E)\langle\sigma\,i|\,, \tag{5.127}$$

since we still consider the situation when each probe P_i is coupled to only one atom i in the electrodes. Thus we obtain

$$K_2(\tau,t) = \hat{H}_{\mathrm{SP}}(\tau)\left[\int_{-\infty}^{+\infty}\left\{\sum_{i\in\mathrm{L(R)}} d_{\mathrm{P}_i}(E)\right\}e^{iE(t-\tau)/\hbar}\,dE\right]\hat{H}_{\mathrm{PS}}(t). \tag{5.128}$$

As a next step, we impose the wideband limit in the probes, e.g. $d_{\mathrm{P}_i} = d$. The above expression now reads

$$K_2(\tau,t) = \gamma_{\mathrm{P}}^2(t) d \left(\hat{I}_{\mathrm{L}} + \hat{I}_{\mathrm{R}}\right) \underbrace{\left[\int_{-\infty}^{+\infty} e^{\imath E(t-\tau)/\hbar}\, dE\right]}_{=2\pi\hbar\delta(t-\tau)} = 2\imath\hbar\,\hat{\Sigma}^{+}\delta(t-\tau), \tag{5.129}$$

where we used the explicit expression for the coupling Hamiltonian, $\hat{H}_{\mathrm{SP}} = \hat{H}_{\mathrm{PS}}^{\dagger} = \gamma_{\mathrm{P}}(t)\left[\hat{I}_{\mathrm{L}} + \hat{I}_{\mathrm{R}}\right]$ and introduced the time-dependent self-energy $\hat{\Sigma}^{\pm}(t)$ such as

$$\hat{\Sigma}^{+}(t) = -\imath\frac{\Gamma(t)}{2}\cdot\left(\hat{I}_{\mathrm{L}} + \hat{I}_{\mathrm{R}}\right), \tag{5.130}$$

$$\hat{\Sigma}^{-}(t) = \hat{\Sigma}^{+}(t)^{\dagger} = \imath\frac{\Gamma(t)}{2}\cdot\left(\hat{I}_{\mathrm{L}} + \hat{I}_{\mathrm{R}}\right), \tag{5.131}$$

with $\Gamma(t) = 2\pi\gamma_{\mathrm{P}}^2(t)d$. Note that we assume that the coupling γ_{P} is the same for all probes but we let it be time-dependent for now.

We can use similar arguments to calculate $K_1(\tau,t)$ [Eq. (5.122)]. In addition, we employ the following initial conditions for the density matrix of the probes

$$\hat{\rho}_{\mathrm{P}}(t_0) = \sum_{i\in\mathrm{L,R}}\int_{-\infty}^{+\infty} f_{\mathrm{P}_i}(E)\hat{d}_{\mathrm{P}_i}(E)\,dE = \int_{-\infty}^{+\infty} d\left[f_{\mathrm{L}}(E)I_{\mathrm{L}} + f_{\mathrm{R}}(E)\hat{I}_{\mathrm{R}}\right]\,dE, \tag{5.132}$$

where $f_{\mathrm{P}_i}(E) = f_{\mathrm{L(R)}}(E)$ for $i \in \mathrm{L(R)}$. This leads to the following expression for $K_1(\tau,t)$

$$\begin{aligned} K_1(\tau,t) &= \int_{-\infty}^{+\infty} \gamma_{\mathrm{P}}(\tau)\gamma_{\mathrm{P}}(t)d^2\, e^{\imath E(t-\tau)/\hbar}\left[f_{\mathrm{L}}(E)\hat{I}_{\mathrm{L}} + f_{\mathrm{R}}(E)\hat{I}_{\mathrm{R}}\right]\,dE = \\ &= \frac{1}{2\pi\imath}\int_{-\infty}^{+\infty} e^{\imath E(t-\tau)/\hbar}\,\hat{\Sigma}_{\tau t}^{<}(E)\,dE, \end{aligned} \tag{5.133}$$

where

$$\hat{\Sigma}_{\tau t}^{<}(E) = \imath\,\mathrm{sgn}\left[\gamma_{\mathrm{P}}(\tau)\right]\mathrm{sgn}\left[\gamma_{\mathrm{P}}(\tau)\right]\sqrt{\Gamma(\tau)\Gamma(t)}\left[f_{\mathrm{L}}(E)\hat{I}_{\mathrm{L}} + f_{\mathrm{R}}(E)\hat{I}_{\mathrm{R}}\right]. \tag{5.134}$$

For time-independent coupling $\hat{\Sigma}_{\tau t}^{<}(E) = \hat{\Sigma}(E)$ [see Eq. (5.87)]. Note that our definition of the self-energy slightly departs from that in Ref. [171], where the factor $\frac{1}{2\pi\imath}$ is incorporated into $\hat{\Sigma}_{\tau t}^{<}(E)$.

By inserting the expressions for K_1 and K_2 into Eq. (5.119) and Eq. (5.121), we obtain

$$\begin{aligned}\hat{\rho}_{\mathrm{SP}}(t)\hat{H}_{\mathrm{PS}}(t) &= \frac{1}{\imath\hbar}\int_{t_0}^{t}\hat{U}_{\mathrm{S}}(t,\tau)K_1(\tau,t)d\tau - \frac{1}{\imath\hbar}\int_{t_0}^{t}\hat{\rho}_{\mathrm{S}}(t,\tau)K_2(\tau,t)d\tau = \\ &= \frac{1}{\imath\hbar}\left(\frac{1}{2\pi\imath}\right)\int_{t_0}^{t}d\tau\int_{-\infty}^{+\infty}dE\,e^{\imath E(t-\tau)/\hbar}\hat{U}_{\mathrm{S}}(t,\tau)\hat{\Sigma}^{<}_{\tau t}(E) + \\ &\quad + \underbrace{\int_{t_0}^{t}\hat{\rho}_{\mathrm{S}}(t,\tau)\hat{\Sigma}^{-}(t)\delta(t-\tau)d\tau}_{\to\hat{\rho}_{\mathrm{S}}(t)\hat{\Sigma}^{-}(t)}. \qquad (5.135)\end{aligned}$$

and

$$\begin{aligned}\hat{U}_{\mathrm{S}}(t,\tau) &= \hat{U}_{0\mathrm{S}}(t,\tau) + \left(\frac{1}{\imath\hbar}\right)^2\int_{\tau}^{t}d\tau'\int_{\tau}^{\tau'}d\tau''\hat{U}_{0\mathrm{S}}(t,\tau')K_2(\tau',\tau'')\hat{U}_{\mathrm{S}}(\tau'',\tau) = \\ &= \hat{U}_{0\mathrm{S}}(t,\tau) + \frac{1}{\imath\hbar}\int_{\tau}^{t}\hat{U}_{0\mathrm{S}}(t,\tau')\hat{\Sigma}^{+}(\tau')\hat{U}_{\mathrm{S}}(\tau',\tau)d\tau'. \qquad (5.136)\end{aligned}$$

The last equation is essentially an expansion of $\hat{U}_{\mathrm{S}}$ around a perturbation $\hat{\Sigma}^{+}$. This suggests that the propagator $\hat{U}_{\mathrm{S}}$ obeys the following equation

$$\imath\hbar\frac{\partial\hat{U}(t,\tau)}{\partial t} = \left[\hat{H}_{\mathrm{S}}(t) + \hat{\Sigma}^{+}(t)\right]\hat{U}_{\mathrm{S}}(t,\tau), \qquad (5.137)$$

where $\hat{H}_{\mathrm{S}}(t)+\hat{\Sigma}^{+}(t)$ is an effective Hamiltonian for S with a self-energy $\hat{\Sigma}^{+}$ [Eq. (5.92)] due to the coupling to the probes.

Finally, by using Eq. (5.135), the equation of motion for the system S [Eq. (5.102)] can be written as

$$\begin{aligned}\imath\hbar\dot{\hat{\rho}}_{\mathrm{S}}(t) &= \left[\hat{H}_{\mathrm{S}}(t),\hat{\rho}_{\mathrm{S}}(t)\right] - \left[\hat{\rho}_{\mathrm{S}}(t)\hat{\Sigma}^{-}(t) - \mathrm{h.c.}\right] - \\ &- \left[\frac{1}{\imath\hbar}\left(\frac{1}{2\pi\imath}\right)\int_{t_0}^{t}d\tau\int_{-\infty}^{+\infty}dE\,e^{\imath E(t-\tau)/\hbar}\,\hat{U}_{\mathrm{S}}(t,\tau)\,\hat{\Sigma}^{<}_{\tau t} - h.c.\right], \qquad (5.138)\end{aligned}$$

with $\hat{U}_{\mathrm{S}}(t,\tau)$ given by Eq. (5.136). The first two terms after the commutator on the right-hand side of the equation are *extraction*, or *drain* terms, which are responsible for the loss of the electrons in the probes. The last two terms are *injection*, or *source* terms, which are responsible for injection of the electrons from the probes into S.

In the case of time-independent Hamiltonian $\hat{H}_{\mathrm{S}}$ and time-independent coupling γ_{P}, the propagator $\hat{U}_{\mathrm{S}}$ and, therefore, the injection terms (IT), can be easily calculated.

However, in the case of the time-dependent Hamiltonian, IT remain non-local in time and need to be approximated. Such approximation will be discussed below.

Dephasing factor

The main idea behind the approximate result for IT is to introduce a *dephasing factor* $e^{-(t-\tau)/\tau_\Delta}$ so that the last two terms in Eq. (5.138) read

$$-\left[\frac{1}{\imath\hbar}\left(\frac{1}{2\pi\imath}\right)\int_{t_0}^{t} d\tau \int_{-\infty}^{+\infty} dE\, e^{\imath E(t-\tau)/\hbar}\underbrace{e^{-(t-\tau)/\tau_\Delta}}\hat{U}_{\mathrm{S}}(t,\tau)\,\hat{\Sigma}^{<}_{\tau t} - h.c.\right], \tag{5.139}$$

where τ_Δ corresponds to an energy scale $\Delta = \hbar/\tau_\Delta$. We also assume that the coupling $\gamma_{\mathrm{P}}(t)$ has been switched on over some early period to a constant value γ_{P}, so that $\Gamma(t)$ has been replaced by Γ and $\hat{\Sigma}^{<}_{\tau t}$ by $\hat{\Sigma}^{<}$. The dephasing factor can be interpreted in two ways:

1. The *relaxation time* τ_Δ introduces dephasing, or decoherence in the injection process so that the injection of electrons from the probes into the leads is decoupled, over the time interval τ_Δ, from the subsequent scattering of electrons by the time-dependent potential in the interior of the central region. This imposes a restriction on the size of the central region and therefore in practical calculations for 1D systems we will always introduce a number of additional buffer sites (N_{d}) on both sides of the device. The value of Δ is determined in such a way that the distance traveled by electrons during the time interval $\tau_\Delta = \Delta/\hbar$ is smaller than the distance between the electrodes and the interior of the central region, e.g. $v_e\tau_\Delta < N_{\mathrm{d}}\, a$, where v_e is the electron group velocity and a is the lattice constant ($a = 1$ in our calculations).

2. It can be shown (see Appendix B and Ref. [171]) that the introduction of the dephasing factor in IT is equivalent to replacing the Fermi-Dirac distributions $f_{\mathrm{L(R)}}(E)$ of the probes by fictitious distributions $\tilde{f}_{\mathrm{L(R)}}(E)$, which have the same chemical potentials $\mu_{\mathrm{L(R)}}$ but are broadened by an amount 2Δ, compared to $f_{\mathrm{L(R)}}(E)$. The consequence of this is an additional broadening, proportional to Δ, in the I-V characteristics calculated with the time-dependent MPB method, compared to the steady-state MPB and the standard NEGF formalism with semi-infinite electrodes.

The advantage of introducing the dephasing factor is that the non-locality in IT can be eliminated. Let us decompose the Hamiltonian of S into two terms, one of which, $\hat{H}_{\mathrm{S}_0}$,

is time-independent while the other, $\hat{v}(t)$, is time-dependent but operates only in the interior of C. Similarly to Eq. (5.115), we can write down the perturbation expansion of $\hat{U}_{\mathrm{S}}$ around $\hat{U}_{\mathrm{S}_0}$

$$\hat{U}_{\mathrm{S}}(t,\tau) = \hat{U}_{\mathrm{S}_0}(t,\tau) + \frac{1}{\imath\hbar}\int_{\tau}^{t} \hat{U}_{\mathrm{S}}(t,\tau')\hat{v}(\tau')\hat{U}_{\mathrm{S}_0}(\tau',\tau), \tag{5.140}$$

where $\hat{U}_{\mathrm{S}_0}(t,\tau) = e^{-\imath\left[\hat{H}_{\mathrm{S}_0}+\Sigma^{+}\right](t-\tau)/\hbar}$. By inserting the above equation into the expression for IT, we obtain a new expression for the first of the Hermitian conjugate terms in Eq. (5.139). Denoted as IT_1, this term reads

$$\begin{aligned}\mathrm{IT}_1 = & -\frac{1}{\imath\hbar}\left(\frac{1}{2\pi\imath}\right)\int_{t_0}^{t} d\tau \int_{-\infty}^{+\infty} dE\, e^{\imath E(t-\tau)/\hbar} e^{-(t-\tau)/\tau_\Delta}\, \hat{U}_{\mathrm{S}_0}(t,\tau)\,\hat{\Sigma}^{<}(E) - \\ & -\left(\frac{1}{\imath\hbar}\right)^2\left(\frac{1}{2\pi\imath}\right)\int_{t_0}^{t} d\tau \int_{\tau}^{t} d\tau' \int_{-\infty}^{+\infty} dE\, e^{\imath E(t-\tau)/\hbar} e^{-(t-\tau)/\tau_\Delta}\, \hat{U}_{\mathrm{S}}(t,\tau') \times \\ & \times \underbrace{\hat{v}(\tau')\,\hat{U}_{\mathrm{S}_0}(\tau',\tau)\,\hat{\Sigma}^{<}(E)}_{\to 0}. \end{aligned} \tag{5.141}$$

The combination of the last three terms in the integral kernel expresses the probability amplitude for a signal to be transmitted over the time-interval $\tau - \tau'$ from the point in L or R to the interior of C, where the time-dependent scattering potential $\hat{v}(t)$ operates. Since $\tau' \leq t$ due to the limits of integration, we have $\tau' - \tau \leq t - \tau$. However, the introduction of the dephasing factor effectively imposes $\tau' - \tau \geq \tau_\Delta$, which prevents the electrons injected into the leads from arriving to the interior of C over the time $\tau' - \tau$. This yields $t - \tau > \tau_\Delta$ and, due to the exponent $e^{-(t-\tau)/\tau_\Delta}$, which is significant only for $t - \tau < \tau_\Delta$, the second term in Eq. (5.141) disappears. The first term can be further re-arranged as follows

$$\begin{aligned} & -\frac{1}{\imath\hbar}\left(\frac{1}{2\pi\imath}\right)\int_{t_0}^{t} d\tau \int_{-\infty}^{+\infty} dE\, e^{\imath E(t-\tau)/\hbar} e^{-(t-\tau)/\tau_\Delta} e^{-\imath\left[\hat{H}_{\mathrm{S}_0}+\Sigma^{+}\right](t-\tau)/\hbar}\,\hat{\Sigma}^{<}(E) = \\ & = -\frac{1}{\imath\hbar}\left(\frac{1}{2\pi\imath}\right)\int_{t_0}^{t} d\tau \int_{-\infty}^{+\infty} dE\, e^{\frac{\imath(t-\tau)}{\hbar}\cdot\left[E-\hat{H}_{\mathrm{S}_0}-\hat{\Sigma}^{+}+\imath\hat{I}\Delta\right]}\,\hat{\Sigma}^{<}(E) = \\ & = -\frac{1}{\imath\hbar}\left(\frac{1}{2\pi\imath}\right)\int_{-\infty}^{+\infty} dE\,\hat{\Sigma}^{<}(E)\frac{\hbar}{\imath}\underbrace{\left[E-\hat{H}_{\mathrm{S}_0}-\hat{\Sigma}^{+}+\imath\hat{I}\Delta\right]^{-1}}_{=\hat{\hat{G}}_{\mathrm{S}}^{+}}\times \\ & \qquad \times e^{\frac{\imath(t-\tau)}{\hbar}\cdot\left[E-\hat{H}_{\mathrm{S}_0}-\hat{\Sigma}^{+}+\imath\hat{I}\Delta\right]}\Big|_{t_0}^{t} = \\ & = -\frac{1}{2\pi\imath}\int_{-\infty}^{+\infty} \hat{\hat{G}}_{\mathrm{S}}^{+}(E)\hat{\Sigma}^{<}(E)\,dE, \end{aligned} \tag{5.142}$$

where

$$\hat{\tilde{G}}_{\mathrm{S}}^{\pm}(E) = \left[E - \hat{H}_{\mathrm{S}_0} - \hat{\Sigma}^{\pm} \pm \imath\hat{I}\Delta\right]^{-1}. \tag{5.143}$$

Finally, bringing together the expressions for the injection and the extraction term, the equation of motion for $\hat{\rho}_{\mathrm{S}}$ reads

$$\begin{aligned} \imath\hbar\dot{\hat{\rho}}_{\mathrm{S}}(t) &= \left[\hat{H}_{\mathrm{S}}(t), \hat{\rho}_{\mathrm{S}}(t)\right] + \hat{\Sigma}^{+}\hat{\rho}_{\mathrm{S}}(t) - \hat{\rho}_{\mathrm{S}}(t)\hat{\Sigma}^{-} + \\ &\quad + \int_{-\infty}^{+\infty} \frac{1}{2\pi\imath}\left[\hat{\Sigma}^{<}(E)\hat{\tilde{G}}_{\mathrm{S}}^{-}(E) - \hat{\tilde{G}}_{\mathrm{S}}^{+}(E)\hat{\Sigma}^{<}(E)\right] dE. \end{aligned} \tag{5.144}$$

Note that we kept the factor $1/2\pi\imath$ instead of incorporating it into $\hat{\Sigma}^{<}$, which is purely imaginary according to our definition [see Eq. (5.87)]. As discussed in Ref. [171], we will set $\Delta = \Gamma/2$ in order to have only one free parameter instead of two. The initial density matrix $\hat{\rho}_{\mathrm{S}}(t_0)$ is constructed from the eigenstates of $\hat{H}_{\mathrm{S}}$ for the system S, which is in equilibrium and disconnected from the probes at the initial time. The equation of motion is integrated numerically using the same time-integration scheme that was used for the dynamic simulations in closed systems (see Section 2.4.4). In addition to the usual commutator in the equation of motion one needs to compute the OB terms. In practice, the coupling to the probes, which enters both injection and extraction terms and is effectively given by Γ, is switched on gradually over a short period of time τ_{Γ} ($\tau_{\Gamma} = 5$ fs in all our simulations) and it is maintained constant afterwards, e.g. $\Gamma(t) = \Gamma$ for $t \geq \tau_{\Gamma}$. The extraction terms are evaluated at each time-step through the time-dependent density matrix $\hat{\rho}_{\mathrm{S}}(t)$ multiplied by $\hat{\Sigma}^{\pm}$. In contrast, the injection terms are time-independent and can be calculated prior to the simulation for a fixed value of the applied bias voltage V, which enters the injection terms through the Fermi-Dirac distributions of the probes embedded in the in-scattering self-energy $\hat{\Sigma}^{<}$ [see Eq. (5.87)]. Another technical detail that makes the calculation of the source terms very straightforward is that in the expression for the retarded (advanced) GF of S [see Eq. (5.143)] the denominator has a finite energy-independent imaginary term $\imath\Delta$ (in addition, $\hat{\Sigma}^{\pm}$ is also imaginary and energy-independent in the wideband limit). This means that $\hat{\tilde{G}}_{\mathrm{S}}^{\pm}(E)$ does not have poles on the real axis and the integration over the energy can be easily performed. In contrast, in standard NEGF calculations of steady-state density and current one deals with the poles of the GFs on the real energy axis, which can be done by performing the integration over the complex contour and by using the Cauchy's residue theorem.

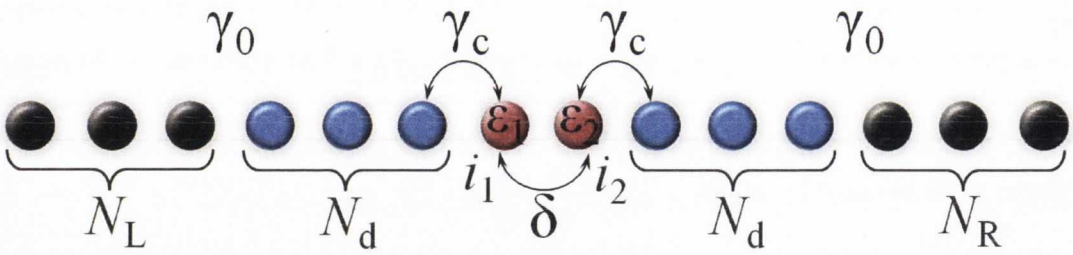

FIGURE 5.6: Test system A. The central region consists of two atoms at positions i_1 and i_2, with the on-site energies ε_1 and ε_2 and the hopping δ between them, embedded in a $2N_{\rm d}$-sites long mono-atomic chain. The electrodes are 1D chains, attached to the left and to the right of the central region. N_α is the number of sites in the lead α, $\alpha = {\rm L, R}$. The hopping in the electrodes and in the chain is the same and is equal to γ_0. The hopping between each atom of the dimer and the neighboring atom is denotes as $\gamma_{\rm c}$.

5.6 Test simulations

5.6.1 Resonant dimer

In order to demonstrate the functionality of the MPB method in both the steady state (SS) and the time-dependent (TD) regimes, we perform test simulations for the system presented in Fig. 5.6. The figure shows only the system S, e.g. electrodes+device, and the electrodes are assumed to be connected to the probes as in the general MPB setup depicted in Fig. 5.5. The central region consists of the dimer, e.g. of two atoms at positions i_1 and i_2, surrounded by two identical atomic chains, having $N_{\rm d}$ atoms each. The electrodes L and R are also modeled as 1D atomic chains with $N_{\rm L}$ and $N_{\rm R}$ atoms, respectively. Each atom in L and R is connected to an external probe. The entire system S is described by a single-band nearest-neighbors TB Hamiltonian [see, for example, Eq. (2.52)] with the following parameters: (a) γ_0 is the hopping in the electrodes and in the chain, (b) δ is the intra-dimer hopping, (c) $\gamma_{\rm c}$ is the hopping between each atom of the dimer and the neighboring atom of the atomic chain, (d) ε_1 and ε_2 are the on-site energies of the dimer atoms (the on-site energies of all other atoms in S are set to zero and so it is for the Fermi energy $E_{\rm F}$).

Figure 5.7 shows the differential conductance of the dimer calculated using SS MPB method for three different configurations of the transport setup. The red curve corresponds to the MPB setup with $N_{\rm L} = N_{\rm R} = 40$, $N_{\rm d} = 20$ and $\Gamma = 0.3$ eV (note that the broadening Γ is in the units of energy) while the green one to the setup with the same

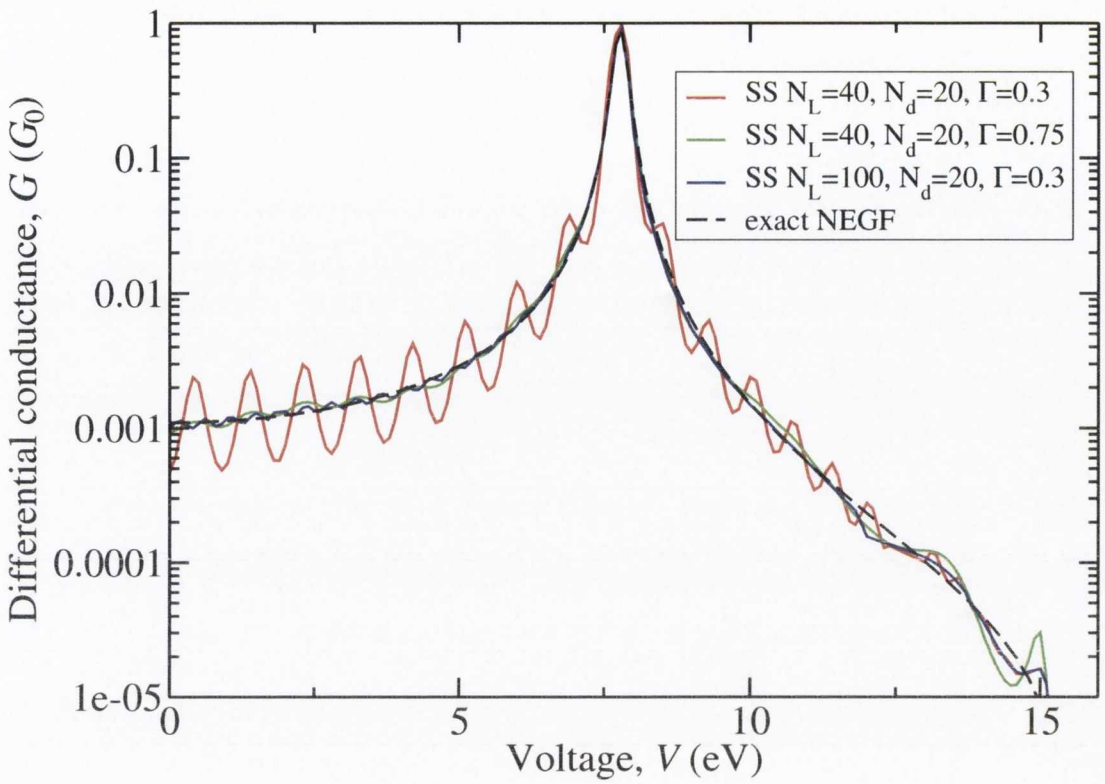

FIGURE 5.7: Differential conductance $G = dI/dV$ of the dimer in the units of $G_0 = 2e^2/h$ as a function of the applied bias voltage V, calculated with SS MPB method for three different sets of parameters of the MPB transport setup. The black-dashed line shows the exact NEGF result. The following parameters in the TB Hamiltonian of S are used: $\gamma_0 = \delta = -3.88$ eV, $\gamma_{\mathrm{c-d}} = -0.5$ eV, $\varepsilon_1 = \varepsilon_2 = 0$. The bias is applied symmetrically, e.g. $\mu_{\mathrm{L(R)}} = \pm V/2$.

lengths of the electrodes and the buffer region but with $\Gamma = 0.75$ eV. In contrast, the differential conductance shown in blue was obtained for the MPB setup with long leads, namely for $N_{\mathrm{L}} = N_{\mathrm{R}} = 100$, $N_{\mathrm{d}} = 20$ and $\Gamma = 0.3$ eV. All three results are compared to the one calculated using the steady-state NEGF method with semi-infinite electrodes, which we refer to as "exact NEGF". For this we used the formalism, discussed in Section 5.4.4, with the current given by Eq. (5.72) and the retarded GF of the semi-infinite 1D TB electrodes calculated via a well-known analytical formula [17, 229]

$$g_\alpha^+(E) = \frac{1}{2\gamma_\alpha^2}\left[E - \varepsilon_\alpha \pm \sqrt{(E-\varepsilon_\alpha)^2 - 4\gamma_\alpha^2}\right], \tag{5.145}$$

where γ_α is the hopping integral in the lead α and ε_α is the on-site energy for all atoms in α. For the system considered here $\gamma_\alpha = \gamma_0$ and $\varepsilon_\alpha = 0$ for $\alpha = \mathrm{L}, \mathrm{R}$. The convention for the sign in front of the square root in Eq. (5.145) is the following: "+" for $E > \varepsilon_\alpha - 2|\gamma_\alpha|$ and "-" for $E < \varepsilon_\alpha - 2|\gamma_\alpha|$.

A noticeable feature in Fig. 5.7 are the oscillations in the differential conductance (red curve) for relatively small N_{L} and small Γ, which is due to the large energy-level spacing in the leads. The oscillations can be significantly suppressed by either increasing Γ for a fixed N_{L} (green curve) or by increasing N_{L} for a fixed Γ (blue curve). The first option is equivalent to introducing a large artificial broadening in the sparse energy-level structure of the electrodes, which, strictly speaking, is not a good approximation to infinitely long leads with continuous spectrum. The other possibility, in which the electrodes are long and Γ is small, indeed offers an approximate solution to the electronic transport problem in the two-terminal setup and the differential conductance calculated in this way is close to that obtained with the exact NEGF.

Further, we use the TD MPB method to calculate the I-V characteristics of the resonant dimer. The results are presented in Fig. 5.8. Again, we use three different sets of parameters for the transport setup. The current through the dimer is calculated as a bond-current through the bond (i_2, i_2+1) [see Eq. 2.60]. The value of the steady-state current for each bias voltage V is obtained from the time-dependent simulation for the corresponding value of V after the steady-state has been established, i.e. when the variation of the current with time becomes negligible (see the inset of Fig. 5.8). The I-V curves constructed in this way are compared to the I-V calculated with SS MPB method for one set of parameters from the previous calculation (see Fig. 5.7). Note that the SS MPB result matches perfectly (on the scale of the graph) the exact NEGF result.

As one can see from Fig. 5.8, in the case of TD MPB the I-V curves have an additional broadening (at resonance) compared to exact NEGF and SS MPB. The broadening is due to the relaxation-time approximation, which was used to derive the equation of motion for $\hat{\rho}_{\mathrm{S}}$ with temporally local extraction terms and time-independent injection terms (see Section 5.5.3.2). The amount of broadening is controlled by $\Delta = \Gamma/2$, therefore as Γ is decreased the agreement between TD MBP and exact NEGF improves. Note that at the same time as Γ is decreased, we increase the length of the electrodes in order to keep a good approximation to the two-terminal setup with semi-infinite leads.

The effect of the dephasing factor on the steady-state transport within TD MPB approach is further illustrated in Fig. 5.9, where we plot the differential conductance of the dimer as a function of the bias voltage for the same parameters as in Fig. 5.8. In the case of exact NEGF the differential conductance approaches $G_0 = 2e^2/h$ at resonance, however, in the case of TD MPB the conductance peak broadens and its

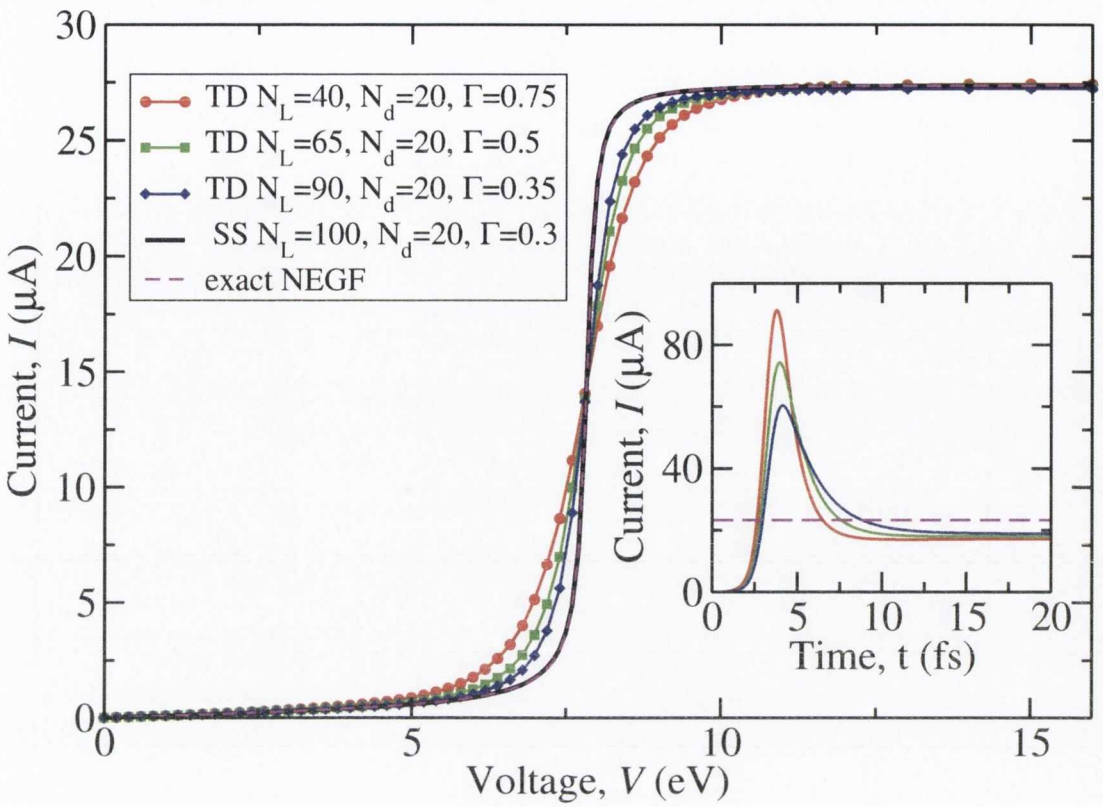

FIGURE 5.8: Current I through the dimer as a function of the applied bias voltage V, calculated with TD MPB method for three sets of parameters and with SS MPB method for one set of parameters. The dashed line shows, for comparison, the exact NEGF result. The inset displays the time evolution of the current for $V = 8$ eV for all three configurations of the TD MPB setup. A horizontal dashed line represents the value of the steady-state current, obtained with exact NEGF for the same value of V, which coincides, on the scale of the graph, with the one obtained with SS MPB method. The parameters in the TB Hamiltonian of S are the same as in Fig. 5.7.

amplitude decreases as $\Delta = \Gamma/2$ increases, which is directly related to the broadening in the corresponding I-V curve. This observation also clarifies the interpretation of the dephasing mechanism as the introduction of the effective broadening in the Fermi-Dirac distributions of the probes. Replacing the initial distributions $f_{\mathrm{L(R)}}(E)$ by the broadened fictitious distributions $\tilde{f}_{\mathrm{L(R)}}(E)$ with the same chemical potentials results in the thermal-like smearing of the conductance peaks as in the presence of the non-zero electronic temperature, although all calculations are performed at $T = 0$. To further illustrate this point we plotted the exact NEGF conductance, calculated using the distributions $f_{\mathrm{L(R)}}(E)$ but with a smearing introduced by $T \neq 0$ (see thin black line in Fig. 5.9), which is, indeed, similar to the broadened TD MPB conductance peaks. One can also notice a small asymmetry of the TD MPB conductance curves with respect to exact NEGF, which is not visible in the I-V characteristics. We associate this effect

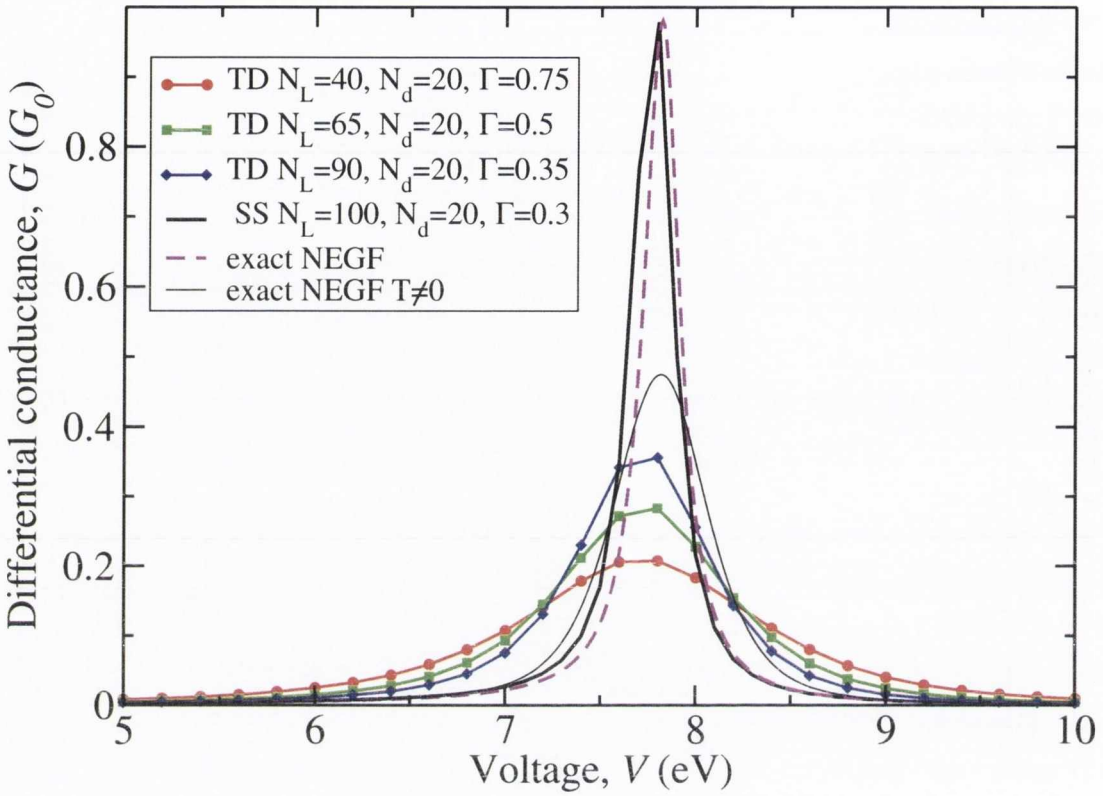

FIGURE 5.9: Differential conductance $G = dI/dV$ of the dimer in the units of $G_0 = 2e^2/h$ as a function of the applied bias voltage V, calculated using TD MPB and SS MPB for the same parameters as in Fig. 5.8. The exact NEGF conductance is shown for two values of the electronic temperature: $T = 0$ (dashed magenta line) and $T = 700K$ (thin black line).

with the discrete nature of the energy-levels in L and R, which may result in a slight shift in the position of the resonance.

Finally, we note that the calculations presented here were used to benchmark our implementation of the MPB method. The results for the differential conductance and the I-V characteristics of the resonant dimer, presented in Fig. 5.7 and Fig. 5.8 agree quantitatively with those reported in Ref. [171].

5.6.2 Spin-excitation in open atomic chain

In this section we use the TD MPB method to study real-time spin dynamics in an atomic chain. This familiar problem, that we have already considered in the previous chapters, has now been recast into a transport problem with open boundaries.

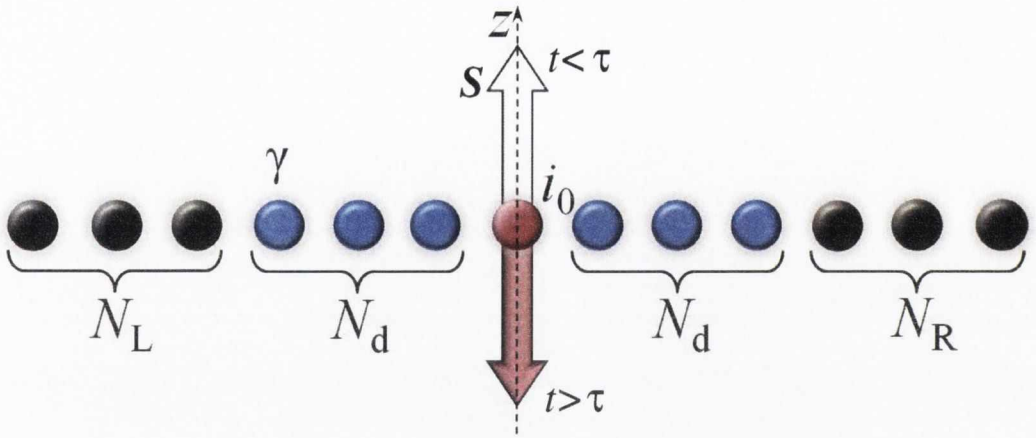

FIGURE 5.10: Test system B. The central region consists of an impurity site at position i_0 with a frozen local spin $\boldsymbol{S}$, embedded in a $2N_{\mathrm{d}}$-atoms long chain, which is attached to two 1D leads with N_α atoms for $\alpha = \mathrm{L}, \mathrm{R}$. During the time-dependent simulation, the orientation of the local spin remains parallel to the positive z-direction for $t < \tau$ but it is flipped at $\tau = 400$ fs and it is kept fixed afterwards. The parameters of the TB Hamiltonian of S are the following: the hopping $\gamma = -1$ eV and the on-site energies $\varepsilon_i = 0$ everywhere in S. The strength of the exchange interaction is given by $J = 10^{-4}\gamma$.

The system S is the same as the test system in the previous section (see Fig. 5.6), with $N_{\mathrm{L}} = N_{\mathrm{R}} = 90$, $\mathrm{N_d} = 30$ and $\Gamma = 0.35$, but instead of the dimer we consider a single localized impurity with a spin $\boldsymbol{S}$, as shown schematically in Fig. 5.10. This is coupled to the itinerant electron spin at the same site via the exchange interaction $J > 0$ (see, for example, Section 4.3 of Chapter 4). The orientation of the local spin is initially fixed along the positive z-direction. The spin-polarization of the 1D system S, generated by the coupling to the local spin, is calculated at the initial time t_0 as $s_i^z(t_0) = \rho_{ii}^{\uparrow\uparrow}(t_0) - \rho_{ii}^{\downarrow\downarrow}(t_0)$ and is shown in Fig. 5.11(b).

The electronic structure of S is again described by a single-band nearest-neighbors TB Hamiltonian with a uniform hopping γ for all sites and on-site energies set to zero. The coupling to the impurity spin acts as a local magnetic field on site i_0. The initial density matrix $\hat{\rho}(t_0)$ is constructed from the eigenvectors of the TB Hamiltonian of S with the local spin parallel to z.

Figure 5.11(a) shows the spatially-resolved time evolution of the absolute value of the spin polarization, $|s_i^z|(t)$, along S. The boarders of the central region are marked with white vertical lines. We skip the initial stage of the dynamics, during which the system undergoes the process of equilibration with the probes, and show the time evolution 380 fs after the start of the simulation, when the system has already reached the

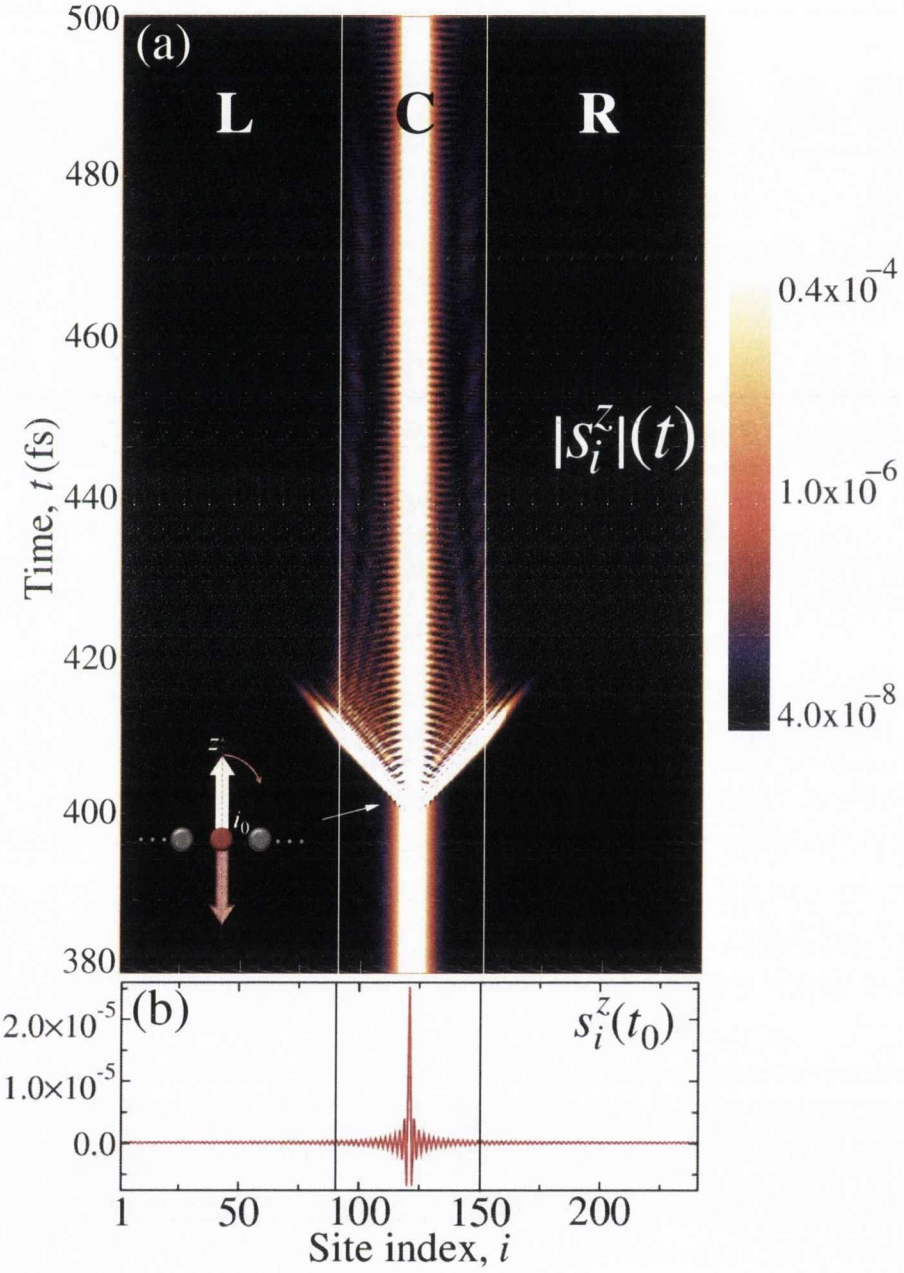

FIGURE 5.11: (a) Spatially-resolved time evolution of the spin-polarization in the electrodes and in the central region, 20 fs before and 100 fs after the spin-excitation. The color shade represents the absolute value of $s_i^z(t)$ and is logarithmically scaled for better contrast. (b) Initial spin-polarization of S as a function of the site index.

steady-state. At time $\tau = 400$ fs an excitation is produced at site i_0, which changes the direction of the local spin $\boldsymbol{S}$ from its initial orientation parallel to z to the opposite direction, where it is kept afterwards.

Bright rays stemming from the impurity site for $t \geq \tau$ correspond to the spin-disturbance generated by the spin-flip. This propagates to the left and to the right of the impurity site and decays gradually in the electrodes. The interferences of spatially and temporally oscillating spin-excitation waves in the central region also average out with time, leading to a new steady-state for $t > 500$ fs.

Note that in the simulations described above the system S was attached to the external probes but without applying the bias voltage, e.g. $\mu_{\mathrm{L}} = \mu_{\mathrm{R}} = 0$. This unique functionality, offered by the TD MPB approach, allowed us to construct a time-resolved portrait of the un-biased spin dynamics in the system with open-boundaries. We anticipate, however, that under applied bias voltage and with fully time-dependent impurity spins, such open-boundary spin-dynamics simulations may be used for non-perturbative time-resolved modeling of STM spectroscopy on atomic clusters comprising magnetic impurities. In the model Hamiltonian approaches, for example in the work by Hurley *et al.* [107], such systems are described by the semi-empirical TB model, with parameters extracted from DFT, where the interaction between the conduction electrons and the spins of magnetic impurities is modeled by the *s-d* Hamiltonian. In order to relate to this static description of inelastic spin transport, the quantum-classical approximation to the *s-d* model employed in Chapter 4 will be extended to fully quantum treatment of the impurity spins. This is the objective of ongoing consideration.

5.7 Summary

In this chapter, we have reviewed some of the fundamental aspects of modeling the electronic transport at the atomic scale and presented the computational scheme for time-dependent transport simulations employed in this Thesis. We started with the formulation of the electronic transport problem in a generic setup, which consists of a nanoscale object bridging two macroscopic electrodes attached to an external battery. The poles of the battery have been replaced by two ideal reservoirs with well-defined chemical potentials, acting as a source and a drain for the charge-carriers. Further, the Landauer approach to the steady-state transport has been discussed, where a problem

of an open system, which interacts dynamically with the reservoirs, has been recast into an open-boundary problem with two semi-infinite electrodes. The famous Landauer formula for the conductance quantum and the phenomenological formula for the steady-state current through a non-interacting scattering region attached to two ballistic electrodes has been revisited. After a general discussion of the Green's function technique in the context of the many-body theory, we have discussed the non-equilibrium Green's function formalism and its application to the steady-state transport in the Landauer setup with infinitely long electrodes. We have outlined the strategy for calculating the steady-state current in terms of the Green's functions of the scattering region and the self-energies due to the presence of the electrodes.

Finally, we have introduced the multiple-probe battery approach to electronic transport. The central idea of the method is to use the finite electrodes with broadened energy levels, which gives an approximation to the semi-infinite leads with continuous spectrum, controlled by the broadening parameter Γ. In the time-dependent formalism, we derived, following Ref. [171], the extended quantum Liouville equation for the density matrix of the system, comprising finite electrodes and the scattering region, with explicit open-boundary terms. Two main approximations have been used in the derivation: (*i*) the wideband limit in the probes and (*ii*) the relaxation-time approximation, which decouples over the time interval τ_Δ the injection of electrons into the leads and their subsequent interaction with the time-dependent scattering potential in the interior of the central region. The first approximation significantly simplifies the formalism while retaining the realistic electronic structure of the electrodes. The second approximation introduces a finite broadening in the Fermi-Dirac distributions of the probes which limits the resolution of the current-voltage characteristics. The latter can be improved by increasing τ_Δ, or, equivalently, by decreasing the energy parameter $\Delta = \hbar/\tau_\Delta$.

In the next chapter, we will apply the time-dependent multiple-probe battery method to a problem, which has recently attracted great interest, namely that of the time-dependent transport through a strongly correlated quantum dot.

Chapter 6

Time-dependent electron transport through a strongly correlated quantum dot

6.1 Introduction

In spite of considerable efforts, the development of accurate theoretical models for the description of electron transport at the nanoscale remains a challenge. As will be illustrated below, the main reason for this is the difficulty in combining an efficient way of modeling the electron transport with an accurate description of the electronic structure.

One of the most commonly used approaches to the simulation of current carrying systems is based on the nonequilibrium Green's function (NEGF) formalism (see Section 5.4 of the previous chapter). When combined with the density functional theory (DFT) for electronic structure calculations, this method underpins the majority of the present state-of-the-art *ab initio* transport calculations [217, 220] and numerical algorithms [29, 66, 124, 152, 210, 216, 240, 241]. A typical DFT+NEGF transport scheme is constructed in a very similar way to the NEGF-based approach to the steady-state transport in a generic two-terminal Landauer setup, that we considered in the previous chapter (see Section 5.4.4). Within this scheme the initial conditions are defined in the spirit of Caroli's "contacting approach" [40, 41, 42, 48], where one assumes that in the remote past the electrodes are disconnected from the device and are in equilibrium with

the external reservoirs, each at a well-defined chemical potential. The coupling between the electrodes and the device (the tunneling Hamiltonian) is assumed to be switched on adiabatically, allowing the steady state to develop. The electronic structure is treated at the DFT-level and the non-equilibrium charge density is calculated self-consistently. The current is obtained by using the Landauer-type formula [see Eq. (5.72)] for the steady-state current through the (generally interacting) scattering region, sandwiched between two non-interacting electrodes.

Despite their popularity, the standard steady-state DFT+NEGF transport schemes have a range of limitations [144]. A major issue, intrinsic to DFT, is the notorious difficulty in describing the electronic structure of strongly correlated systems, which has been attributed to the shortcomings of the commonly used approximations to the exchange-correlation (XC) functional. In fact, the simplest and the most popular approximation is the local density approximation (LDA), in which the XC functional depends on the density at the point, where the functional is evaluated, and takes the value corresponding to that of the homogeneous electron gas. Clearly, such approximation fails for systems, where the density fluctuates rapidly or is extremely localized, e.g. for systems, which behave differently from the homogeneous electron gas. This is indeed the case when electron correlations are strong. It has been recognized that one of the most significant incorrect features of the traditional approximate XC functionals is the lack of the so-important derivative discontinuity [201, 202].

6.1.1 Derivative discontinuity in static DFT

Hohenberg and Kohn have established that for a system of N electrons, subject to an external potential $v_{\text{ext}}(\boldsymbol{r})$, there exist an energy functional $E_v[n]$, such that the minimization of $E_v[n]$ with respect to the variation of the charge density $n(\boldsymbol{r})$, with a constraint $\int d^3r\, n(\boldsymbol{r}) = N$, yields the ground-state density $n(\boldsymbol{r})$ and the ground-state total energy E of the system. This is the essence of the Hohenberg-Kohn theorems [98]. The variation of the energy functional, with the number of particles conservation constraint, can be performed by introducing the Lagrange multiplier μ such as

$$\delta \left\{ E_v[n] - \mu \int d^3r\, n(\boldsymbol{r}) \right\} = 0. \tag{6.1}$$

The Euler-Lagrange equation for the density $n(\boldsymbol{r})$ then reads

$$\frac{\delta E_v[n]}{\delta n(\boldsymbol{r})} = \mu, \tag{6.2}$$

where

$$\mu = \frac{\partial E}{\partial N}. \tag{6.3}$$

Due to the formal similarity of Eq. (6.3) to the definition of a chemical potential for an open system, which can exchange energy and particles with a reservoir, μ has been associated with a chemical potential. However, fundamental questions arise about the applicability of the HK theorems and, as a consequence, of DFT, to systems with a non-integer number of particles, which indeed might be the case in transport calculations, where the system is open to external reservoirs. In particular, it is not clear whether the total energy E is defined for a fractional particle number N and whether it is differentiable with respect to N.

In fact, the positive answer to both questions leads to a paradox. Consider a system consisting of two well-separated neutral atoms A and B in the empty space, with respective chemical potentials μ_A and μ_B, such that $\mu_B < \mu_A$. The total energy of the system E_{AB} is given by the sum of the separate atomic energies E_A and E_B. It then follows from Eq. (6.1)-(6.3), that a fluctuation in the charge density, which shifts a fraction $\eta > 0$ of the electron charge from A to B, lowers the total energy, e.g. $E_{AB} = \eta\,(\mu_B - \mu_A) < 0$. This essentially means that molecules would dissociate at large separations with fractional charges on the constituent atoms, which contradicts the reality.

Perdew *et al.* [201, 202] have extended the HK theorems to the case of non-integer particle numbers, by considering the quantum-mechanical state of an open system as a statistical mixture of pure states, corresponding to different particle numbers. In the simplest case, the wave function Ψ_N of a system with $N = M + \eta$ electrons, where M is an non-negative integer ($M \geq 0$) and $0 \leq \eta \leq 1$, is a statistical mixture of the wave functions Ψ_M and Ψ_{M+1}, which correspond respectively to the states with M and $M+1$ electrons. The respective probabilities of each state are $1-\eta$ and η, which gives $(1-\eta)M + \eta(M+1) = M + \eta$. The charge density of the N-electron state is then given by

$$n(\boldsymbol{r}) = (1-\eta)n_M(\boldsymbol{r}) + \eta\, n_{M+1}(\boldsymbol{r}), \tag{6.4}$$

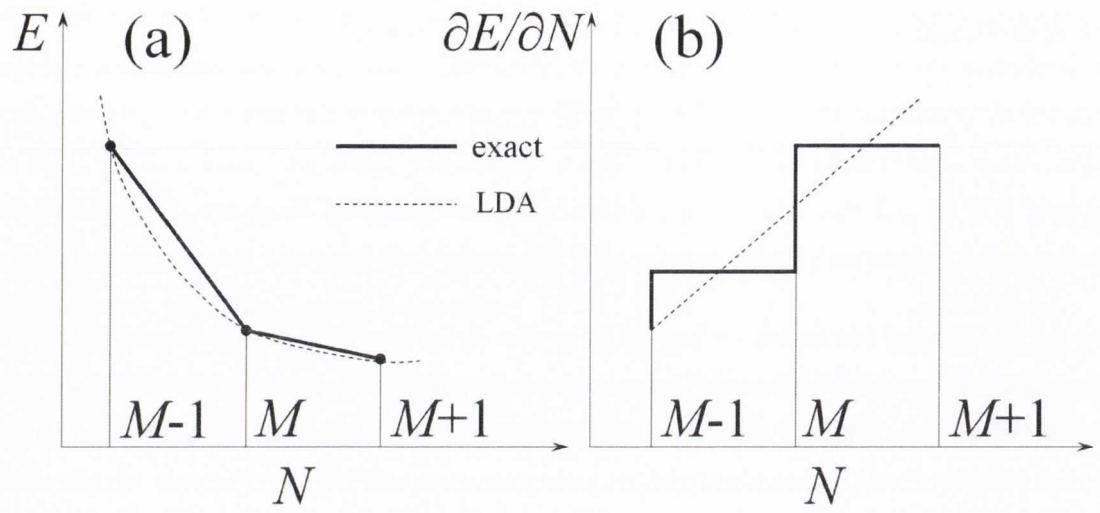

FIGURE 6.1: Schematic of the dependence of the total energy, E, (a) and the derivative of the total energy, $\partial E/\partial N$, (b) on the fractional particle number N. The *exact* total energy, as defined by Perdew *et al.* [202], has a derivative discontinuity at integer occupation, which means that its derivative ($\partial E/\partial N$) has a discontinuity at the integer value of N. The total energy obtained by using a local approximation to the XC functional, such as LDA, does not exhibit a derivative discontinuity and has a non-linear behavior between integer occupations.

where $n_M(n_{M+1})$ is the charge density of the state with $M(M+1)$ electrons. The minimization of the total energy functional $E_v[n]$ with respect to variations of the charge density, which conserve the number of electrons ($N = M + \eta$), yields the lowest average energy

$$E = (1-\eta)E_M + \eta\, E_{M+1}, \tag{6.5}$$

where $E_M(E_{M+1})$ is the total energy of the systems with $M(M+1)$ electrons, subject to the external potential $v_{\text{ext}}(\boldsymbol{r})$.[1]

It follows from Eq. (6.5) that the dependence of the total energy E on the fractional particle number N is a series of straight-line segments between the integer values, as shown schematically on Fig. 6.1(a). This means that E is a continuous function of N, however, its derivative, $\partial E/\partial N = \mu$, has discontinuities at integer particle numbers [see a schematic illustration in Fig. 6.1(b)]. This is referred to as the *derivative discontinuity* of the total energy.

[1]It can be shown [202] that the minimization over the entire ensemble of pure states (not only over the two states with M and $M+1$ electrons) leads to the same lowest energy as the one in Eq. (6.5), as far as the curve E_M versus M is concave upwards (see Fig. 6.1).

If we consider a single atom with an integer nuclear charge Z, then the chemical potential μ, which is discontinuous at $N = Z$, can be calculated in two limits, e.g. for $Z - 1 \leq N \leq Z$ ($M = Z - 1$) and for $Z \leq N \leq Z + 1$ ($M = Z$). This can be written as

$$\mu = \begin{cases} E_Z - E_{Z-1} \equiv -I, & Z - 1 \leq N \leq Z\,, \\ E_{Z+1} - E_Z \equiv -A, & Z \leq N \leq Z + 1\,, \end{cases} \tag{6.6}$$

where I is the *ionization potential*, or the energy required to remove an electron from an isolated atom or molecule, and A is the *electron affinity*, or the energy released when an electron is added to a neutral atom or molecule to form a negative ion. Therefore the size of the derivative discontinuity, defined as the difference between the values of $\partial E/\partial N$, calculated in the limit $N \to Z$ for N approaching Z from the right ($N > Z$) and from the left ($N < Z$), is equal to $I - A$. Note that the presence of the derivative discontinuity in the occupation-dependence of the total energy resolves the issue with the dissociation of atoms at large separations: even if an infinitesimal positive fractional charge η is added to the atom B, the chemical potential μ_B will jump discontinuously by $I - A > 0$, making the exchange of fractional charges between the atoms energetically unfavorable (in the periodic table I of a given atom is bigger than A of any other atom).

Notably, the total energy, entering the formulation of Perdew *et al.*, is assumed to be *exact*. In practical DFT calculations, however, the ground-state density and energy are constructed from the fictitious KS orbitals φ_α^σ ($\sigma = \uparrow, \downarrow$ is the spin-index for the orbital α), which satisfy the self-consistent single-particle Schrödinger equation

$$\left[-\frac{\hbar^2}{2m} \bigtriangledown^2 + v_{\text{ext}}(\boldsymbol{r}) + \int d^3r' \, \frac{n(\boldsymbol{r}')}{|\boldsymbol{r} - \boldsymbol{r}'|} + \frac{\delta E_{\text{XC}}[n]}{\delta n(\boldsymbol{r})} \right] \varphi_\alpha^\sigma(\boldsymbol{r}) = \epsilon_\alpha^\sigma \varphi_\alpha^\sigma(\boldsymbol{r}), \tag{6.7}$$

where the spin-resolved density is expressed in terms of the KS orbitals such as

$$n^\sigma(\boldsymbol{r}) = \sum_\alpha f_\alpha^\sigma \, |\varphi_\alpha^\sigma(\boldsymbol{r})|^2, \tag{6.8}$$

and the total charge density is given by

$$n(\boldsymbol{r}) = n^\uparrow(\boldsymbol{r}) + n^\downarrow(\boldsymbol{r}). \tag{6.9}$$

In Eq. (6.8) f_α^σ are the occupation numbers for orbitals φ_α^σ, distributed according to the Fermi-Dirac statistics.

The third term in the square brackets on the left-hand side of the KS equation [see Eq. (6.7)] is the Hartree, or Coulomb potential v_{H}, which is given by the derivative of the Hartree, or Coulomb energy $U[n]$ with respect to the charge density, e.g. $v_{\mathrm{H}}[n](\boldsymbol{r}) = \delta U[n]/\delta n(\boldsymbol{r})$, where $U[n]$ reads

$$U[n] = \frac{1}{2}\int d^3r \int d^3r' \frac{n(\boldsymbol{r})n(\boldsymbol{r}')}{|\boldsymbol{r}-\boldsymbol{r}'|}. \tag{6.10}$$

The last term is the XC potential, v_{XC}, which, similarly to v_{H}, is given by the derivative of the XC energy $E_{\mathrm{XC}}[n]$ with respect to the charge density, e.g. $v_{\mathrm{XC}}[n](\boldsymbol{r}) = \delta E_{\mathrm{XC}}[n]/\delta n(\boldsymbol{r})$.

Importantly, the XC energy, which contains the remaining part of the electron-electron interaction, is unknown and needs to be approximated. The simplest approximation to E_{XC} is the LDA, and its spin-polarized version, the local spin density approximation (LSDA) [134]. In the LSDA the XC energy functional is calculated as

$$E_{\mathrm{XC}}^{\mathrm{LSDA}}[n^{\uparrow}, n^{\downarrow}] = \int d^3r\, n(\boldsymbol{r}) e_{\mathrm{XC}}(n^{\uparrow}, n^{\downarrow}), \tag{6.11}$$

where $e_{\mathrm{XC}}(n^{\uparrow}, n^{\downarrow})$ is the XC energy density of the homogeneous electron gas. The LSDA can be extended to include the terms depending on the gradient of the charge density, e.g. terms depending on $\bigtriangledown n^{\sigma}(\boldsymbol{r})$. This is realized in the generalized gradient approximation (GGA) [200]. The latter is therefore capable of better describing systems with rapidly fluctuating charge density, however, it still uses the homogeneous electron gas as a reference system and it is still local.

It can be shown that the KS eigenvalues, or the orbital energies $\epsilon_{\alpha}^{\sigma}$, obey the following relations, known as the Janak's theorem [112]

$$\epsilon_{\alpha}^{\sigma} = \frac{\partial E}{\partial f_{\alpha}^{\sigma}}. \tag{6.12}$$

Hence the energy of the maximum occupied KS orbital, which is usually referred to as the highest occupied molecular orbital (HOMO), coincides with the chemical potential, given by Eq. (6.6).

After the KS equations have been solved self-consistently, the ground-state charge density $n(\boldsymbol{r})$ is constructed from the KS orbitals using Eqs. (6.8)-(6.9) and the total

energy of the system $E_{\rm tot}$ is given by

$$E_{\rm tot} = \sum_{\alpha\sigma} \left\langle \varphi_\alpha^\sigma \right| - \frac{\hbar^2}{2m} \nabla^2 \left| \varphi_\alpha^\sigma \right\rangle f_\alpha^\sigma + \int d^3r\, n(\boldsymbol{r})\, v_{\rm ext}(\boldsymbol{r}) + U[n] + E_{\rm XC}[n], \quad (6.13)$$

where the first term on the right-hand side is the non-interacting kinetic energy and the second one represents the energy of the interaction with the external potential $v_{\rm ext}(\boldsymbol{r})$. An alternative expression for the total energy reads [264]

$$E_{\rm tot} = \sum_{\alpha\sigma} f_\alpha^\sigma \epsilon_\alpha^\sigma + E_{\rm XC}[n] - \int d^3r\, v_{\rm XC}[n](\boldsymbol{r}) - \frac{1}{2} \int d^3r \int d^3r' \frac{n(\boldsymbol{r}) n(\boldsymbol{r}')}{|\boldsymbol{r} - \boldsymbol{r}'|}, \quad (6.14)$$

where $f_\alpha^\sigma = f(\epsilon_\alpha^\sigma - E_{\rm F})$, with $f(E)=1/\left[\exp(E/k_{\rm B}T) + 1\right]$ being the Fermi-Dirac distribution and $E_{\rm F}$ the Fermi energy, determined in such a way that $\int d^3r\, n(\boldsymbol{r})=N$. The last three terms on the right-hand side of Eq. (6.14) are usually referred to as the double counting corrections to the first term, which is simply the sum of all KS eigenvalues, weighted with occupation numbers obtained from the Fermi-Dirac distribution.

As was shown earlier, the fundamental result of the density functional theory for open systems with fractional particle number is the existence of the derivative discontinuity of the total energy at integer occupation. We will now illustrate how this result is affected by the approximations usually made to the otherwise unknown XC functional.

The derivative discontinuity of the total energy, which in fact coincides with the *fundamental gap* of the N-electron system [47, 199], defined as the difference between the ionization potential and the electron affinity, can be written as

$$E_g = \lim_{\eta\to 0} \left\{ \left. \frac{\delta E_v[n]}{\delta n(\boldsymbol{r})} \right|_{N+\eta} - \left. \frac{\delta E_v[n]}{\delta n(\boldsymbol{r})} \right|_{N-\eta} \right\} = \Delta_{\rm KS} + \Delta_{\rm XC}, \quad (6.15)$$

where $\Delta_{\rm KS}$ is called the KS single-particle gap, which is equal to the difference between the energy of the lowest unoccupied molecular orbital ($\epsilon^N_{\rm LUMO}$) and that of the highest occupied molecular orbital ($\epsilon^N_{\rm HOMO}$) for the N particles system, e.g. $\Delta_{KS} = \epsilon^N_{\rm LUMO} - \epsilon^N_{\rm HOMO}$. The contribution $\Delta_{\rm XC}$ comes from the XC energy and is given by

$$\Delta_{\rm XC} = \lim_{\eta\to 0} \left\{ \left. \frac{\delta E_{\rm XC}[n]}{\delta n(\boldsymbol{r})} \right|_{N+\eta} - \left. \frac{\delta E_{\rm XC}[n]}{\delta n(\boldsymbol{r})} \right|_{N-\eta} \right\} = v^+_{\rm XC} - v^-_{\rm XC}, \quad (6.16)$$

where we have introduced $v^\pm_{\rm XC} = \lim_{\eta\to 0} v_{\rm XC}|_{N\pm\eta}$. It is clear that the existence of the derivative discontinuity in the total energy, e.g. the existence of E_g, implies the

existence of the derivative discontinuity in E_{XC} (Δ_{XC}) and, as a consequence, the discontinuity in v_{XC} at integer occupation. However, most of the approximate XC functionals used in practice, such as LDA and GGA, lack the derivative discontinuity ($\Delta_{\mathrm{XC}} \to 0$) and have non-linear behavior between integer occupations, as illustrated in Fig. 6.1.

It is widely accepted that these incorrect features have profound consequences on the DFT calculations performed with such functionals [47, 199]. The obvious drawback of neglecting Δ_{XC} is the incorrect estimation of the fundamental gap. This, in turn, leads to underestimation of chemical barriers and band gaps of insulators and semiconductors compared to experimental values [269], and to errors in calculations of charge-transfer processes and transport [248, 249]. Several strategies have been proposed to deal with the issues mentioned above, which include the construction of more advanced XC functionals [199]. In particular, it has been shown that the *self-interaction error* [203], which is present in the typical approximations to the XC functional, is partially responsible for the suppression of the derivative discontinuity. They also lead to the incorrect estimation of ionization potentials for molecules and contribute to incorrect positions being calculated for the valence bands of semiconductors. Approximate self-interaction correction schemes have been developed [69, 198], which remove these errors, although without restoring in full the derivative discontinuity, and offer significant improvement over the traditional XC functionals, in particular for calculations of electron transport in molecular junctions [248, 249].

To conclude the discussion on the limitations of DFT, we would like to point out that the latter is a formally exact theory and the limitations come solely from the approximations used in practical implementations. The question then naturally arises as to whether the KS DFT, equipped with a numerically exact XC functional exhibiting a derivative discontinuity, can accurately describe the electron transport in a nanojunction, comprising a nanoscale object like a quantum dot or a molecule, weakly coupled to macroscopic electrodes. This is prototypical example of a system, where the derivative discontinuity is of great importance. The role of the derivative discontinuity in calculating the transport through a nanojunction, described by the Anderson impurity model [5], has been discussed in several recent works [22, 234, 253].

In the work by Bergfield *et al.* [22] a novel XC functional has been proposed, which is based on the Bethe-ansatz solution of the Anderson impurity model, with a parametrization that allows one to consider arbitrary coupling and correlation strengths. The DFT

calculations of transport using this functional reproduce the exact results but only at zero temperature and in the linear-response regime. In particular, the conductance plateau, predicted by the exact solution of the Anderson impurity model for temperatures below the Kondo temperature (see further discussion in Section 6.2.2), is recovered.

A similar result was obtained by Stefanucci and Kurth [234]. The authors derived a new approximate XC functional for the Anderson impurity model within the finite-temperature DFT framework, where the temperature effects are introduced by connecting an isolated impurity, or a quantum dot, to a thermal bath. Importantly, such XC functional exhibits a derivative discontinuity at integer occupation in the zero-temperature limit. The DFT+NEGF approach, which employs this functional, is also able to reproduce the conductance plateau at $T = 0$. However, at finite temperature, the conductance is overestimated by an order of magnitude, compared to the exact result, obtained with the numerical renormalization group (NRG) approach. Hence the method, described in Ref. [234], can not describe the behavior of the system above the Kondo temperature, when instead of the plateau one expects to see two distinct peaks (for a single-level quantum dot), as the Coulomb blockade picture is restored. The authors suggest that this discrepancy might be due to the lack of the dynamical contribution to the XC functional within the static DFT+NEGF approach.

These results indicate that the DFT+NEGF scheme equipped with advanced XC functionals can potentially provide a complete solution for electron transport at least in the zero-bias (and the zero-temperature) limit. However, further implications arise at finite bias, where conceptual concerns reflect on the very applicability of the ground-state electronic structure theory, which DFT is, to the description of non-equilibrium electron transport, especially if electron correlations are significant [133, 262].

6.1.2 Steady state versus time-dependent approach

The KS eigenvalues ϵ_α^σ correspond to the fictitious single-particle KS orbitals φ_α^σ and therefore do not coincide with the true single-particle eigenstates of the many-electron system. Strictly speaking, the only observables, obtained from the KS equations [see Eq. (6.7)], that have a physical meaning are the ground-state charge density and the ground-state total energy of the system (we can add to this list ϵ_{HOMO}, which coincides with the chemical potential). Hence the transmission coefficients, calculated with the

DFT+NEGF method, have resonances at the KS excitation energies, which do not necessarily coincide with the true excitation energies. In addition, the information about transient and ac regimes is not available within the steady-state DFT+NEGF transport scheme.

In view of these problems, a considerable effort has been put into the development of time-dependent approaches to transport (see, for example, Refs. [144, 219, 265] and references therein), in particular methods based on time-dependent (TD) DFT [170]. The latter, by construction, provides a more suitable framework to study dynamical processes. A theoretical foundation of TDDFT is provided by the Runge-Gross (RG) theorem [215], an analogue of the HK theorems of standard DFT, which establishes a unique mapping between the TD external potential $v_{\text{ext}}(\boldsymbol{r}, t)$ of the system and its TD electron density $n(\boldsymbol{r}, t)$. In the TD version of the KS scheme an auxiliary system of non-interacting electrons, moving in TD effective potential, is constructed and the corresponding TD equations of motion are solved. The main advantage of the TDDFT-based approaches is the possibility to investigate transport beyond the steady state, i.e. to study transient and ac responses, and to get access to the true excitation energies.

However, most of TDDFT-based approaches still suffer from the shortcomings of static DFT unless non-local approximation to the XC functional are used [145]. Other conceptual concerns have also been raised, for example, whether the steady state can be achieved within the TD approach if the electrodes are treated as non-interacting [235], which is usually the case in practical calculations.

It is important to mention that TDDFT has been established for isolated systems. In contrast to this, in the transport setup one deals with effectively *infinite* system, which consists of the scattering region in contact with macroscopic or mesoscopic electrodes. Several conceptually different strategies have been proposed to extend the TDDFT framework to include the electronic open-boundary conditions. Following the classification proposed by Y. Wang *et al.* in Ref. [265], the TDDFT formulations can be divided into several groups according to how the transport boundary conditions are treated:

1. The first group of methods is suited for the investigation of *closed* nonequilibrium systems, where macroscopically large leads are approximated by finite atomic clusters. The advantage of such approximation is that the TDDFT formalism for isolated systems can be applied to the electron transport problem without

any changes. However, it is clear that the steady state can be established only in the transient regime before the finite-size effects in the leads start to affect the transport [33, 43, 250]. In addition, it is not straightforward to introduce an applied bias in this case. The method has been used to calculate quasi steady-state currents in finite nanoscale junctions [33].

2. Another strategy, originally proposed by Kamenev and Kohn [120], is to develop an approach that does not assume the presence of two reservoirs, maintained at two different chemical potentials, as in the standard two-terminal Landauer setup. A practical scheme for calculations of electron transport in molecular devices, based on this idea, has been developed by Burke and co-workers [32, 133]. This approach takes advantage of the periodic boundary conditions in the electronic circuit, or the *ring* topology, thus avoiding the conceptual difficulties of having two different chemical potentials. The system is put on a ring, threaded by a magnetic flux, which is equivalent, through a gauge transformation, to applying a spatially uniform electric field throughout the entire system. The finite system is then propagated using the single-particle KS master equation[2] with a dissipative term, which accounts for the coupling between the system and a heat bath, or a reservoir.

3. The third group of methods relies on the separation of the system into the device region and two semi-infinite leads, similarly to the treatment within the standard NEGF approach. The TD KS equations are then solved for the central region, with the effect of the leads accounted for by properly defined self-energies. Several practical scheme, based on this idea, has been proposed [235, 280]. An interesting *ab initio* methodology has been developed recently by Zheng *et al.* [279, 280]. In their work a numerical scheme is proposed based on the combination of TDDFT and quantum dissipation theory. In particular, a self-energy density functional is introduced, which effectively describes the dissipative interactions of the device region and the environment, leading to TD equations of motion for the reduced density matrix of the device.

[2]In general, a master equation is a phenomenological set of first-order differential equations, which describe the time evolution of the probability for a system to occupy a particular state of a discrete set of states. The master equation approach is widely used for modeling of the electronic transport [189]. The quantum Liouville equation with a dissipative term, or the *Lindblad equation* [57, p. 28], can be viewed as a generalization of the master equation. It describes the evolution of an open quantum system coupled to a reservoir, beyond the Hamiltonian dynamics.

Another theoretical approach, which belongs to the last group, has been proposed by Stefanucci *et al.* [144, 235]. This approach uses the Cini (partition-free) scheme [45] in which, in contrast to the "contacting approach", the entire system electrodes+device is driven out of equilibrium by applying an external, local in both space and time, TD potential. Such perturbation can represent an electric field, generated by putting the system between two capacitor plates far away from the system boundaries, or by directly modifying the on-site potential in the electrodes, e.g. by introducing a shift in their on-site energies.

More recently this scheme, further equipped with a novel XC functional carrying the physical derivative discontinuity, has been used by Kurth *et al.* [145] to study the TD transport through a quantum dot in the Coulomb blockade (CB) regime. We will refer to this work extensively throughout this chapter. In particular, the authors have put forward an important novel description of CB as an intrinsically dynamical process, which is inaccessible by conventional steady-state transport models. In the dynamical CB regime, the system does not evolve towards the steady state but remains in the dynamical state, characterized by rapidly oscillating currents, which correspond to charging and discharging of the quantum dot.

6.1.3 Combining a new approach to electron transport with a novel exchange-correlation functional

In the work, presented in this chapter, we use the TD multiple-probe battery approach [171, 247] (TD MPB) to investigate the electron transport through a strongly correlated open quantum dot. We have shown in Section 5.5 of the previous chapter that the TD MPB time-propagation scheme is based on the integration of the Liouville-von Neumann equation of motion for the reduced density matrix of the system, where open boundaries are introduced through explicit source and drain terms. For the TD Hamiltonian of the quantum dot, entering the equation of motion, we adopt the description used by Kurth *et al.* [145]. This is based on the adiabatic Bethe ansatz local-density approximation [38, 158] (adiabatic BALDA, or ABALDA) to the XC functional, which exhibits the derivative discontinuity at half-filling.

By investigating the real-time evolution of the current through the quantum dot, we indeed observe, in agreement with Kurth *et al.*, that for a certain set of parameters the

system does not reach a steady state but rather remains in a dynamical state, characterized by current oscillations. Further, we attempt to establish a link between the time-dependent and the steady-state pictures of transport. In particular, we construct the current-voltage characteristics of the quantum dot from TD simulations, performed for a wide range of parameters (we calculate the time-averaged current in the long-time limit in cases when the steady state is not achieved). Importantly, we observe a drop of the current as a function of the source-drain voltage and, as a consequence, negative differential conductance (NDC) above critical bias voltages, which is not reproduced at the mean-field (Hartree) level of description.

This is particularly interesting in view of some recent contrasting results. On the one hand a number of studies, based on several distinct many-body approaches [28, 61, 187] to non-equilibrium transport through an interacting dot, attribute NDC in the I-V characteristics mainly to electron-electron interactions. On the other hand, it has been demonstrated by Bâldea and Köppel [17] that in the case of the exactly solvable model for a non-interacting dot within the steady state formalism, the finite bandwidth in the electrodes can lead to pronounced NDC in a wide range of parameters. In our work we find a numerical proof that this result can be generalized to the interacting case and TD transport. Our calculations suggest, however, that for the system considered here, the NDC is due to a combination of two effects, namely electron-electron interaction on the dot *and* the finite bandwidth of the electrodes.

We will start, in the following section, with a brief reminder of the basic physics of quantum dots, in particular of Coulomb blockade. We will then introduce the model system and our theoretical framework, i.e. the DFT-based description of a strongly correlated quantum dot with the BALDA XC functional and its extension to the time-dependent regime. Finally, we will present the results on time-dependent and steady-state transport properties of a correlated quantum dot coupled to one-dimensional (1D) non-interacting leads, obtained with the TD MPB method.

6.2 Phenomenology of quantum dots

Quantum dots are small metallic or semiconductor islands in which electrons are confined [140]. When the size of the dot is comparable to the Fermi wavelength λ_F of the electrons that occupy it, the system exhibits a discrete, or *quantized*, energy spectrum. Due to discrete energy levels quantum dots share many properties of atoms

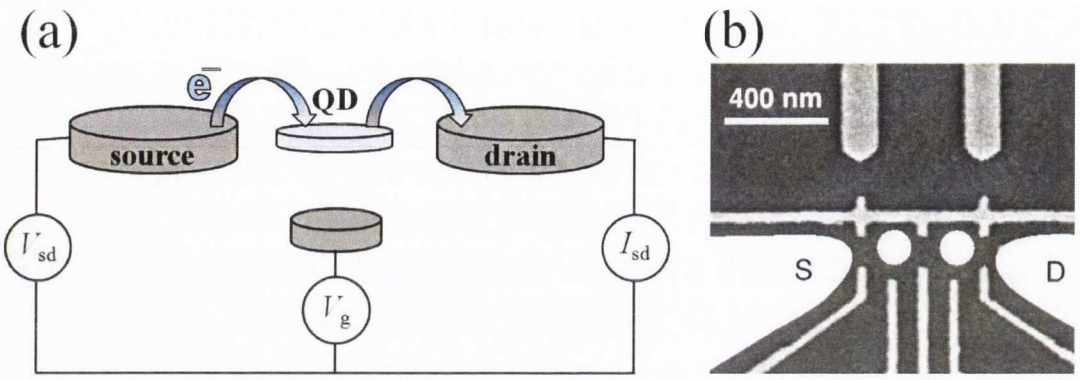

FIGURE 6.2: (a) Schematic of a quantum dot in lateral geometry. The quantum dot (QD) is coupled to a source and a drain electrode via tunnel barriers, allowing the current through the device, I_{sd}, to be measured as a function of the applied bias voltage, V_{sd}, and the gate voltage, V_g. (b) Scanning electron microscope image of a GaAs-(Ga,Al)As double quantum dot device, showing the gate electrodes (light gray) on top of the surface (dark gray). The two white circles indicate the two quantum dots, connected via tunable tunnel barriers to the source (S) and to the drain (D) electrodes, indicated in white (from Ref. [65]).

and are sometimes called "artificial atoms". It is important to bear in mind, however, that the typical size of a quantum dot is $L \approx 100$ nm and the energy-level spacing is $\Delta\epsilon \approx 0.1$ meV. In contrast, the characteristic length and energy scales of atoms differ by roughly four orders of magnitude ($L \approx 0.1$ nm and $\Delta\epsilon \approx 1$ eV). Therefore quantum dots open up new opportunities for experimental research, which are not available in atoms.

From a fundamental point of view, the possibility to probe a small entity of confined interacting electrons, for example via transport measurements, is already an exciting prospect in itself. However, the great interest in quantum dots in the past decade has been also fueled by the possibility of building new technological applications. Some of the recent applications, that take advantage of the remarkable properties of quantum dots, in particular their optical properties, include quantum dot lasers [153] and the use of quantum dots as novel efficient reagents for biomedical imaging [116]. Quantum dot systems are also considered as promising candidates for solid-state-based quantum computing [162] with basic quantum operations already demonstrated experimentally [204].

In a real experimental transport setup, a quantum dot can be connected via tunneling junctions to source and drain reservoirs, in order to allow electron transport across the system. By attaching current and voltage probes to these reservoirs, one can measure

the electronic properties of the dot in response to the applied bias voltage, or source-drain voltage, $V_{\rm sd}$. The dot can be also coupled to one or more gate electrodes, which can be used to tune the local electrostatic potential of the dot, $V_{\rm g}$, with respect to the reservoirs. Such a device, which is usually called a *single-electron transistor* [122], is shown schematically in Fig. 6.2(a). Similar and even more complex devices, for example, consisting of two coupled quantum dots, as the one presented in Fig. 6.2(b), can be fabricated and studied experimentally. The ultimate limit would be a device, which consists of a single atom sandwiched between two contacts. Such "single-atom transistor" incorporating a transition-metal (Co) complex, designed in such a way that electron transport occurs through well-defined charge states of a single atom, has been realized experimentally [195]. This device exhibits prototypical quantum phenomena, such as Coulomb blockade and the Kondo effect.

Lateral quantum dot systems, as the one shown in Fig. 6.2(b), are formed by gate depletion of a two-dimensional electron gas at the interface between two semiconductors. Such systems are perhaps the most studied as they offer the highest degree of tunability and can also be investigated theoretically by using relatively simple models. The *constant interaction* (CI) model [139], which we will consider below, offers a convenient description of some of the fundamental results of transport experiments on quantum dots and also provides an intuitive explanation of the Coulomb blockade phenomenon.

6.2.1 Coulomb blockade

In the CI model the effect of the Coulomb interaction among the electrons in the dot, and between the electrons in the dot and those in the environment, is expressed in terms of a single parameter, a constant capacitance C. The latter can be decomposed into three terms

$$C = C_{\rm s} + C_{\rm d} + C_{\rm g}, \tag{6.17}$$

where $C_{\rm s}$ is the capacitance between the dot and the source electrode, $C_{\rm d}$ between the dot and the drain electrode (the drain is grounded), and $C_{\rm g}$ between the dot and the local gate. The energy $E(N)$ of a N-electron quantum dot can be then calculated as

$$E(N) = \frac{[-|e|(N - N_0) + C_{\rm s}V_{\rm sd} + C_{\rm g}V_{\rm g}]^2}{2C} + \sum_{n=1}^{N} \epsilon_n, \tag{6.18}$$

where N_0 is the number of electrons in the dot at zero gate voltage. The terms $C_s V_{sd}$ and $C_g V_g$ represent the charge on the dot, induced respectively by the source-drain voltage and by the gate voltage.[3] The last term in Eq. (6.18) is a sum over all the occupied single-particle energy levels ϵ_n, which are assumed to be independent of the number of electrons and of the Coulomb interaction on the dot (they can depend, however, on an applied magnetic field).

It is convenient to define the chemical potential of the dot. This can be written as

$$\mu = E(N) - E(N-1) = \left(N - N_0 - \frac{1}{2}\right) E_C - \frac{E_C}{|e|}\left(C_s V_{sd} + C_g V_g\right) + \epsilon_N, \qquad (6.19)$$

where $E_C = e^2/C$ is the *charging energy* and ϵ_N is the highest occupied single-particle energy level. The chemical potential measures the energy required for adding the N-th electron to the dot and, therefore, the above expression essentially describes the transition between the $(N-1)$- and the N-electron ground state. We can then define the effective energy levels of the dot $\mu(N)$, corresponding to the chemical potentials for different electron numbers (see Fig. 6.3). These discrete levels are separated by the so-called *addition energy*

$$E_{add}(N) = \mu(N+1) - \mu(N) = E_C + \Delta\epsilon, \qquad (6.20)$$

where E_C gives a purely electrostatic contribution, while $\Delta\epsilon$ is simply the difference between two consecutive single-particle quantum levels ϵ_{N+1} and ϵ_N, e.g. $\Delta\epsilon = \epsilon_{N+1} - \epsilon_N$.

Due to the conservation of energy, the electron transport through the dot can occur only if the chemical potential level μ falls within the *bias window*, which is defined by the region of energy between the chemical potential of the source and that of the drain (μ_L and μ_R, respectively), e.g. for $\mu_L \geq \mu \geq \mu_R$ with $V_{sd} = \mu_L - \mu_R$ (V_{sd} is in the units of eV). Only if these conditions are satisfied, an electron can tunnel from the source onto the dot, and then tunnel off to the drain, without either a loss or a gain in energy, since two consecutive chemical potential levels are separated by the energy barrier $E_{add} = E_C + \Delta\epsilon$. In fact, the charging energy E_C can be quite large (of the order of few meV) due to a very small capacitance of the dot. Figures 6.3(a) and (b) show the linear-response regime. If the alignment of the chemical potential levels of

[3]Note that the expression of the form $Q^2/2C$ describes the energy stored by a capacitor with a capacitance C and a charge Q on each of the plates.

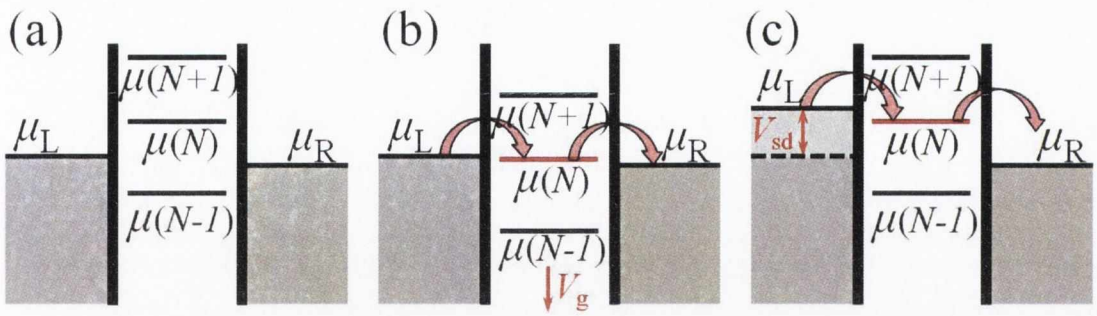

FIGURE 6.3: A schematic illustration of the effective energy level structure of the quantum dot in the constant interaction model. (a) Linear-response regime. If no level falls within the bias window between the chemical potentials of the source ($\mu_{\rm L}$) and of the drain ($\mu_{\rm R}$) electrodes, than the number of electrons on the dot is fixed due to Coulomb blockade and is equal to $N-1$ for a particular case shown here. As a result, no current flows through the dot. (b) By changing the gate voltage, the position of the quantum dot levels shift, which results in lifting the Coulomb blockade. The level $\mu(N)$ now falls within the bias window so that the number of electrons on the dot can alternate between N and $N-1$, resulting in a single-electron tunneling current. (c) By applying the source-drain voltage, the chemical potential of the source electrode ($\mu_{\rm L}$) is effectively shifted upwards. The level $\mu(N)$ falls within the bias window and the Coulomb blockade is lifted, allowing the current to flow through the dot.

the dot with respect to $\mu_{\rm L}$ and $\mu_{\rm R}$ is such as shown in Fig. 6.3(a), the energy required for the transition from $\mu(N-1)$ to $\mu(N)$, e.g. for adding an extra electron to the dot, is simply not available. As a result, the number of electrons in the dot remains fixed and no current can flow through the dot. This effect is known as *Coulomb blockade.*

The Coulomb blockade can be lifted by either changing the gate voltage or the source-drain voltage. Let us consider the first possibility. Changing $V_{\rm g}$ is equivalent to tuning the electrostatic potential locally on the dot with respect to that of the reservoirs. This effectively shifts the entire "ladder" of chemical potential levels up or down depending on the sign of $V_{\rm g}$. The result of shifting the levels by the gate voltage is shown in Fig. 6.3(b). Now the level $\mu(N)$ is within the bias window and the N-th electron can tunnel from the source electrode onto the dot. After it tunnels off to the drain, another electron is supplied by the source so that effectively the number of electrons on the dot is alternating between $N-1$ and N. This process is called *single-electron tunneling.*

The dependence of the current (conductance) through the dot in the linear-response regime, obtained by sweeping the gate voltage and measuring the current, exhibits peaks at certain values of the gate voltage as shown in Fig. 6.4 [a schematic illustration is shown in Fig. 6.4(a) and an actual experimental observation reported in Ref. [208]

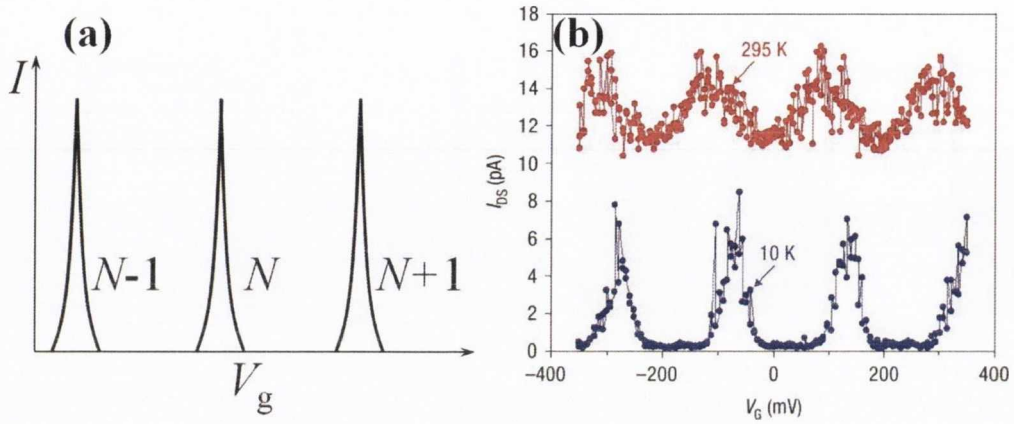

FIGURE 6.4: (a) A schematic illustration of the Coulomb blockade oscillations. The dependence of the current (I) through the dot as a function of the gate voltage (V_g) in the linear-response regime exhibits peaks, corresponding to single-electron tunneling events. In the valleys between the peaks the number of electrons is fixed due to Coulomb blockade. (b) Experimentally observed Coulomb blockade oscillations in the gate-voltage dependence of the current through a Coulomb island at two different temperatures (from Ref. [208]). The contrast between the Coulomb blockade valleys and peaks gets sharper at lower temperature.

is shown in Fig. 6.4(b)]. The peaks occur every time one of the chemical potential levels is aligned with μ_L and μ_R, allowing the single-electron tunneling current to flow through the dot. In the valleys between the peaks, the number of electrons on the dot is fixed due to Coulomb blockade.[4] The distance between the peaks corresponds to the addition energy E_{add} and therefore provides information about the energy spectrum of the quantum the dot.

Another way to lift the Coulomb blockade is achieved by changing the source-drain voltage, V_{sd}. For asymmetrically applied bias (the drain is grounded), increasing V_{sd} is equivalent to shifting up the chemical potential of the source electrode [see Fig. 6.3(c)]. This increases the separation between μ_L and μ_R and, if the chemical potential level of the dot falls within the bias window, the current can flow. As a result, the I-V characteristic of the quantum dot, e.g. the current measured as a function of the applied bias voltage, exhibits a "step" [see Fig. 6.5(a)] every time an electron is added to the dot, e.g. every time a new chemical potential level is dragged into the bias

[4]Note that the number of electrons on the dot (N) is a well-defined quantity as long as the conductance of the tunnel junctions connecting the dot to the electrodes is small compared to the conductance quantum $G_0 = 2e^2/h$ ($G_0 = e^2/h$ for non spin-degenerate systems). In quantum dot devices formed in semiconductor heterostructures the conductance of the tunnel junctions can be tuned continuously. Increasing the conductance of the junctions gradually leads to distortion of the periodic pattern in $G(V_g)$ or $I(V_g)$, where G is the conductance, due to mesoscopic conductance fluctuations.

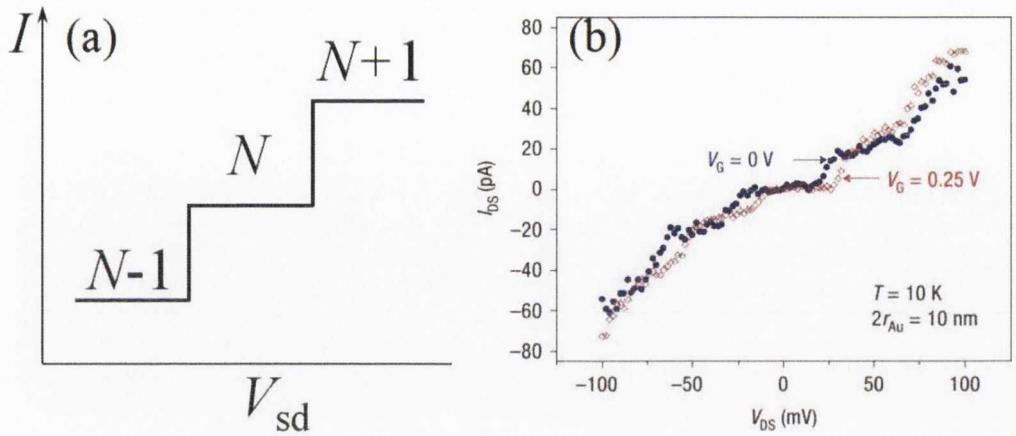

FIGURE 6.5: (a) A schematic illustration of the "Coulomb staircase". The current through the quantum dot (I) as a function of the source-drain voltage (V_{sd}) is a series of "steps", corresponding to incremental charging of the dot. (b) Experimentally measured I-V characteristics of a Coulomb island for two different values of the gate voltage (from Ref. [208]).

window. Such behavior is known as the "Coulomb staircase" and has been observed experimentally [see Fig. 6.5(b)].

In transport experiments on quantum dots, one usually measures the current or differential conductance, dI/dV_{sd}, while varying the bias voltage for a series of different values of the gate voltage. The resulting pattern, shown schematically in Fig. 6.6(a), is referred to as the "Coulomb diamond". Inside the diamond-shaped regions, the number of electrons is fixed due to Coulomb blockade, and no current can flow. The region, in which the number of electrons is equal to N, is marked in gray in Fig. 6.6(a). Outside these regions, the Coulomb blockade is lifted and the tunneling of electrons can occur. An example of the experimental observation of the "Coulomb diamond" in a GaAs-(Ga,Al)As quantum dot from Ref. [86], is shown in Fig. 6.6(b). The main difference between the experimental data and a schematic illustration, presented in Fig. 6.6(a), is a number of additional lines emerging from the edges of the diamond-shaped regions, which indicate transport through excited states.

Although the CI model provides an elementary understanding of how the quantization of charge and energy in quantum dots leads to effects like Coulomb blockade and Coulomb oscillations, it is based on a number of crude approximations. In this model the Coulomb interaction is parametrized by a classical ad hoc parameter - the capacitance of the dot C - and it is expressed in terms of the charging energy E_C of a single electron charge on a capacitor. In addition, one assumes that the single-particle levels

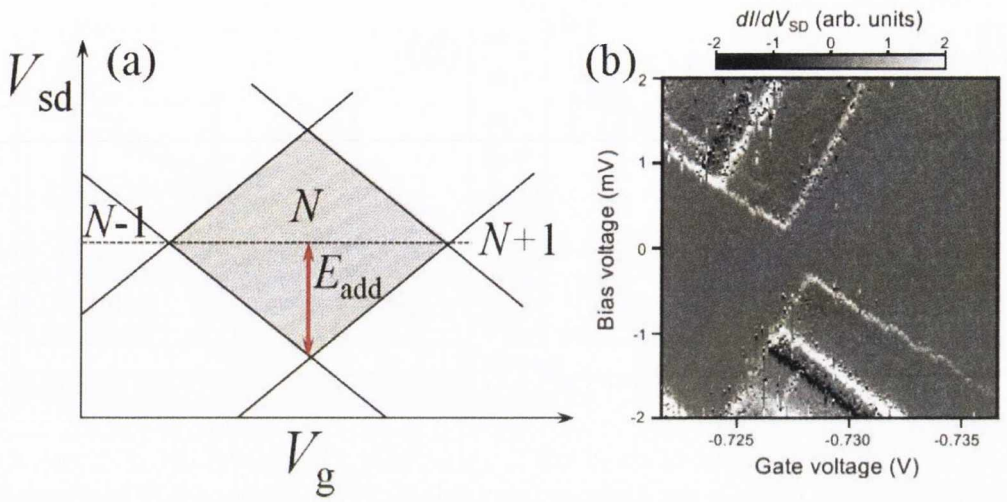

FIGURE 6.6: (a) A schematic illustration of the "Coulomb diamond" in the differential conductance as a function of the source-drain and the gate voltages. The number of electrons is fixed and the current is zero inside the diamond-shaped regions. The edges of the "diamonds" indicate the onset of the current. The addition energy E_{add} can be determined from the graph. (b) Experimentally measured differential conductance of the GaAs-(Ga,Al)As quantum dot as a function of the source-drain and the gate voltages (from Ref. [86]).

of the dot do not depend on the number of electrons and on the electron-electron interaction, which is not the case in real many-electron systems. Such assumption is, in principle, justified when the energy level spacing $\Delta\epsilon$ is much larger that the characteristic energy of interactions, expressed through the charging energy E_C. This condition is partially satisfied in few-electron vertical quantum dots but does not hold in lateral quantum dots, where the transport measurements contradict the predictions of the model [139]. For a rigorous treatment of intricate electron-electron interaction effects, advanced quantum models are required. This will be the subject of Section 6.3.

We will finish the overview of the phenomenology of quantum dots by discussing yet another fundamental phenomenon observed in quantum dot systems, namely the *Kondo effect*.

6.2.2 Kondo effect in quantum dots

As the temperature is lowered, the phonon-scattering contribution to the resistivity of a metal decreases. Therefore, it is expected that the resistivity will decrease and saturate to a finite value determined by scattering from crystal defects. However, a series of

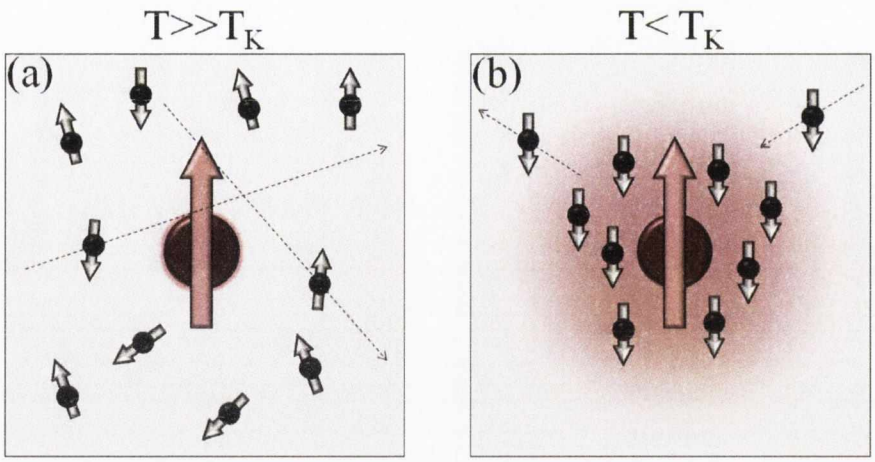

FIGURE 6.7: A magnetic impurity embedded in a metallic host. (a) At high temperatures ($T >> T_K$) the effective interaction between the spins of the conduction electrons and the spin of the impurity is almost zero and therefore the impurity acts as a normal non-magnetic defect. (b) At temperatures below the Kondo temperature (T_K) a bound-state (a singlet) is formed between the spin of the impurity and the surrounding conduction electrons of the host, leading to the screening of the impurity and therefore to the enhancement of scattering and the increase in the resistivity of the metal.

experiments performed in the early 1930s revealed that the resistivity of noble metals, such as Au, measured at temperatures as low as 10 K, exhibits a minimum and increases as the temperature is lowered further. This effect remained unexplained for a long time. It was later realized that the resistivity minimum is related to the presence of dilute magnetic impurities in a metal. A breakthrough in the theoretical understanding of this phenomenon occurred in 1964 when Kondo applied the *s-d* model to the impurity problem and found that in the third-order perturbation theory the electron-impurity scattering has logarithmic divergences in the zero-temperature limit [135]. This work has led to the formation of a new research topic named the "Kondo problem", e.g. the problem of a magnetic impurity embedded in a non-magnetic host. This problem was fully solved in 1975 by Wilson [270], using the NRG approach. Importantly, it has been shown that below the characteristic temperature, the so-called Kondo temperature (T_K), a magnetic impurity forms a singlet with the surrounding sea of conduction electrons, which leads to the increase of the resistivity (see Fig. 6.7).

The concept of a magnetic impurity in a host metal can be also applied to single-electron transistors: a quantum dot, which possesses a spin, behaves like a magnetic impurity and the electrons, tunneling between the electrodes and the dot, act as the conduction electrons of the host. The expectation that the Kondo physics should

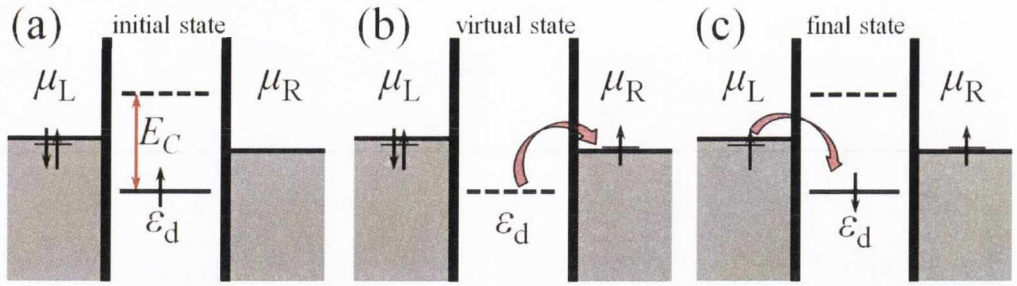

FIGURE 6.8: The Kondo resonance in the single-level quantum dot attached to the source and the drain electrodes. (a) In the initial state the energy level of the dot is below the chemical potentials of the electrodes and is occupied by an electron with spin up. Here we consider the linear-response regime, e.g. $V_{sd} \approx 0$ and $\mu_{L/R} \approx E_F$. (b) Due to quantum uncertainty, the spin-up electron can tunnel off to the drain, leaving the dot in a classically forbidden virtual state with a hole below E_F. (c) If a spin-down electron then tunnels from the source onto the dot, the final state of the system is such as if the spin of the electron on the dot has been flipped and an excitation has been produced at the Fermi level of the leads.

manifest itself in the transport properties of quantum dots has been confirmed by the experimental observations of the Kondo effect in small semiconductor quantum dots in the late 1990s [49, 79]. It appeared, however, that the interplay between the tunneling electrons and the quantum dot has a different effect on the conductance (resistivity) compared to that between the impurity and conduction electrons in a bulk metal. For temperatures below T_K the conductance of a quantum dot increases as a new mechanism for transport becomes available.

Let us consider a quantum dot with a single spin-degenerate level, attached to two electrodes in the linear response regime, e.g. for $V_{sd} \approx 0$. The level of the dot, which has energy ϵ_d, is below the Fermi level of the leads and it is occupied by a spin-up electron. The energy cost of adding another electron to the dot is given by the charging energy E_C (we will see in the next section that for a single-level quantum dot, described by the Anderson impurity model, this is expressed through the Coulomb repulsion parameter U). However, due to the Heisenberg uncertainty principle, the spin-up electron can momentarily tunnel out of the dot into the drain electrode, leaving the quantum dot in the otherwise prohibited *virtual state* with no electrons [see Fig. 6.8(b)]. If an electron with a spin down then tunnels from the source onto the dot, the system is found in the state shown in Fig. 6.8(c). It appears as if the spin of the electron on the dot has been flipped. The combination of many of such cycles generates a new state, or a new conduction channel, at the Fermi level of the leads, known as the *Kondo resonance* and observed in quantum dots at temperatures below T_K.

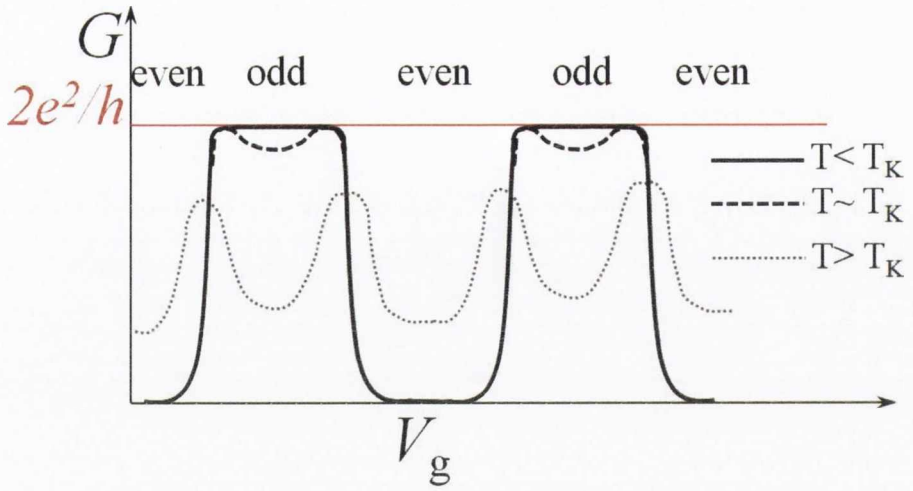

FIGURE 6.9: A cartoon illustrating the characteristic features of the linear-response conductance (G) of the quantum dot, which exhibits the Kondo effect, as a function of the gate voltage (V_g). If the number of electrons on the dot is odd, the Kondo resonance occurs, leading to an increase in the conductance and to a plateau in $G(V_g)$. With increasing T the conductance plateau is suppressed [238].

So far we considered the simplest case, in which the dot is occupied with one electron and therefore has a spin $S = 1/2$. However, the same arguments can be used in the general case of a quantum dot with an odd number of electrons, which also has $S = 1/2$. For a dot with an even number of electrons and $S = 0$ the Kondo resonance does not occur. As the number of electrons on the dot can be controlled by the gate voltage, the linear-response conductance of the quantum dot as a function of V_g displays the pattern shown in Fig. 6.9. As one can see from the graph, the system is alternating between the high- and the low-conductance regimes. The former corresponds to odd number of electrons and is sometimes called the Kondo plateau, while the latter corresponds to even number of electrons on the dot. For temperatures above T_K the odd-even asymmetry of the conductance is lifted and the familiar Coulomb blockade regime is recovered.

We will further comment on the possibility of describing the Kondo physics of quantum dots by means of the Anderson impurity model in the following section. Note, however, that we do not fully address this topic in the present work due to the inherent limitations of our model.

6.3 Lattice density functional theory for a strongly correlated quantum dot

6.3.1 Model system and transport setup in the multiple-probe assembly

We consider the model system depicted in Fig. 6.10. This is the simplest model for a single-electron transistor, which consists of a single-level quantum dot attached to two finite 1D leads, each having $N_{\mathrm{L/R}}$ atoms. Since we will use the TD MPB method to study electron transport in this system, we include two N_{d}-sites long atomic chains on each side of the dot. This is a necessary condition for the introduction of a generic dephasing mechanism in the injection process within the TD MPB approach (see Section 5.5.3.2).

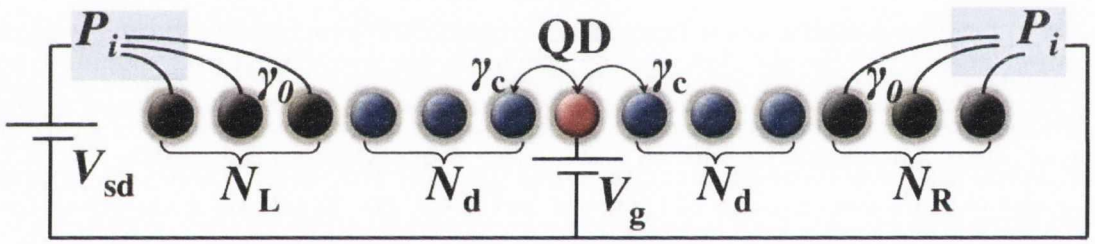

FIGURE 6.10: Model system: a quantum dot attached to two 1D leads, each comprising $N_{\mathrm{L/R}}$ sites. Here γ_0 is the hopping integral in the leads and γ_{c} is the lead-dot hopping. V_{g} denotes the gate voltage, acting locally on the dot, and V_{sd} is the source-drain voltage applied across the entire system. In the multiple-probe assembly, each atom i in L and R is coupled to an external probe P_i. The probes, connected to L(R) have a Fermi-Dirac distribution $f_{\mathrm{L}}(f_{\mathrm{R}})$ and a chemical potential $\mu_{\mathrm{L}}(\mu_{\mathrm{R}})$ with $V_{\mathrm{sd}} = \mu_{\mathrm{L}} - \mu_{\mathrm{R}}$.

6.3.2 Anderson impurity Hamiltonian for an interacting nano-junction

The Anderson impurity model [5] is a paradigmatic model in condensed matter physics, among other models such as the Hubbard model and the *s-d* model, that have been developed for the description of strongly correlated systems. Starting from the pioneering works of Hubbard [104, 105] in 1960s, the investigation of magnetic and transport

properties of strongly correlated systems using these basic models have contributed to the understanding of intriguing phenomena originating from electron correlations, such as metal-insulator phase transition, high-T_c superconductivity, heavy fermion effects and the Kondo effect. These models also played an important role in the development of advanced theoretical tools for electronic structure calculations of strongly correlated materials, such as the *dynamical mean-field theory* (DMFT) [6, p. 47].[5]

The Anderson impurity model was originally introduced to study the Kondo problem. In the case of a linear dispersion relation for the conduction band, the exact solution of the model is provided by the Bethe ansatz [255]. In the general case, a powerful tool is the NRG, which was first applied to the Kondo Hamiltonian[6] and later to the Anderson impurity model [142, 270].

The Anderson impurity model has been also used for the description of quantum dot systems within the transport picture [175], such as the one depicted in Fig. 6.10, where the quantum dot, attached to two non-interacting electrodes, plays the role of a single impurity. The total Hamiltonian of the system thus reads

$$\hat{H}_{\mathrm{S}} = \sum_{\alpha=\mathrm{L,R}} \hat{H}_{\alpha} + \hat{H}_{\mathrm{T}} + \hat{H}_{\mathrm{QD}}. \tag{6.21}$$

Here the first term is the nearest-neighbors single-orbital tight-binding (TB) Hamiltonian of the left (α=L) and right (α=R) lead, written as

$$\hat{H}_{\alpha} = \sum_{i,\sigma} \varepsilon_{i\alpha}\, \hat{c}^{\sigma\dagger}_{i\alpha}\, \hat{c}^{\sigma}_{i\alpha} + \sum_{i,\sigma} \left(\gamma_0\, \hat{c}^{\sigma\dagger}_{i\alpha}\, \hat{c}^{\sigma}_{i+1\alpha} + h.c. \right), \tag{6.22}$$

where $\varepsilon_{i\alpha}$ are the on-site energies and γ_0 is the hopping integral; $\hat{c}^{\sigma\dagger}_{i\alpha}(\hat{c}^{\sigma}_{i\alpha})$ is the creation (annihilation) operator for an electron with spin σ (σ=$\uparrow, \downarrow$) at the atomic site i in the

[5]The DMFT method takes advantage of the great simplifications that arise in the theory of strongly correlated electrons if the problem is treated in large-dimensional space ($d \to \infty$) [180], or equivalently for lattices with a large number of nearest neighbors. This allows one to map the lattice problem with strongly correlated electrons onto an effective impurity problem with local time- or energy-dependent (dynamical) mean-field, where the dependence of the field on the wave vector, responsible for spatial correlations, can be neglected in the limit $d \to \infty$. An important result, obtained with the DMFT applied to the Hubbard model [74], is the famous three-peak spectral structure with a central quasi-particle peak at the Fermi energy and two broad side peaks corresponding to lower and upper Hubbard bands. This structure was later observed in experimental spectra and was used to explain, for instance, the metal-insulator transition with increasing the Coulomb interaction strength.

[6]The Kondo Hamiltonian, or the Kondo impurity model, is the fully quantum *s-d* model, which can in fact be derived from the Anderson impurity model in the case of extremely localized impurity. As shown by Schrieffer and Wolff [224] the two models become equivalent in the limit of small *s-d* mixing.

lead α (the index $i = 1, .., N_\alpha$ runs from left to right for α=R and vice versa for α=L). Note that the two atomic chains on both the sides of the dot are also described by a TB model with the hopping integral γ_0 and they are included in the Hamiltonian of the leads. Therefore, despite the addition of the two atomic chains, which are not part of the leads, the Hamiltonian in Eq. (6.21) does not deviate from the standard one [31, p. 152].

The second term in Eq. (6.21) describes the tunneling between the quantum dot and the two adjacent sites and it is given by

$$\hat{H}_{\mathrm{T}} = \sum_{\sigma} \left(\gamma_{\mathrm{c}}\, \hat{c}_0^{\sigma\dagger}\, \hat{c}_{1\mathrm{L}}^{\sigma} + \gamma_{\mathrm{c}}\, \hat{c}_0^{\sigma\dagger}\, \hat{c}_{1\mathrm{R}}^{\sigma} + h.c. \right), \tag{6.23}$$

where $\hat{c}_0^{\sigma\dagger}(\hat{c}_0^{\sigma})$ is the creation (annihilation) operator for an electron with spin σ on the dot and γ_{c} is the hopping integral between the dot and site i=1 in the lead α.

Finally, the Hamiltonian of the quantum dot reads

$$\hat{H}_{\mathrm{QD}} = \sum_{\sigma} V_{\mathrm{g}}\, \hat{n}_0^{\sigma} + U\, \hat{n}_0^{\uparrow} \hat{n}_0^{\downarrow}. \tag{6.24}$$

The first term represents the non-interacting single-particle part of the Hamiltonian, with V_{g} being the on-site energy of the dot, acting as a local gate voltage. The second term describes the Coulomb interaction between two electrons with opposite spins on the dot, with U ($U \geq 0$) being the charging energy, which expresses the strength of the Coulomb repulsion. Here $\hat{n}_0^{\sigma}$=$\hat{c}_0^{\sigma\dagger}\, \hat{c}_0^{\sigma}$ is the dot site-occupation operator.

The intra-atomic Coulomb repulsion term ($U\, \hat{n}_0^{\uparrow} \hat{n}_0^{\downarrow}$) reduces the probability of the double occupation and the energy cost of putting two electrons on the dot is determined by the value of U. In a more general form, it is the basis of the Hubbard model, which is given by the following the Hamiltonian

$$H_{\mathrm{Hubbard}} = \sum_{ij\sigma} \gamma_{ij} \hat{c}_i^{\dagger} \hat{c}_j + \sum_{i} U\, \hat{n}_i^{\uparrow} \hat{n}_i^{\downarrow}, \tag{6.25}$$

where γ_{ij} s the hooping matrix element between sites i and j and $\hat{n}_i^{\sigma}$=$\hat{c}_i^{\sigma\dagger}\, \hat{c}_i^{\sigma}$ is the electron number operator for site i and spin σ. Clearly, the expression of the form $U\, \hat{n}_i^{\uparrow} \hat{n}_i^{\downarrow}$ is an approximation to a more general two-body interaction Hamiltonian

$$H_{\mathrm{int}} = \sum U_{\nu_1\nu_2\nu_3\nu_4} \hat{c}_{\nu_1}^{\dagger}\, \hat{c}_{\nu_2}^{\dagger}\, \hat{c}_{\nu_3} \hat{c}_{\nu_4},$$

where ν_l is the composite index, which includes the spin. The simplified interaction term only takes into account the Coulomb repulsion between electrons on the same site, which is indeed the dominant contribution to the electron-electron interaction for systems that can be described in terms of localized orbitals.

The standard approach to electron transport through an interacting nanojunction is the Keldysh nonequilibrium Green's function formalism (see Section 5.4.3 of the previous chapter), where the nonequilibrium state is realized through the adiabatic switching-on of the lead-dot coupling. For an open quantum dot, described by the Anderson impurity model, a formula for the electric current beyond the linear-response regime has been proposed and the derivation can be found in the textbook of Haug and Jauho [90, p. 170].

In practice, the current can be calculated by using the approximate expression for the Green's function (GF) of the dot in the presence of the tunneling between the dot and the electrodes. Within this approximation higher order correlations, responsible for the spin-flip events on the dot during the tunneling process, are explicitly omitted. Therefore the Kondo physics is not accessible by this approach. In particular, the linear-response conductance, calculated by using the approximate GF, always displays two Coulomb peaks as a function of the gate voltage, with the separation between the peaks controlled by the charging energy U. The first peak is due to the presence of the conduction channel, when the empty and the singly-occupied states are degenerate and one electron can be added to the dot. The second peak comes from another possible channel, which is open when the singly- and the doubly-occupied states are degenerate and the second electron is added. This result can be found in the textbook of Bruus and Flensberg [31, p. 166]. The results of our own calculations of the linear response conductance are presented in Appendix C.

However, in order to account for Kondo-like correlations, a more careful treatment is needed. This was done, for example, in the work of Hershfield, Davies and Wilkins [93, 94], who calculated the non-linear I-V characteristics and differential conductance of the quantum dot, described by the Anderson impurity model, by using the second-order (in U) perturbation theory. Their calculations reveal a signature of the Kondo resonance near the Fermi energy.

In fact, it is practically impossible to solve the problem exactly (analytically) and therefore any careful treatment of electron transport in the interacting case requires

the use of perturbation techniques, which is in general a difficult task.[7] Alternatively, one can use numerical many-body methods to solve the problem non-perturbatively. Recently, a number of numerical approaches based on the Keldysh formalism have been developed, such as the extension of quantum Monte Carlo (QMC) to the nonequilibrium situations [267] and the time-dependent density matrix RG (TD-DMRG) for quantum dots coupled to one-dimensional reservoirs [28].

The lattice density functional theory (LDFT) provides a method for calculating the ground-state properties of strongly-correlated systems, which has the advantage of its computational feasibility over many-body methods. A numerical approach, based on the extension of LDFT with a suitable XC functional to time-dependent phenomena, combined with open-boundary conditions for quantum transport, offers an alternative solution for the nonequilibrium transport problem in interacting nanojuctions.

6.3.3 Bethe-Ansatz Local Density Approximation

LDFT was originally proposed by Gunnarsson and Schönhammer [84, 222] as an extension of the standard *ab initio* DFT to lattice models. In the LDFT framework the HK theorems and the KS scheme are reformulated in terms of the site occupation, n_i, instead of the electron density $n(\boldsymbol{r})$. As standard DFT, LDFT is also in principle exact and it is only limited by the accuracy of a particular approximation to the XC functional. In the most commonly used approximation (LDA) the XC energy is approximated locally by that of the homogeneous electron gas, which plays the role of a *reference system*, whose properties, including correlations, are transferred by the LDA into the DFT-description of the system under study. The main idea behind the most popular improvements upon the LDA is to deal with the local approximation, for example, by introducing the dependence of the XC energy on the gradient of the electron density like in GGA.

A different strategy has been suggested for constructing approximate XC functional for LDFT: one can keep the local density but try to choose a better reference system

[7] A natural approach, which is to do a perturbation expansion in terms of the tunneling Hamiltonian, is not applicable in this case due to the fact that the unperturbed Hamiltonian is the two-body interacting Hamiltonian of the dot. The latter is not quadratic in terms of creation and annihilation operators and therefore the Wick's theorem, which transforms an arbitrary product of creation and annihilation operators into a sum of normal ordered products (creation operators are to the left of annihilation operators), does not apply in this case. This makes the usual perturbation expansion impossible. The perturbation theory can be instead constructed in terms of the charging energy U [187].

(different from the homogeneous electron gas). In fact, a large class of low-dimensional models can be solved exactly, for example, by Bethe ansatz. Therefore the solutions of these models in the homogeneous case can be used to construct an LDA functional. This can be then applied to the problems in the inhomogeneous case within the LDFT framework, which is much less restricted in terms of the size of the problem compared to exact many-body techniques [3].

Lima *et al.* [158] proposed a formulation of the LDA for a 1D homogeneous (infinite) Hubbard model with a uniform hopping γ [see Eq. (6.25)] based on the exact Bethe-ansatz (BA) solution [155]. In order to construct an approximate XC function, a parametrization of the total energy density (total energy per site) must be obtained as a function of U and the band-filling n, which is a constant for a homogeneous Hubbard model. The parametrization, proposed by Lima *et al.*, analytically interpolates between three limits, in which the exact analytic expressions for the total energy can be extracted from the BA solution: (*i*) $U \to 0$ and any $n \leq 1$, (*ii*) $U \to \infty$ and any $n \leq 1$, and (*iii*) $n = 1$ and any U. The proposed expression for the BA energy density reads

$$e^{\mathrm{BA}}[n, U] = -\frac{2\beta(U)}{\pi} \sin\left[\frac{\pi n}{\beta(U)}\right], \tag{6.26}$$

where $\beta(U)$ is a parameter that can be determined for each value of U by solving the following transcendental equation

$$-\frac{2\beta}{\pi} \sin\left(\frac{\pi}{\beta}\right) = -4 \int_0^\infty dx \, \frac{J_0(x) J_1(x)}{x \left[1 + \exp(Ux/2|\gamma|)\right]}. \tag{6.27}$$

In the above equation J_0 and J_1 are respectively the zero and first order Bessel functions. The expression on the right-hand side is the exact BA expression for the total energy at half-filling. The parameter β is thus determined in such a way, that for $n = 1$ Eq. (6.26) becomes exact for any U. In addition, Eq. (6.26) is constructed in such a way that it coincides with the exact BA result in the other two limits, namely $U = 0$ ($\beta = 2$) and $U \to \infty$ ($\beta = 1$). It has been shown that between these limits the exact and the approximate XC energies agree quantitatively [158].

In order to construct the BA XC energy $e_{\mathrm{XC}}^{\mathrm{BA}}[n, U]$, one needs to subtract from the total energy $e^{\mathrm{BA}}[n, U]$ the Hartree energy, $e_{\mathrm{H}}[n, U]$ and the non-interacting kinetic energy, $e[n, U = 0]$, as it is done in *ab initio* DFT. The BA XC potential $v_{\mathrm{XC}}^{\mathrm{BA}}[n, U]$, is then

given by the functional derivative of $e_{\rm XC}^{\rm BA}[n,U]$

$$v_{\rm XC}^{\rm BA}[n,U] \equiv \frac{\delta e_{\rm XC}^{\rm BA}[n,U]}{\delta n} = \frac{\delta\left(e^{\rm BA}[n,U] - e_{\rm H}[n,U] - e[n,U=0]\right)}{\delta n}. \tag{6.28}$$

The approximate Bethe-ansatz LDA (BALDA) potential is then defined as a local counterpart of $v_{\rm XC}^{\rm BA}[n,U]$

$$v_{\rm XC}^{\rm BALDA}[n_i,U] = v_{\rm XC}^{\rm BA}[n,U]\Big|_{n\to n_i}. \tag{6.29}$$

We can now apply this strategy to the many-body Hamiltonian of the quantum dot in Eq. (6.24). Within the LDFT framework this can be mapped onto an effective single-particle KS Hamiltonian, which reads

$$\hat{H}_0 = \sum_\sigma v_{\rm KS}\left[n_0\right]\,\hat{n}_0^\sigma. \tag{6.30}$$

Here n_0 is the charge density of the dot and $v_{\rm KS}$ is the effective Kohn-Sham potential, which is written as a sum of three terms

$$v_{\rm KS}\left[n_0\right] = V_{\rm g} + \frac{n_0}{2}\,U + v_{\rm XC}\left[n_0\right]. \tag{6.31}$$

The second and third terms are respectively the Hartree and the XC potential. Before the XC potential can be approximated, we need to make some modifications to the original BALDA potential. Since the latter is derived for a uniform Hubbard model with the Coulomb interaction U and the nearest-neighbors hopping γ, the relevant parameter in this case is U/γ. In the case of a weakly coupled quantum dot the relevant parameter is, in fact, U/γ_c with $\gamma_c << \gamma$. The modified BALDA potential, specifically tailored to a nonuniform configuration with a weakly coupled dot, has been introduced in Ref. [145]. The only difference with respect to the original potential is that in the limit $\gamma_c \to 0$, the XC potential of the isolated dot is correctly reproduced.

Following Kurth *et al.*, we define the BALDA potential for the dot such as

$$v_{\rm XC}^{\rm BALDA}\left[n_0\right] = \theta(1-n_0)v_{\rm XC}^{(<)}\left[n_0\right] - \theta(n_0-1)v_{\rm XC}^{(<)}\left[2-n_0\right], \tag{6.32}$$

where

$$v_{\rm XC}^{(<)}\left[n_0\right] = -\frac{Un_0}{2} - 2\gamma_c\left[-\cos\left(\frac{\pi n_0}{2}\right) + \cos\left(\frac{\pi n_0}{\beta}\right)\right]. \tag{6.33}$$

Here the parameter β is determined for each U from Eq. (6.27) with γ substituted by γ_c.

As the original BALDA potential, $v_{\rm XC}^{\rm BALDA}$ exhibits a discontinuity at n_0=1, i.e. at the phase transition of the 1D Hubbard model, which corresponds to opening of the gap in the energy spectrum. In practice, we use a continuous approximation to the BALDA potential [145], where the true discontinuity, expressed through the Heaviside step function $\theta(n_0)$, is replaced by a function $f(n_0) = 1/(e^{-n_0/a} + 1)$ with a being a smoothing parameter. This gives $\theta(1 - n_0) = f(1 - n_0)$ and $\theta(n_0 - 1) = 1 - f(1 - n_0)$. We use $a = 10^{-7}$, which guarantees a very sharp slope at $n_0 = 1$. Figure 6.11 shows the BALDA potential, $v_{\rm XC}$ (we omit the BALDA notation for simplicity), defined in Eq. 6.32, and the total effective KS potential [see Eq. (6.31)] as functions of the occupation of the dot for three different values of U.

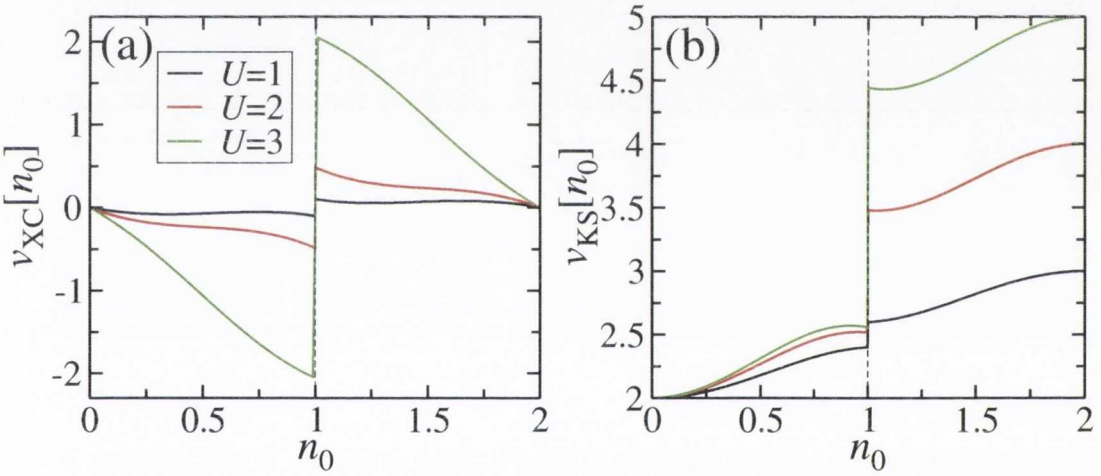

FIGURE 6.11: (a) The BALDA potential ($v_{\rm XC}$) and (b) the total effective KS potential ($v_{\rm KS}$) as functions of the occupation of the dot (n_0) for $U = 1$, $U = 2$ and $U = 3$. The following parameters are used: $\gamma_c = -0.3$ eV, $V_{\rm g} = 2$ eV.

In our simulations we consider three levels of description: (*i*) $U = 0$, or non-interacting case, for which the effective potential of the dot is simply given by $v_{\rm KS}$=$V_{\rm g}$, (*ii*) $v_{\rm XC} \to 0$, or the Hartree approximation, where the potential on the dot is $v_{\rm H}$=$V_{\rm g} + U\, n_0/2$; and (*iii*) the full discontinuous effective potential, given by Eq. (6.31), which we refer to as $v_{\rm KS}$ for clarity.

We introduce the time-dependence in the Hamiltonian of the quantum dot, by means of the adiabatic approximation, where $v_{\rm KS}$ is assumed to depend on time only through

the instantaneous charge density of the dot

$$v_{\mathrm{KS}}(t) = v_{\mathrm{KS}}[n_0(t)]. \tag{6.34}$$

The XC BALDA potential in the adiabatic approximation reads

$$v_{\mathrm{XC}}^{\mathrm{BALDA}}(t) = v_{\mathrm{XC}}^{\mathrm{BALDA}}[n_0(t)]. \tag{6.35}$$

Such approximation to the XC functional is referred to as adiabatic BALDA (ABALDA).

The question of the applicability of such adiabatic local approximation to the description of non-equilibrium transport in strongly correlated systems has been addressed in recent two works respectively by Uimonen *et al.* [257] and Khosravi *et al.* [126] In particular, a comparative study between the TDDFT approach with ABALDA (TDDFT+ABALDA) and many-body perturbation theory, applied to the out-of- equilibrium Anderson impurity model, has been carried out in Ref. [257]. The results obtained with both approaches have been tested against numerically exact results obtained with TD-DMRG. It was found that, in general, the TDDFT+ABALDA approach is in good qualitative agreement with many-body perturbation theory over a wide range of parameters. However, in many cases it overestimates the steady-state currents. This problem was linked to the shortcomings of the local approximation to the XC functional and to the absence of electron correlations inside the electrodes. Moreover, it was demonstrated in Ref. [126] that the inclusion of dynamical correlations, or memory effects, might eliminate the multistability in the density and the current, which can be found within the TDDFT+ABALDA approach. These are strong indications that more advanced, non-local both in space and time, approximations to the XC functional are required. However, as was demonstrated in Ref. [145] and as it will be shown here, the ABALDA already provides valuable insights into TD transport in strongly correlated systems.

6.3.4 Transport equations

The calculations of electron transport in the system depicted in Fig. 6.10 are performed using the MPB method. Since the latter was describe in detail in the previous chapter, here we restrict ourselves to a brief summary. In the TD MPB approach the time-dependent equation of motion for the density matrix $\hat{\rho}_{\mathrm{S}}(t)$ of the system in the presence

of the external probes reads

$$
\begin{aligned}
i\hbar\,\dot{\hat{\rho}}_{\rm S}(t) &= \Big[\hat{H}_{\rm S}(t),\hat{\rho}_{\rm S}(t)\Big] + \hat{\Sigma}^{+}\,\hat{\rho}_{\rm S}(t) - \hat{\rho}_{\rm S}(t)\,\hat{\Sigma}^{-} + \\
&+ \frac{1}{2\pi\imath}\int_{-\infty}^{\infty}\Big[\hat{\Sigma}^{<}(E)\,\hat{G}_{\rm S}^{-}(E) - \hat{G}_{\rm S}^{+}(E)\,\hat{\Sigma}^{<}(E)\Big]\,dE\,.
\end{aligned}
\tag{6.36}
$$

The first two terms after the commutator are extraction (drain) terms, while the last one is the injection (source) term. $\hat{G}^{+}$ ($\hat{G}^{-}$) is the retarded (advanced) Green's function of the system and it is given by

$$
\hat{G}^{\pm}(E) = \Big(E\,\hat{I}_{\rm S} - \hat{H}_{\rm S_0} - \hat{\Sigma}^{\pm} \pm i\,\hat{I}_{\rm S}\,\Delta\Big)^{-1}\,, \tag{6.37}
$$

where $\hat{H}_{\rm S_0} = \sum_{\alpha={\rm L,R}}\hat{H}_{\alpha} + \hat{H}_{\rm T} + \sum_{\sigma} V_{\rm g}\,\hat{n}_0^{\sigma}$ is the time-independent part of $\hat{H}_{\rm S}(t)$ [see Eq. (6.21)] and Δ is a dephasing factor. The self-energies due to the presence of the external probes and the in-scattering self-energy are written as

$$
\hat{\Sigma}^{\pm} = \mp i\,\frac{\Gamma}{2}\,\hat{I}_{\rm L} \mp i\,\frac{\Gamma}{2}\,\hat{I}_{\rm R}\,, \tag{6.38}
$$

$$
\hat{\Sigma}^{<}(E) = \imath\Big[f_{\rm L}(E)\,\hat{I}_{\rm L} + f_{\rm R}(E)\,\hat{I}_{\rm R}\Big]\,, \tag{6.39}
$$

with the broadening Γ defined as $\Gamma = 2\pi\gamma_P^2 d$, where γ_P is the coupling to the probes, assumed to be identical for all sites in the leads, and d is an energy-independent constant, which represents the surface density of states of the probes (constant) within the wide-band limit; $\hat{I}_{\rm M}$ is the identity operator in region M (M=L, R, S).

In order to investigate the open-boundary electron dynamics in the time domain, Eq. (6.36) is numerically-integrated by using the fourth-order Runge-Kutta (RK4) algorithm [206, p. 704]. As initial condition, we use the density matrix $\hat{\rho}_{\rm S}(t_0)$ of an isolated dot (not coupled to the probes), constructed from the eigenstates of the Hamiltonian $\hat{H}_{\rm S}$. The open boundary terms are switched on over a short time interval of 5 fs and maintained throughout the simulation. The current through the dot is then calculated as a bond current between the dot and the adjacent site on the right [see the definition of the bond current in Eq. (2.60)]. The typical parameters of the MPB setup used in our simulations, unless specified otherwise, are $N_{\rm L/R} = 90$ and $N_{\rm d} = 20$. We have tested that further increasing the size of the system does not lead to significant difference in the *I-V* characteristics. In order to have one free parameter instead of two, we use the condition $\Delta{=}\Gamma/2$, which has been discussed in detail in Ref. [171], and $\Gamma = 0.35$ eV in our simulations.

In the following section we report the results of the investigation of electron transport through a strongly correlated quantum dot. First, the *I-V* characteristics of a non-interacting quantum dot, calculated by using the TD MPB method, are compared to the analytic results, obtained with the NEGF approach. In the non-interacting case we will also discuss possible sources of NDC in the *I-V* characteristics. In the second part of Section 6.4, we will present the results of the time-dependent transport calculations for the dot in the CB regime. Finally, we will propose an explanation for the observed NDC in the *I-V* characteristics.

6.4 Results

6.4.1 Non-interacting case

As a test of the applicability of the TD MPB method we first examine the non-interacting case ($U = 0$). For this situation, we directly compare the *I-V* characteristics obtained from the TD simulations to the ones calculated by using the standard NEGF-based Landauer solution, which we refer to as exact NEGF. The comparison is presented in Fig. 6.12, where the current is plotted as a function of the source-drain voltage for the non-interacting level aligned with the Fermi level in the leads ($V_g = E_F = 0$). In the case of the TD MPB approach, the value for the steady-state current is obtained from the TD simulation for the corresponding value of V_{sd} after the steady-state has been established, i.e. when the variation of the current with time becomes negligible. In the case of the exact NEGF method, we use the well-known analytical expression for the non-equilibrium current through a non-interacting resonant level (NIRL), coupled to two semi-infinite electrodes (see Ref. [17] and Ref. [90, p. 165])

$$I_{EN} = \frac{2e}{h} \int dE \, \frac{\Gamma_L(E)\Gamma_R(E)}{[E - V_g - \Lambda(E)]^2 + [\Gamma(E)/2]^2} \times [f_L(E) - f_R(E)] \,. \tag{6.40}$$

Here $\Lambda(E) = \Lambda_L(E) + \Lambda_R(E)$ and $\Gamma(E) = \Gamma_L(E) + \Gamma_R(E)$ represent, respectively, the real and the imaginary part of the total self-energy due to the presence of electrodes, with $\Lambda_{L(R)}$ and $\Gamma_{L(R)}$ given by

$$\Lambda_{L(R)}(E) = \frac{\gamma_c}{2\gamma_0^2} E_{L(R)}, \tag{6.41}$$

$$\Gamma_{L(R)}(E) = \frac{\gamma_c^2}{\gamma_0^2} \theta(2\gamma_0 - |E_{L(R)}|) \sqrt{4\gamma_0^2 - E_{L(R)}^2} \,, \tag{6.42}$$

where $E_\alpha \equiv E - \varepsilon_\alpha$, ε_α being the on-site energy in the lead α (α =L, R). To obtain the expression for the current within the NIRL model, we have employed the same analytical expression for the surface GF of a one-dimensional semi-infinite TB lead that was used for the calculation of the *I-V* characteristics of the resonant dimer in Section 5.6.1 of the previous chapter [see Eq. (5.145)].

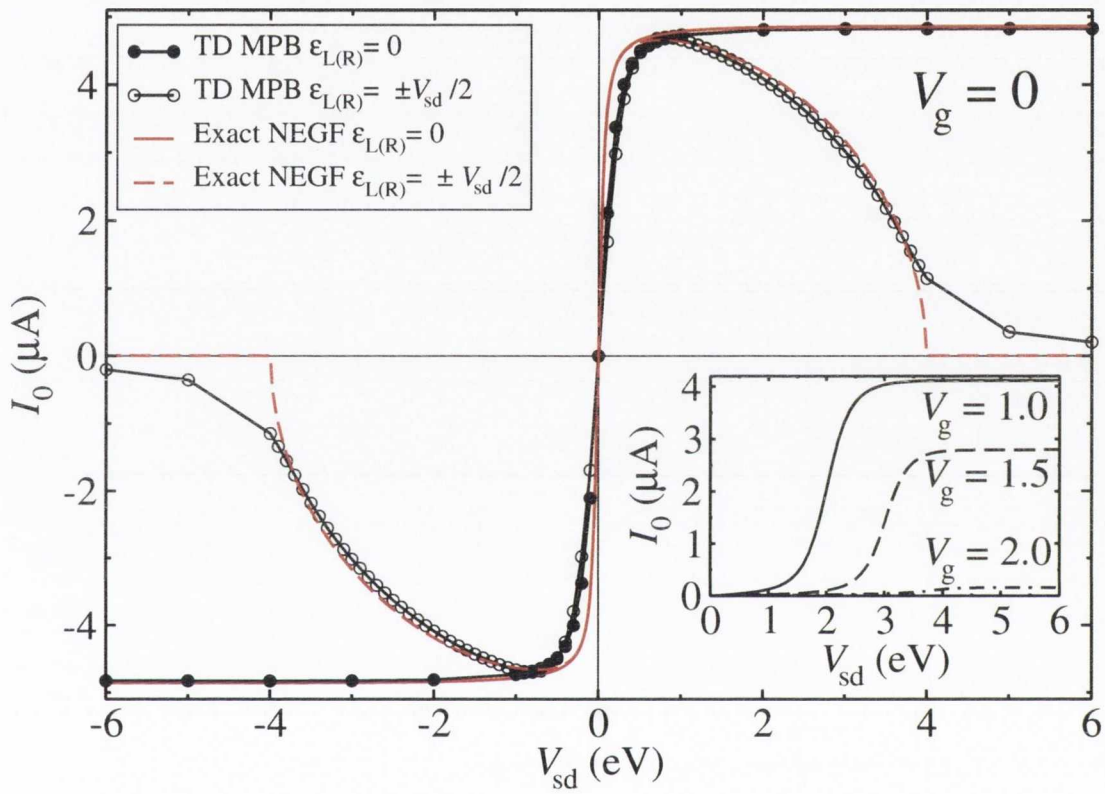

FIGURE 6.12: Current through the quantum dot, I_0, as a function of the source-drain voltage, V_{sd}, for zero gate voltage (V_g=0), calculated using the both exact NEGF and the TD MPB method, and for two configurations of the leads: $\varepsilon_{L/R}$=0 and $\varepsilon_{L/R}$=±V_{sd}/2. The inset shows the *I-V* characteristics obtained with the TD MPB approach for $\varepsilon_{L/R}$=0 and three different gate voltages, V_g=1.0, 1.5 and 2.0 eV. The following parameters are used: γ_0=−1.0 eV, γ_c=−0.1 eV and E_F=0. The source-drain voltage is applied symmetrically, $\mu_{L/R}$=E_F ± V_{sd}/2. In order to achieve a better agreement with the exact NEGF results we use the improved MPB setup with $N_{L(R)}$ = 250, N_d = 90 and Γ = 0.15.

We consider two possible limits for the on-site energies in the electrodes: (*i*) the highly conducting regime with ε_α=0 for all atoms in α =L, R and (*ii*) the weakly conducting regime for which the on-site energies in L(R) are shifted in accordance with the respective electrochemical potential, $\varepsilon_{L(R)}$=±V_{sd}/2. As expected, the difference between the *I-V* curves calculated in these two limits becomes significant at large bias, since

the transmission in case (*ii*) rapidly drops to zero once the bias voltage exceeds the bandwidth of the leads ($4|\gamma_0|$). This high-bias NDC effect, stemming entirely from the finite electrode band-with, is a well-understood feature of steady-state transport in low-dimensional, yet uncorrelated, electron systems [17]. We also note that the low-bias agreement between the two transport limits can, in principle, be extended to arbitrarily high biases $V_{\rm sd}$ by increasing $\gamma_0 > V_{\rm sd}/4$.[8]

An encouraging result is that for both the transport limits the TD MPB method reconstructs rather well the exact NEGF *I-V*. The agreement is particularly good in the highly conducting limit. The smearing of the abrupt *I-V* features at low bias and again the NDC drop at $V_{\rm sd} \lesssim 4\gamma_0$ for the weakly conducting limit are inherent to the TD MPB method [171]. These are due to the dephasing factor, which simplifies the equation of motion for the density matrix by eliminating temporal non-localities in the injection process.

In order to eliminate the drop in the current at large bias voltages and to focus on the electron interaction in the quantum dot, we will use the $\varepsilon_{\rm L(R)}$=0 limit in all the further calculations presented. In this case, the saturation current at high voltages is entirely determined by the position of the resonant level, set by the gate voltage $V_{\rm g}$ (see the inset of Fig 6.12), relatively to the electrodes band center. As the resonant the level approaches the band-edge of the leads ($V_g \lesssim 2\gamma_0$), the saturation current decreases. In Section 6.4.2.2 we will recognize the contribution of the latter effect to the drop in the current as a function of the source-drain voltage.

6.4.2 Interacting case

6.4.2.1 Time-dependent transport

While in the non-interacting case the TD current through the dot always reaches the steady-state, in the case when electron-electron interaction is considered this is not guaranteed. In fact for certain values of the source-drain voltage, for which the charge density of the dot approaches unity, the system is driven into a dynamical state, where current, density and on-site potential oscillate [145] without ever reaching a steady-state.

[8] We have established that if $|\gamma_0|$ is increased from 1 eV to 3.88 eV, the results for the current, obtained by using two limits for the on-site energies of the leads, differ by at most 3% for $V_{\rm sd}$=4 eV and for $V_{\rm g}$ ranging between 0 and 1 eV.

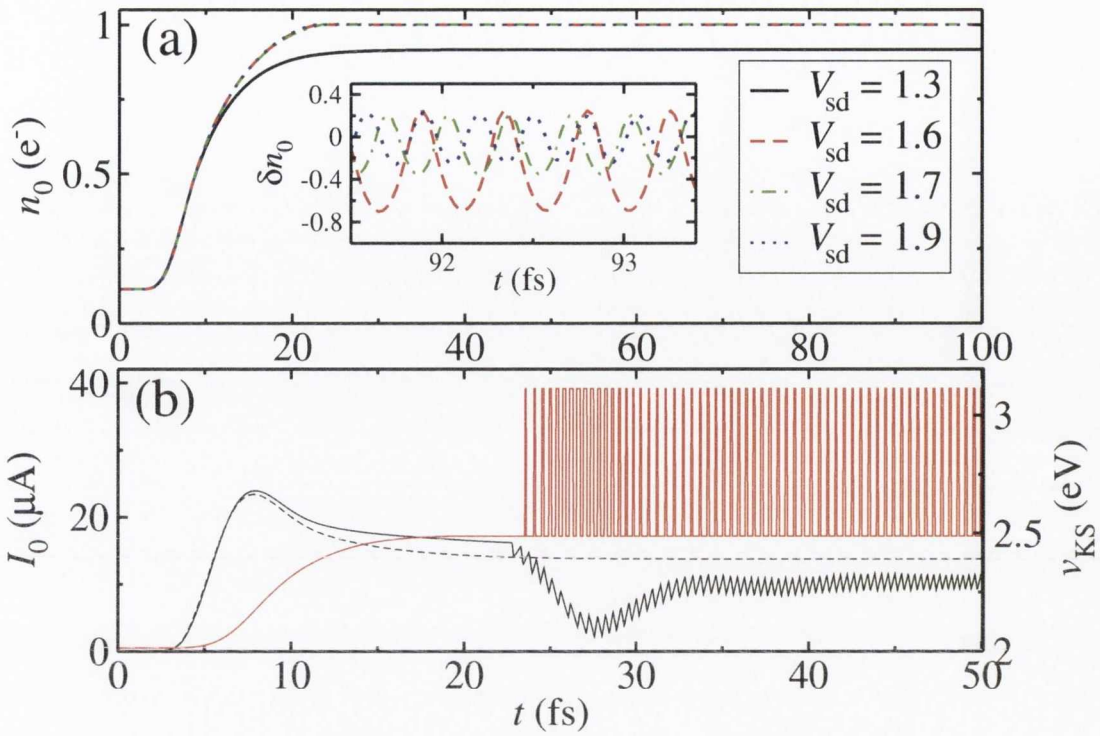

FIGURE 6.13: Real-time evolution of the quantum dot: (a) Charge density of the dot (n_0) for four different values of the source-drain voltage, V_{sd}=1.3, 1.6, 1.7, and 1.9 eV. The inset shows the fluctuation of the density around unity, δn_0, defined as $\delta n_0 = (n_0 - 1) \times 10^3$. (b) Current through the dot, I_0, for two values of V_{sd}: V_{sd}=1.6 eV (black solid line), which corresponds to the oscillating regime, and V_{sd}=1.3 eV (black dashed line) where no oscillations are observed. Note that the corresponding Kohn-Sham potential (v_{KS}) [red solid line] is also in the oscillating regime (V_{sd}=1.6 eV). The following parameters are used: γ_0=−1.5 eV, γ_c=−0.3 eV, E_F=1.5 eV, U=2.0 eV, $\varepsilon_{L(R)}$=0 is taken as a reference of energy. The source-drain voltage is applied asymmetrically ($\mu_L = E_F + V_{sd}$, $\mu_R = E_F$).

The question we address here is whether such dynamical state can be captured by the MPB method. The results of our calculations are shown in Fig. 6.13. For all values of the source-drain voltage below a critical value V_{sd}^{cr} a steady-state is achieved. However, for source-drain voltages above V_{sd}^{cr}, oscillations indeed develop in all the transport-related quantities. As shown in Fig. 6.13 for this range of V_{sd} the density quickly reaches the critical value of $n_0 = 1$. At the same time the first jump of the on-site potential occurs, followed by a series of almost rectangular pulses [see Fig. 6.13(b)]. Due to the derivative discontinuity at $n_0 = 1$, the on-site potential reaches an oscillating regime, abruptly alternating in time between two values, one just below and the other just above the discontinuity. This translates into oscillations of the charge density around $n_0 = 1$ [see the inset in see Fig. 6.13(a)] and also into oscillations in the current

[Fig. 6.13(b)]. The oscillations in all calculated quantities are in the femtosecond and sub-femtosecond range.

Below, we elaborate on the dynamical features observed for different values of $V_{\rm sd}$. The height of the pulses in $v_{\rm KS}(t)$ is equal to the height of the jump of $v_{\rm KS}[n_0]$ at the derivative discontinuity and it is mainly governed by the value of the charging energy U. The width of the pulses increases with increasing $V_{\rm sd}$. This essentially means that the larger is $V_{\rm sd}$, the longer the system tends to stay in the state with a larger on-site potential, corresponding to the density $n_0 > 1$. Further increasing $V_{\rm sd}$ will finally lead to a steady-state. The exact value of the threshold voltage, $V_{\rm sd}^{\rm cr}$, is difficult to determine since the on-site potential changes with time. From simple considerations, however, we established that $V_{\rm sd}^{\rm cr} \geq v_{\rm KS}[\bar{n}]$, where $\bar{n}$ is a value of the charge density just below 1. For the set of parameters used here $V_{\rm sd}^{\rm cr} \approx 1.5$ eV.

As discussed by Kurth *et al.*, the dynamical state of the quantum dot described above is a manifestation of dynamical Coulomb blockade. By applying a large enough source-drain voltage the dot can be charged. However, when the charge reaches the critical value $n_0 = 1$, the on-site potential immediately increases by an amount proportional to the Coulomb repulsion U, thus preventing further charging. This essentially corresponds to the CB regime. In addition, the TD simulations reveal that in this regime the quantum dot is alternating between two states, separated by an energy barrier determined by U. These two states correspond to the fluctuation of the charge on the dot around $n_0 = 1$, which originates from the fact that the BALDA potential has a discontinuity at $n_0 = 1$ but it is a smoothly varying function of n_0 away from this occupation.

It follows from the discussion that the dynamics of the quantum dot in the CB regime, calculated with the TD MPB method, is in a good agreement with the results reported in Ref. [145] both qualitatively and quantitatively. We have established numerically that the two different methods reproduce practically identical dynamical trajectories for all the observables in the long-time limit in the case of an interacting system. The remaining differences are limited to the early stage of the time evolution. A characteristic feature of the on-site potential of the dot, observed in Ref. [145], is a transition period just after the start of the oscillations, where the series of rectangular pulses in the time-dependent $v_{\rm KS}$ is preceded by a larger pulse whose width increases with $V_{\rm sd}$. This characteristic transient pulse is not present in our calculations (see Fig. 6.13).

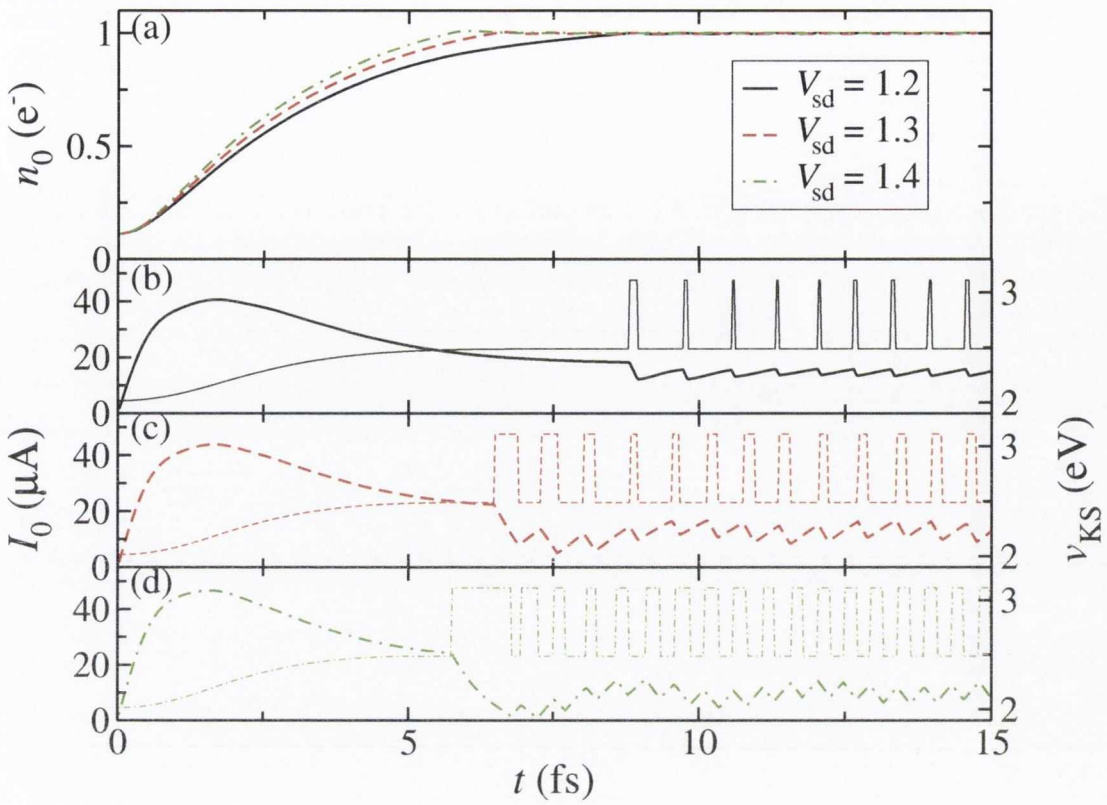

FIGURE 6.14: Real-time evolution of the quantum dot in the closed-boundary setup: (a) Charge density of the dot (n_0) for three different values of the source-drain voltage, V_{sd}=1.2, 1.3, and 1.4 eV. Current through the dot, I_0, [thick lines] and the corresponding Kohn-Sham potential, v_{KS}, [thin lines] for (b) V_{sd}=1.2 eV, (c) V_{sd}=1.3 eV, and (d) V_{sd}=1.4 eV. The parameters are the same as in Fig. 6.13. The source-drain voltage is applied as a rigid shift of the on-site energies in the left lead.

In order to establish to what extent the transient pulse is determined by the initial conditions, we performed TD simulations for the same system as shown in Fig. 6.10 but without attaching the external probes, i.e. for a closed-boundary finite system. Instead, we applied the source-drain voltage as a rigid shift of the on-site energies in the left lead, i.e. a term $V_{sd} \sum_{i=1,\sigma}^{N_\alpha} \hat{c}_{i\alpha}^{\sigma\dagger} \hat{c}_{i\alpha}^{\sigma}$ has been added to the Hamiltonian $\hat{H}_\alpha$ for α = L [see Eq. (6.22)] at the start of the TD simulation. We used longer leads [$N_{L(R)}$=220] and limited the time of the simulations to 100 fs, which is sufficient to observe the time propagation before the reflections from the finite boundaries start to affect the dynamics. The time-dependence of the charge density, current and on-site potential, obtained from the closed-boundary simulation, is presented in Fig. 6.14. In contrast to our open-boundary simulations, we indeed observed qualitatively the same transient regime as in Ref. [145]. This is mainly characterized by an earlier onset of

the CB oscillations for larger source-drain voltages and by the increase of the width of the first pulse in the time-dependence of the Kohn-Sham potential with increasing V_{sd}.

Finally, we note that in the earlier works by Rodrigues *et al.* [212, 213] the effect of electronic correlations on the transport properties of a quantum dot in the CB regime has also been addressed. The authors performed a time-dependent study of the Anderson impurity model, based on the decoupling procedure to solve the equation of motion for a single-particle operator [104]. By varying the parameters of the dot and the value of the applied bias voltage, they identified a special region of the parameter space, in which no stationary solution is possible. This region clearly corresponds to the CB regime. In the time-dependent simulations the authors observed highly non-linear self-sustained oscillations in the current and in the charge density in the picosecond range. Although these are qualitatively and quantitatively different from those found in Ref. [145] and in our work, they have also been attributed to strong correlations. It is worth mentioning that the interest in Coulomb interaction-induced nonlinearities and multistubilities in quantum transport, can be traced back to the observation of nonlinear effects in three-dimensional double-barrier heterostructures [80], manifested as a bistability in the negative differential resistance region of the I-V characteristics.

6.4.2.2 Steady-state transport from time-dependent simulations

In the previous section we demonstrated that, within a certain range of parameters, the discontinuity of the DFT potential prevents the quantum dot from evolving towards the steady state. Outside such range, however, a steady-state is achievable. Here we determine the steady-state current through the dot for various gate voltages and map out the corresponding I-V curves. For situations, where the dot is trapped in oscillations, we take as steady-state current its time-average in the long-time limit.

The linear response conductance as a function of V_{g} is depicted in Fig. 6.15. This is calculated as the finite-difference ratio $\Delta I_0/\Delta V_{\mathrm{sd}}$ close to zero bias (for the very low but finite bias $\Delta V_{\mathrm{sd}} = 0.01$ eV) and represents an approximation to the zero-bias differential conductance. In the non-interacting case, the conductance is composed of a single peak centered at around V_{g}=1.5 eV, which corresponds to the Fermi level of the leads. This is expected from the steady-state picture of transport through a non-interacting resonant level. In principle the width of the resonance peak is given by the dot-lead hopping integral γ_{c}. In our TD MPB calculations, however, there is an

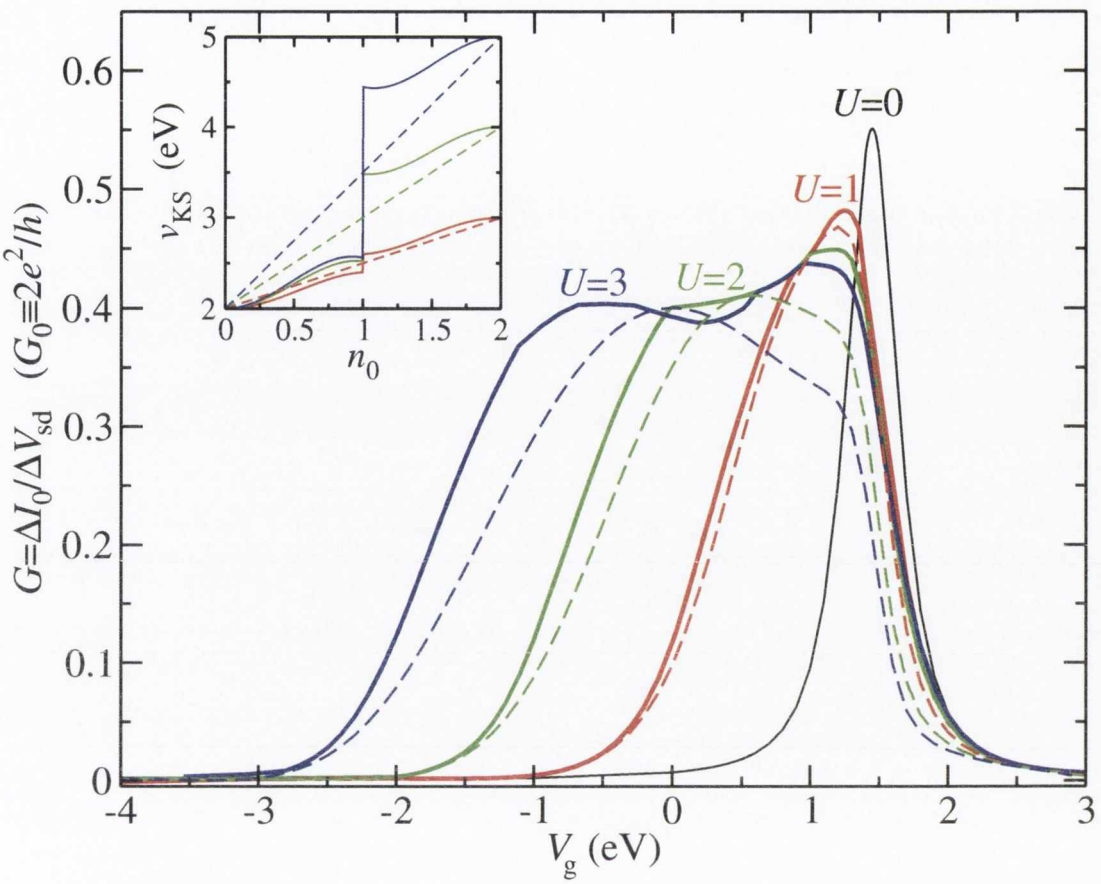

FIGURE 6.15: Differential conductance of the dot as a function of the gate voltage (V_g) for the Kohn-Sham potential, v_{KS}, [thick solid lines] and for the Hartree potential, v_H, [dashed lines] with U=1, 2, and 3 eV, and for the non-interacting case (thin solid line). The inset shows a comparison between the density-dependence of v_{KS} (solid lines) and v_H (dashed lines) for the same values of U. Parameters are the same as those of Fig. 6.13 and $V_{sd} = 0.01$ eV.

additional resonance broadening factor (τ_Δ) related to the dephasing condition in the equations of motion. Its corresponding energy unit, $\Delta = \hbar/\tau_\Delta$, can be associated to a fictitious temperature, smearing the electronic energy distributions in the leads [171]. As a result, a suppression of the transmission resonance proportional to $1/\Delta$ is also expected. This is the reason why the amplitude of the conductance peak in the non-interacting case (see Fig. 6.15) is below the conductance quantum $G_0 = 2e^2/h$.

In the interacting case the Anderson impurity model predicts a conductance plateau for $T < T_K$ and two distinct Coulomb peaks in the conductance as a function of the gate voltage for $T > T_K$ (see Fig. 6.9). While the former is a signature of the Kondo effect for a singly-occupied dot, the latter are manifestation of charge quantization at

the dot and correspond to each of the two integer electron number states, in which the dot is inhabited by one or two electrons, respectively. Hence in the zero-temperature limit and for zero bias one expects to see the conductance plateau. Recently reported results [22, 234] suggest that the DFT+NEGF approach with the XC functional, which, like the BALDA one, exhibits a derivative discontinuity at integer occupation, is able to reproduce this behavior quantitatively. This is an indication that our time-dependent approach might also be able to describe the zero-temperature linear-response regime.[9] Below we describe our findings.

In the case of the Hartree approximation, the gate-voltage dependence of the conductance represents a broad asymmetric peak, whose width is proportional to U. In the case of the full discontinuous effective potential (v_{KS}), one can distinguish a special range of the gate voltages, roughly between the position of the $U = 0$ resonance level, $V_{\mathrm{res}} = E_{\mathrm{F}}$, and the value $V_{\mathrm{res}} - U$, for which we observe features in the conductance quite different from the Hartree-only case. The width of this region increases with increasing U and is given by the value of the jump of the on-site potential $v_{\mathrm{KS}}[n_0]$ at the discontinuity. For the TD calculations with v_{KS} and for V_{g} in this range no steady-state is achieved. Hence, the conductance curves in this region of V_{g}, which resemble a plateau for large U, carry some degree of arbitrariness, associated with the interpretation of the time-averaged TD current. In fact, for those gate voltages, which drive the charge density of the dot close to unity, even the calculation of the ground-state is problematic from a numerical viewpoint, because of the derivative discontinuity. In such cases we used the following iterative procedure. Let V_{g}^0 be the value of the gate voltage, for which the ground-state (initial) density is calculated self-consistently, while $V_{\mathrm{g}}^0 + \delta V_{\mathrm{g}}$ is the value of the gate voltage for which the self-consistent calculation does not converge. In this case, the final density, obtained at the end of the TD simulation with V_{g}=V_{g}^0, is taken as initial density for the simulation with V_{g}=$V_{\mathrm{g}}^0 + \delta V_{\mathrm{g}}$.

In Fig. 6.16, we present a more detailed comparison between the transport-related quantities, calculated for v_{KS} and v_{H} for a particular value of U ($U = 2$) and for $U = 0$. The region of the gate voltages, for which no steady state is found, is marked on the graph by the dashed vertical red lines. The most striking difference between the results obtained with the Hartree approximation and with the full discontinuous effective potential can be seen in the gate-voltage dependence of the charge density

[9] Note that our model is the zero-temperature one. The only thermal-like effects enter the TD MPB formulation through a dephasing mechanism in the process of injection of carriers from the battery into the leads, which acts like a fictitious temperature, smearing the Fermi-Dirac distributions in the leads.

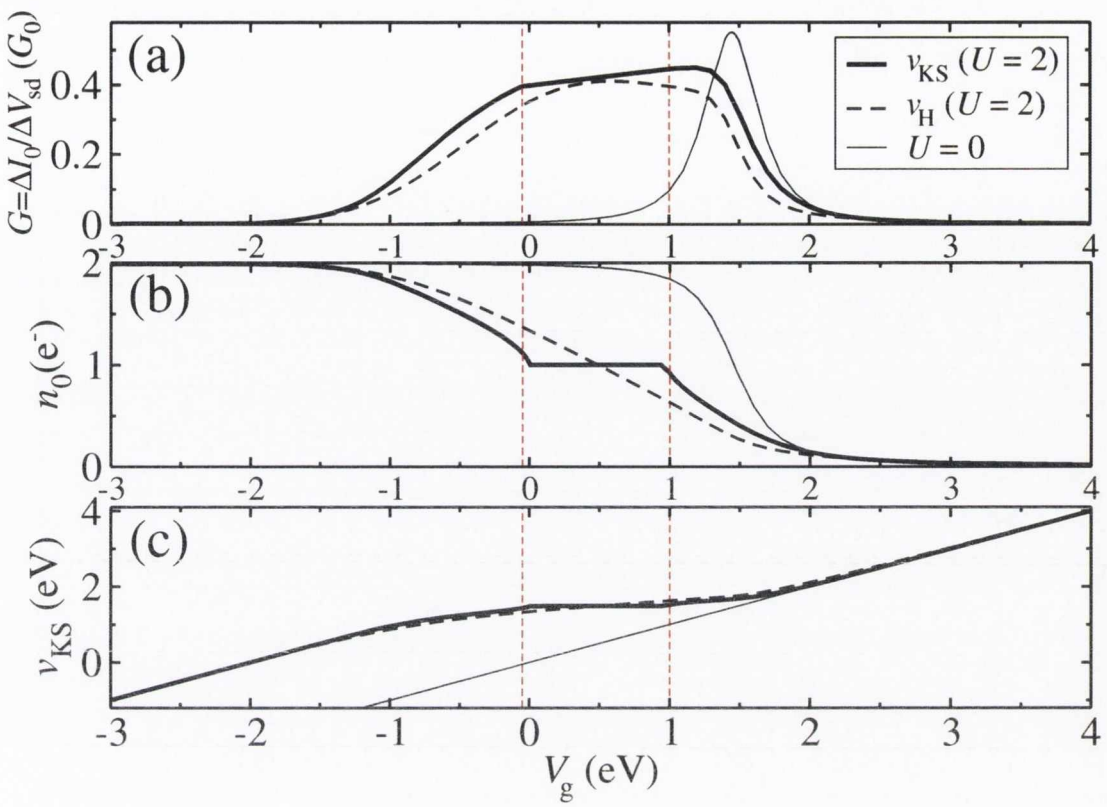

FIGURE 6.16: (a) Differential conductance, (b) charge density and (c) the Kohn-Sham potential of the dot as functions of the gate voltage (V_g) for the full discontinuous potential, v_{KS}, [thick solid lines] and for the Hartree potential, v_H, [dashed lines] with U=2 eV, and for the non-interacting case (thin solid line). The vertical dashed lines on all three panels mark the range of gate voltages, for which the charge density of the dot is around unity and therefore no steady state is found due to the derivative discontinuity. Parameters are the same as those of Fig. 6.13 and $V_{sd} = 0.01$ eV.

[see Fig. 6.16(b)]. In the case of v_H the discharging of the dot with increasing V_g is monotonic. In contrast, in the case of v_{KS} the dependence exhibits an almost step-like feature at $n_0 = 1$ due to the discontinuity. If fact, for all values of V_g in the special range the time-averaged charge density is approximately unity, e.g. the dot is singly-occupied. The smoothing of the discrete step for the values of V_g outside this range, is determined entirely by the shape of $v_{KS}[n_0]$ away from the discontinuity: $v_{KS}[n_0]$ has an upward slope for $0 \leq n_0 < 1$ and $1 < n_0 \leq 2$ [see Fig. 6.11(b)].

In the same way, from the time-averages in the long time-limit, we map out the I-V characteristics of the interacting dot (v_{KS}) at a given V_g (see Fig. 6.17). A remarkable feature of the I-V curves is the drop of the current and therefore the negative differential

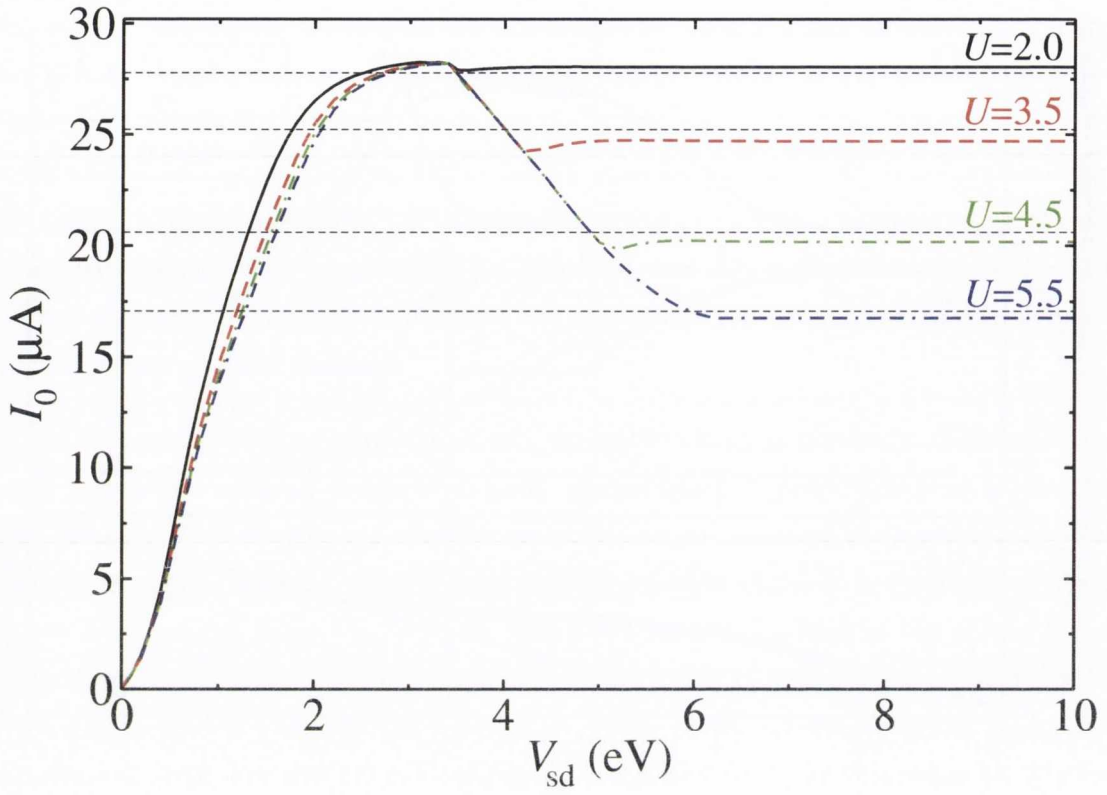

FIGURE 6.17: Current through the dot, I_0, as a function of the source-drain voltage, V_{sd}, for v_{KS} and different values of U. The horizontal dashed lines represent the corresponding saturation currents I_S (see text for the exact definition). The following parameters are used: γ_0=−3.88 eV, γ_c=−0.5 eV, E_F=1.5 eV, V_g=2.0 eV.

conductance (NDC) at large source-drain voltages, which is almost negligible for small U but increases with increasing U.

For all values of U the current initially increases with increasing V_{sd} as the dot is charging. It then reaches its maximum value as the charge density approaches $n_0 = 1$. This point corresponds to a threshold source-drain voltage V_{sd}^{cr}, which is roughly the same for all values of U. Beyond V_{sd}^{cr}, the system is driven into a dynamical state (where the steady-state current is calculated by averaging out the oscillations). In the limit of very large V_{sd}, the dot recovers its long-time tendency to a steady state and the average current saturates. At saturation and beyond, the dot occupation is above 1 and the on-site potential assumes a value above the discontinuity. Hence, the on-site energy at the dot is proportional to the jump of the v_{KS} at $n_0 = 1$, i.e. it is proportional to U.

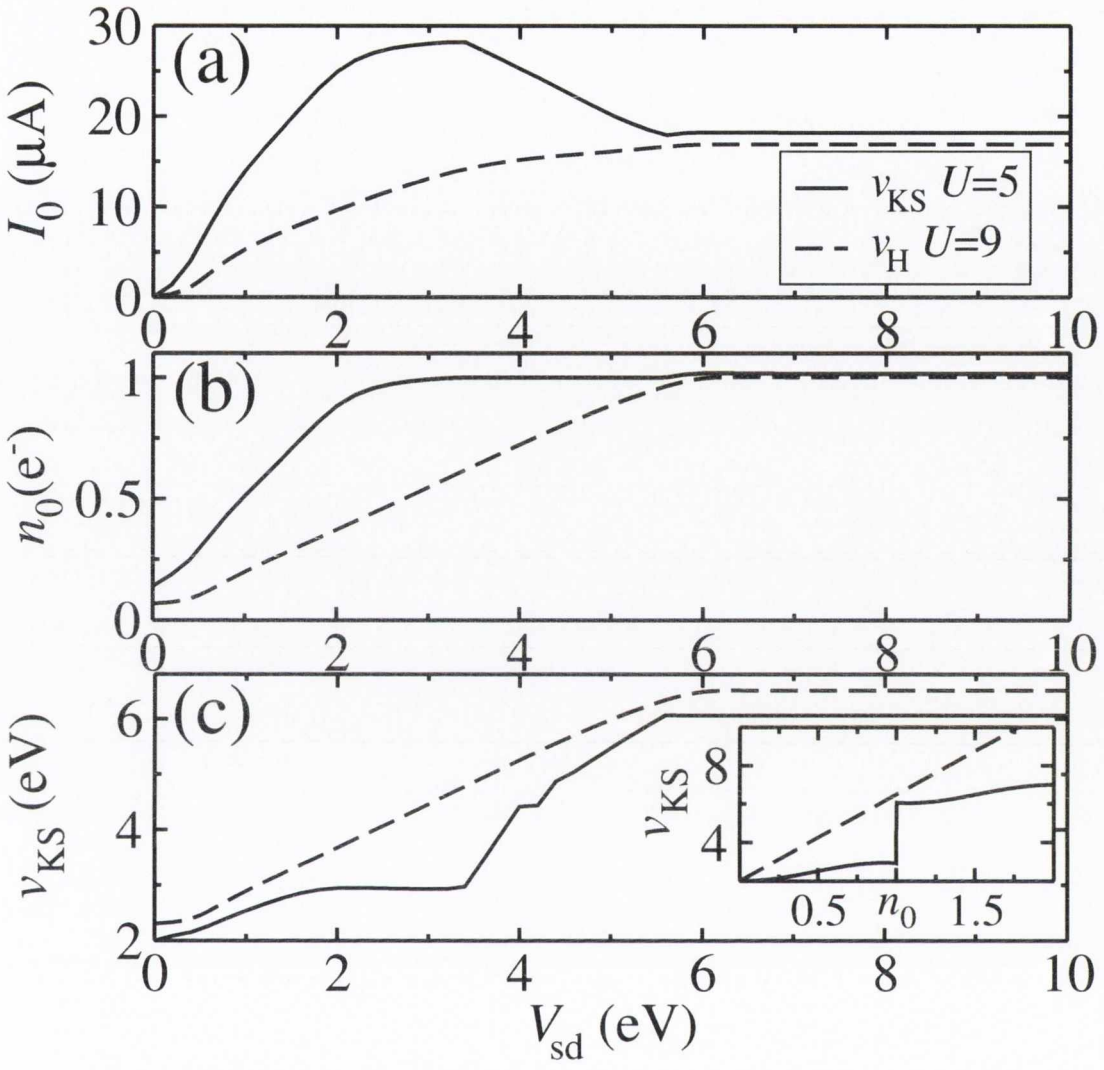

FIGURE 6.18: Current (a), density (b) and on-site potential (c) of the dot as a function of the source-drain voltage, V_{sd}, for v_{KS} with $U = 5$ eV and for v_H with $U = 9$ eV. The inset shows v_{KS} and v_H as functions of the dot density for the corresponding values of U. The parameters are the same as those in Fig. 6.17.

As discussed in Section 6.4.1 for the non-interacting case, the saturation current decreases with increasing the dot on-site potential, because of the finite bandwidth of the electrodes. For the same reason here the drop of the current becomes larger when U increases. In fact a large U corresponds to a large value of the steady-state on-site potential, which then approaches the electrodes' band-edge. In order to confirm this conjecture, we compare the saturation current I_S calculated at finite U, with that for U=0 and V_g equal to the steady-state on-site potential corresponding to that obtained at the same U. Indeed I_S matches quite well the value of the current obtained at large

source-drain voltages in the I-V characteristics of the interacting dot (see horizontal dashed lines next to each curve in Fig. 6.17). This argument can obviously be reversed, i.e. the NDC cannot be observed, if the variation of the on-site potential at the derivative discontinuity, determined by U, is much smaller than the electrodes' bandwidth. For instance, for the same set of parameters used before for the dot+electrodes system, such NDC-free situation is found for $U = 2$ eV ($U \ll 4|\gamma_0|$ for $\gamma_0 = 3.88$ eV). In this case the drop of the current above $V_{\rm sd}^{\rm cr}$ is practically negligible.

Importantly, the NDC displayed in Fig. 6.17 is not found in I-V curves calculated within the Hartree approximation, even for large values of U (see Fig. 6.18). When comparing calculations at the Hartree level with those performed with the complete Kohn-Sham potential we intentionally use different U. These are selected in such a way that the value of the potential at $n_0 = 1$ is identical in the two calculations [see the inset in Fig. 6.18(c)], i.e. in such a way that the two calculations give the same saturation current. At variance with the complete Kohn-Sham case, in the Hartree only problem the current, as well as the density and the on-site potential, monotonically increase with $V_{\rm sd}$ until the saturation is reached. Based on these numerical results we can argue that the existence of the discontinuity in $v_{\rm XC}$ (i.e. the derivative discontinuity in the XC energy) is a necessary condition for the occurrence of the NDC in the I-V characteristics. The shallow increase of the on-site potential with the charging, produced by the opening of the bias window, keeps the resonant level away from the electrodes band edge and allows the current to rise. Once the on-site charge exceeds $n_0 = 1$ and the resonant level energy shoots up towards the band-edge, the currents drops. The averaged dynamical current monotonically approaches its saturation value corresponding to a steady-state solution.

6.5 Summary

In this chapter, we have investigated the electronic transport through a strongly correlated quantum dot by using the multiple-probe battery method for time-dependent simulations of open systems. Our aim was two-fold. Firstly, we tested the applicability of this new method to a problem involving strong correlations as in Coulomb blockade and compared the results to those obtained by Kurth *et al.* in Ref. [145], where a conceptually different approach to time-dependent transport was employed. In particular, the results reported in Ref. [145] suggest a novel picture of Coulomb blockade as

an intrinsically dynamical process, during which the system does not evolve towards the steady state. Our investigations of the real-time dynamics of the quantum dot confirmed these findings. Indeed, we observed self-sustained oscillations in the current, density and effective on-site potential, which originate from the derivative discontinuity of the approximate exchange-correlation potential used.

Secondly, we addressed the question of how the results, obtained from the time-dependent simulations, can be related to a more familiar steady-state picture of transport through a strongly correlated quantum dot. In particular, we calculated the time-averaged current through the dot in the long-time limit in two regimes: (*i*) varying the local-gate voltage for a small but finite source-drain voltage, i.e. the linear response regime; (*ii*) varying the source-drain voltage for a fixed local-gate voltage. In the first regime, we have demonstrated the effect of the Coulomb repulsion strength on the shape of the conductance curves. In the second regime, we have found that the *I-V* characteristics of the quantum dot exhibit a drop in the current and, as a consequence, a negative differential conductance, which increases with increasing the charging energy U. The observed NDC occurs at a critical bias voltage and for a range of parameters, for which the dot is in the oscillatory Coulomb blockade state and no steady state is found. Moreover, the NDC is present only when the quantum dot is described at DFT level in which the approximate XC potential exhibits the derivative discontinuity at unitary occupation. Our calculations suggest, however, that the full explanation of the current drop and of the NDC needs to take into account also the effect of the realistic band structure of the electrodes, namely the finite bandwidth.

Chapter 7

Conclusions and Future work

With the growing interest in exploring and exploiting the spin degree of freedom for applications in data storage and processing, there is an increased need for a detailed atomistic description of spin dynamics. A number of methodological and computational schemes for atomistic magneto-dynamics been developed so far [72, 144, 191, 225, 231, 254]. Although large-scale fully *ab initio* simulations of magnetic systems are still computationally expensive, approximate methods for spin dynamics are becoming feasible [225] and have been already applied to realistic materials with complex magnetic ordering at the atomic scale [8].

A less explored area, compared to magneto-dynamics of isolated systems, is that of real-time simulations of spin transport and current-driven spin dynamics in nanoscale and atomic-scale systems. These however are potentially powerful tools for understanding and modeling of next generation electronic devices. As the techniques for fabrication and manipulation of nanoscale systems are being perfected, the focus of the experimental and theoretical research is shifting towards investigations of electron transport in nanoscale junctions [211]. Numerical algorithms for first-principles calculations of electronic transport in such devices have been firmly established in the case of steady-state transport [210]. In contrast, the extension of the existing methods to time-dependent phenomena is a relatively new avenue of research. Yet the importance of time-dependent effects in electron transport, inaccessible by standard steady-state approaches, has been already recognized [145, 219, 272].

In view of these developments, the main objective of the present dissertation has been that of constructing a time-dependent computational scheme, capable of describing

the time evolution of spin systems under current-carrying conditions. Our strategy has been to first implement a fully atomistic time-dependent method for spin dynamics in isolated systems and further extend it to include electronic open-boundary conditions. The method has been developed in the spirit of the tight-binding model but it is transferable to more accurate first-principles methods such as density functional theory [70].

We began in Chapter 2 by providing an overview of the underlying theoretical and computational framework for closed-boundary simulations of spin dynamics. This is based on the integration of the quantum Liouville equation [283], which is the analogue of the time-dependent Schrödinger equation for mixed ensembles and describes the time evolution of the density matrix, associated with a given system. We then discussed the implementation based on the tight-binding model and on the Ehrenfest approximation to spin dynamics. The latter is a spin-version of the well-known method for molecular dynamics (bearing the same name) [100, 102], which allows one to separate electronic and spin degrees of freedom and to treat them onto two different platforms - as quantum and classical variables, respectively. However, unlike in the Born-Oppenheimer approximation [27], which is also used in molecular dynamics and is the basis for adiabatic *ab initio* spin dynamics [9], the two subsystems interact with each other dynamically.

In Chapter 3 we investigated the charge-only dynamics in mono-atomic chains. Our long-time dynamical simulations allowed us to map out the excitation spectra by calculating the Fourier transform of the dynamical charge-density distribution along the chain over both the space and time coordinates. The spectra revealed a number of interesting features, which vary systematically with the system parameters and bear a close resemblance to the excitation spectra of one-dimensional Heisenberg spin chains [56, 183].

In Chapter 4 we focused on the electrostatic gate control of the dynamical exchange interaction between two well-separated localized spin-impurities, linked by a mono-atomic wire. The spin dynamics was treated at the Ehrenfest level, with the interaction between the impurity spins and the itinerant electrons spins described by the s-d model [275]. We showed that by applying an electrostatic gate in the middle of the wire particular resonance conditions can be created, for which the dynamics becomes highly non-linear.

Chapter 5 was entirely devoted to the theory of electron transport in nanoscale junctions. We started with the general formulation of the electron transport problem in the two-terminal Landauer setup and then incrementally added new concepts to the discussion. In particular, we described the nonequilibrium Green's function (NEGF) approach to the steady-state transport [90]. We then presented our implementation of the multiple-probe battery (MPB) method [171, 247] for the description of the time evolution of current-carrying systems.

In the MPB transport setup a central region (device) is attached to two large but finite electrodes, with each atom in the electrodes coupled to an external probe via a Hamiltonian matrix element. The probes, attached to the left and to the right electrode, represent the opposite poles of the battery. The electric current flow is generated by the potential difference at the contacts between the battery and the electrodes, which is introduced as the difference between the chemical potentials of the left- and the right-hand side probes. The time-dependent version of the method is based on the integration of the effective quantum Liouville equation with explicit source and drain terms. These are derived with the help of two main approximations, namely the wide-band limit in the probes (but not in the electrodes) and the presence of the dephasing, or decoherence, mechanism in the process of injection of carries from the probes into the electrodes. We have implemented a spin-polarized time-dependent and steady-state versions of the MPB method. As a test we have performed quantum-classical time-domain simulations of spin-excitations in atomic chains.

The simplicity and generality of the MPB method makes it well-suited for the implementation of first-principles schemes for spin dynamics. An ideal platform for this is provided by time-dependent density functional theory, within the time-propagation formalism using a localized atomic orbital basis set [176, 230]. In addition, the MPB method can be parametrized in such a way that a reasonable approximation to transport in a conventional two-terminal setup with semi-infinite leads can be obtained even for relatively small electrode size (few tens of atoms). The size of the buffer region between the device and the electrodes, which has to be long enough for the injection to be considered incoherent, may be also reduced by using two- or three-dimensional slabs instead of mono-atomic chains. In this case, due to the additional degrees of freedom, the speed of the signal, propagating from the leads to the interior of the central region, is decreased. Therefore the dephasing condition may be satisfied for a smaller number of atoms, compared to the one-dimensional case. These simplifications can, in principle, reduce the system size down to a range accessible by first-principles calculations.

Examples of systems, that we envision as possible candidates for first-principles-based time-dependent simulations of transport, include quantum point contacts - narrow atomic-sized constrictions between wide conducting regions (electrodes) [258, 260].

Another possible line of research, this time within the model-Hamiltonian framework, is to combine some of the methods discussed in Chapter 4 with the MPB approach to transport. Recently the unique spectroscopic capabilities of the low-temperature scanning tunneling microscope (STM), combined with *in situ* manipulation and imaging techniques, have been used to study magnetic and electronic properties of quantum nanostructures [91]. In particular, it has become possible to measure the conductance spectra of isolated and magnetically coupled transition-metal atoms (Fe, Co, Mn) deposited on non-magnetic substrates [97, 193]. This has stimulated theoretical efforts to explain the features found in experimental I-V curves, in particular associated with the spin-flip processes (see Ref. [107] and references within). A recent theoretical work on spin-transport properties of monoatomic magnetic chains and individual transition-metal atoms has been very successful in quantitatively describing the experimental results [106, 107]. The calculations are based on the s-d model, which describes the coupling between the conduction electrons spins and the spins of magnetic atoms. The electron transport is described within the steady-state NEGF formalism. However, in this work the inelastic spin-flip scattering processes are introduced perturbatively, up to a certain order in the s-d exchange interaction. This is due to the fact that in the NEGF formalism the many-body Green's function of the system in the presence of electron tunneling has to be calculated via a perturbation expansion of the interaction (s-d) Hamiltonian. In contrast, we expect that our numerical scheme for time-dependent spin transport, within the approximations inherent to the MPB method, is able to deal with arbitrary interaction strengths as it does not rely on the perturbation theory. Our immediate objective is to extend the quantum-classical model, presented in Chapter 4, to a fully quantum s-d Hamiltonian [275] and to further incorporate it into the MPB transport setup. With these numerical tools we intend to address the problem of spin-flip inelastic electron tunneling spectroscopy from a time-dependent perspective.

Finally, in Chapter 6 we presented a time-dependent study of electron transport through a strongly-correlated quantum dot. The many-body Hamiltonian of the dot, described by the Anderson impurity model [5], has been mapped onto an effective single-particle Kohn-Sham Hamiltonian in the framework of the adiabatic lattice density functional theory. We used the Bethe-ansatz local density approximation (BALDA) for the exchange-correlation (XC) functional, proposed by Lima *et al.* [158]. Notably, this

approximate functional has a derivative discontinuity at integer occupation, a fundamental property of the exact XC functional [47, 199, 202]. In the time-dependent regime, we found self-sustained oscillations in all transport-related properties (calculated as functions of time) in the range of parameters corresponding to the Coulomb blockade regime. This behavior, originating from the derivative discontinuity of the XC functional, has been previously observed in the calculations by Kurth *et al.* [145], where the same description for the quantum dot was used but the time-dependent electron transport was treated in a conceptually different way. In addition, we were able to calculate, from dynamical simulations in the long-time limit, the I-V characteristics of the dot and the linear-response conductance as a function of the gate voltage. Recent studies suggest that the zero-temperature linear-response conductance in the Anderson impurity model, calculated from the Kohn-Sham levels for a numerically exact XC functional [22, 253] and for a novel temperature-dependent functional which exhibits a derivative discontinuity [234], reproduces closely that computed with many-body approaches. Our results for the linear-response conductance, calculated with the BALDA functional, qualitatively agree with these findings.

In the case of the I-V characteristics, we found a negative differential conductance (NDC) at some critical bias voltages, which becomes more pronounced with increasing the charging energy U (this parameter expresses the strength of electron-electron interaction on the dot). Although the Hartree (mean-field) calculations do not reproduce this result, we showed that the NDC is primarily caused by the finite bandwidth of the electrodes. The effect of the electron-electron interaction on the steady-state transport through a Coulomb island has also been addressed in several recent works by using many-body perturbation theory [61, 187] and time-dependent density matrix renormalization group (TD-DMRG) [28]. These studies also found NDC in the I-V curves, which occurs at large bias voltages and increases with increasing U. In all the above mentioned works the NDC has been attributed mainly to electron-electron interactions. Therefore it would be instructive to further compare our results to those obtained with many-body approaches, which did not use the wideband approximation in the electrodes. This is the case for the TD-DMRG-based study, reported in Ref. [28], where finite electrodes with realistic band structure were used. In a certain range of the parameter space, particularly for large bias voltages and large Coulomb interaction strengths, one may expect that the finite-bandwidth contribution to NDC is not negligible and great care should be taken when attributing NDC solely to electron-electron interactions [17].

Appendix A

Adiabatic perturbation in a two-level system

We consider a system which consists of two sites (a dimer), described by a tight-binding Hamiltonian with on-site energies $\varepsilon_1 = \varepsilon_2 = \varepsilon_0$ and a hopping integral $\gamma \neq 0$ between the sites. A time-dependent perturbation in the on-site potential of the first site is introduced at the initial moment of time $t = t_0$ such than $\varepsilon_1 \to \varepsilon_0 + V(t)$.

The Hamiltonian matrix $H(t)$ corresponding to the Hamiltonian of the system $\hat{H}(t)$ at subsequent moment of time t after the perturbation, expressed in the basis of the localized atomic orbitals $|1\rangle$ and $|2\rangle$, reads

$$H(t) = \begin{pmatrix} \varepsilon_0 + V(t) & \gamma \\ \gamma & \varepsilon_0 \end{pmatrix} . \tag{A.1}$$

We further assume that the gate potential was introduced in the remote past ($t_0 \to -\infty$) and $V(t) = V$ for all times t later than t_0. The eigenstates of the Hamiltonian $\hat{H}(t)$ thus read

$$e_1(t) \equiv e_1 = \frac{1}{2}\left(2\varepsilon_0 + V - \sqrt{4\gamma^2 + V^2}\right), \tag{A.2}$$

$$e_2(t) \equiv e_2 = \frac{1}{2}\left(2\varepsilon_0 + V + \sqrt{4\gamma^2 + V^2}\right). \tag{A.3}$$

The dependence of the two eigenstates on the value of V is presented in Fig. A.1. It follows immediately from the figure that the two curves corresponding to e_1 and e_2 lie

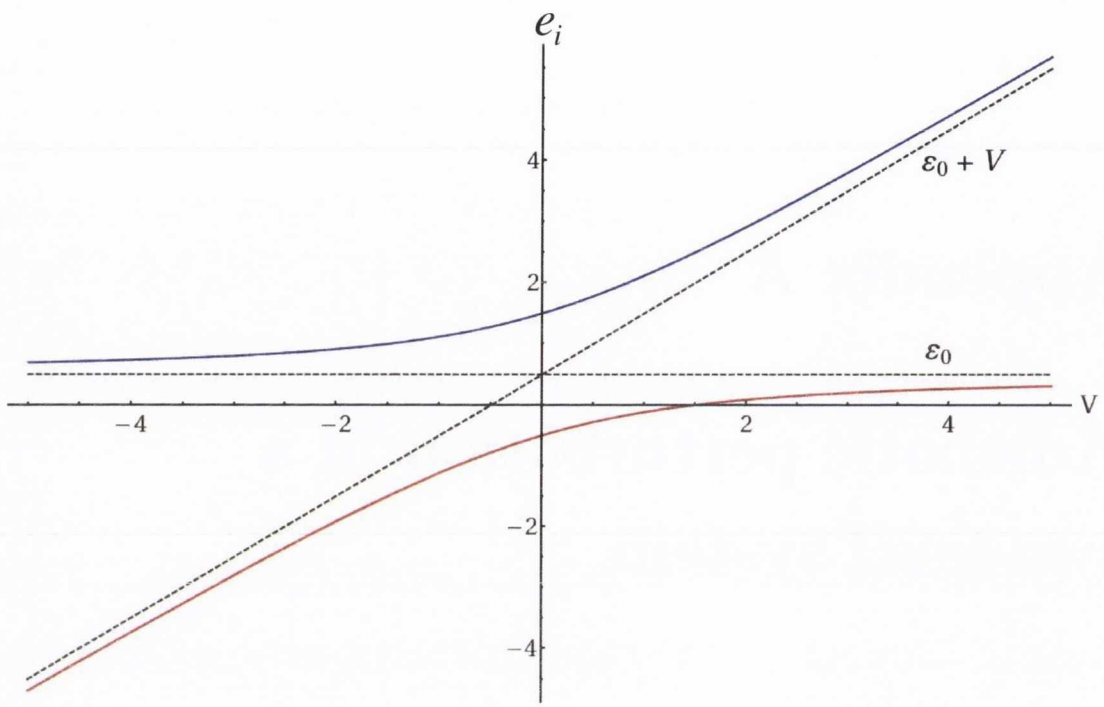

FIGURE A.1: Adiabatic variation of eigenvalues of $\hat{H}(t)$ with the gate potential V: $e_1(t)$ [red] and $e_2(t)$ [blue]. The dashed lines show the diabatic eigenvalues ε_0 and $\varepsilon_0 + V$.

in the area defined by two asymptotes, namely, $e_1^0 = \varepsilon_0$ and $e_2^0 = \varepsilon_0 + V$. Since in the case of the non-zero hopping γ the eigenvalues of $\hat{H}(t)$, given by Eq. (A.2) and Eq. (A.3), can not be degenerate, an avoided crossing [149, p. 302] is formed between $e_1(V)$ and $e_2(V)$ around $V = 0$. The asymptotic values e_1^0 and e_2^0 are given by the diagonal elements of the Hamiltonian matrix [see Eq. (A.1)], e.g. by the eigenvalues of $\hat{H}$ in the case of isolated sites ($\gamma = 0$), and can be referred to as diabatic eigenvalues. The diabatic eigenstates describe the evolution of the system in the case of an infinitely short perturbation. This can be intuitively understood as follows. If the time scale of the perturbation τ is much smaller than the characteristic time of the interaction [$\hbar/\gamma$ for the system described by Eq. (A.1)], the system will not change its configuration over the time-interval τ and its constituents would evolve independently. In the case of the dimer with the gate potential V applied to one of the atoms, the eigenvalues corresponding to the diabatic eigenstates $\varepsilon_0 + V$ and ε_0 are the atomic orbitals $|1\rangle$ and $|2\rangle$, respectively.

We note that the purpose of the derivation presented in this Appendix is merely to

illustrate the concept of the avoided crossing for a system subject to a dynamic perturbation in the form of an electrostatic gate potential, as discussed in Chapter 4. The example considered here is similar to a more canonical example of a two-level system in an external magnetic field.

Appendix B

Multiple probe approach: derivations

B.1 Perturbative expansion of the time-evolution operator

Here we provide a proof for the following equation [see Eq. (5.115)]

$$\hat{U}(t,\tau) = \hat{U}_0(t,\tau) + \frac{1}{\imath\hbar}\int_{\tau}^{t} \hat{U}(t,\tau')V(\tau')\hat{U}_0(\tau',\tau)d\tau'. \tag{B.1}$$

Let us denote the left-hand side of Eq. (B.1) as M and the right-hand side as N. By using the equation of motion for $\hat{U}$ [see Eq. (5.107)], we find

$$\frac{\partial M}{\partial t} = \frac{1}{\imath\hbar}\hat{H}(t)M. \tag{B.2}$$

In order to calculate the derivative of N we use the Leibniz integral rule

$$\begin{aligned}
\frac{\partial N}{\partial t} &= \frac{\partial \hat{U}_0(t,\tau)}{\partial t} + \frac{\partial}{\partial t}\frac{1}{\imath\hbar}\int_\tau^t \hat{U}(t,\tau')\hat{V}(\tau')\hat{U}_0(\tau',\tau)d\tau' = \\
&= \frac{1}{\imath\hbar}\hat{H}_0(t)\hat{U}_0(t,\tau) + \frac{1}{\imath\hbar}\underbrace{\hat{U}(t,t)}_{=\hat{I}}\cdot\underbrace{\hat{V}(t)}_{=\hat{H}(t)-\hat{H}_0(t)}\cdot\hat{U}_0(t,\tau) + \\
&\quad + \frac{1}{\imath\hbar}\int_\tau^t \underbrace{\frac{\partial \hat{U}(t,\tau')}{\partial t}}_{=\frac{1}{\imath\hbar}\hat{H}(t)\hat{U}(t,\tau')}\hat{V}(\tau')\hat{U}_0(\tau',\tau)d\tau' = \\
&= \frac{1}{\imath\hbar}\hat{H}_0(t)\hat{U}(t,\tau') + \frac{1}{\imath\hbar}\left(\hat{H}(t)-\hat{H}_0(t)\right)\hat{U}_0(t,\tau) + \\
&\quad + \left(\frac{1}{\imath\hbar}\right)^2\int_\tau^t \hat{H}(t)\hat{U}(t,\tau')\hat{V}(\tau')\hat{U}_0(\tau',\tau)d\tau' = \\
&= \frac{1}{\imath\hbar}\left(\hat{H}(t)\hat{U}_0(t,\tau) + \frac{1}{\imath\hbar}\int_\tau^t \hat{H}(t)\left[\hat{U}(t,\tau')\hat{V}(\tau')\hat{U}_0(\tau',\tau)d\tau'\right]\right) = \\
&= \frac{1}{\imath\hbar}\hat{H}(t)\left(\underbrace{\hat{U}_0(t,\tau) + \frac{1}{\imath\hbar}\int_\tau^t \hat{U}(t,\tau')\hat{V}(\tau')\hat{U}_0(\tau',\tau)d\tau}_{=N}\right). \qquad \text{(B.3)}
\end{aligned}$$

Thus we have

$$\frac{\partial M}{\partial t} = \frac{1}{\imath\hbar}\hat{H}(t)M, \qquad \text{(B.4)}$$

$$\frac{\partial N}{\partial t} = \frac{1}{\imath\hbar}\hat{H}(t)N. \qquad \text{(B.5)}$$

Assuming the initial conditions for M and N are the same, we find

$$M = N. \quad \square \qquad \text{(B.6)}$$

B.2 Calculation of the open-boundary terms

In this section we derive the expression for $\hat{\rho}_{\mathrm{SP}}(t)$ given by Eq. (5.118). In order to do this, we will re-write the formal solution of the Liouville-von Neumann equation for the total density matrix $\hat{\rho}(t)$ [Eq. (5.103)] in the matrix form. For this we need the matrix representations of the total density matrix $\hat{\rho}(t)$ and the corresponding propagator $\hat{U}(t)$, which have been already introduced and are given by Eq. (5.100) and Eq. (5.108), respectively. We also need the block-matrix representation of the density matrix at the

initial time t_0, which can be written as

$$\hat{\rho}(t_0) = \begin{pmatrix} \hat{\rho}_{\mathrm{S}}(t_0) & 0 \\ 0 & \hat{\rho}_{\mathrm{P}}(t_0) \end{pmatrix}, \tag{B.7}$$

where we assumed that $\hat{\rho}_{\mathrm{SP}}(t_0) = \hat{\rho}_{\mathrm{PS}}(t_0) = 0$. Hence, the equation for $\hat{\rho}(t)$ in the matrix form reads

$$\begin{aligned} \begin{pmatrix} \hat{\rho}_{\mathrm{S}}(t) & \hat{\rho}_{\mathrm{SP}}(t) \\ \hat{\rho}_{\mathrm{PS}}(t) & \hat{\rho}_{\mathrm{P}}(t) \end{pmatrix} &= \begin{pmatrix} \hat{U}_{\mathrm{S}}(t,t_0) & \hat{U}_{\mathrm{SP}}(t,t_0) \\ \hat{U}_{\mathrm{PS}}(t,t_0) & \hat{U}_{\mathrm{P}}(t,t_0) \end{pmatrix} \begin{pmatrix} \hat{\rho}_{\mathrm{S}}(t_0) & 0 \\ 0 & \hat{\rho}_{\mathrm{P}}(t_0) \end{pmatrix} \\ &\quad \begin{pmatrix} \hat{U}^{\dagger}_{\mathrm{S}}(t,t_0) & \hat{U}^{\dagger}_{\mathrm{SP}}(t,t_0) \\ \hat{U}^{\dagger}_{\mathrm{PS}}(t,t_0) & \hat{U}^{\dagger}_{\mathrm{P}}(t,t_0) \end{pmatrix}. \end{aligned} \tag{B.8}$$

By solving this matrix equation, the following expression for the off-diagonal element $\hat{\rho}_{\mathrm{SP}}(t)$ of the total density matrix is obtained

$$\hat{\rho}_{\mathrm{SP}}(t) = \hat{\rho}^{\dagger}_{\mathrm{PS}}(t) = \hat{U}_{\mathrm{SP}}(t,t_0)\hat{\rho}_{\mathrm{P}}(t_0)\hat{U}^{\dagger}_{\mathrm{P}}(t,t_0) + \hat{U}_{\mathrm{S}}(t,t_0)\hat{\rho}_{\mathrm{S}}(t_0)\hat{U}^{\dagger}_{\mathrm{SP}}(t,t_0). \tag{B.9}$$

Let us denote the first term on the right-hand side of Eq. (B.9) as T_1 and the second one as T_2.

We perform the same procedure with Eq. (5.117), which represents the perturbative expansion of $\hat{U}^{\dagger}$, e.g. we substitute the full effective propagator $\hat{U}^{\dagger}$, the free propagator $\hat{U}^{\dagger}_0$ and the interaction Hamiltonian $\hat{V}^{\dagger} = \hat{H}^{\dagger}_{\mathrm{SP}} + \hat{H}^{\dagger}_{\mathrm{PS}}$, entering the equation, by their matrix representations. The following equation is thus obtained

$$\begin{aligned} \begin{pmatrix} \hat{U}^{\dagger}_{\mathrm{S}}(t,t_0) & \hat{U}^{\dagger}_{\mathrm{SP}}(t,t_0) \\ \hat{U}^{\dagger}_{\mathrm{PS}}(t,t_0) & \hat{U}^{\dagger}_{\mathrm{P}}(t,t_0) \end{pmatrix} &= \begin{pmatrix} \hat{U}^{\dagger}_{0\mathrm{S}}(t,t_0) & 0 \\ 0 & \hat{U}^{\dagger}_{0\mathrm{P}}(t,t_0) \end{pmatrix} \\ &\quad - \frac{1}{\imath\hbar}\int_{t_0}^{t} d\tau \begin{pmatrix} \hat{U}^{\dagger}_{\mathrm{S}}(\tau,t_0) & \hat{U}^{\dagger}_{\mathrm{SP}}(\tau,t_0) \\ \hat{U}^{\dagger}_{\mathrm{PS}}(\tau,t_0) & \hat{U}^{\dagger}_{\mathrm{P}}(\tau,t_0) \end{pmatrix} \\ &\quad \begin{pmatrix} 0 & \hat{H}^{\dagger}_{\mathrm{SP}}(\tau) \\ \hat{H}^{\dagger}_{\mathrm{PS}}(\tau) & 0 \end{pmatrix} \begin{pmatrix} \hat{U}^{\dagger}_{0\mathrm{S}}(t,\tau) & 0 \\ 0 & \hat{U}^{\dagger}_{0\mathrm{P}}(t,\tau) \end{pmatrix}. \end{aligned} \tag{B.10}$$

By solving the above equation for each element of the matrix on the left-hand side, we find

$$\hat{U}_{\mathrm{S}}^{\dagger}(t,t_0) = \hat{U}_{0\mathrm{S}}^{\dagger}(t,t_0) - \frac{1}{\imath\hbar}\int_{t_0}^{t} \hat{U}_{\mathrm{SP}}^{\dagger}(\tau,t_0)\hat{H}_{\mathrm{PS}}(\tau)\hat{U}_{0\mathrm{S}}^{\dagger}(t,\tau)d\tau, \tag{B.11}$$

$$\hat{U}_{\mathrm{P}}^{\dagger}(t,t_0) = \hat{U}_{0\mathrm{P}}^{\dagger}(t,t_0) - \frac{1}{\imath\hbar}\int_{t_0}^{t} \hat{U}_{\mathrm{PS}}^{\dagger}(\tau,t_0)\hat{H}_{\mathrm{SP}}(\tau)\hat{U}_{0\mathrm{P}}^{\dagger}(t,\tau)d\tau, \tag{B.12}$$

$$\hat{U}_{\mathrm{SP}}^{\dagger}(t,t_0) = -\frac{1}{\imath\hbar}\int_{t_0}^{t} \hat{U}_{\mathrm{S}}^{\dagger}(\tau,t_0)\hat{H}_{\mathrm{SP}}(\tau)\hat{U}_{0\mathrm{P}}^{\dagger}(t,\tau)d\tau. \tag{B.13}$$

By inserting Eq. (B.12) into T_1 and Eq. (B.13) into T_2, and obtain

$$T_1 = \hat{U}_{\mathrm{SP}}(t,t_0)\hat{\rho}_{\mathrm{P}}(t_0)\hat{U}_{0\mathrm{P}}(t,t_0) - \\ -\frac{1}{\imath\hbar}\int_{t_0}^{t} \hat{U}_{\mathrm{SP}}(t,t_0)\hat{\rho}_{\mathrm{P}}(t_0)\hat{U}_{\mathrm{PS}}^{\dagger}(\tau,t_0)\hat{H}_{\mathrm{SP}}(\tau)\hat{U}_{0\mathrm{P}}^{\dagger}(t,\tau)d\tau, \tag{B.14}$$

$$T_2 = -\frac{1}{\imath\hbar}\int_{t_0}^{t} \underbrace{\hat{U}_{\mathrm{S}}(t,t_0)\hat{\rho}_{\mathrm{S}}(t_0)\hat{U}_{\mathrm{S}}^{\dagger}(\tau,t_0)}_{=\hat{\rho}_{\mathrm{S}}(t,\tau)} \hat{H}_{\mathrm{SP}}(\tau)\hat{U}_{0\mathrm{P}}^{\dagger}(t,\tau)d\tau = \\ -\frac{1}{\imath\hbar}\int_{t_0}^{t} \hat{\rho}_{\mathrm{S}}(t,\tau)\hat{H}_{\mathrm{SP}}(\tau)\hat{U}_{0\mathrm{P}}^{\dagger}(t,\tau)d\tau. \tag{B.15}$$

Since the second terms on the right-hand sides of Eq. (B.14) and Eq. (B.15) are 0, we obtain the final expression for $\hat{\rho}_{\mathrm{SP}}(t)$

$$\hat{\rho}_{\mathrm{SP}}(t) = \hat{U}_{\mathrm{SP}}(t,t_0)\hat{\rho}_{\mathrm{P}}(t_0)\hat{U}_{0\mathrm{P}}(t,t_0) - \frac{1}{\imath\hbar}\int_{t_0}^{t} \hat{\rho}_{\mathrm{S}}(t,\tau)\hat{H}_{\mathrm{SP}}(\tau)\hat{U}_{0\mathrm{P}}(t,\tau)d\tau. \tag{B.16}$$

This coincides with Eq. (5.118). □

B.3 Dephasing factor in the injection terms

The purpose of this section is to demonstrate that the introduction of the dephasing factor $e^{-(t-\tau)/\tau_\Delta}$ in the injection terms is equivalent to replacing the Fermi-Dirac distributions of the probes $f_\alpha(E)$ with effective broadened distributions $\tilde{f}_\alpha(E)$ for $\alpha = \mathrm{L},\mathrm{R}$. Let us consider the following integral

$$\int_{-b}^{0} e^{-t/\tau_\Delta} e^{\imath\omega t}\, d\omega, \tag{B.17}$$

where $t > 0$ and $b > 0$. The limits of integration $\int_{-b}^{0}$ can be extended to $\int_{-\infty}^{+\infty}$ as follows

$$\int_{-b}^{0} e^{-t/\tau_\Delta} e^{\imath\omega t}\, d\omega = \int_{-\infty}^{+\infty} e^{-t/\tau_\Delta} e^{\imath\omega t} \cdot [\theta(\omega + b) - \theta(\omega)]\, d\omega, \tag{B.18}$$

where the difference between the Heaviside step functions in the square bracket satisfies

$$[\theta(\omega + b) - \theta(\omega)] \begin{cases} \geq 0, \omega \in [-b, 0] \\ < 0, \omega \in (-\infty, b) \bigcup (0, +\infty) \end{cases}. \tag{B.19}$$

One of the available smooth analytical approximations to the Heaviside step function $\theta(x)$ reads

$$\theta(x) = \lim_{k \to +\infty} \left[\frac{1}{2} + \frac{1}{\pi} \arctan(kx) \right]. \tag{B.20}$$

For finite k, $\theta(x) = \left[\frac{1}{2} + \frac{1}{\pi} \arctan(kx)\right]$ is an approximation to the Heaviside step function with a smoothing parameter k. By inserting the above equation into Eq. (B.18), we obtain

$$\int_{-b}^{0} e^{-t/\tau_\Delta} e^{\imath\omega t}\, d\omega = \int_{-\infty}^{+\infty} e^{\imath\omega t} e^{-t/\tau_\Delta} \left\{ \frac{1}{\pi} \arctan[k(\omega + b)] - \frac{1}{\pi} \arctan(k\omega) \right\} d\omega. \tag{B.21}$$

Let us denote

$$\tilde{f}(\omega, b) = \frac{1}{\pi} \{\arctan[k(\omega + b)] - \arctan(k\omega)\}. \tag{B.22}$$

For $b \to +\infty$, $\arctan[k(\omega + b)] \to \frac{\pi}{2}$ and we get

$$\tilde{f}(\omega) \equiv \lim_{b \to +\infty} \tilde{f}(\omega, b) = \frac{1}{2} - \frac{1}{\pi} \arctan(k\omega). \tag{B.23}$$

Figure B.1 shows the distribution $\tilde{f}(\omega)$ as a function of the argument ω for two values of the smoothing parameter k, namely for $k = 10$ and $k = 100$ and for a very large (positive) k ($k \to \infty$). Assuming that $\tau_\Delta = k$ is large enough so that $e^{-t/\tau_\Delta} \to 1$, Eq. (B.21) can be re-written as

$$\int_{-b}^{0} e^{-t/\tau_\Delta} e^{\imath\omega t}\, d\omega = \int_{-\infty}^{+\infty} e^{\imath\omega t} \tilde{f}(\omega) d\omega, \tag{B.24}$$

where $\tilde{f}(\omega)$ is given by Eq. (B.23) with $k = \tau_\Delta$. Finally, by converting the argument of the distribution $\tilde{f}$ into the energy-domain, we obtain

$$\tilde{f}_\alpha(E) = \frac{1}{2} - \frac{1}{\pi} \arctan\left[(E - \mu_\alpha)/\Delta\right], \tag{B.25}$$

where $\alpha = \mathrm{L}, \mathrm{R}$. The fictitious distributions $\tilde{f}_\alpha(E)$ satisfy $\tilde{f}_\alpha(\mu_\alpha) = 1/2$ and $\tilde{f}_\alpha(+\infty) = 0$, similarly to the original Fermi-Dirac distributions $f_\alpha(E)$. While in the zero-temperature limit ($T = 0$) $f_\alpha(E)$ are step functions, the fictitious distributions $\tilde{f}_\alpha(E)$ are step functions smoothened by 2Δ. □

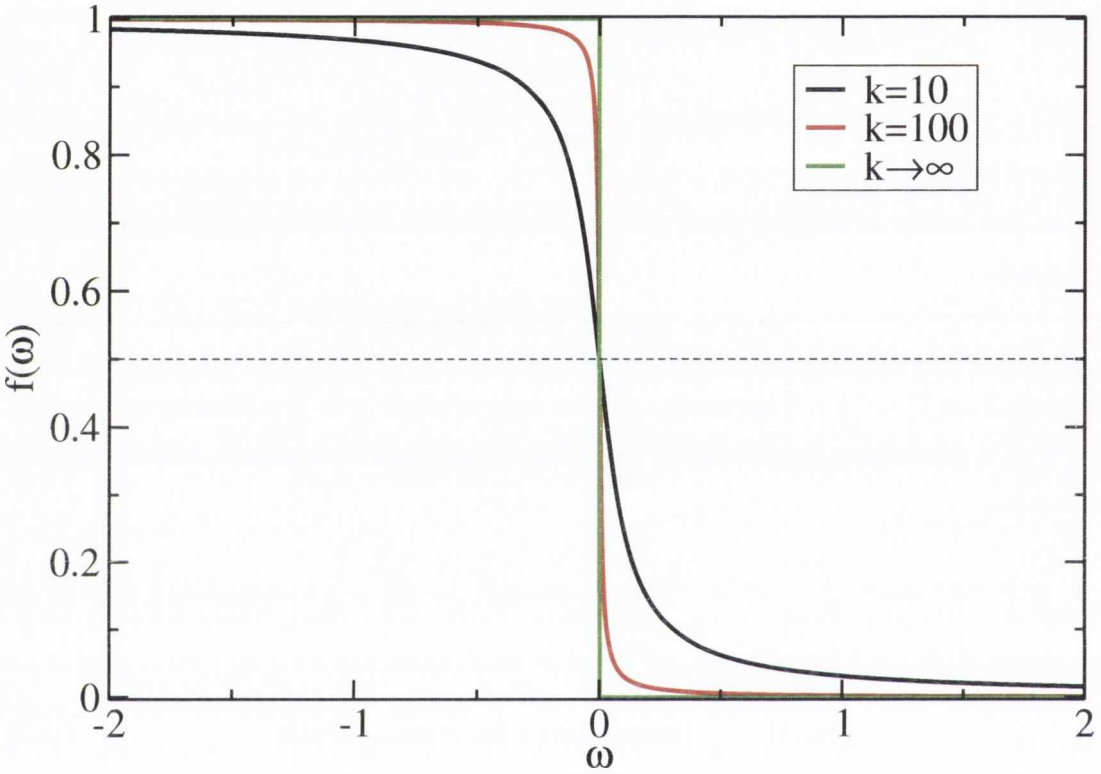

FIGURE B.1: The distribution $\tilde{f}(\omega)$ as a function of ω for $k = 10$, $k = 100$ and a very large positive k ($k \to \infty$).

Appendix C

Anderson impurity model for a strongly correlated quantum dot: approximate solution

We consider electron transport through a Coulomb island (quantum dot) between two one-dimensional semi-infinite non-interacting leads, described by the Anderson impurity model. The Hamiltonian of the system reads

$$\begin{aligned}\hat{H}_{\mathrm{S}} = \sum_{\alpha=\mathrm{L,R}} \sum_{i,\sigma} \varepsilon_{i\alpha}\, \hat{c}_{i\alpha}^{\sigma\dagger}\, \hat{c}_{i\alpha}^{\sigma} \;&+\; \sum_{\alpha=\mathrm{L,R}} \sum_{i,\sigma} \left(\gamma_0\, \hat{c}_{i\alpha}^{\sigma\dagger}\, \hat{c}_{i+1\alpha}^{\sigma} + h.c.\right) \\ &+\; \sum_{\sigma} \left(\gamma_{\mathrm{c}}\, \hat{c}_{0}^{\sigma\dagger}\, \hat{c}_{1\mathrm{L}}^{\sigma} + \gamma_{\mathrm{c}}\, \hat{c}_{0}^{\sigma\dagger}\, \hat{c}_{1\mathrm{R}}^{\sigma} + h.c.\right) \\ &+\; \sum_{\sigma} \epsilon_{\mathrm{d}}^{\sigma}\, \hat{n}_{0}^{\sigma} + U\, \hat{n}_{0}^{\uparrow} \hat{n}_{0}^{\downarrow}, \end{aligned} \tag{C.1}$$

where $\varepsilon_{i\alpha}$ are the on-site energies, γ_0 is the hopping integral and $\hat{c}_{i\alpha}^{\sigma\dagger}(\hat{c}_{i\alpha}^{\sigma})$ is the creation (annihilation) operator for an electron with spin σ (σ=$\uparrow,\downarrow$) at the atomic site i of the lead α; $\hat{c}_{0}^{\sigma\dagger}(\hat{c}_{0}^{\sigma})$ is the creation (annihilation) operator for an electron with spin σ on the dot and γ_{c} is the hopping integral between the dot and site i=1 in the lead α. In the Hamiltonian of the dot (last two terms) $\epsilon_{\mathrm{d}}^{\sigma}$ is the on-site energy of the dot, which can be controlled by the local gate voltage V_{g}, U ($U \geq 0$) is the charging energy, which expresses the strength of the Coulomb repulsion, and $\hat{n}_{0}^{\sigma}$=$\hat{c}_{0}^{\sigma\dagger}\, \hat{c}_{0}^{\sigma}$ is the site-occupation operator of the dot. We will further assume that $\epsilon_{\mathrm{d}}^{\uparrow} = \epsilon_{\mathrm{d}}^{\downarrow} = \epsilon_{\mathrm{d}}$.

The spin-resolved Green's function (GF) of the dot in isolation is given by

$$\hat{g}^{\sigma\sigma}(E) = \frac{1 - n_0^{\bar{\sigma}}}{E - \epsilon_\mathrm{d}} + \frac{n_0^{\bar{\sigma}}}{E - \epsilon_\mathrm{d} - U}, \tag{C.2}$$

where $\bar{\sigma}$ denotes the spin opposite to σ and n_0^σ is the spin-density of the dot. For the retarded (advanced) GF $E \equiv \lim_{\epsilon \to 0^+} E \pm \imath\epsilon$.

As a next step, one needs to introduce the coupling to the leads. In the simplest case, the retarded (advanced) GF of the interacting dot in the presence of the tunneling between the dot and the leads can be written as [90, p. 171]

$$\hat{G}^{\sigma\sigma,\pm}(E) = \frac{1 - n_0^{\bar{\sigma}}}{E - \epsilon_\mathrm{d} - \hat{\Sigma}^\pm} + \frac{n_0^{\bar{\sigma}}}{E - \epsilon_\mathrm{d} - U - \hat{\Sigma}^\pm}, \tag{C.3}$$

where we have introduced the self-energy $\hat{\Sigma}$ due to the coupling to both leads, which now substitutes the infinitesimal ϵ in the expression for the GF of the isolated dot. By neglecting the real part of the self-energy in the wideband limit and by assuming that the broadening matrix Γ is an energy-independent constant ($\Gamma = 2\pi\gamma_c^2 d$ with d being the density of states in the leads), we can substitute $\Sigma^\pm$ in Eq. (C.3) by $\mp\imath\Gamma/2$.

The spectral function is then given by

$$\begin{aligned} \hat{A}^{\sigma\sigma}(E) &\equiv -\frac{1}{\pi}\Im\hat{G}^{\sigma\sigma,+}(E) = \\ &= \frac{1}{2\pi}\left[\frac{\Gamma\left(1 - n_0^{\bar{\sigma}}\right)}{\left(E - \epsilon_\mathrm{d}\right)^2 + \left(\Gamma/2\right)^2} + \frac{\Gamma n_0^{\bar{\sigma}}}{\left(E - \epsilon_\mathrm{d} - U\right)^2 + \left(\Gamma/2\right)^2}\right]. \end{aligned} \tag{C.4}$$

The spectral function is represented by the sum of two Lorentzians, centered respectively at ϵ_d and $\epsilon_\mathrm{d} + U$. This two-peak structure corresponds to the Coulomb blockade physics: the first peak, located at $E = \epsilon_\mathrm{d}$, corresponds to adding an electron to the dot, while the second peak, centered around $E = \epsilon_\mathrm{d} + U$, corresponds to adding an extra electron, which requires the energy U.

In order to calculate the total current I through the Coulomb island, we use the general formula for the steady-state current

$$\begin{aligned} I &= \sum_\sigma \frac{\imath e}{2h}\int dE\, Tr\left\{\left[\hat{\Gamma}_\mathrm{L}(E) - \hat{\Gamma}_\mathrm{R}(E)\right]\hat{G}^<(E) + \right. \\ &+ \left.\left[f_\mathrm{L}(E)\hat{\Gamma}_\mathrm{L}(E) - f_\mathrm{R}\hat{\Gamma}_\mathrm{R}(E)\right]\cdot\left[\hat{G}^+(E) - \hat{G}^-(E)\right]\right\}^\sigma, \end{aligned} \tag{C.5}$$

where $\Gamma_\alpha = \Gamma/2$ for $\alpha = \mathrm{L}, \mathrm{R}$. Here $\hat{G}^{\pm}$ is given by the approximate expression in Eq. (C.3). The trace can be omitted in the case of a single level quantum dot since the dimension of all matrices entering Eq. (C.5) is unity.

It can be shown that in the case of proportionate couplings, e.g. for $\Gamma_\mathrm{L} = \lambda\Gamma_\mathrm{R}$, where λ is a constant (here $\lambda = 1$), the above expression for the current can be re-written in a simplified form

$$I = \sum_\sigma \frac{ie}{h} \int dE \, [f_\mathrm{L}(E) - f_\mathrm{L}(E)] \frac{\Gamma_\mathrm{L}\Gamma_\mathrm{R}}{\Gamma_\mathrm{L} + \Gamma_\mathrm{R}} \left[\hat{G}^{\sigma\sigma,+}(E) - \hat{G}^{\sigma\sigma,-}(E)\right]. \tag{C.6}$$

Here f_α is the Fermi-Dirac distribution in the lead α.

Finally, in the linear-response regime the expression for the current reads

$$I = \sum_\sigma \frac{ie}{h} \int dE \, \frac{\Gamma_\mathrm{L}\Gamma_\mathrm{R}}{\Gamma_\mathrm{L} + \Gamma_\mathrm{R}} \left[\hat{G}^{\sigma\sigma,+}(E) - \hat{G}^{\sigma\sigma,-}(E)\right] \left[-\frac{\partial f(E)}{\partial E}\right], \tag{C.7}$$

where $f(E) = 1/\left\{1 + \exp\left[(E - E_\mathrm{F})/k_\mathrm{B}T\right]\right\}$ with E_F being the Fermi level of the leads ($E_\mathrm{F} = 0$ in our calculations). This has to be solved self-consistently together we the equations for the spin-densities n^σ. The latter are calculated as equilibrium spin-densities

$$n^\sigma = -\frac{1}{\pi} \int f(E) \Im \hat{G}^{\sigma\sigma,+}(E) \, dE. \tag{C.8}$$

The calculated linear-response conductance and the total charge density of the dot are plotted in Fig. C.1 as functions of $\epsilon_\mathrm{d}/\Gamma$ for several values of the charging energy. In the non-interacting case ($U = 0$) the conductance exhibits a single peak, centered around $E_\mathrm{F} = 0$, which is expected from the steady-state picture of transport through a non-interacting resonant level. In the interacting case, two distinct peaks are formed, centered respectively around E_F and around $E_\mathrm{F} - U$. These are manifestation of charge quantization at the dot and correspond to each of the two integer electron number states, in which the dot is inhabited by one or two electrons, respectively.

The discharging of the dot with increasing the on-site potential ϵ_d, with the respect to the Fermi level in the leads, is shown in Fig. C.1(b). While in the $U = 0$ case the charge density drops rapidly from $n_0 = 2$ to $n_0 = 0$ with a sharp resonance at E_F, in the interacting case the charge density is approximately unity for the gate voltages in the range $[E_\mathrm{F} - U, E_\mathrm{F}]$. This corresponds to the valley between the two conductance peaks, where the current is zero and the number of electrons on the dot is fixed. Note

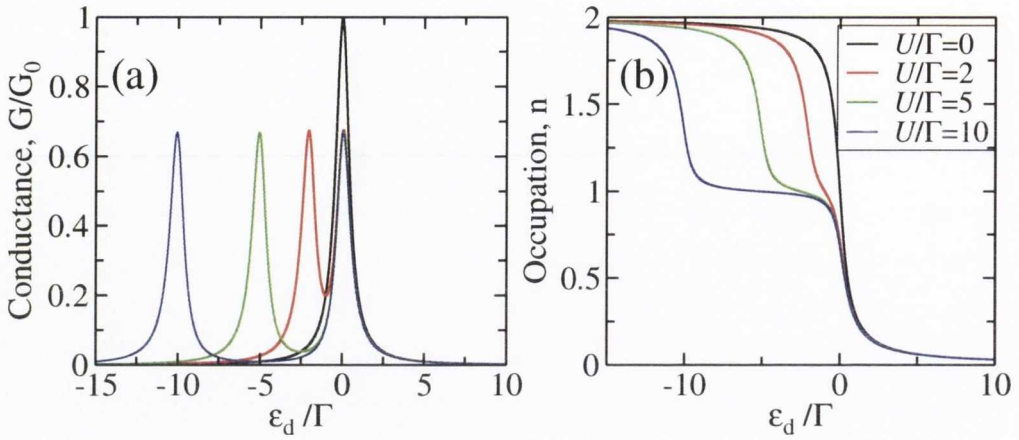

FIGURE C.1: (a) The normalized linear-response conductance G/G_0 ($G_0 = 2e^2/h$) as a function of ε_d/Γ for $U/\Gamma = 0$, $U/\Gamma = 2$, $U/\Gamma = 5$, and $U/\Gamma = 10$. (b) The total occupation of the quantum dot, $n = \sum_\sigma n^\sigma$ ($n^\uparrow = n^\downarrow$), as a function of ε_d/Γ for the same values of U/Γ.

that we observed similar trend in the gate-voltage dependence of the charge density, when the dot was described at the DFT-level with the XC functional approximated by the BALDA [see Fig. 6.16(b)]. However, in that case the charge density was unity due to the fact that for $V_g \in [E_F - U, E_F]$ the dot was in the dynamical state, characterized by the oscillation in all calculated quantities and by $n_0 \approx 1$ at the discontinuity. In contrast to Fig. C.1, we did not observe two distinct peaks in the linear-response conductance, obtained with the BALDA. Instead, the conductance curve for $V_g \in [E_F - U, E_F]$ resembles a plateau corresponding to the odd number of electrons on the dot ($n = 1$), which is in principle a correct feature of the Anderson impurity model at zero temperature. It is important to mention, however, that in this range of gate voltages the current was calculated as a time-average current in the long-time limit and the conductance curve carries some degree of arbitrariness.

Appendix D

Publications stemming from this work

- A. Pertsova, M. Stamenova and S. Sanvito, *Electrical control of spin dynamics in finite one-dimensional systems*, Phys. Rev. B **84**, 155436 (2011).
- A. Pertsova, M. Stamenova and S. Sanvito, *Time-dependent electron transport through a strongly correlated quantum dot: Multiple-probe open boundary conditions approach*, arXiv:1204.0937v1 [cond-mat.mes-hall] (also submitted to PRB).
- A. Pertsova and S. Sanvito, *Time-dependent simulations of spin inelastic electron tunneling spectroscopy on atomic clusters* (in preparation).

Bibliography

[1] *Moores law.* Encyclopædia Britannica. Encyclopædia Britannica Online Academic Edition, Encyclopædia Britannica Inc., 2012.

[2] M. Abramowitz and I. A. Stegun. *Handbook of Mathematical Functions: With Formulas, Graphs, and Mathematical Tables.* Dover Publications, 1964.

[3] A. Akande and S. Sanvito. Electric field response of strongly correlated one-dimensional metals: A Bethe ansatz density functional theory study. *Phys. Rev. B*, **82**:245114, 2010.

[4] J. Åkerman. Toward a universal memory. *Science*, **308**:508, 2005.

[5] P. W. Anderson. Localized magnetic states in metals. *Phys. Rev.*, **124**:41, 1961.

[6] V. Anisimov and Y. Izyumov. *Electronic Structure of Strongly Correlated Materials.* Springer, 2010.

[7] V. P. Antropov, B. N. Harmon, and A. N. Smirnov. Aspects of spin dynamics and magnetic interactions. *J. Magn. Magn. Mater.*, **200**:148, 1999.

[8] V. P. Antropov, M. I. Katsnelson, B. N. Harmon, M. van Schilfgaarde, and D. Kusnezov. Spin dynamics in magnets: Equation of motion and finite temperature effects. *Phys. Rev. B*, **54**:1019, 1996.

[9] V. P. Antropov, M. I. Katsnelson, M. van Schilfgaarde, and B. N. Harmon. *Ab initio* spin dynamics in magnets. *Phys. Rev. Lett.*, **75**:729, 1995.

[10] N. W. Ashcroft and N. D. Mermin. *Solid State Physics.* Harcourt College Publishing, 1976.

[11] R. C. Ashoori. Electrons in artificial atoms. *Nature (London)*, **379**:413, 1996.

[12] M. Atatüre, J. Dreiser, A. Badolato, and A Imamoglu. Observation of Faraday rotation from a single confined spin. *Nature Physics*, **3**:101, 2007.

[13] D. D. Awschalom, R. Epstein, and R. Hanson. The Diamond Age of Spintronics. *Sci. Am.*, **297**(4):84, 2007.

[14] D. D. Awschalom and M. E. Flatté. Challenges for semiconductor spintronics. *Nature Physics*, **3**:153, 2007.

[15] R. Baer, T. Seideman, S. Ilani, and D. Neuhauser. Ab initio study of the alternating current impedance of a molecular junction. *J. Chem. Phys.*, **120**:3387, 2004.

[16] M. N. Baibich, J. M. Broto, A. Fert, F. Nguyen Van Dau, F. Petroff, P. Etienne, G. Creuzet, A. Friederich, and J. Chazelas. Giant magnetoresistance of (001)Fe/(001)Cr magnetic superlattices. *Phys. Rev. Lett.*, **61**:2472, 1988.

[17] I. Bâldea and H. Köppel. Sources of negative differential resistance in electric nanotransport. *Phys. Rev. B*, **81**:193401, 2010.

[18] M. T. Batchelor. The Bethe ansatz after 75 years. *Physics Today*, **60**:36, 2007.

[19] E. Beaurepaire, J.-C. Merle, A. Daunois, and J.-Y. Bigot. Ultrafast spin dynamics in ferromagnetic nickel. *Phys. Rev. Lett.*, **76**:4250, 1996.

[20] J. Berezovsky, M. H. Mikkelsen, N. G. Stoltz, L. A. Coldren, and D. D. Awschalom. Picosecond coherent optical manipulation of a single electron spin in a quantum dot. *Science*, **320**:349, 2008.

[21] L. Berger. Emission of spin waves by a magnetic multilayer traversed by a current. *Phys. Rev. B*, **54**:9353, 1996.

[22] J. P. Bergfield, Z.-F. Liu, K. Burke, and C. A. Stafford. Bethe ansatz approach to the Kondo effect within density-functional theory. *Phys. Rev. Lett.*, **108**:066801, 2012.

[23] S. Bhattacharjee, L. Nordström, and J. Fransson. Atomistic spin dynamic method with both damping and moment of inertia effects included from first principles. *Phys. Rev. Lett.*, **108**:057204, 2012.

[24] G. Binasch, P. Grünberg, F. Saurenbach, and W. Zinn. Enhanced magnetoresistance in layered magnetic structures with antiferromagnetic interlayer exchange. *Phys. Rev. B*, **39**:4828, 1989.

[25] G. Blumberg, P. Littlewood, A. Gozar, B. S. Dennis, N. Motoyama, H. Eisaki, and S. Uchida. Sliding density wave in $Sr_{14}Cu_{24}O_{41}$ ladder compounds. *Science*, **297**:584, 2002.

[26] L. Bogani and W. Wernsdorfer. Molecular spintronics using single-molecule magnets. *Nature Materials*, **7**:179, 2008.

[27] M. Born and J. R. Oppenheimer. On the quantum theory of molecules. *Ann. Physik*, **84**:457, 1927 [Translated by S. M. Blinder with emendations by B. Sutcliffe and W. Geppert, 2002].

[28] E. Boulat, H. Saleur, and P. Schmitteckert. Twofold advance in the theoretical understanding of far-from-equilibrium properties of interacting nanostructures. *Phys. Rev. Lett.*, **101**:140601, 2008.

[29] M. Brandbyge, J.-L. Mozos, P. Ordejón, J. Taylor, and K. Stokbro. Density-functional method for nonequilibrium electron transport. *Phys. Rev. B*, **65**:165401, 2002.

[30] W. F. Brown. Domains, micromagnetics, and beyond: Reminiscences and assessments. *J. Appl. Phys.*, **49**:1937, 1978.

[31] H. Bruus and K. Flensberg. *Many-body Quantum Theory In Condensed Matter Physics: An Introduction.* Oxford University Press, 2004.

[32] K. Burke, R. Car, and R. Gebauer. Density functional theory of the electrical conductivity of molecular devices. *Phys. Rev. Lett.*, **94**:146803, 2005.

[33] N. Bushong, N. Sai, and M. Di Ventra. Approach to steady-state transport in nanoscale conductors. *Nano Lett.*, **5**:2569, 2005.

[34] M. Büttiker. Four-terminal phase-coherent conductance. *Phys. Rev. Lett.*, **57**:1761, 1986.

[35] M. Büttiker, Y. Imry, R. Landauer, and S. Pinhas. Generalized many-channel conductance formula with application to small rings. *Phys. Rev. Lett.*, **31**:6207, 1985.

[36] J. Cao, Q. Wang, and H. Dai. Electron transport in very clean, as-grown suspended carbon nanotubes. *Nat. Mat.*, **4**:745, 2005.

[37] K. Capelle and B. L. Györffy. Exploring dynamical magnetism with time-dependent density-functional theory: From spin fluctuations to Gilbert damping. *EPL (Europhysics Letters)*, **61**:354, 2003.

[38] K. Capelle, N. A. Lima, and L. N. Oliveira. In N. I. Gidopoulos and S. Wilson, editors, *Progress in Theoretical Chemistry and Physics*. Kluwer Academic Publishers, 2003.

[39] K. Capelle, G. Vignale, and B. L. Györffy. Spin currents and spin dynamics in time-dependent density-functional theory. *Phys. Rev. Lett.*, **87**:206403, 2001.

[40] C. Caroli, R. Combescot, D. Lederer, P. Nozieres, and D. Saint-James. A direct calculation of the tunnelling current: II. Free electron description. *J. Phys. C: Solid State Phys.*, **4**:2598, 1971.

[41] C. Caroli, R. Combescot, P. Nozieres, and D. Saint-James. Direct calculation of the tunnelling current. *J. Phys. C: Solid State Phys.*, **4**:916, 1971.

[42] C. Caroli, R. Combescot, P. Nozieres, and D. Saint-James. A direct calculation of the tunnelling current: IV. Electron-phonon interaction effects. *J. Phys. C: Solid State Phys.*, **5**:21, 1972.

[43] C. Cheng, J. Evans, and T. Van Voorhis. Simulating molecular conductance using real-time density functional theory. *Phys. Rev. B*, **74**:155112, 2006.

[44] D. Chiba, M. Sawicki, Y. Nishitani, Y. Nakatani, F. Matsukura, and H. Ohno. Magnetization vector manipulation by electric fields. *Nature*, **455**:515, 2008.

[45] M. Cini. Time-dependent approach to electron transport through junctions: General theory and simple applications. *Phys. Rev. B*, **22**:5887, 1980.

[46] M. Cini. *Topics and Methods in Condensed Matter Theory*. Springer, 2007.

[47] A. J. Cohen, P. Mori-Sánchez, and W. Yang. Insights into current limitations of density functional theory. *Science*, **321**:792, 2008.

[48] R. Combescot. A direct calculation of the tunnelling current: III. Effect of localized impurity states in the barrier. *J. Phys. C: Solid State Phys.*, **4**:2611, 1971.

[49] S. M. Cronenwett, T. H. Oosterkamp, and L. P. Kouwenhoven. A tunable Kondo effect in quantum dots. *Science*, **281**:540, 1998.

[50] J. C. Cuevas and E. Scheer. *Molecular Electronics: An Introduction to Theory and Experiment.* World Scientific, 2010.

[51] Y. Cui and C. M. Lieber. Functional nanoscale electronic devices assembled using silicon nanowire building blocks. *Science*, **291**:851, 2001.

[52] S. Das Sarma. Spintronics. *American Scientist*, **89**(6):516, 2001.

[53] C. Dekker. Carbon nanotubes as molecular quantum wires. *Physics Today*, **52**:22, 1999.

[54] S. O. Demokritov (Ed.). *Spin Wave Confinement.* Pan Stanford Publishing, 2009.

[55] O. Derzhko. Jordan-Wigner fermionization and the theory of low-dimensional quantum spin models. Dynamic properties. In J. Jedrzejewski, editor, *Condensed Matter Physics in the Prime of* 21^{st} *century: Phenomena, Materials, Ideas, Methods*, Proceedings of the 43rd Karpacz Winter School of Theoretical Physics, page 35. World Scientific, 2008.

[56] J. des Cloizeaux and J. J. Pearson. Spin-wave spectrum of the antiferromagnetic linear chain. *Phys. Rev.*, **128**:2131, 1962.

[57] M. Di Ventra. *Electrical Transport in Nanoscale Systems.* Cambridge University Press, 2008.

[58] M. Di Ventra and T. N. Todorov. Transport in nanoscale systems: the microcanonical versus grand-canonical picture. *J. Phys.: Condens. Matter*, **16**:8025, 2004.

[59] T. Dietl, D. D. Awschalom, M. Kaminska, and H. Ohno (Eds.). *Spintronics, Volume 82 (Semiconductors and Semimetals).* Elsevier, Amsterdam, 2008.

[60] P. A. M. Dirac. The quantum theory of the electron. *Proc. R. Soc. Lond. A*, **117**:610, 1928.

[61] B. Doyon. New method for studying steady states in quantum impurity problems: The interacting resonant level model. *Phys. Rev. Lett.*, **99**:076806, 2007.

[62] A. Driskill-Smith, D. Apalkov, V. Nikitin, X. Tang, S. Watts, D. Lottis, K. Moon, A. Khvalkovskiy, R. Kawakami, X. Luo, A. Ong, E. Chen, and M. Krounbi. Latest advances and roadmap for in-plane and perpendicular STT-RAM. 3rd IEEE International Memory Workshop (IMW), page 1. IEEE, 2011.

[63] U. Ebels, D. Houssameddine, I. Firastrau, D. Gusakova, C. Thirion, B. Dieny, and L. D. Buda-Prejbeanu. Macrospin description of the perpendicular polarizer-planar free-layer spin-torque oscillator. *Phys. Rev. B*, **78**:024436, 2008.

[64] M. Eltschka, M. Wötzel, J. Rhensius, S. Krzyk, U. Nowak, M. Kläui, T. Kasama, R. E. Dunin-Borkowski, L. J. Heyderman, H. J. van Driel, and R. A. Duine. Nonadiabatic spin torque investigated using thermally activated magnetic domain wall dynamics. *Phys. Rev. Lett.*, **105**:056601, 2010.

[65] J. M. Elzerman, R. Hanson, L. H. W van Beveren, S. Tarucha, L. M. K. Vandersypen, and L. P. Kouwenhoven. Semiconductor few-electron quantum dots as spin qubits. In W. D. Heiss, editor, *Quantum Dots: A Doorway To Nanoscale Physics*, volume 667 of *Lecture Notes in Physics*. Springer, 2005.

[66] F. Evers, F. Weigend, and M. Koentopp. Conductance of molecular wires and transport calculations based on density-functional theory. *Phys. Rev. B*, **69**:235411, 2004.

[67] L. D. Faddeev and L. A. Takhtajan. What is the spin of a spin wave? *Phys. Lett. A*, **85**:375, 1981.

[68] A. Fert. Nobel lecture: Origin, development, and future of spintronics. *Rev. Mod. Phys.*, **80**:1517, 2008.

[69] A. Filippetti, C. D. Pemmaraju, S. Sanvito, P. Delugas, D. Puggioni, and V. Fiorentini. Variational pseudo-self-interaction-corrected density functional approach to the *ab initio* description of correlated solids and molecules. *Phys. Rev. B*, **84**:195127, 2011.

[70] C. Fiolhais, F. Nogueira, and M. A. L. Marques (Eds.). *A Primer in Density Functional Theory*. Lecture Notes in Physics, Vol. 620. Springer, 2003.

[71] G. D. Fuchs, A. L. Falk, V. V. Dobrovitski, and D. D. Awschalom. Spin coherence during optical excitation of a single nitrogen-vacancy center in diamond. *Phys. Rev. Lett.*, 108:157602, Apr 2012.

[72] M. Fühnle, R. Drautz, R. Singer, D. Steiauf, and D.V. Berkov. A fast ab initio approach to the simulation of spin dynamics. *Computational Materials Science*, **32**:118, 2005.

[73] K. Galatsis, A. Khitun, R. Ostroumov, K. L. Wang, W. R. Dichtel, E. Plummer, J. F. Stoddart, J. I. Zink, Jae Young Lee, Ya-Hong Xie, and Ki Wook Kim. Alternate state variables for emerging nanoelectronic devices. *Nanotechnology, IEEE Transactions on*, **8**:66, 2009.

[74] A. Georges and G. Kotliar. Hubbard model in infinite dimensions. *Phys. Rev. B*, **45**:6479, 1992.

[75] T. Giamarchi. *Quantum Physics in One Dimension.* Oxford University Press, Oxford, 2004.

[76] T. L. Gilbert. A Lagrangian formulation of the gyromagnetic equation of the magnetic field. *Phys. Rev.*, **100**:1243, 1955 [Abstract only; full report, Armor Research Foundation Project No. A059, Supplementary Report, May 1, 1956] (unpublished).

[77] T. L. Gilbert. A phenomenological theory of damping in ferromagnetic materials. *Magnetics, IEEE Transactions on*, **40**:3443, 2004.

[78] K. Gilmore, Y. U. Idzerda, and M. D. Stiles. Identification of the dominant precession-damping mechanism in Fe, Co, and Ni by first-principles calculations. *Phys. Rev. Lett.*, **99**:027204, 2007.

[79] D. Goldhaber-Gordon, H. Shtrikman, D. Mahalu, D. Abusch-Magder, U. Meirav, and M. A. Katner. Kondo effect in a single-electron transistor. *Nature (London)*, **391**:156, 1998.

[80] V. J. Goldman, D. C. Tsui, and J. E. Cunningham. Observation of intrinsic bistability in resonant tunneling structures. *Phys. Rev. Lett.*, **58**:1256, 1987.

[81] P. Grünberg, R. Schreiber, Y. Pang, M. B. Brodsky, and H. Sowers. Layered magnetic structures: Evidence for antiferromagnetic coupling of Fe layers across Cr interlayers. *Phys. Rev. Lett.*, **57**:2442, 1986.

[82] F. S. M. Guimarães, D. F. Kirwan, A. T. Costa, R. B. Muniz, D. L. Mills, and M. S. Ferreira. Carbon nanotube: A low-loss spin-current waveguide. *Phys. Rev. B*, **81**:153408, 2010.

[83] F. S. M. Guimarães, A. T. Costa, R. B. Muniz, and M. S. Ferreira. Graphene-based spin-pumping transistor. *Phys. Rev. B*, **81**:233402, 2010.

[84] O. Gunnarsson and K. Schönhammer. Density-functional treatment of an exactly solvable semiconductor model. *Phys. Rev. Lett.*, **56**:1968, 1986.

[85] J. A. Gupta, R. Knobel, N. Samarth, and D. D. Awschalom. Ultrafast manipulation of electron spin coherence. *Science*, **292**:5526, 2001.

[86] R. Hanson. *Electron spins in semiconductor quantum dots.* PhD thesis, Delft University of Technology, Netherlands, 2005.

[87] R. Hanson and D. D. Awschalom. Coherent manipulation of single spins in semiconductors. *Nature (London)*, **453**:1043, 2008.

[88] R. Hanson, O. Gywat, and D. D. Awschalom. Room-temperature manipulation and decoherence of a single spin in diamond. *Phys. Rev. B*, **74**:161203, 2006.

[89] R. Hanson, L. P. Kouwenhoven, J. R. Petta, S. Tarucha, and L. M. K. Vandersypen. Spins in few-electron quantum dots. *Rev. Mod. Phys.*, **79**:1217, 2007.

[90] H. Haug and A.-P. Jauho. *Quantum Kinetics in Transport and Optics of Semiconductors.* Springer, 1996.

[91] A. J. Heinrich, J. A. Gupta, C. P. Lutz, and D. M. Eigler. Single-atom spin-flip spectroscopy. *Science*, **306**(5695):466, 2004.

[92] W. R. Hendee and C. J. Morgan. Magnetic resonance imaging. Part I–physical principles. *West J Med.*, **141**:491, 2011.

[93] S. Hershfield, J. H. Davies, and J. W. Wilkins. Probing the Kondo resonance by resonant tunneling through an Anderson impurity. *Phys. Rev. Lett.*, **67**:3720, 1991.

[94] S. Hershfield, J. H. Davies, and J. W. Wilkins. Resonant tunneling through an Anderson impurity. I. Current in the symmetric model. *Phys. Rev. B*, **46**:7046, 1992.

[95] B. Hillebrands and K. Ounadjela (Eds.). *Spin Dynamics in Confined Magnetic Structures I.* Springer, 2002.

[96] C. F. Hirjibehedin, C.-Y. Lin, A. F. Otte, M. Ternes, C. P. Lutz, B. A. Jones, and A. J. Heinrich. Large magnetic anisotropy of a single atomic spin embedded in a surface molecular network. *Science*, **317**:1199, 2007.

[97] C. F. Hirjibehedin, C. P. Lutz, and A. J. Heinrich. Spin coupling in engineered atomic structures. *Science*, **312**:1021, 2006.

[98] P. Hohenberg and W. Kohn. Inhomogeneous electron gas. *Phys. Rev.*, **136**:B864, 1964.

[99] T. Holstein and H. Primakoff. Field dependence of the intrinsic domain magnetization of a ferromagnet. *Phys. Rev.*, **58**:1098, 1940.

[100] A. P. Horsfield, D. R. Bowler, and A. J. Fisher. Open-boundary Ehrenfest molecular dynamics: towards a model of current induced heating in nanowires. *J. Phys.: Condens. Matter*, **16**:L65, 2004.

[101] A. P. Horsfield, D. R. Bowler, A. J. Fisher, T. N. Todorov, and M. J. Montgomery. Power dissipation in nanoscale conductors: classical, semi-classical and quantum dynamics. *J. Phys.: Condens. Matter*, **16**:3609, 2004.

[102] A. P. Horsfield, D. R. Bowler, A. J. Fisher, T. N. Todorov, and C. G. Sánchez. Beyond Ehrenfest: correlated non-adiabatic molecular dynamics. *J. Phys.: Condens. Matter*, **16**:8251, 2004.

[103] D. Houssameddine, U. Ebels, B. Delaët, B. Rodmacq, I. Firastrau, F. Ponthenier, M. Brunet, C. Thirion, J.-P. Michel, L. Prejbeanu-Buda, M.-C. Cyrille, O. Redon, and B. Dieny. Spin-torque oscillator using a perpendicular polarizer and a planar free layer. *Nat. Mat.*, **6**:447, 2007.

[104] J. Hubbard. Electron correlations in narrow energy bands. *Proc. R. Soc. London A*, **276**:238, 1963.

[105] J. Hubbard. Electron correlations in narrow energy bands. III. An improved solution. *Proc. R. Soc. London A*, **281**:401, 1964.

[106] A. Hurley, N. Baadji, and S. Sanvito. Perturbative approach to the Kondo effect in magnetic atoms on nonmagnetic substrates. *Phys. Rev. B*, **84**:115435, 2011.

[107] A. Hurley, N. Baadji, and S. Sanvito. Spin-flip inelastic electron tunneling spectroscopy in atomic chains. *Phys. Rev. B*, **84**:035427, 2011.

[108] S. Ikeda, J. Hayakawa, Y. Ashizawa, Y. M. Lee, K. Miura, H. Hasegawa, M. Tsunoda, F. Matsukura, and H. Ohno. Tunnel magnetoresistance of 604% at 300 K by suppression of Ta diffusion in CoFeB/MgO/CoFeB pseudo-spin-valves annealed at high temperature. *Appl. Phys. Lett.*, **93**:082508, 2008.

[109] A. Imamoglu, D. D. Awschalom, G. Burkard, D. P. DiVincenzo, D. Loss, M. Sherwin, and A. Small. Quantum information processing using quantum dot spins and cavity QED. *Phys. Rev. Lett.*, **83**:4204, 1999.

[110] Y. Imry and R. Landauer. Conductance viewed as transmission. *Rev. Mod. Phys.*, **71**:S306, 1999.

[111] H. Jahn and E. Teller. Low-dimensional systems: Theory, preparation, and some applications. In L. M. Liz-Marzán and M. Giersig, editors, *Proceedings of the NATO Advanced Research Workshop held in Puszczykowo, Poland, 16-19 May 2002*, volume 91 of *Series: NATO Science Series II: Mathematics, Physics and Chemistry*, page 220. North-Holland, 2003.

[112] J. F. Janak. Proof that $\partial E/\partial n_i = \epsilon$ in density-functional theory. *Phys. Rev. B*, **18**:7165, 1978.

[113] R. Jansen. Silicon spintronics. *AAPPS Bulletin*, **18**, N.5:21, 2008.

[114] F. Jelezko, T. Gaebel, I. Popa, A. Gruber, and J. Wrachtrup. Observation of coherent oscillations in a single electron spin. *Phys. Rev. Lett.*, **92**:076401, 2004.

[115] M. Johnson and R. H. Silsbee. Interfacial charge-spin coupling: Injection and detection of spin magnetization in metals. *Phys. Rev. Lett.*, **55**:1790, 1985.

[116] T. M Jovin. Quantum dots finally come of age. *Nature Biotechnology*, **21**:32, 2003.

[117] G. S. Joyce. Classical Heisenberg model. *Phys. Rev.*, **155**:478, 1967.

[118] M. Julliere. Tunneling between ferromagnetic films. *Phys. Lett. A*, **54**:225, 1975.

[119] L. P. Kadanoff and G. Baym. *Quantum statistical mechanics: Green's function methods in equilibrium and nonequilibrium problems.* W.A. Benjamin, 1962.

[120] A. Kamenev and W. Kohn. Landauer conductance without two chemical potentials. *Phys. Rev. B*, **63**:155304, Mar 2001.

[121] M. Karbach and G. Müller. Introduction to the Bethe ansatz I. *Computers in Physics*, **11**:36, 1997.

[122] M. A. Kastner. The single electron transistor and artificial atoms. *Annalen der Physik*, **9**:885, 2000.

[123] T. Kasuya. Electrical resistance of ferromagnetic metals. *Prog. Theor. Phys.*, **16**:58, 1956.

[124] S.-H. Ke, H. U. Baranger, and W. Yang. Electron transport through molecules: self-consistent and non-self-consistent approaches. *Phys. Rev. B*, **70**:085410, 2004.

[125] L. V. Keldysh. Diagram technique for nonequilibrium processes. *Sov. Phys. JETP*, **20**:1018, 1965.

[126] E. Khosravi, A.-M. Uimonen, A. Stan, G. Stefanucci, S. Kurth, R. van Leeuwen, and E. K. U. Gross. Correlation effects in bistability at the nanoscale: Steady state and beyond. *Phys. Rev. B*, **85**:075103, 2012.

[127] J. M. Kikkawa and D. D. Awschalom. Lateral drag of spin coherence in gallium arsenide. *Nature (London)*, **397**:139, 1998.

[128] J. M. Kikkawa and D. D. Awschalom. Resonant spin amplification in n-type GaAs. *Phys. Rev. Lett.*, **80**:4313, 1998.

[129] J. S. Kilby. Turning potential into realities: the invention of the integrated circuit. *Nobel Lecture*, 2000.

[130] A. V. Kimel, A. Kirilyuk, P. A. Usachev, R. V. Pisarev, A. M. Balbashov, and Th. Rasing. Ultrafast non-thermal control of magnetization by instantaneous photomagnetic pulses. *Nature (London)*, **435**:655, 2005.

[131] A. Kirilyuk, A. V. Kimel, and Th. Rasing. Ultrafast optical manipulation of magnetic order. *Rev. Mod. Phys.*, **82**:2731, 2010.

[132] S. I. Kiselev, J. C. Sankey, N. I. Krivorotov, N. C. Emley, J. R. Schoelkopf, R. A. Buhrman, and D. C. Ralph. Microwave oscillations of a nanomagnet driven by a spin-polarized current. *Nature (London)*, **425**:380, 2003.

[133] M. Koentopp, C. Chang, K. Burke, and R. Car. Density functional calculations of nanoscale conductance. *J. Phys.: Condens. Matter*, **20**:083203, 2008.

[134] W. Kohn and L. J. Sham. Self-consistent equations including exchange and correlation effects. *Phys. Rev.*, **140**:A1133, 1965.

[135] J. Kondo. Resistance minimum in dilute magnetic alloys. *Prog. Theor. Phys.*, **32**:37, 1964.

[136] J. Kondo. Theory of Dilute Magnetic Alloys. In F. Seitz, D. Turnbull, and Ehrenreich, editors, *Solid State Physics*, volume 23, page 183. Academic Press, 1969.

[137] F. H. L. Koppens, C. Buizert, K. J. Tielrooij, I. T. Vink, K. C. Nowack, T. Meunier, L. P. Kouwenhoven, and L. M. K. Vandersypen. Driven coherent oscillations of a single electron spin in a quantum dot. *Nature (London)*, **442**:766, 2006.

[138] W. Koshibae, N. Furukawa, and N. Nagaosa. Real-time quantum dynamics of interacting electrons: Self-organized nanoscale structure in a spin-electron coupled system. *Phys. Rev. Lett.*, **103**:266402, 2009.

[139] L. P. Kouwenhoven, D. G. Austing, and S. Tarucha. Few-electron quantum dots. *Rep. Prog. Phys.*, **64**:701, 2001.

[140] L. P. Kouwenhoven, C. M. Marcus, P. L. McEuen, S. Tarucha, R. M. Westervelt, and N. S. Wingreen. Electron transport in quantum dots. In L. L. Sohn, L. P. Kouwenhoven, and G. Schönl, editors, *Mesoscopic Electron Transport*, page 105. Kluwer Academic, 1997.

[141] S. Krause, L. Berbil-Bautista, G. Herzog, M. Bode, and R. Wiesendanger. Current-induced magnetization switching with a spin-polarized scanning tunneling microscope. *Science*, **317**:1537, 2007.

[142] H. R. Krishna-murthy, J. W. Wilkins, and K. G. Wilson. Renormalization-group approach to the Anderson model of dilute magnetic alloys. I. Static properties for the symmetric case. *Phys. Rev. B*, **21**:1003, 1980.

[143] R. Kubo. The fluctuation-dissipation theorem. *Rep. Prog. Phys.*, **29**:255, 1966.

[144] S. Kurth, G. Stefanucci, C.-O. Almbladh, A. Rubio, and E. K. U. Gross. Time-dependent quantum transport: A practical scheme using density functional theory. *Phys. Rev. B*, **72**:035308, 2005.

[145] S. Kurth, G. Stefanucci, E. Khosravi, C. Verdozzi, and E. K. U. Gross. Dynamical Coulomb blockade and the derivative discontinuity of time-dependent density functional theory. *Phys. Rev. Lett.*, **104**:236801, 2010.

[146] E. A. Laird, C. Barthel, E. I. Rashba, C. M. Marcus, M. P. Hanson, and A. C. Gossard. Hyperfine-mediated gate-driven electron spin resonance. *Phys. Rev. Lett.*, **99**:246601, 2007.

[147] B. Lake, D. A. Tennant, C. D. Frost, and S. E. Nagler. Quantum criticality and universal scaling of a quantum antiferromagnet. *Nature Materials*, **4**:329, 2005.

[148] L. D. Landau and E. M. Lifshitz. Theory of the dispersion of magnetic permeability in ferromagnetic bodies. *Phys. Z. Sowietunion*, **8**:153, 1935.

[149] L. D. Landau and E. M. Lifshitz. *Quantum Mechanics: Non-Relativistic Theory.* Course of Theoretical Physics, Volume 3, 3d edition, Elsevier, 1981.

[150] R. Landauer. Spatial variation of currents and fields due to localized scatterers in metallic conduction. *IBM Journal of Research and Development*, **1**(3):223, 1957.

[151] R. Landauer. Electrical resistance of disordered one-dimensional lattices. *Philosophical Magazine*, **21**:863, 1970.

[152] N. D. Lang. Resistance of atomic wires. *Phys. Rev. B*, **52**:5335, 1995.

[153] N. N. Ledentsov. Quantum dot laser. *Semicond. Sci. Technol.*, **26**:014001, 2011.

[154] W. Liang, M. P. Shores, M. Bockrath, J. R. Long, and H. Park. Kondo resonance in a single-molecule transistor. *Nature (London)*, **417**:725, 2002.

[155] E. H. Lieb and F. Y. Wu. The one-dimensional Hubbard model: a reminiscence. *Phycica A: Statistical Mechanics and its Applications*, **321**:1, 2002.

[156] A. I. Liechtenstein, M. I. Katsnelson, V. P. Antropov, and V. A. Gubanov. Local spin density functional approach to the theory of exchange interactions in ferromagnetic metals and alloys. *J. Magn. Magn. Mater.*, **67**:65, 1987.

[157] A. I. Liechtenstein, M. I. Katsnelson, and V. A. Gubanov. Exchange interactions and spin-wave stiffness in ferromagnetic metals. *Journal of Physics F: Metal Physics*, **14**:L125, 1984.

[158] N. A. Lima, M. F. Silva, L. N. Oliveira, and K. Capelle. Density functionals not based on the electron gas: Local-density approximation for a Luttinger liquid. *Phys. Rev. Lett.*, **90**:146402, 2003.

[159] E. Lipparini. *Modern Many-Particle Physics: Atomic Gases, Quantum Dots and Quantum Fluids.* World Scientific, 2003.

[160] K. L. Liu and S. H. Vosko. A time-dependent spin density functional theory for the dynamical spin susceptibility. *Can. J. Phys.*, **67**:1015, 1989.

[161] S. Lloyd. Ultimate physical limits to computation. *Nature (London)*, **406**:1047, 2000.

[162] D. Loss and D. P. DiVincenzo. Quantum computation with quantum dots. *Phys. Rev. A*, **57**:120, 1998.

[163] S. Loth, M. Etzkorn, C. P. Lutz, D. M. Eigler, and A. J. Heinrich. Measurement of fast electron spin relaxation times with atomic resolution. *Science*, **329**:1628, 2010.

[164] S. Loth, K. von Bergmann, M. Ternes, A. F. Otte, C. P. Lutz, and A. J. Heinrich. Contolling the state of quantum spins with electric currents. *Nature Physics*, **6**:340, 2010.

[165] J. Maciejko. *An introduction to Nonequilbrium Many-body Theory.* Unpublished, 2007.

[166] G. D. Mahan. *Many-Particle Physics.* Springer, 3d edition, 2000.

[167] J. Mallinson. On damped gyromagnetic precession. *Magnetics, IEEE Transactions on*, **23**:2003, 1987.

[168] A. Manchon, A. Pertsova, A. Ryzhanova, A. Vedyayev, and B. Dieny. Currents and torques due to spin-dependent diffraction in ferromagnetic/spin spiral bilayers. *Journal of Physics: Condensed Matter*, **20**:505213, 2008.

[169] M. Mantega. PhD thesis, University of Dublin, Ireland, 2012.

[170] M. A. L. Marques, C. A. Ullrich, F. Nogueira, A. Rubio, K. Burke, and E. K. U. Gross (Eds.). *Fundamentals of Time-Dependent Density Functional Theory.* Springer, 2012.

[171] E. J. McEniry, D. R. Bowler, D. Dundas, A. P. Horsfield, S. G. Sánchez, and T. N. Todorov. Dynamical simulation of inelastic quantum transport. *J. Phys.: Condens. Matter*, **19**:196201, 2007.

[172] E. J. McEniry, T. N. Todorov, and D. Dundas. Current-assisted cooling in atomic wires. *J. Phys.: Condens. Matter*, **21**:195304, 2009.

[173] C. D. Mee and E. D. Daniel (Eds.). *Magnetic recording technology.* McGraw-Hill, 1996.

[174] Y. Meir and N. S. Wingreen. Landauer formula for the current through an interacting electron region. *Phys. Rev. Lett.*, **68**:2512, 1992.

[175] Y. Meir, N. S. Wingreen, and P. A. Lee. Transport through a strongly interacting electron system: Theory of periodic conductance oscillations. *Phys. Rev. Lett.*, **66**:3048, 1991.

[176] S. Meng and E. Kaxiras. Real-time, local basis-set implementation of time-dependent density functional theory for excited state dynamics simulations. *J. Chem. Phys.*, **129**:054110, 2008.

[177] J. Merino and O. Gunnarsson. Simple model for scanning tunneling spectroscopy of noble metal surfaces with adsorbed Kondo impurities. *Phys. Rev. B*, **69**:115404, 2004.

[178] N. D. Mermin. Absence of ordering in certain classical systems. *J. Math. Phys.*, **8**:1061, 1967.

[179] N. D. Mermin and H. Wagner. Absence of ferromagnetism or antiferromagnetism in one- or two-dimensional isotropic heisenberg models. *Phys. Rev. Lett.*, **17**:1133, 1966.

[180] W. Metzner and D. Vollhardt. Correlated lattice fermions in d=∞ dimensions. *Phys. Rev. Lett.*, **62**:324, 1989.

[181] J. Miltat, G. Albuquerque, and A. Thiaville. An introduction to micromagnetics in the dynamic regime. In B. Hillebrands and K. Ounadjela, editors, *Spin Dynamics in Confined Magnetic Structures I*, volume 83 of *Topics in Applied Physics*, page 1. Springer, 2002.

[182] T. Miyazaki and N. Tezuka. Giant magnetic tunneling effect in $Fe/Al_2O_3/Fe$ junction. *J. Magn. Magn. Mater.*, **139**:L231, 1995.

[183] G. Müller, H. Thomas, H. Beck, and J. C. Bonner. Quantum spin dynamics of the antiferromagnetic linear chain in zero and nonzero magnetic field. *Phys. Rev. B*, **24**:1429, 1981.

[184] E. B. Myers, D. C. Ralph, J. A. Katine, R. N. Louie, and R. A. Buhrman. Current-induced switching of domains in magnetic multilayer devices. *Science*, **285**:867, 1999.

[185] N. Nagaosa. *Quantum Field Theory in Strongly Correlated Electronic Systems.* Springer, 1998.

[186] B. Naydenov, M. Mantega, I. Rungger, S. Sanvito, and J. J. Boland. Scattered surface charge density: A tool for surface characterization. *Phys. Rev. B*, **84**:195321, 2011.

[187] A. Nishino, T. Imamura, and N. Hatano. *I-V* characteristics of an open quantum dot with a Coulomb interaction: Extension of the Landauer formula with exact scattering eigenstates. *Phys. Rev. B*, **83**:035306, 2011.

[188] A. Nitzan and M. A. Ratner. Electron transport in molecular wire junctions. *Science*, **300**:1384, 2003.

[189] B. Novakovic and I. Knezevic. Quantum master eqautions in electronic transport. In D. Vasileska and S. M. Goodnick, editors, *Nano-electronic Devices: Semiclassical and Quantum Transport Modeling*, page 249. Springer, 2011.

[190] K. C. Nowack, F. H. L. Koppens, Yu. V. Nazarov, and L. M. K. Vandersypen. Coherent control of a single electron spin with electric fields. *Science*, **318**:1430, 2007.

[191] U. Nowak, O. N. Mryasov, R. Wieser, K. Guslienko, and R. W. Chantrell. Spin dynamics of magnetic nanoparticles: Beyond Brown's theory. *Phys. Rev. B*, **72**:172410, 2005.

[192] P. Orellana and F. Claro. A terahertz molecular switch. *Phys. Rev. Lett.*, **90**:178302, 2003.

[193] A. F. Otte, M. Ternes, S. Loth, C. P. Lutz, C. F. Hirjibehedin, and Heinrich A. J. Spin excitations of a Kondo-screened atom coupled to a second magnetic atom. *Phys. Rev. Lett.*, **103**:107203, 2009.

[194] D. A. Papaconstantopoulos. *Handbook of the band structure of elemental solids.* Plenum Press, 1986.

[195] J. Park, A. N. Pasupathy, J. I. Goldsmith, C. Chang, Y. Yaish, J. R. Petta, M. Rinkoski, J. P. Sethna, H. D. Abruña, P. L. McEuen, and D. C. Ralph. Coulomb blockade and the Kondo effect in single-atom transistors. *Nature (London)*, **417**:722, 2002.

[196] J. N. Pedersen and A. Wacker. Tunneling through nanosystems: Combining broadening with many-particle states. *Phys. Rev. B*, **72**:195330, 2005.

[197] P. S. Peercy. The drive to miniaturization. *Nature (London)*, **406**:1023, 2000.

[198] C. D. Pemmaraju, T. Archer, D. Sanchez-Portal, and S. Sanvito. Atomic-orbital-based approximate self-interaction correction scheme for molecules and solids. *Phys. Rev. B*, **75**:045101, 2007.

[199] J. P. Perdew. Density functional theory and the band gap problem. *Int. J. Quantum Chem.*, **28**:497, 2009.

[200] J. P. Perdew, K. Burke, and M. Ernzerhoff. Generalized gradient approximation made simple. *Phys. Rev. Lett.*, **77**:3865, 1996.

[201] J. P. Perdew and M. Levy. Physical content of the exact Kohn-Sham orbital energies: Band gaps and derivative discontinuities. *Phys. Rev. Lett.*, **51**:1884, 1983.

[202] J. P. Perdew, R. G. Parr, M. Levy, and J. L. Balduz. Density-functional theory for fractional particle number: Derivative discontinuities of the energy. *Phys. Rev. Lett.*, **49**:1691, 1982.

[203] J. P. Perdew and A Zunger. Self-interaction correction to the density-functional approximations for many-electron systems. *Phys. Rev. B*, **23**:5048, 1981.

[204] J. R. Petta, A. C. Johnson, J. M. Taylor, E. A. Laird, A. Yacoby, M. D. Lukin, C. M. Marcus, M. P. Hanson, and A. C. Gossard. Coherent manipulation of coupled electron spins in semiconductor quantum dots. *Science*, **309**:2180, 2005.

[205] C. P. Poole. *Electron Spin Resonance: A Comprehensive Treatise on Experimental Techniques.* Dover Publications, 1997.

[206] W. H. Press, S. A. Teukolsky, W. T. Vetterling, and B. P. Flannery. *Numerical Recipes in Fortran 77. The Art of Scientific Computing.* Cambridge University Press, 2nd edition, 1992.

[207] D. C. Ralph and M. D. Stiles. Current perspectives: Spin transfer torques. *J. Magn. Magn. Mater.*, **320**:1190, 2008.

[208] V. Ray, R. Subramanian, P. Bhadrachalam, L.-C. Ma, C.-U. Kim, and S. Jin Koh. CMOS-compatible fabrication of room-temperature single-electron devices. *Nature Nanotechnology*, **3**:603, 2008.

[209] A. R. Rocha. *Theoretical and computational aspects of electronic transport at the nanoscale.* PhD thesis, University of Dublin, Ireland, 2007.

[210] A. R. Rocha, V. M. García-Suárez, S. Bailey, C. Lambert, J. Ferrer, and S. Sanvito. Spin and molecular electronics in atomically generated orbital landscapes. *Phys. Rev. B*, **73**:085414, 2006.

[211] A. R. Rocha, V. M. García-Suárez, S. W. Bailey, C. J. Lambert, J. Ferrer, and S. Sanvito. Towards molecular spintronics. *Nature Materials*, **4**:335, 2005.

[212] E. S. Rodrigues, E. V. Anda, and P. Orellana. Time-dependent current oscillations through a quantum dot. *Phys. Rev. B*, **61**:8312, 2000.

[213] E. S. Rodrigues, E. V. Anda, P. Orellana, and H. N. Nazareno. Non-linear effects in resonant tunnelling through a quantum dot. *Solid State Communications*, **111**:217, 1999.

[214] M. A. Ruderman and C. Kittel. Indirect exchange coupling of nuclear magnetic moments by conduction electrons. *Phys. Rev.*, **96**:99, 1954.

[215] E. Runge and E. K. U. Gross. Density-functional theory for time-dependent systems. *Phys. Rev. Lett.*, **52**:997, 1984.

[216] I. Rungger and S. Sanvito. Algorithm for the construction of self-energies for electronic transport calculations based on singularity elimination and singular value decomposition. *Phys. Rev. B*, **78**:035407, 2008.

[217] D. A. Ryndyk, R. Gutierrez, B. Song, and G. Cuniberti. Green function techniques in the treatment of quantum transport at the molecular scale. In K. Yamanouchi W. Zinth I. Burghardt V. May D. A. Micha A. W. Castleman, J. P. Toennies and E. R. Bittner, editors, *Energy Transfer Dynamics in Biomaterial Systems*, volume 93 of *Springer Series in Chemical Physics*, page 213. Springer, 2009.

[218] R. Salikhov, R. Abrudan, F. Brüssing, St. Buschhorn, M. Ewerlin, D. Mishra, F. Radu, I.A. Garifullin, and H. Zabel. Precessional dynamics and damping in Co/Cu/Py spin valves. *Appl. Phys. Lett.*, **99**:092509, 2011.

[219] C. G. Sánchez, M. Stamenova, S. Sanvito, D. R. Bowler, A. P. Horsfield, and T. N. Todorov. Molecular conduction: Do time-dependent simulations tell you more than the Landauer approach? *J. Chem. Phys.*, **124**:214708, 2006.

[220] S. Sanvito. Chapter 7 Electron transport theory for large systems, in Computational Nanoscience. In *Computational Nanoscience*. The Royal Society of Chemistry, 2011.

[221] S. Sanvito. Molecular spintronics. *Chem. Soc. Rev.*, **40**:3336, 2011.

[222] K. Schönhammer, O. Gunnarsson, and R. M. Noack. Density-functional theory on a lattice: Comparison with exact numerical results for a model with strongly correlated electrons. *Phys. Rev. B*, **52**:2504, 1995.

[223] A. Scrinzi, M. Yu. Ivanov, R. Kienberger, and D. M. Villeneuve. Attosecond physics. *J. Phys. B: At. Mol. Opt. Phys.*, **39**:R1, Jun 2006.

[224] J. R. Shrieffer and P. A. Wolff. Relation between the Anderson and Kondo Hamiltonians. *Phys. Rev.*, **149**:491, 1966.

[225] B. Skubic, J. Hellsvik, L. Nordström, and O. Eriksson. A method for atomistic spin dynamics simulations: implementation and examples. *J. Phys.: Condens. Matter*, **20**:315203, 2008.

[226] J. C. Slater and G. F. Koster. Simplified LCAO method for the periodic potential problem. *Phys. Rev.*, **94**:1498, 1954.

[227] J. Slonczewski. Current-driven excitation of magnetic multilayers. *J. Magn. Magn. Mater.*, **159**:L1, 1996.

[228] M. E. Smith and J. H. Strange. NMR techniques in materials physics: a review. *Measurement Science and Technology*, **7**:449, 1996.

[229] M. Stamenova. *Atomistic simulations of spin dynamics.* PhD thesis, University of Dublin, Ireland, 2009.

[230] M. Stamenova and S. Sanvito. Dynamical exchange interactions in spin-dimers based on the time-dependent spin density functional theory (in preparation).

[231] M. Stamenova and S. Sanvito. Atomistic spin dynamics. In A. V. Narlikar and Y. Y. Fu, editors, *Oxford handbook on nanoscience and technology*, volume 1: Basic Aspects of *Oxford Handbooks in Physics Series.* Oxford University Press, 2010.

[232] C. Stamm, T. Kachel, N. Pontius, R. Mitzner, T. Quast, K. Holldack, S. Khan, C. Lupulescu, E. F. Aziz, M. Wietstruk, H. M. Dürr, and M. Eberhardt. Femtosecond modification of electron localization and transfer of angular momentum in nickel. *Nature Materials*, **6**:740, 2007.

[233] G. Stefanucci and C.-O. Almbladh. Time-dependent partition-free approach in resonant tunneling systems. *Phys. Rev. B*, **69**:195318, 2004.

[234] G. Stefanucci and S. Kurth. Towards a description of the Kondo effect using time-dependent density functional theory. *Phys. Rev. Lett.*, **107**:216401, 2011.

[235] G. Stefanucci, S. Kurth, E. K. U. Gross, and A. Rubio. Time-dependent transport phenomena. volume 161 of *Molecular and Nano Electronics: Analysis, Design and Simulation*, page 247. Elsevier, 2006.

[236] M. D. Stiles. Interlayer exchange coupling. *J. Magn. Magn. Mater.*, **200**:322, 1999.

[237] A. Sweetman, S. Jarvis, R. Danza, and P. Moriarty. Effect of the tip state during qPlus noncontact atomic force microscopy of Si(100) at 5 K: Probing the probe. *Beilstein J. Nanotechnol.*, **3**:25, 2012.

[238] S. Tarucha, K. Ono, T. Fujisawa, W. G. Van der Wiel, and L. P. Kouwenhoven. Interactions, spins and the Kondo effect in quantum-dot systems. In J. P. Bird, editor, *Electron Transport in Quantum dots.*

[239] G. Tatara and H. Kohno. Theory of current-driven domain wall motion: Spin transfer versus momentum transfer. *Phys. Rev. Lett.*, **92**:086601, 2004.

[240] J. Taylor, H. Guo, and J. Wang. *Ab initio* modeling of open systems: Charge transfer, electron conduction, and molecular switching of a C_{60} device. *Phys. Rev. B*, **63**:121104, 2001.

[241] J. Taylor, H. Guo, and J. Wang. *Ab initio* modeling of quantum transport properties of molecular electronic devices. *Phys. Rev. B*, **63**:245407, 2001.

[242] S. Teufel. *Adiabatic Perturbation Theory in Quantum Dynamics.* Springer, 2003.

[243] A. Thiaville, Y. Nakatani, J. Miltat, and N. Vernier. Domain wall motion by spin-polarized current: a micromagnetic study. *J. Appl. Phys.*, **95**:7049, 2004.

[244] L. Thomas, M. Hayashi, X. Jiang, R. Moriya, C. Rettner, and S. Parkin. Resonant amplification of magnetic domain-wall motion by a train of current pulses. *Science*, **315**:1553, 2007.

[245] T. N. Todorov. Time-dependent tight binding. *J. Phys.: Condens. Matter*, **13**:10125, 2001.

[246] T. N. Todorov. Tight-binding simulations of current-carrying nanostructures. *J. Phys.: Condens. Matter*, **14**:3049, 2002.

[247] T. N. Todorov, D. Dundas, and E. J. McEniry. Nonconservative generalized current-induced forces. *Phys. Rev. B*, **81**:075416, 2010.

[248] C. Toher and S. Sanvito. Efficient atomic self-interaction correction scheme for nonequilibrium quantum transport. *Phys. Rev. Lett.*, **99**:056801, 2007.

[249] C. Toher and S. Sanvito. Effects of self-interaction corrections on the transport properties of phenyl-based molecular junctions. *Phys. Rev. B*, **77**:155402, 2008.

[250] J. K. Tomfohr and O. F. Sankey. Time-dependent simulation of conduction through a molecule. *Phys. Status Solidi B*, **226**:115, 2001.

[251] S. Tomonaga. *The Story of Spin.* The University of Chicago Press, 1997.

[252] D. M. Toyli, C. D. Weis, G. D. Fuchs, T. Schenkel, and D. D. Awschalom. Chip-scale nanofabrication of single spins and spin arrays in diamond. *Nano Lett.*, **10**:3168, 2010.

[253] P. Tröster, P. Schmitteckert, and F. Evers. Transport calculations based on density functional theory, Friedel's sum rule, and the Kondo effect. *Phys. Rev. B*, **85**:115409, 2012.

[254] S.-H. Tsai and D. P. Landau. Spin dynamics: An atomistic simulation tool for magnetic systems. *Computing in Science & Engineering*, **10**:72, 2008.

[255] A. M. Tsvelick and P. B. Wiegmann. Exact results in the theory of magnetic alloys. *Adv. Physics*, **32**:453, 1983.

[256] I. Tudosa, C. Stamm, A. B. Kashuba, F. King, H. C. Siegmann, J. Stohr, G. Ju, B. Lu, and D. Weller. The ultimate speed of magnetic switching in granular recording media. *Nature*, **428**:831, 2004.

[257] A.-M. Uimonen, E. Khosravi, A. Stan, G. Stefanucci, S. Kurth, R. van Leeuwen, and E. K. U. Gross. Comparative study of many-body perturbation theory and time-dependent density functional theory in the out-of-equilibrium Anderson model. *Phys. Rev. B*, **84**:115103, 2011.

[258] H. van Houten and C. Beenakker. Quantum point contacts. *Physics Today*, **49**:22, 1996.

[259] M. van Kampen. *Ultrafast spin dynamics in ferromagnetic metals*. PhD thesis, Technische Universiteit Eindhoven, Netherlands, 2003.

[260] B. J. van Wees, H. van Houten, C. W. J. Beenakker, J. G. Williamson, L. P. Kouwenhoven, D. van der Marel, and C. T. Foxon. Quantized conductance of point contacts in a two-dimensional electron gas. *Phys. Rev. Lett.*, **60**:848, 1988.

[261] G. Vignale. Time-dependent current density functional theory. In M. A. L. Marques, C. A. Ullrich, F. Nogueira, A. Rubio, K. Burke, and E. K. U. Gross, editors, *Fundamentals of Time-Dependent Density Functional Theory*, volume 837 of *Lecture notes in Physics*, page 457. Springer, 2012.

[262] G. Vignale and M. Di Ventra. Incompleteness of the Landauer formula for electronic transport. *Phys. Rev. B*, **79**:014201, 2009.

[263] A. Šiber. Dynamics and (de)localization in a one-dimensional tight-binding chain. *Am. J. Phys.*, **74**:692, 2006.

[264] R. Vuilleumier. Density functional theory based ab initio molecular dynamics using Car-Parrinello approach. In G. Ciccotti M. Ferrario and K. Binder, editors, *Computer Simulations in Condensed Matter: From Materials to Chemical Biology. Volume 1*, page 223. Springer, 2006.

[265] Y. Wang, C.-Y. Yam, Th. Frauenheim, G. H. Chen, and T. A. Niehaus. An efficient method for quantum transport simulations in the time domain. *Chemical Physics*, **391**(1):69, 2011.

[266] E. W. Weisstein. *Titchmarsh Theorem.* From MathWorld–A Wolfram Web Resource. http://mathworld.wolfram.com/TitchmarshTheorem.html.

[267] P. Werner, T. Oka, and A. J. Millis. Diagrammatic Monte Carlo simulation of nonequilibrium systems. *Phys. Rev. B*, **79**:035320, 2009.

[268] D. A. Wharam, T. J. Thornton, R. Newbury, M. Pepper, H. Ahmed, J. E. F. Frost, D. G. Hasko, D. C. Peacock, D. A. Ritchie, and G. A. C. Jones. One-dimensional transport and the quantisation of the ballistic resistance. *J. of Phys. C*, **21**:L209, 1988.

[269] D. L. Whitenack, Y. Zhang, and A. Wasserman. Density functional theory for fractional particle number: derivative discontinuity of the total energy at the maximum number of bond electrons. *Phys. Rev. A*, **85**:042504, 2012.

[270] K. G. Wilson. The renormalization group: Critical phenomena and the Kondo problem. *Rev. Mod. Phys.*, **47**:733, 1975.

[271] N. S. Wingreen, A.-P. Jauho, and Y. Meir. Time-dependent transport through a mesoscopic structure. *Phys. Rev. B*, **48**:8487, 1993.

[272] G. O. Xianlong, M. Polini, D. Rainis, M. P. Tosi, and G. Vignale. Time-dependent current-density-functional theory of spin-charge separation and spin drag in one-dimensional ultracold fermi gases. *Phys. Rev. Lett.*, **101**:206402, 2008.

[273] K.-H. Yang and J. O. Hirschfelder. Generalizations of classical Poisson brackets to include spin. *Phys. Rev. A*, **22**:1814, 1980.

[274] K. Yosida. Magnetic properties of Cu-Mn alloys. *Phys. Rev.*, **106**:893, 1957.

[275] K. Yosida. *Theory of Magnetism.* Springer, 1996.

[276] A. M. Zagoskin. *Quantum Theory of Many-Body Systems: Techniques and Applications.* Springer, 1998.

[277] G. Zhang, W. Hübner, E. Beaurepaire, and J.-Y. Bigot. Laser-induced ultrafast demagnetization: Femtomagnetism, a new frontier? In B. Hillebrands and K. Ounadjela, editors, *Spin Dynamics in Confined Magnetic Structures I*, volume 83 of *Topics in Applied Physics*, page 245. Springer, 2002.

[278] S. Zhang and Z. Li. Roles of nonequilibrium conduction electrons on the magnetization dynamics of ferromagnets. *Phys. Rev. Lett.*, **93**:127204, 2004.

[279] X. Zheng, G. H. Chen, Y. Mo, S. K. Koo, H. Tian, C. Y. Yam, and Y. J. Yan. Time-dependent density functional theory for quantum transport. *J. Chem. Phys.*, **133**:114101, 2010.

[280] X. Zheng, F. Wang, C. Y. Yam, Y. Mo, and G. H. Chen. Time-dependent density-functional theory for open systems. *Phys. Rev. B*, **75**:195127, 2007.

[281] J.-G. Zhu and Y. Zheng. The micromagnetics of magnetoresistive random access memory. In B. Hillebrands and K. Ounadjela, editors, *Spin Dynamics in Confined Magnetic Structures I*, volume 83 of *Topics in Applied Physics*, page 1. Springer, 2002.

[282] Y. Zhu, J. Maciejko, T. Ji, H. Guo, and J. Wang. Time-dependent quantum transport: Direct analysis in the time domain. *Phys. Rev. B*, **71**:075317, 2005.

[283] D. Zubarev, V. Morosov, and G. Ropke. *Statistical Mechanics of Nonequilibrium Processes.* Academic Verlag, 1996.

[284] I. Žutić, J. Fabian, and S. Das Sarma. Spintronics: Fundamentals and applications. *Rev. Mod. Phys.*, **76**:323, 2004.